A NEW APPROACH TO MODEL FRICTION LOSSES IN THE WATER-ASSISTED PIPELINE TRANSPORTATION OF HEAVY OIL AND BITUMEN

By

M M A Sayeed Rushd

A thesis submitted in partial fulfillment of the requirements for the degree of

Doctor of Philosophy
in
Chemical Engineering

Department of Chemical and Materials Engineering
University of Alberta

ABSTRACT

Water lubricated pipe flow technology is an economic alternative for the long distance transportation of viscous oils like heavy oil and bitumen. The lubricated flow regime involves an oil-rich core surrounded by a turbulent water annulus. Energy consumption associated with this type of pipeline transportation system is orders of magnitude lower than comparable systems used to transport oil alone. In industrial applications of this technology, a thin oil film is always observed to coat the pipe wall. The natural process of wall coating during the lubrication is often referred to as “wall-fouling”. A wall-fouling layer can result in ultra-high values of hydrodynamic roughness (~ 1 mm). A detailed study of the hydrodynamic effects produced by wall-fouling is critical to the design and operation of oil/water pipelines, as the viscous layer can increase the pipeline pressure loss (and pumping power requirements) by 15 times or more. However, the hydrodynamic effects of wall-fouling in modeling the frictional pressure loss of water lubricated pipelines have not been addressed previously.

In the first phase of this research, the wall-fouling layer was replicated by coating a wall of a customized flow cell with a thin layer of viscous oil. The hydrodynamic effects of the wall-coating layer were experimentally investigated. The hydrodynamic roughness was determined in terms of Nikuradse sand grain equivalent by predicting the measured pressure gradients using commercial CFD software (ANSYS CFX 13.0). The CFD-based simulation process was validated using data produced as part of the current research as well as data obtained from the literature. In addition, the physical roughness was characterized by surface measurement, which was also used to corroborate the hydrodynamic roughness determined with the CFD simulation. This investigation brings previously unknown hydrodynamic effects of viscous wall-coating to light.

Next a parametric investigation of the hydrodynamic effects caused by the wall-coating of viscous oil was conducted. The controlled parameters included the thickness of the wall-coating layer, oil viscosity and water flow rate. For each set of test conditions, the pressure loss across the test section was measured and the hydrodynamic effect of the wall-coating on the pressure loss was determined. The CFD procedure that was developed previously was used to determine the hydrodynamic roughness produced by each different wall-coating. The same procedure was also applied for a set of pipeloop test results published elsewhere. Thus, the effects of wall-coating thickness, oil viscosity and water flow rate on the hydrodynamic roughness were evaluated. An interesting outcome of this parametric study is a novel correlation for the roughness produced by a wall-coating layer of viscous oil.

In the final phase of this research, a new method to model pressure loss in a water-assisted pipeline was introduced based on the results of the previous two phases. The hydrodynamic effects produced by the wall-fouling layer were incorporated in the new model as input parameters. The most important of these parameters were the thickness of wall-fouling layer and the equivalent hydrodynamic roughness it produces. The current CFD model was developed on the ANSYS-CFX platform. It captures the dominant effects of the thickness of the wall-fouling layer and the water hold-up, i.e., the *in situ* thickness of the lubricating water-annulus on frictional pressure loss. It was validated using test data obtained from tests conducted at the Saskatchewan Research Council's Pipe Flow Technology Centre using 100 mm and 260 mm pipelines. Compared to existing models, the new model produces more accurate predictions.

The results of the current research are directly applicable to pipeline systems in which a viscous wall-coating is produced, including water lubricated bitumen transport in the oil

sands industry, Cold Heavy Oil Production with Sand (CHOPS) and Steam Assisted Gravity Drainage (SAGD) surface production/transport lines. Other potential beneficiaries of this work are the pharmaceutical and polymer industries, as flow systems in these industries can involve viscous wall-fouling. It will also be useful for industries that deal with bio-fouling on walls like oceanic shipping (ships' bodies and hulls) and hydropower industries (pipes and channels). Most importantly, this research is expected to be immediately adopted in the non-conventional oil industry for pipeline design, operations troubleshooting and incorporation in pipeline leak detection algorithms.

PREFACE

Most of the works presented henceforth was conducted in the Pipeline Transport Processes Research Group Laboratory at the University of Alberta.

Chapter 2 consists of the literature review. It is my original, independent work. The relevant parts of this chapter have been used in the manuscripts.

A version of Chapter 3 has been submitted to the Journal of Hydraulic Engineering. I was the lead investigator, responsible for all major areas of concept formation, data collection and analysis, as well as manuscript composition. Ashraful Islam primarily contributed to manuscript edits. Sean Sanders was the supervisory author on this project and was involved throughout the project in concept formation and manuscript composition.

A version of Chapter 4 was published in the proceedings of SPE Heavy Oil Conference 2015 (Calgary, AB, Canada). Another version of the chapter has been submitted to the Journal of Petroleum Science. I was the lead investigator, responsible for all major areas of concept formation, data collection and analysis, as well as the majority of manuscript composition. A part of the data used in this project was collected by Melissa McKibben and co-workers in the Pipe Flow Technology Centre, Saskatchewan Research Council. Proper permission was obtained prior to using the data. Sean Sanders was the supervisory author on this project. He was involved throughout the project in concept formation and manuscript edits.

I was the lead investigator for the project presented in Chapter 5. A version of this chapter has been submitted to the Canadian Journal of Chemical Engineering. I was responsible for all major areas of concept formation, data analysis, as well as the majority of manuscript composition. All of the data used in this project was collected by Melissa McKibben and co-workers in the Pipe Flow Technology Centre, Saskatchewan Research Council. Proper permission was obtained for using the data. Sean Sanders was the supervisory author on this project and was involved throughout the project in concept formation and manuscript edits.

DEDICATION

My beloved mother, Rowshan Ara Begum.

ACKNOWLEDGMENTS

The absolute owner of all thanks and praises is Allah ﷲ (the Nature), Who is the Creator and the Sustainer of every existence. We would not exist and enjoy pleasure of the beautiful life on earth without His mercy. He is the most Merciful and most Gracious. He is the One, the Unique, the Absolute, the Perfect and the Pure. He does not need, but deserves our gratitude. I thank Allah ﷲ to ordain for me the honor of pursuing PhD degree at the University of Alberta, which is one of the renowned universities on earth.

I thank my parents, especially my mother, Rowshan Ara Begum for the inspiration which was fundamental to the initiation of my PhD program. Actually, it was my mother's prayer that acted as the seed for the germination of this dissertation. Her role was essential to the development of my personality. My father, Mohammad Mustafa Kamal also played an important role in the growth and development of myself. He deserves my especial gratitude as he taught me how to deal with the practicality of life and how to be patient in difficult times. My wife, Noor Hafsa also deserves my appreciation for her kind patience and support.

I am grateful to my supervisor, Sean Sanders. His guidance and support was remarkable in completing my PhD degree. His quite unique style of supervision helped me developing my very own way of doing research. Amazingly he charged my personal research battery to its optimum limit. He also inspired me to be a teacher in future with real time engineering experience.

Terry Runyon deserves my thanks. Without her kind assistance and support, it would not be possible to do the works required for this research. I am thankful to Kofi Freeman Adane for his advice, teaching, reviewing, criticism, support and assistance. David Breakey should be thanked especially for his important assistance in finalizing the thesis. Support from a number of other persons was also significant for this research. I thank Walter Henwood, Richard Cooper, Les Dean, Al Leskow, Imran Shah, Roohi Shokri and Ashraful Islam for their collaborative and individual contribution to my research.

This research was conducted through the support of the *NSERC Industrial Research Chair in Pipeline Transport Processes* (RSS). I acknowledge the support of Canada's Natural Sciences and Engineering Research Council (NSERC) and the sponsoring companies:

Canadian Natural Resources Limited, CNOOC-Nexen Inc., Saskatchewan Research Council Pipe Flow Technology Centre^{TM}, Shell Canada Energy, Suncor Energy, Syncrude Canada Ltd., Total, Teck Resources Ltd. and Paterson & Cooke Consulting Engineers Ltd.

TABLE OF CONTENTS

APPENDICES

LIST OF FIGURES

LIST OF TABLES

LIST OF SYMBOLS

Roman characters

A	Cross-sectional area perpendicular to flow direction (m^2)
A_c	Cross sectional area of oil core (m^2)
A_p	Surface area on a test plate (m^2)
C_w	Water fraction by volume by volume
C_{wi}	Input water fraction by volume
D	Diameter (m)
D_{eff}	Effective diameter of a fouled pipe (m)
D_c	Average diameter of oil core (m)
D_h	Hydraulic diameter (m)
D_{ij}	A tensor
$\%\Delta D_h$	Percentile reduction in hydraulic diameter (%), Eq. (4.1)
f	Friction factor
H	Height of the flow domain (m)
h_{eff}	Effective height (m)
H_o	In-situ volume fraction of oil
h_{tp}	Height of the test plate (m)
H_w	In-situ volume fraction of water
k	Turbulent kinetic energy (J/kg)
k_s	Hydrodynamic (Nikuradse sand grain) equivalent roughness (m)
k_s^+	Dimensionless hydrodynamic roughness
L	Length of the flow domain (m)
m_w	Mass flow rate of water (kg/s)
P_{ij}	Reynolds stress production tensor (N/m^2)
ΔP	Pressure drop (Pa)
$\Delta P/L$	Pressure gradient (Pa/m)
$\%\Delta P/L$	Percentile increment in pressure gradient (%), Eq. (4.2)
Q_o	Volumetric flow rater of oil (m^3/s)
Q_w	Volumetric flow rate of water (m^3/s)
R	Pipe radius (m)
R^2	Coefficient of determination

R^+	Dimensionless pipe radius
R_a	Average roughness (m)
Re	Reynolds number
Re_a	System specific *Re* proposed by Arney et al. (1993)
Re_w	Water Reynolds number
R_{rms}	Root Mean Square roughness (m)
R_{sk}	Skewness of roughness
R_z	Peak-to-Valley average (m)
S_i	Sum of body forces (N)
T	Temperature (°C)
t_c	Average thickness of wall-fouling/coating layer (m)
t_a	Thickness or width of water annulus (m)
U	Local velocity (m/s)
u^+	Dimensionless velocity
u_i^+	Dimensionless velocity in region i (Table 2.2)
u_τ	Friction or shear velocity (m/s)
U_i	Velocity vector (m/s)
U_n	Local velocity in region *n* (Table 2.2)
V	Average velocity (m/s)
V_w	Superficial velocity of water (m/s)
V_o	Superficial velocity of oil (m/s)
V_c	Velocity of oil core (m/s)
W	Width of the flow domain (m)
y	Distance with respect to the pipe wall (m)
y^+	Dimensionless distance from wall
y_c	Distant of the core from the pipe wall (m)
y_c^+	Dimensional distant of the core from the pipe wall

Greek characters

δ_{ij}	Identity matrix or Kronecker delta function
ε	Dissipation rate of kinetic energy (J/kg.s)
Φ_{ij}	Pressure-strain tensor
μ	Viscosity (Pa.s)

μ_o	Viscosity of oil (Pa.s)
μ_t	Turbulent viscosity (Pa.s)
μ_w	Viscosity of water (Pa.s)
μ^+	Dimensionless viscosity
v_w	Kinematic viscosity of water (m^2/s)
$v*$	Friction/Shear velocity (m/s)
ρ	Density (kg/m^3)
ρ_c	Density of the equivalent liquid considered by Arney et al. (1993) (kg/m^3)
ρ_m	Density of the equivalent liquid proposed by Rodriguez et al. (2009)
ρ_o	Density of oil (kg/m^3)
ρ_w	Density of water (kg/m^3)
ω	Specific energy dissipation (1/s)
τ_{ij}	Stress tensor (Pa)
τ_w	Wall shear stress (Pa)

Abbreviations

CAF	Core annular flow
CFD	Computational fluid dynamics
CWAF	Continuous water assisted flow
DNS	Direct Numeric Simulation
ID	Internal Diameter (m)
LES	Large Eddy Simulation
LPF	Lubricated Pipe Flow
NS	Navier Stokes (equations)
RANS	Reynolds Averaged Navier Stokes (equations)
RSM	Reynolds Stress Model
SLF	Self-lubricated flow
SRC	Saskatchewan Research Council

CHAPTER 1
INTRODUCTION

1.1. Background

Canadian reserves of non-conventional oils are some of the most important petroleum resources in the world (Nunez et al. 1998, CAPP 2015). The reserves primarily comprise two categories of non-conventional oils: heavy oil and bitumen. These oils are highly asphaltic, dense and viscous compared to conventional oils, such as Brent and West Texas Intermediate (Saniere et al. 2004, Martinez-Palou et al. 2011). Densities of these non-conventional oils are comparable to that of water (Bjoernseth 2013). Viscosities of heavy oil or bitumen can be greater than that of water by more than 5 orders of magnitude at room temperature (Ashrafi et al. 2011). These viscous oils are extracted using a variety of mining and *in situ* technologies in Canada. After extraction, the viscous oil typically must be transported from the production site to a central processing/upgrading facility. Numerous pipeline transportation methods are available, with conventional methods involving viscosity reduction through heating or dilution with condensate (Nunez et al. 1998, Saniere et al. 2004, Martinez-Palou et al. 2011, Hart 2014).

The present study is focused on the lubricated pipe flow (LPF) of heavy oils and bitumen, where a water annulus separates the viscous oil from the pipe wall. It is an alternative flow technology that is more economic and environmentally friendly than conventional heavy oil transportation technologies (Jean et al. 2005, McKibben and Gillies 2009). The benefit of LPF is that the annular water layer is found in the high shear region near the pipe wall, and thus much lower pumping energy input is required than if the viscous oil were transported alone at comparable process conditions (Arney et al. 1993, Joseph et al. 1999, McKibben et al. 2000b, Crivelaro et al. 2009, Rodriguez et al. 2009, Vuong et al. 2009, Strazza et al. 2011, McKibben and Gillies 2009).

A number of industrial scale applications of LPF have been reported in the literature. For example, a 6 inch diameter and 38.9 km long lubricated pipeline was successfully operated by Shell for more than 12 years in California (Joseph et al. 1997). The frictional pressure loss for this pipeline was orders of magnitude less than that for transporting only heavy oil and quite comparable to the loss for transporting only water (Bjornseth 2013). Up to 30% water by volume was added to operate the pipeline. At Lake Maracaibo in Venezuela, multiple water lubricated pipelines were used to transport heavy oil from the well clusters in the Orinoco Belt to a processing facility (Nunez et al. 1998). One of the challenges to operate these lubricated pipelines was cumulative wall-fouling, the buildup of oil on the inner wall of the pipe. Operational measures like increasing water fraction or water flow rate and changing the water chemistry were taken to control the buildup of fouling. However, it was not possible to stop wall-fouling completely. This flow technology was also used to transport heavy fuel oil in Spain (Bjornseth 2013). Syncrude Canada Ltd is currently using a 35 km long and 36 inch diameter pipeline to transport bitumen froth from a remote mine and extraction plant to upgrading facilities (Joseph et al. 1999, Schaan et al. 2002, Sanders et al. 2004). The froth is a mixture of 60% bitumen, 30% water and 10% solids. The requirement of adding water to this pipeline is negligible as water is already present in the mixture. During pipeline transportation, water droplets migrate from the bulk of the mixture to the high shear region near the pipe wall to form a sheath surrounding the bitumen-rich core. The lubrication process also produces a fouling layer of oil on the pipe wall. The wall-fouling thickness has been reported to be approximately 5% of the pipe's internal diameter under certain flow conditions (Joseph et al. 1999, Schaan et al. 2002). At present, Brazilian oil producers are working on ways to produce heavy oil from off-shore reservoirs by applying water lubricated flow in vertical pipelines (Bannwart et al. 2012, Gadelha et al. 2013).

Wall-fouling is a concern during lubricated pipe flow of heavy oil or bitumen (Nunez et al. 1998, Saniere et al. 2004). The probable flow regime in an LPF pipeline is schematically presented in Figure 1.1. In this figure, a fouling oil layer is shown to surround a thin water annulus that lubricates the oil-rich core. The mechanism of wall fouling has not previously been studied in any detail, although early experiments suggested the fouling layer is a natural consequence of the lubrication process (Joseph et al. 1999, Schaan et al. 2002, Vuong et al. 2009). Frictional pressure losses in a fouled pipe are much higher (by an order of magnitude or more) than those measured for an unfouled pipe (Arney et al. 1996), but still much lower than would be expected for transporting only heavy oil or bitumen. It has been found in repeated tests that the formation of this wall coating is practically unavoidable in industrial-scale applications of LPF technology (Joseph et al. 1999, McKibben et al. 2000b, Rodriguez et al. 2009, McKibben and Gillies 2009). Different degrees of wall fouling occur depending on the specific operating conditions, e.g., water cut, oil viscosity and superficial velocity (Joseph et al. 1999, Schaan et al. 2002, Rodriguez et al. 2009, Vuong et al. 2009). This kind of application of LPF where, under regular operating conditions, it must be accepted that the pipe wall is fouled with a layer of heavy oil is sometimes referred to as "continuous water assisted flow", or CWAF (McKibben et al. 2000b).

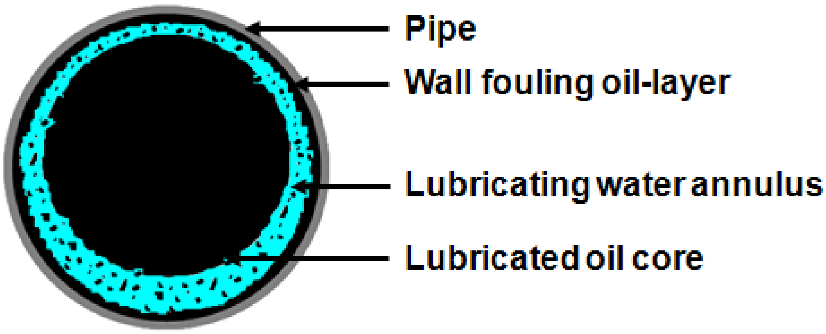

Figure 1.1. Hypothetical presentation of the flow regime in a water lubricated pipeline.

An important challenge in the general application of LPF technology is the lack of a reliable model to predict pressure loss on the basis of flow conditions (McKibben et al. 2000b, Shook et al. 2002, McKibben and Gillies 2009). The issue is that although a number of empirical, semi-mechanistic and numerical models have been proposed, these models are only appropriate for idealized applications of this technology or they are highly system-specific. Notable examples of models with limited applicability include those of Arney et al. (1993), Ho and Li (1994), Joseph et al. (1999), McKibben et al. (2000b) and Rodriguez et al. (2009).

The performance of existing models is demonstrated by comparing the predictions of five different models with experimental results collected for a pilot-scale LPF system in Figure 1.2. The pressure losses and flow rates are presented in this figure as dimensionless numbers: specifically, the water equivalent friction factor (f) and Reynolds number (Re_w), which are defined as follows:

$$f = \frac{\Delta P}{L}\frac{D}{2\rho_w V^2} \text{ ………… } (1.1)$$

$$Re_w = \frac{DV\rho_w}{\mu_w} \text{ …………..} (1.2)$$

where $\Delta P/L$ is the pressure gradient, D is the internal pipe diameter, V is the bulk velocity, and ρ_w and μ_w represent water density and viscosity, respectively. The experiments were conducted in 2 inch and 4 inch horizontal pipelines to collect data under typical CWAF operating conditions (McKibben et al., 2000b). The heavy oil had a density of 984 kg/m^3 and a viscosity of 24.9 Pa.s at 25°C. As shown in Figure 1.2, the models proposed by Arney et al. (1993), Ho and Li (1994) and Rodriguez et al. (2009) under predict the experimental values of *f* by an order of magnitude. This is due to the fact that these models were developed based on idealized applications of LPF technology, where the degree of fouling was negligible. On the other hand, the models of Joseph et al. (1999) and McKibben et al. (2000b) were developed using the pressure loss data collected from practical applications of LPF, involving appreciable wall-fouling, which explains why these models can provide better predictions.

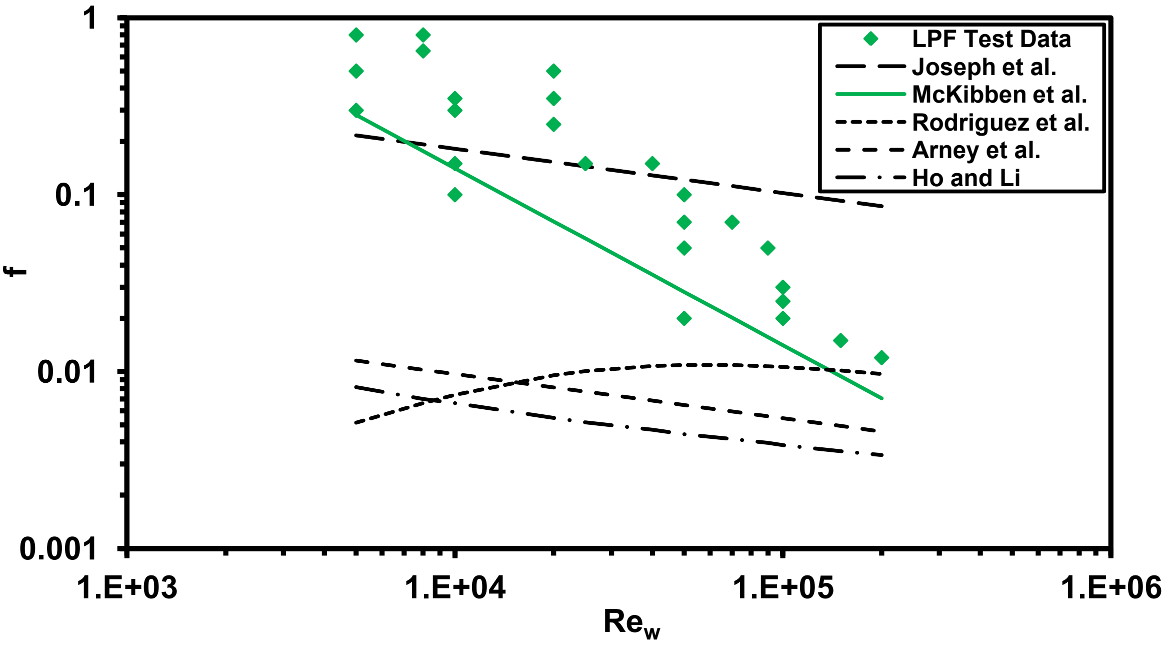

Figure 1.2. Comparison of experimental results and model predictions for an LPF system (experimental data of McKibben et al. 2000b).

As shown in Figure 1.2, models developed for LPF without wall-fouling cannot be applied to the LPF that involves wall-fouling and vice versa. Most of the existing models are empirical, i.e., rely on experimental data and thus cannot be extrapolated or applied to other situations. None of the existing models addressed specifically the effect of a fouling oil layer on pressure losses, although the importance of the viscous wall-coating layer on the pressure losses has been reported in the literature (see, for example, Brauner 1963, Shook et al. 2002 and Rodriguez et al. 2009).

Brauner (1963) found a layer of viscous wall-coating in a pipe to become rippled or physically rough when water flowed through the pipe under turbulent flow conditions. He estimated the equivalent hydrodynamic roughness, i.e., equivalent sand grain roughness produced by the viscous rough surface, to be on the order of 1 mm. The equivalent sand grain roughness is the hydrodynamic scale for a physically rough surface (White 1999). The concept was introduced by Nikuradse (1933). He experimentally determined the sand grain equivalent of commercial steel pipes to be approximately 0.05 mm, which is roughly two orders of magnitude lower than the equivalent roughness estimated for the viscous wall-coating.

Similar to Brauner (1963), Shook et al. (2002) found the friction factor for the water flowing in an oil-fouled pipe to be an order of magnitude greater than for water flowing in a clean pipe. The experiments were conducted in a 6 inch diameter pipe. The pipe wall was fouled during the lubricated pipe flow of bitumen. After completing a set of LPF tests, the bitumen-rich core was flushed from the pipeline with room temperature water. The flowing water had little effect on the wall fouled with bitumen for 20 – 30 minutes. This wall-fouling layer caused the higher friction. Rodriguez et al. (2009) found higher pressure losses for the LPF with wall-fouling compared to that for the LPF without wall-fouling. They conducted lab-scale experiments without wall-fouling in a 1 inch diameter glass pipe and used the data to develop a model. They found this model to under predict the pressure loss data obtained from pilot-scale tests conducted in a 3 inch steel pipe and identified the reason to be wall-fouling. The effect of wall-fouling was taken into account by empirically adjusting a coefficient in their initial model.

1.2. Research Motivation and Objective

Although wall-fouling is known to provide a significant contribution to the pressure loss in an LPF system, the hydrodynamic effects produced by this layer are yet to be studied in any detail. This is the primary motivation of the current research. The main objective of this study is to investigate the effects of wall-fouling on energy consumption (i.e., the frictional pressure losses) in LPF systems with fouled walls, i.e., in continuous water assisted flow (CWAF) applications. The aim is to develop a new modeling approach to predict the frictional pressure losses and to improve modeling capabilities by analyzing the physical mechanisms responsible for pressure losses in a CWAF pipeline. The research is conducted in three phases:

1) The hydrodynamic contributions of a wall-fouling layer are investigated using a purpose-built flow cell. The experiments involve coating one wall of the flow cell with viscous oil and measuring the pressure losses. Simulations are then conducted with the Computational Fluid Dynamics (CFD) software ANSYS CFX 13.0 to determine the hydrodynamic roughness of the oil layer. The CFD-based simulation procedure is validated with data produced as part of the current experimental program and, also, with data available in the literature. The key steps of this phase are:

   - Design, fabricate and commission an experimental apparatus (flow cell) that provided the ability to study the hydrodynamic effects produced by wall-coating layers of oils of different viscosities.
   - Develop a new procedure to quantify the hydrodynamic roughness produced by a layer of viscous oil coated on a wall of the flow cell.

2) The simulation procedure validated in the first phase is applied here. Experiments are done with the same flow cell but sample oils having very different viscosities are tested. Experimental data from pipeline tests conducted in the Saskatchewan Research Council's Pipe Flow Technology Centre are also used. The major components of this phase are:

   - Determine the equivalent hydrodynamic roughnesses produced by the oil layers of different viscosities.
   - Correlate the equivalent roughness produced by a wall-coating layer to a measurable parameter, such as the thickness of the coating layer.

3) The results of the previous phases are applied to introduce a new modeling approach to predict pressure losses in CWAF pipelines. The new approach is developed on the basis of the data provided by the Saskatchewan Research Council's Pipe Flow Technology Centre. The most important steps of this phase are:

   - Determine the equivalent hydrodynamic roughness produced by wall-fouling layers in different CWAF pipelines.
   - Analyze the results and correlate the equivalent roughness to the important flow variables, e.g., mixture flow rate and water fraction.

- Test the performance of the new modeling approach against the performance of existing models.

1.3. Thesis Structure

The dissertation is organized in a paper-based format. Chapters 3, 4 and 5 each contain a manuscript submitted for publication. Chapter 2 provides a literature review, which is the starting point of the current research. The importance of adding this research to the current knowledge-base is highlighted in this chapter.

Chapter 3 describes the experimental and the simulation techniques developed using a simple rectangular flow cell and the CFD software package ANSYS CFX 13.0, respectively. The flow cell is used to experimentally investigate the hydrodynamic effects produced by a wall-coating layer of heavy oil. The equivalent roughness produced by the viscous wall-coating is determined using CFD simulations, which is a new approach. The validation of this new CFD-based method is included in this chapter. In Chapter 4, the focus is on a parametric study of the hydrodynamic roughness produced by a viscous wall. The major parameters studied here are the thickness of the wall-coating, the oil viscosity and the flow rate (or Reynolds number) of water. A new correlation between the coating thickness and the corresponding equivalent roughness is presented in this chapter. Thus, the contents of Chapters 3 and 4 demonstrate the hydrodynamic effects caused by the viscous wall-coating, which is an idealistic simulation of wall-fouling in a continuous water assisted flow pipeline. These two chapters also make it evident that the large equivalent roughness resulting from a viscous wall-coating can be correlated to a measurable process parameter, such as the physical thickness of the wall-coating layer.

Chapter 5 builds on the knowledge gained from the previous chapters and addresses the core objective of the thesis, which is the development of a new approach to model frictional pressure losses in CWAF pipelines. The development and application of the new methodology are explained in this chapter. This modeling method is capable of taking into account the hydrodynamic effects of the wall-fouling and water “hold up” or *in situ* water fraction. The new approach provides more accurate predictions of frictional pressure losses compared to the existing models, and is much more broadly applicable than any existing model.

Chapter 6 presents a summary of the key findings of Chapters 2 to 5 and includes a concluding discussion of the results. Recommendations to advance the current research through future studies are also presented in this chapter.

The Appendices are presented at the end of the thesis. All data, error analyses, experimental evidences, photographs and detailed descriptions are incorporated in this section.

1.4. Contributions

A new approach to model CWAF pressure losses

The most important contribution of this study is a new approach to model pressure losses for the many different flow/operating conditions that are grouped under the CWAF category. Compared with existing models, the new model is more accurate and more broadly applicable to industrial oil-water flows where wall-fouling is a reality. Here pressure losses are predicted using CFD simulation of turbulent water flow on the fouling oil layer. The equivalent hydrodynamic roughness produced by the wall-fouling layer is determined using a novel correlation, which is another significant contribution of the current project. Important process conditions, such as mixture flow rate and water fraction, are used to predict the hydrodynamic roughness by this correlation. The new modeling methodology will be beneficial for designing, operating and troubleshooting pipeline systems in which a viscous wall-coating is produced, including water lubricated heavy oil and/or bitumen transport in the non-conventional oil industry, Cold Heavy Oil Production with Sand (CHOPS) and Steam Assisted Gravity Drainage (SAGD) surface production/transport lines.

A new procedure to determine unknown hydrodynamic roughness

A new methodology to determine unknown equivalent hydrodynamic roughness produced by an actual rough surface is one more contribution of the current work. Compared to the existing methods, the implementation of the new approach is easier, more economic and less uncertain. It requires CFD simulation of the flow conditions. The new method was used in this study to determine equivalent hydrodynamic roughnesses produced by appreciably different surfaces, such as solid walls, sandpapers, bio-fouling layers and wall-coating layers of viscous oils.

A novel correlation for the hydrodynamic roughness of a viscous wall

An additional contribution of this research is a simple correlation between the physical thickness of a viscous wall-coating layer and the equivalent hydrodynamic roughness produced by its rough surface when only water flows over it. This correlation was developed using data obtained from the wall-coating tests conducted in the flow cell and the experiments executed in a fouled pipe. It can be used to estimate the equivalent roughness directly from a measured or known value of the thickness of a wall-coating or -fouling layer under turbulent flow conditions.

CHAPTER 2
LITERATURE REVIEW

In this chapter, a critical review of the literature relevant to the current study is presented. The most important part of this chapter is the review of the literature related to water lubricated transportation of viscous oils like heavy oil and bitumen. Previous studies are discussed, analyzed and the limitations of existing models in predicting pressure losses are described. The review conducted here highlights the importance of the current work and shows why a more reliable model is required. In addition to lubricated pipe flow, two other topics are important to this project: Computational Fluid Dynamics (CFD) modeling of single phase turbulent flows and characterization of hydrodynamic roughness. The literature related to these subjects is quite extensive, and so the review presented here focuses on specific topics within those broader areas that are foundational to the present study.

2.1. Lubricated Pipe Flow

Lubricated pipe flow (LPF) refers to the water lubricated pipeline transportation of heavy oil or bitumen. It is a specific flow regime in which a continuous layer of water can be found in the high shear region near pipe wall. As wall shear stresses are balanced by pressure losses in pipeline transportation, this flow system requires significantly less pumping energy than would be required to transport the viscous oil alone at comparable process conditions (Arney et al. 1993, Joseph et al. 1999, McKibben et al. 2000b, Rodriguez et al. 2009, Crivelaro et al. 2009, Strazza et al. 2011). Successful operation of a lubricated pipeline is dependent on a few critical flow conditions which are discussed here. The purpose of this section is to point out the actual flow situation in the applied form of this flow technology, which is the focus of this research.

The preliminary requirement for establishing lubricated pipe flow is the simultaneous pumping of heavy oil/bitumen and water in the pipeline. This kind of pumping into a horizontal pipeline can result in different flow regimes, depending upon the oil and water superficial velocities and oil properties (Charles et al. 1961, Joseph et al. 1997, Bannwart et al. 2004). The prominent flow regimes are dispersed, stratified flow, bubbles, slugs and lubricated flows. The boundaries between the flow regimes are not well defined (Joseph et al. 1997). Transition from one flow regime to another one can be qualitatively described on the basis of regime transitions in gas-liquid flow systems (McKibben et al. 2000a). At lower flow rates of the fluids, stratified flow can be expected (Taitel and Dukler 1976, Holland and Bragg 1995). In such a flow regime, the relative positions of the oil and water are determined by the effect of gravity, i.e., the difference between the densities of the liquids. If the density of oil is less than that of water, oil is likely to float on water and vice versa. The stratified flow regime can be transformed into bubble or slug flow by increasing the water flow rate. The increased flow rate increases the kinetic energy and turbulence of the water, resulting in waves at the oil-water interface, which ultimately breaks the stratified oil into bubbles or slugs. Further increases of water flow rate can be expected to split bubbles or slugs into smaller droplets of oil. On the other hand, increasing oil flow rate at a constant water flow promotes coalescence of bubbles or slugs, which is likely to result in the water lubricated flow regime in a pipe (Charles et al. 1961, Bannwart et al. 2004).

The minimum velocity for the mixture of heavy oil and water required to obtain the water lubricated flow regime in a horizontal pipeline has been reported to be 0.1 – 0.5 m/s for different applications (Ooms et al. 1984, Joseph et al. 1999, McKibben et al. 2000b, McKibben et al. 2007, Rodriguez et al. 2009). In addition to the minimum velocity criterion, sustainable lubricated pipe flow also requires a minimum water fraction, typically between 10% and 30% (Nunez et al. 1998). A greater percentage of lubricating water does not cause a significant reduction in the pressure loss; even if it reduces the pressure loss to some extent, it also reduces the amount of oil transported per unit of energy consumed (McKibben et al. 2000b, Sanders et al. 2004, McKibben et al. 2007, McKibben and Gillies 2009). Water lubrication is usually identified from pressure loss measurements (McKibben et al. 2000b), as establishment of lubricated pipe flow is typically associated with a significant and nearly instantaneous reduction in frictional pressure losses (Sanders et al. 2004).

A significant concern during the application of lubricated pipe flow is that a minor fraction of the transported oil tends to adhere to the pipe wall, which eventually leads to the formation of an oil-layer on the pipe wall (Nunez et al. 1998, Joseph et al. 1999, Joseph et al. 1997, McKibben et al. 2000b, Shook et al. 2002, Schaan et al. 2004, Saniere et al. 2004, Rodriguez et al. 2009). Frictional pressure losses in a “fouled” pipe, i.e. with an oil coating on the wall, are higher compared to those for transportation of the same mixture in an unfouled pipe (Arney et al. 1996, Rodriguez et al. 2009). Nevertheless, the frictional losses with wall-fouling are substantially lower than that would be expected for transporting only heavy oil or bitumen (Shook et al. 2002, Sanders et al. 2004, McKibben et al. 2007), which is demonstrated by the results presented in Table 2.1. In this table, the pressure gradient for LPF with wall-fouling is compared with the values for transporting only water and only heavy oil at the same throughput. It should be noted that wall-fouling does not appear to destabilize the annular (lubricated) flow regime even though it produces higher friction losses (Joseph et al. 1997, Shook et al. 2002, Schaan et al. 2004).

Table 2.1. Comparison of pressure gradients for different flow conditions (Experimental data from McKibben et al. 2000b)

Temperature (°C)	Pipe diameter (mm)	Superficial velocity (m/s)	Flow condition	Pressure gradient (kPa/m)	Source
39	53	0.96	Water alone (viscosity ~ 0.001 Pa.s)	0.2	Calculation
			LPF with wall-fouling (Water content ~ 30% by volume)	1.4	Experiment
			Heavy oil alone (viscosity ~ 6.45 Pa.s)	70.5	Calculation

Wall-fouling is practically unavoidable in the water lubricated pipeline transportation of viscous oils (Joseph et al. 1999, McKibben et al. 2000b, Sanders et al. 2004, McKibben et al. 2007, McKibben and Gillies 2009, Rodriguez et al. 2009). Varying degrees of wall-fouling are experienced in the applications of this pipe-flow technology. Different descriptions have been used in the literature to classify these applications, for example:

a) Core annular flow (Arney et al. 1993, Ho and Li 1994)
b) Self-lubricated flow (Joseph et al. 1999)
c) Continuous water assisted flow (McKibben et al. 2000b, McKibben and Gillies 2009)

Lubricated pipe flow has been used in this thesis to refer to any of these flow types, despite the fact that they exhibit quite different characteristics. Each flow is described in greater detail, below.

Core annular flow (CAF) primarily denotes an idealized or conceptual version of lubricated pipe flow . It involves a core of viscous oil lubricated by a water annulus through a pipe with a clean (unfouled) wall (Ooms et al. 1984, Arney et al. 1993, Ho and Li 1994). Many research studies published in the 1980's and 1990's focused exclusively on CAF (e.g., Oliemans et al. 1987, Arney et al. 1993, Ho and Li 1994). In such studies wall-fouling was avoided through judicious selection of operating conditions, e.g., water cut and pipe construction material. In pilot-scale and industrial operations, attempts to operate CAF pipeline typically involved serious mitigation strategies to manage wall-fouling. In most published cases, wall-fouling could not be avoided (see, for example, Joseph et al. 1999 and Rodriguez et al. 2009).

In terms of industrial operations, self-lubricated flow (SLF) and continuous water assisted flow (CWAF) are most common. Self-lubricated flow refers to the water lubricated pipeline transportation of bitumen froth, which is a viscous mixture containing approximately 60% bitumen, 30% water and 10% solids by volume (Joseph et al. 1999, Schaan et al. 2002, Sanders et al. 2004). The water fraction in the froth lubricates the flow; additional water is usually not added. In a SLF pipeline, water assist appears to be intermittent (Joseph et al. 1999, Shook et al. 2000, McKibben and Gillies 2009) and the oil core may touch the pipe wall at times. Continuous water assisted flow denotes the pipeline transportation of heavy oil or bitumen when the water lubrication is more stable and the oil core touches the pipe wall infrequently (McKibben et al. 2000a, McKibben et al. 2000b, McKibben et al. 2007, McKibben and Gillies 2009). The water (~ 20% - 30% by volume) required to produce lubricated flow is added to a CWAF pipeline. Both of these categories of lubricated pipe flow involve wall-fouling. For example, the thickness of wall-fouling in a 150 mm SLF pipeline was measured to vary from 5.5 mm to 8.5 mm depending on the mixture velocity (Schaan et al., 2002). These experiments were conducted at 25°C with bitumen froth. In a 100 mm CWAF pipeline, the thickness of the wall-fouling layer was found to be ≤ 5 mm (McKibben et al. 2007, McKibben and Gillies 2009). The value was dependent primarily on the operating temperature and mixture velocity.

2.2. Modeling Pressure Losses in Lubricated Pipe Flow

Lubricated pipe flow is a promising alternative technology, which has been applied in very specific industrial contexts to transport non-conventional oils like heavy oil and bitumen (Joseph et al. 1997, Nunez et al. 1998, Sanders et al. 2004, Saniere et al. 2004, Jean et al. 2005, Bannwart et al. 2012) with limited success in many cases. A challenge in the broader application of LPF technology is the lack of a reliable model to predict frictional pressure losses, even though numerous empirical (e.g., Joseph et al. 1999 and McKibben et al. 2000b), semi-mechanistic (e.g., Arney et al., 1993, McKibben and Gillies 2009, Rodriguez et al.

2009) and idealized models (e.g., Oliemans et al. 1987, Ho and Li 1994, Crivelaro et al. 2009, de Andrade et al. 2012, Sakr et al. 2012) have been proposed to date. The existing models can be classified as either single-fluid or two-fluid models. A critical analysis of these models is important to underscore their limitations and to realize the need to develop a new modeling approach.

2.2.1. Single-fluid models

Single-fluid models are also called equivalent fluid models and generally take an engineering approach to predict pressure gradients for lubricated pipe flow. The flow system is represented as a hypothetical liquid under similar process conditions. In some cases, this hypothetical liquid is water (e.g., Joseph et al. 1999, McKibben et al. 2000b, McKibben and Gillies 2009 and Rodriguez et al. 2009). In other cases, the properties of this liquid are determined using the mixture properties (e.g., Arney et al. 1993). A single-fluid model usually considers the flow of the equivalent liquid to be turbulent. The friction factor (f) is suggested to be inversely proportional to the n^th^ power of a representative Reynolds number (Re), i.e. $f = K/Re^n$. The constants K and n are either determined empirically or are simply assigned. The Reynolds number is defined with respect to the properties of the hypothetical liquid and the pipeline conditions. In the single-fluid approach, the Reynolds number is defined based on an equivalent density (ρ) and viscosity (μ), while the pipeline conditions are considered through the pipe diameter (D) and average mixture velocity (V). The basis for single-fluid models is often the Blasius formula ($f = 0.079/Re^{0.25}$), which was originally proposed for the turbulent flow of water in a smooth pipe. Hydrodynamic roughness of the pipe-wall and/or wall-fouling layer can be accounted for in single fluid models by proposing different values of K compared to the Blasius value (K = 0.079). Detailed descriptions of three representative single-fluid models are presented below.

Arney et al. (1993) proposed a single-fluid model for core annular flow. In this model, f is correlated to a system specific Reynolds number (Re_a):

$f = 0.079/Re_a^{0.25}, Re_a > 4000$...........(2.1)

$\Delta P/L = f\,\rho_c V^2/2D$ ....(2.2)

The viscosity of the equivalent liquid is considered to be equal to that of water (μ_w). Empirical expressions are used to correlate the density of this hypothetical liquid (ρ_c) to the densities of oil (ρ_o) and water (ρ_w):

$Re_a = \rho_c DV/\mu_w$ ……………………...(2.3)
$\rho_c = H_w \rho_w + (1 - H_w)\rho_o$ ………………...(2.4)

The correlating parameter is the hold-up ratio (H_w) or *in situ* water fraction, which is further connected to input water fraction (C_{wi}) through another empirical expression:

$H_w = C_{wi}[1 + 0.35(1 - C_{wi})]$ ………..………(2.5)

Joseph et al. (1999) proposed a single-fluid model for the self-lubricated flow (SLF) of bitumen froth that involves a viscous mixture of bitumen, water and solids. In this model, a "Blasius-type" equation is used to correlate the friction factor (f) with the water Reynolds number (Re_w):

$f = 0.079K_j/Re_w^{0.25}$ ……………...(2.6)

The flow complexities of SLF are incorporated in Eq. (2.6) with respect to an empirically determined value of K_j. The value of K_j is assumed to be a function of temperature only: $K_j = 23$ at 35 – 47°C and $K_j = 16$ at 49 – 58°C; that is, water content is presumed to have no effect on K_j. Frictional pressure losses predicted using this model are 15 – 40 times greater than those expected for water flowing alone under identical conditions. The utility of this model for predicting frictional pressure losses for self-lubricating flows of bitumen froth or CWAF flows has been proven to be extremely limited (McKibben et al. 2000b, McKibben and Gillies 2009).

Rodriguez et al. (2009) proposed a semi-mechanistic model for core annular flow with and without wall-fouling. The proposed equations for friction factor and pressure gradients are:

$f = K_r/Re_w^{0.25}$ ……………...(2.7)

$\Delta P/L = f\,\rho_w V^2/2D$ …………....(2.8)

Where,

$K_r = b(1 - H_o)^{-0.25}[1 - (1 - \rho_o/\rho_w)H_o]^{0.75}[1 + (s - 1)H_o]^{-1.75}$………(2.9)

$b = 0.16\ (less\ fouled\ pipe)$

$\quad = 0.76\ (highly\ fouled\ pipe)$

In Eq. (2.9), H_o is the “oil holdup ratio” or *in situ* volume fraction of oil and s is the “slip ratio”, which are determined from the following empirical equations:

$V_o(1 - H_o) - 1.17V_wH_o - 0.02H_o^{1.79} = 0$…………..(2.10)

$s = 1.17 + \frac{0.05}{V_w}H_o^{0.8}$……………..(2.11)

Here, V_o and V_w are superficial velocities of oil and water, respectively.

In Figure 2.1, the predictions of the single-fluid models presented earlier are compared with measured values of pressure losses obtained from CWAF tests conducted at the SRC Pipe Flow Technology Centre (McKibben et al. 2007, McKibben and Gillies 2009). The data are available in Appendix 9.

The analysis presented in Figure 2.1 reveals the major limitation of single-fluid models to be their system-specificity. As can be observed from Figure 2.1(A), the model proposed by Arney et al. (1993) appreciably under predicts the experimental results for CWAF tests. This is, most likely, because the model was developed based on CAF data. The CAF experiments were conducted in a 15.9 mm glass pipeline. The glass pipe was selected to control wall-fouling and also to visualize the flow regime. It should be mentioned that wall-fouling is a natural outcome of the lubrication process in any LPF pipeline. Complete elimination of such fouling in a steel pipe requires expensive modification of internal surface properties (see, for example Arney et al., 1996). Thus, it should be expected that any CAF model is likely to under predict pressure gradients for CWAF.

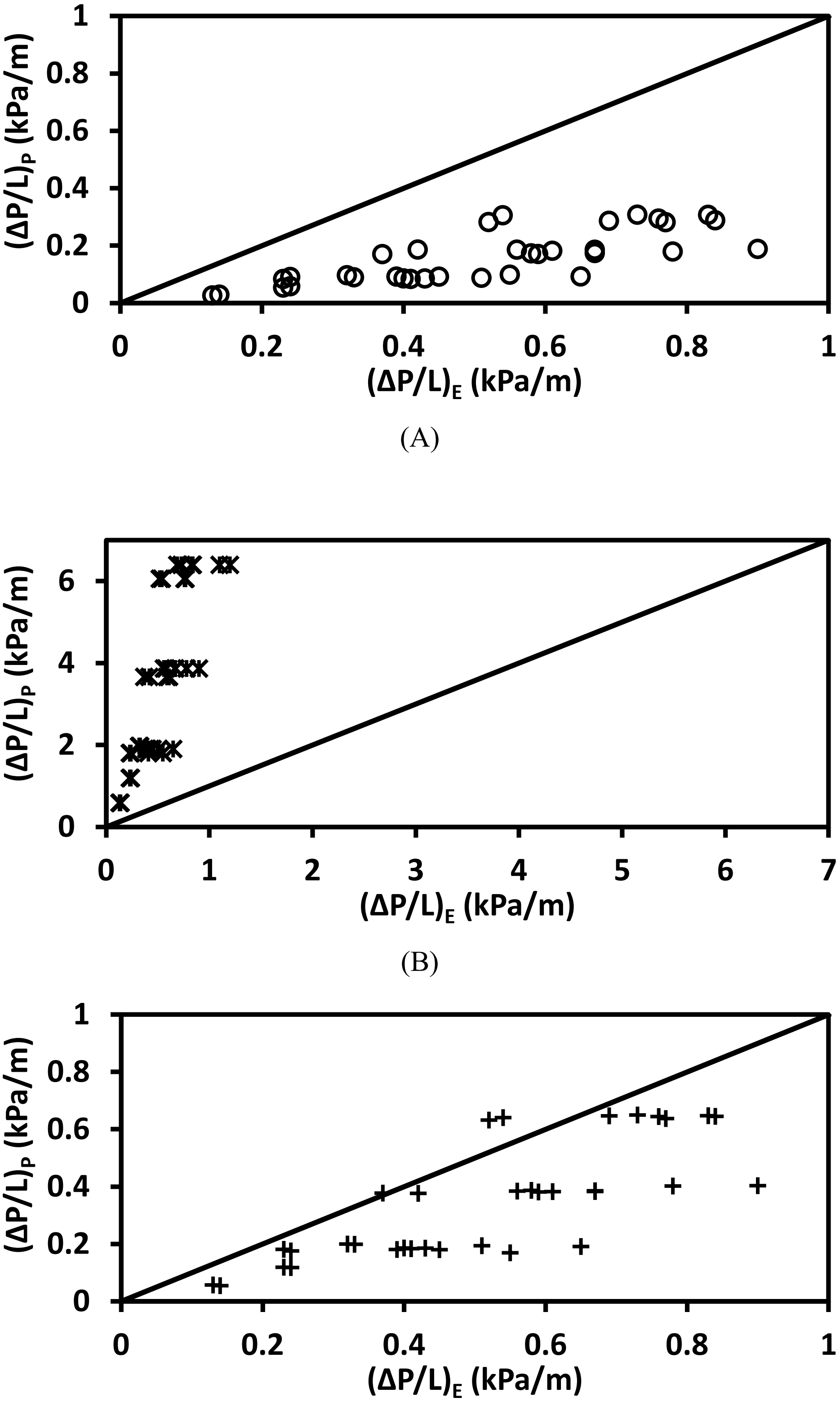

Figure 2.1. Comparison of measured pressure gradients, $(\Delta P/L)_E$, with predictions, $(\Delta P/L)_p$, from 3 different single-fluid models: (A) Arney et al. (1993), (B) Joseph et al. (1999) and (C) Rodriguez et al. (2009). Experimental data of McKibben and Gillies (2009).

The results shown in Figure 2.1(B) demonstrate the poor performance of the model developed by Joseph et al. (1999). This model significantly over predicts the CWAF data. The primary reason is that it was developed on the basis a large data set of SLF tests conducted in 25 mm and 600 mm steel pipes. The lubricated flow regime in a SLF pipeline involves significant wall-fouling and frequent contact between the oil-core and the pipe-wall (Schaan et al. 2002, McKibben and Gillies 2009), both of which contribute to high pressure losses compared to other CWAF applications. That is why an empirical model developed using SLF data should not be applied to CWAF applications. It should be noted that the SLF model (Joseph et al. 1999) cannot take into account the impacts of important process variables, including water content (C_w) and oil properties (μ_o and ρ_o). The most important process variables for this model are V and D.

Compared to the models of Arney et al. (1993) and Joseph et al. (1999), better performance of the semi-mechanistic model proposed by Rodriguez et al. (2009) can be seen in Figure 2.1(C). This model was developed for "non-ideal" CAF systems having some wall-fouling. The experiments were conducted with 74.6 mm and 26.6 mm PVC pipes and a 77 mm steel pipe. Although measures were taken to control wall-fouling, it could not be eliminated. Wall-fouling was especially noticeable in the steel pipe. That is why two different values of the coefficient b in Eq. (2.9) are proposed for "less fouled" and "highly fouled" pipe condition. Even so, this model fails to predict the trend of the data properly.

As shown here, single-fluid models generally take an empirical approach to predict pressure loss for lubricated pipe flow. The effects of operating conditions, including wall-fouling, are usually accounted for in these models through the use of empirical constants and the actual physical mechanisms governing pressure losses in a water lubricated pipeline are mostly disregarded.

2.2.2. Two-fluid models

Most two-fluid models have been proposed for core annular flow in a smooth pipe; that is, hydrodynamic roughness is usually neglected in these models. As a result, this kind of model is not applicable to self-lubricated flow or continuous water assisted flow. However, two-fluid models are more mechanistic compared to single-fluid models. The actual mechanism of pressure loss in a water lubricated flow system is usually addressed to some extent in these models. A few examples of two-fluid models are discussed below.

Oliemans et al. (1987) described the mechanism of pressure loss in their pioneering model for a CAF system. They identified the major factor contributing to frictional pressure loss to be the shear in the turbulent water annulus. They also addressed two more important issues by using empirical correlations: wave or physical roughness sculpted on the oil-water interface and water holdup. As pioneer researchers in this field, they used idealized concepts, e.g., Reynolds lubrication theory and Prandtl's mixing-length. Their model systematically under predicted the measured values of pressure losses when used by the researchers and, also, its implementation is not at all straightforward.

Ho and Li (1994) adapted the key features of the methodology described by Oliemans et al. (1987) and developed an improved model. They recognized the major source of frictional pressure loss in core annular flow to be shear in the turbulent water annulus and modeled turbulence using Prandtl's mixing-length model. They also considered the oil core to be a plug with a rough surface, but did not try to quantify this roughness. The complexity of physical roughness was simplified using the concept of hydrodynamic roughness. An idealized core annular flow regime was sub-divided into four hypothetical zones:

1. laminar sub-layer on the smooth pipe wall,
2. turbulent flow of the water annulus,
3. laminar sub-layer on the rough core surface and
4. plug core moving at a uniform velocity.

These sub-layers are presented in Figure 2.2, which also shows the dimensionless distances of each of these zones from the pipe wall. The velocity profiles for the sub-layers are often presented in these non-dimensional terms. The flow rate and pressure drop relationships for the annulus and the core can be obtained by integrating these velocity profiles with respect to the dimensionless distance. The equations describing the velocity profiles in each zone and the flow rates of two fluids (water and oil) are presented in Table 2.2.

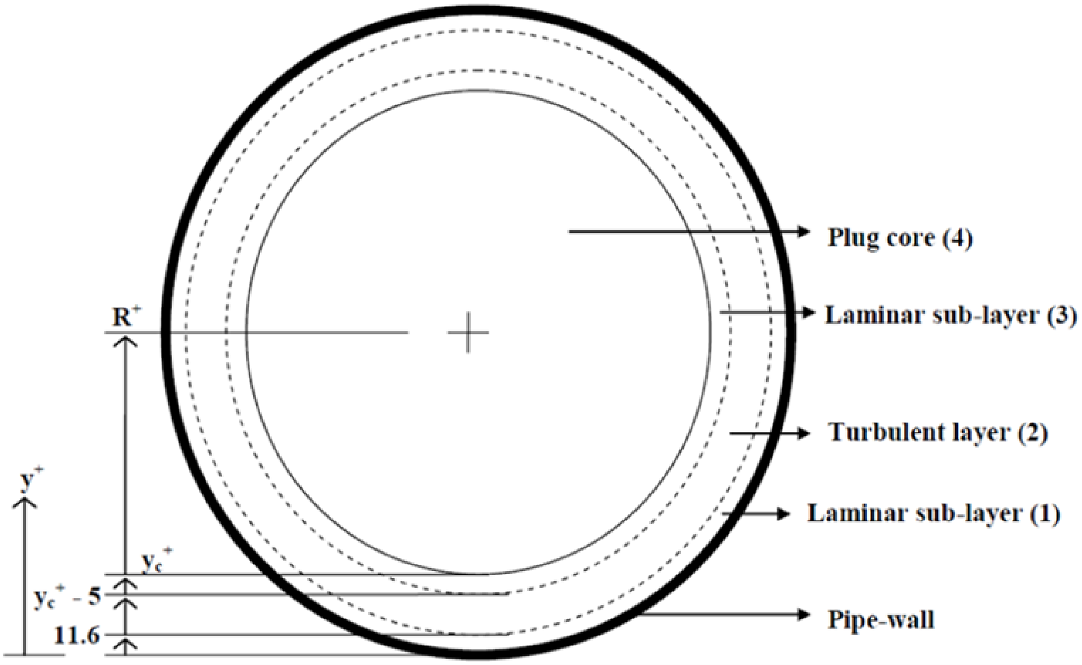

Figure 2.2. Hypothetical sub-division of perfect or ideal core annular flow into four zones, showing dimensionless distances from the pipe wall (Ho and Li 1994).

Table 2.2. Velocity profiles and equations relating flow rates and pressure losses (Ho and Li 1994)

Zone (Figure 2.2)	**Equations**	**Range**
Laminar sub-layer (1)	$u_1^+ = y^+$ ……….(2.12)	$0 \leq y^+ \leq 11.6$
Turbulent layer (2)	$u_2^+ = 2.5\ln(y^+) + 5.5$ ……….(2.13)	$11.6 \leq y^+ \leq y_c^+ - 5$
Laminar sub-layer (3)	$u_3^+ = 2.5\ln(y_c^+ - 5) - y_c^+ + 10.5 + y^+$ …..(2.14)	$y_c^+ - 5 \leq y^+ \leq y_c^+$
Plug core (4)	$u_4^+ = 2.5\ln(y_c^+ - 5) + 10.5$ ………(2.15)	$y_c^+ \leq y^+ \leq R^+$
(1) + (2) + (3)	$Q_w = 2\pi(\nu_w^2/v^*)[(2.5R^+y_c^+ - 1.25y_c^{+2})\ln(y_c^+ - 5) + 3R^+y_c^+ - 2.125y_c^{+2} - 13.6R^+]$ …….(2.16)	$0 \leq y^+ \leq y_c^+$
(4)	$Q_o = \pi(\nu_w^2/v^*)(R^+ - y_c^+)^2[2.5(\ln y_c^+ - 5) + 10.5]$ ……………(2.17)	$y_c^+ \leq y^+ \leq R^+$

The primary focus of Ho and Li (1994) was the water annulus in core annular flow. The thickness of this annulus was the most significant parameter in thier pressure drop model. This thickness was empirically determined. Moreover, they considered the water-annulus and oil core to be perfectly concentric. Perfect core annular flow is an idealized situation. Experimental investigations and hydrodynamic considerations suggest the oil core to be eccentric (Ooms et al. 1984; Oliemans et al. 1987). The eccentricity of the oil core is likely to affect the pressure losses in core annular flow (Huang et al. 1994).

Although the model suggested by Ho and Li (1994) involves some simplifications, it very closely addresses the physical mechanism of pressure loss in a water lubricated pipeline without any wall-fouling. According to this model, the frictional pressure gradients in core annular flow can be predicted on the basis of the flow rates of oil and water. The capability of this model to predict pressure gradients for continuous water assisted flow is presented in Figure 2.3. Model predictions are plotted in this figure as a function of experimental data. The same data set (Appendix 9) was used earlier to assess the similar performance of single-fluid models. The Ho and Li model consistently under predicts the measurements. This is because the experimental data are for a CWAF system that involves considerable wall-fouling and, most likely, oil core eccentricity, while the two-fluid model was suggested for perfect core annular flow in a smooth pipe.

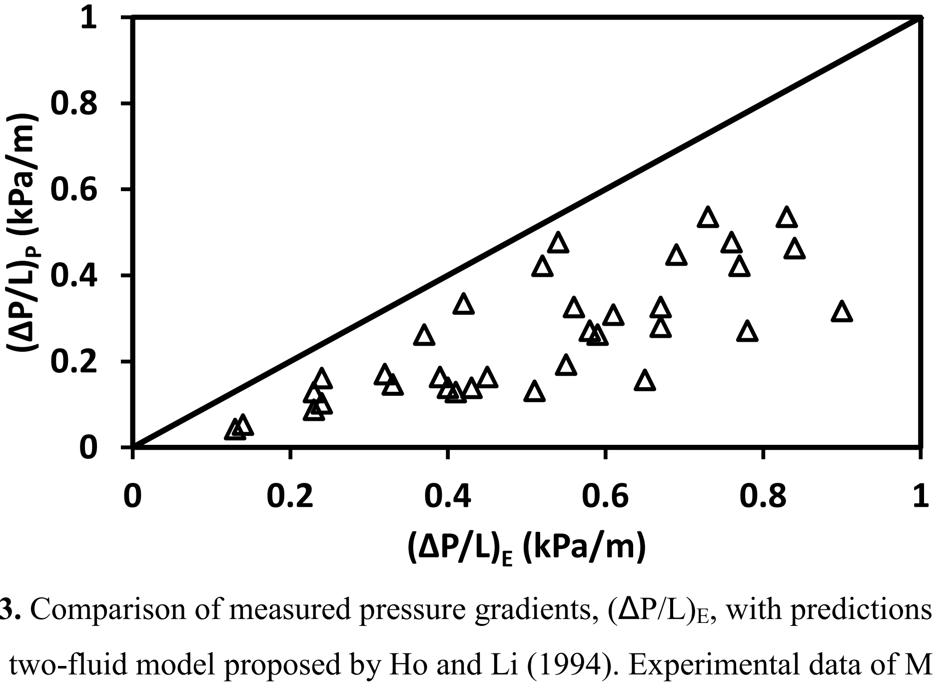

Figure 2.3. Comparison of measured pressure gradients, $(\Delta P/L)_E$, with predictions, $(\Delta P/L)_p$, from the two-fluid model proposed by Ho and Li (1994). Experimental data of McKibben and Gillies (2009).

The Ho and Li (1994) model accounts for the effects of water content in addition to velocity, pipe diameter and water properties (μ_w and ρ_w). Compared with single-fluid models, the capability of this two-fluid model in incorporating the effect of C_w is superior; see, for example, the results presented in Figures 2.1 and 2.3. In Figure 2.1, predicted values of pressure gradients are concentrated around distinct results and do not follow the trend of the measured values. For the Ho and Li (1994) model, the predicted values at least follow the trend of measured values because this model is sensitive to not only V and D but also C_w.

Crivelaro et al. (2009), de Andrade et al. (2012) and Sakr et al. (2012) used two-fluid modeling approaches to predict frictional pressure losses of core annular flow. They used the idea of a turbulent annulus containing water and a laminar core containing viscous oil. The turbulence of the water annulus was modeled with standard k-ε and k-ω models using different versions of the commercial CFD package, ANSYS CFX. Although these turbulence models might show some superiority over Prandtl's mixing-length model used by Ho and Li (1994), they are meant for isotropic turbulence and are not suggested for turbulent flow that involves anisotropy or very rough surfaces (Mothe and Sharif 2006, Zhang et al. 2011, Bonakdari et al. 2014). This modeling approach is also computationally expensive; it requires one to solve the governing equations for both phases (annular water and oil core), which leads to longer convergence times compared to solving the equations for only one phase (water annulus). Using an anisotropic model (e.g., a ω-based Reynolds Stress Model, ω-RSM), instead of isotropic k-ε or k-ω model, makes this modeling approach even more computationally expensive; convergence for a steady-state solution needs more than 24 hours. Moreover, the default mixture model of ANSYS CFX was used in this methodology to model the interphase transfer of mass and momentum. The correlations required to account for interfacial mixing were not validated for CAF. Most importantly, the simulation results of these models were not validated against measured (experimentally determined) pressure gradients.

The following can be concluded on the basis of the previous discussion:

(i) Existing models cannot be relied upon to predict frictional pressure losses in a CWAF pipeline;
(ii) CFD-based two-fluid models are more capable of capturing the physics of pressure losses in a lubricated pipeline compared to single-fluid models;
(iii) Instead of using existing complicated and unreliable two-fluid models, it would be better to develop a more simplified and more broadly approach to model frictional pressure losses in a lubricated pipe flow system.

2.3. CFD Modeling of Single Phase Turbulent Flow

The objective of this research is to develop a CFD-based modeling approach to predict frictional pressure loss in a CWAF system. The new model is a two-fluid CFD model, which requires simulating turbulent flow of the water in the annulus in a lubricated pipeline. Also, the experimental studies done to support this new modeling approach required the use of CFD simulations of flow conditions, which involved the turbulent flow of water over a highly rough surface in a rectangular flow cell. Consequently, it is important to discuss the background of CFD models available for modeling single phase turbulent flow and to provide justification for selecting the specific turbulence model used in this research.

Modeling single phase turbulent flow based on various CFD methodologies is a widely accepted scientific approach (White 1999). Most CFD models depend on the idea of decomposing the fluctuating turbulent flow into time-averaged mean motion and time-independent fluctuations. Application of this concept transforms the Navier-Stokes (NS) equations into a new set of equations known as Reynolds Averaged Navier Stokes (RANS) equations (Bird et al. 2001). The disintegration process produces additional terms of turbulent stresses to make the system of equations "unclosed" with more unknowns than the number of equations. For the closure, the turbulent stresses in the RANS equations are modeled through correlation with the average values of flow components, such as velocity (Pope 2000). The simplified forms of continuity (mass conservation) and RANS equations for an incompressible single phase fluid in Eulerian form can be presented as follows:

$$\frac{\partial U_i}{\partial x_i} = 0 \text{ .... } (2.18)$$

$$\frac{\partial U_i}{\partial t} + U_j \frac{\partial U_i}{\partial x_j} = -\frac{1}{\rho}\frac{\partial p}{\partial x_i} + \frac{\partial}{\partial x_j}\left(\frac{\mu}{\rho}\frac{\partial U_i}{\partial x_j} - \tau_{ij}\right) + S_i \text{............. } (2.19)$$

where x_i's represent the coordinate axes (x, y and z), U_i's are the mean velocities in the x (stream-wise), y (lateral) and z (vertical) directions, p is the pressure, ρ is the fluid density, μ is the fluid viscosity, S_i is the sum of body forces and τ_{ij} are the components of the Reynolds stress tensor. The models available in the literature for the Reynolds stresses (τ_{ij}) can be divided into two broad categories: eddy-viscosity models and Reynolds stress models (Wallin 2000, Sodja 2007).

Eddy-viscosity models were developed based on the concept of a hypothetical term known as eddy-viscosity (μ_t), which is considered to produce turbulent stresses caused by macroscopic velocity fluctuations (Bird et al. 2001). These models can further be divided into three major groups (Wallin 2000, Sodja 2007): zero-equation models (e.g., Prandtl's mixing-length model), one-equation models (e.g., k-model) and two-equation models (e.g., k-ε and k-ω model). At present, zero- and one-equation models are considered too simple to capture the complexities of engineering problems; two-equation models are generally used in such cases (Wallin 2000, Davidson 2011). The most commonly used two-equation models are the k-ε and k-ω models (Sodja 2007). A significant limitation of this group of models is that they are meant to describe isotropic turbulence (Aupoix et al. 2011, Fletcher et al. 2009). That is, only the significant components of the Reynolds stresses can be computed with two-equation models. As a result, the group of two-equation models is practically limited to flows where anisotropy is not important (Fletcher et al. 2009, Amano et al. 2010). It should be mentioned that the turbulent water annulus in a CWAF pipeline can experience both anisotropy and rough surfaces (Joseph et al. 1999, Shook et al. 2002, Rodriguez et al. 2009, McKibben and Gillies 2009). These models are also not suggested for turbulent flow in narrow channels and over very rough surfaces (see, for example, Mothe and Sharif 2006, Bonakdari et al. 2014).

Anisotropic turbulence can be addressed using Reynolds Stress Models (RSM), in which the hypothetical concept of eddy-viscosity is discarded (Aupoix et al. 2011). Examples of such anisotropic models include ω Reynolds Stress Model (ω-RSM), Explicit Algebraic Reynolds Stress Model and Differential Reynolds Stress Model (Davidson 2011). In these higher level, more elaborate turbulence models, Reynolds stresses are directly computed with six individual transport equations (Pope 2000). One more equation is used for the energy dissipation. Thus the closure for the RANS equations is obtained by solving seven transport equations. These models are considered more universal compared to eddy-viscosity models (Wallin 2000, Sodja 2007, Davidson 2011, Aupoix et al. 2011). The penalty for this flexibility is a high degree of complexity in the associated mathematical system. The increased number of transport equations requires increased computational resources compared to two-equation models. Even so, different Reynolds stress models were used successfully to simulate flow conditions involving anisotropy and very rough surfaces (e.g., Mothe and Sharif 2006, Fletcher et al. 2009, Amano et al. 2010, Zhang et al. 2011, Bonakdari et al. 2014).

In the current research, an idealized study of the hydrodynamic roughness produced by wall-fouling layer in a CWAF pipeline was conducted with a wall-coating layer of viscous oil (μ_o ~ 21 000 Pa.s) in a rectangular flow cell. The oil surface became rippled or rough when water was circulated through the flow cell under turbulent conditions ($Re_w > 10^4$). This rough surface of wall-coating produced very large values of equivalent hydrodynamic roughness (k_s) compared to the k_s values associated with an uncoated, clean surface. Details of the study are available in Chapters 3 and 4. The comparative performance of a two-equation model (k-ω) and a RSM (ω-RSM) is presented here for a specific process condition in Figure 2.4. As shown in the figure, ω-RSM predicts the measured values of pressure losses very well, while the same measured values are under predicted when the k-ω model is used. This is because the process conditions involved turbulent flow of water over a very rough surface in a narrow flow cell, which is almost certain to produce anisotropic turbulence. Comparable analyses were also conducted for other flow conditions involving various rough surfaces (e.g., solid wall, sandpapers, wall-biofouling layers and wall-coating layers of heavy oils) in different flow cells and the k-ω model did not allow for accurate predictions, while the ω-RSM did. This analysis and the supporting literature clearly indicated that a RSM (e.g., ω-RSM) would be a better choice than a two-equation model (e.g., k-ω model) for simulating flow conditions that involves anisotropy and very rough surfaces.

It is worth mentioning that turbulence is a very complex phenomenon. Although RANS methodology is computationally economic and feasible, this method is not capable of solving NS equations without averaging the flow variables with a steady-state assumption. The local unsteady features of turbulence are compromised in this averaging process (Sodja 2007). Most important of these features is that the turbulent structure is comprised of eddies. The scale of the turbulent eddies varies over orders of magnitude (Aupoix et al. 2011). Computational resolution of these eddies requires solution of the differential NS equations without modeling. Two methods are available: Large Eddy Simulation (LES) and Direct Numeric Simulation (DNS). The requirement of computational resources is extremely high for these simulation techniques (Sodja 2007). For example, the computational time in DNS is of the order of the Reynolds number to the third power (Re^3) if a computing rate of 1 gigaflop is assumed. Similar effort in LES is usually ten times less when DNS is used. Industrial scale flow systems can involve $Re > 10^5$. For the current work, Re is in the range of $10^4 - 10^6$. Clearly, LES and DNS are not realistic approaches for this research.

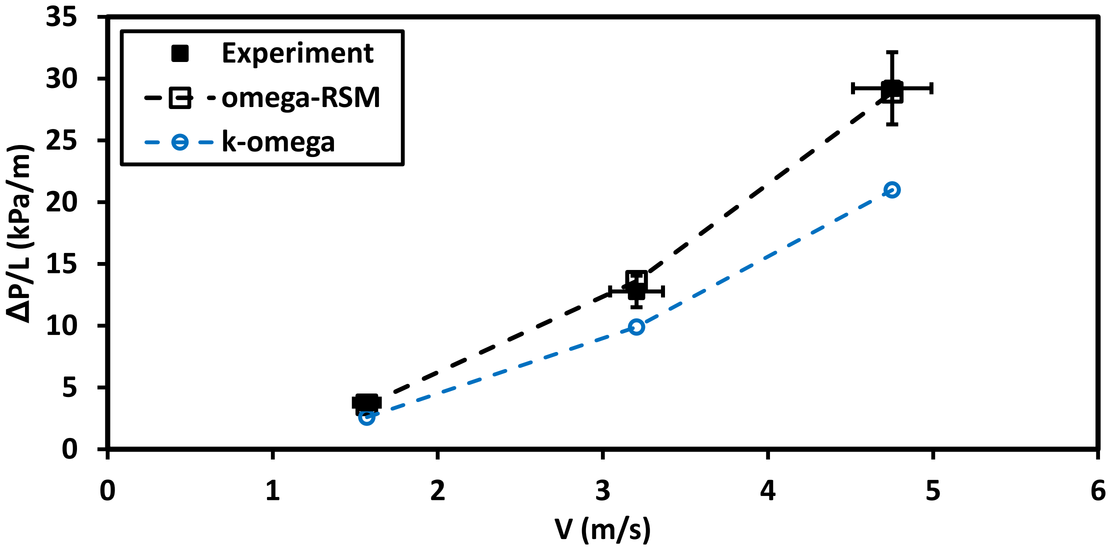

Figure 2.4. Comparison of experimental pressure gradients with simulation results (apparatus: 25.4 mm × 15.9 mm × 2000 mm rectangular flow cell; average coating thickness, $t_c = 1.0$ mm; equivalent hydrodynamic roughness, $k_s = 3.5$ mm; $10^4 < Re_w < 10^5$).

2.4. Hydrodynamic Roughness of Wall-fouling

The wall-fouling in continuous water assisted flow is actually a coating film of viscous oil on the pipe wall; the relative velocity of this viscous film is negligible (Joseph et al. 1999, McKibben et al. 2000b, Shook et al. 2002, Schaan et al. 2002, Vuong et al. 2009). The turbulent water annulus flows over the film while lubricating the oil-core and produces rough rippled texture on the viscous surface (Joseph et al. 1999, McKibben and Gillies 2009). Previous studies suggest that this kind of rough wall can significantly increase the hydrodynamic roughness compared to the typical roughness of, for example, commercial steel pipe (Brauner 1963, Picologlou et al. 1980, Shook et al. 2002). One of the objectives of the current research is to determine the equivalent hydrodynamic roughness produced by a wall-coating layer of viscous oil. Different procedures available in the literature to determine hydrodynamic roughness are discussed in this section; the purpose is to explain the basis of the procedures used in this research.

The engineering scale for the hydrodynamic roughness produced by a physically rough wall is the sand grain equivalent, k_s (Nikuradse 1950, White 1999, Shockling et al. 2007, Langelandsvik et al. 2008, Flack and Schultz 2010a). The concept of k_s is widely used to characterize commercial pipes, large channels and even biofilms fouling solid walls (Bayazit 1976, Kandlikar et al. 2005, Picologlou et al. 1980, Barton et al. 2008, Lambert et al.

2009, Beer et al. 1994, Schultz 2000, Schultz 2007). Unlike the asperities on a metal surface, a biofilm is conformable, but it can still substantially increase the frictional pressure loss beyond what would be predicted for a pipe or channel with clean walls. Higher hydrodynamic roughness due to bio-fouling also significantly increases the energy consumed by a bio-fouled ship. The equivalent hydrodynamic roughness produced by a biofilm is dependent on the flow conditions, its physical characteristics and thickness. Interestingly, analogous behavior was also produced by different viscous oil coatings (Brauner 1963, Shook et al. 2002). However, the hydrodynamic roughness produced by a viscous wall-coating has not been studied in detail.

Most of the previous studies of different rough surfaces estimated the equivalent hydrodynamic roughness by conducting experiments in a wind or water tunnel (Schultz and Swain 2000, Antonia and Krogstad 2001, Bergstrom et al. 2002, Schultz and Flack 2003), a flow channel (Kandlikar et al. 2005, Andrewartha et al. 2008, Andrewartha 2010) or a pipe (Adams et al. 2012, Barton et al. 2005, Farshad et al. 2002, Shockling et al. 2006, Barton et al. 2008, Lambart et al. 2009). The measured parameters were either velocity profile or pressure gradient. Usually, velocity profile was measured in a rectangular tunnel or flow channel comprised of three smooth walls and one rough wall. The profile was used to calculate k_s on the basis of correlations like "the law of the wall". The reliability of the velocity measurement was subject to the size of the flow cell; a large channel was required to ensure that the velocity profile would not be affected by secondary flows produced by the walls. On the other hand, pressure gradients were commonly measured for the pipeline tests. The measured values were used to estimate k_s using the Darcy-Weisbach equation and a correlation like the Colebrook or Churchill formula. The prerequisite for using these equations is the uniformity in roughness over the physical wall. Thus, the existing methodologies for the experimental determination of k_s for a rough surface require one or both of the following:

(i) A fairly large rectangular flow cell and measurement of velocity profile
(ii) A cylindrical pipe and measurement of pressure losses

That is, if the experiments are conducted in a small rectangular channel having asymmetric wall roughness and pressure losses are measured instead of velocity profiles, the existing methodologies cannot be used conveniently. This combination would require a new method for determining k_s. In the present study, it is shown that CFD simulations can be utilized for this purpose.

Another way of estimating the equivalent sand grain roughness (k_s) is to measure the physical roughness. Many correlations for k_s based on the corresponding physical roughness for different systems have been proposed (see, for example, Langelandsvik et al. 2008, Bons 2010, Flack and Schultz 2010a, Flack and Schultz 2010b, Unal et al. 2012). However, there is no universally accepted correlation between k_s and actual roughness. The major impediment to developing a widely accepted correlation is the complexity involved in characterizing the actual surface roughness, which is usually 3D in nature. The typical statistical parameters used for characterizing physical roughness are:

a) Center line average roughness (R_a): It is defined as the arithmetic mean of the departures of the profile from a mean value (Eq. 2.20). The average roughness of a rough profile measured along a surface is shown schematically in Figure 2.5.

$$R_a = \frac{1}{l}\int_0^l |Z(x)|dx \approx \frac{\sum_{i=1}^{n}|Z_i(x)|}{n} \text{...........(2.20)}$$

b) Root mean square roughness (R_{rms}): It is the root mean square average of the departures of the roughness profile from a mean value (Eq. 2.21). Figure 2.5 shows schematically R_{rms} in comparison to R_a.

$$R_{rms} = \sqrt{\frac{1}{l}\int_0^l Z^2(x)\,dx} \approx \sqrt{\frac{\sum_{i=1}^{n} Z_i^2(x)}{n}} \text{...............(2.21)}$$

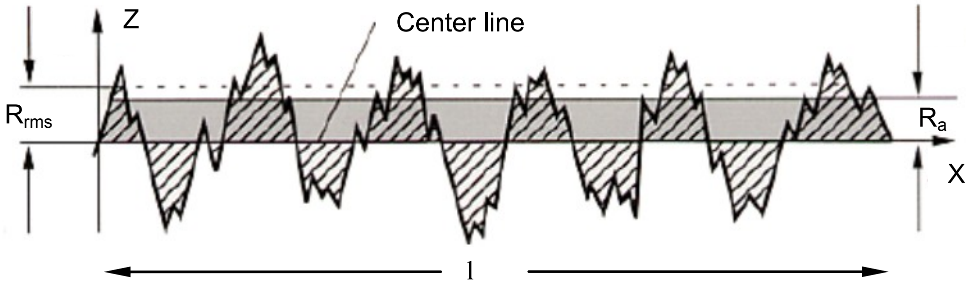

Figure 2.5. Schematic presentation of average roughness (R_a) and rms roughness (R_{rms}) based on BCM (2015).

c) Average peak to valley roughness (*R_z*): It is the average difference between a specified number of highest peaks and deepest valleys. The heights are usually measured from a line parallel to the mean line that does not cross the profile. Figure 2.5 shows schematically R_z calculated from five roughness depths of five successive sample lengths.

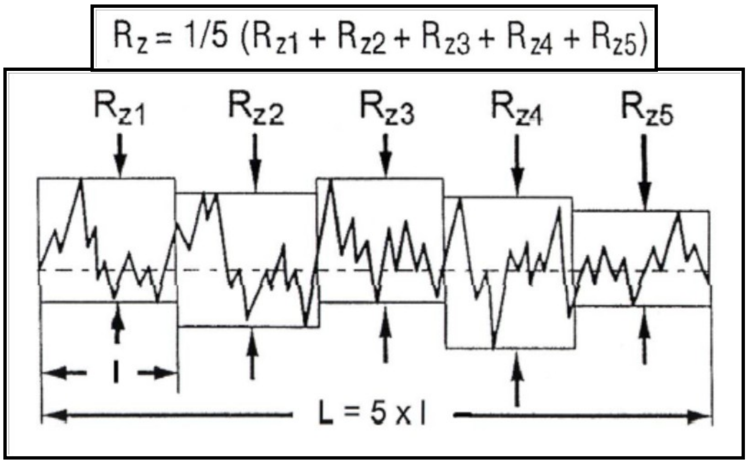

Figure 2.6. Schematic presentation of average peak to valley roughness (R_z) based on BCM (2015).

d) Skewness (R_{sk}): It is an indicator of asymmetry and deviation from a normal distribution (Eq. 2.22). $R_{sk} > 0$ indicates a positively skewed distribution with more peaks than valleys. $R_{sk} < 0$ indicates the opposite, i.e. more valleys than peaks. $R_{sk} = 0$ indicates a symmetry between peaks and valleys in the roughness profile.

$$R_{sk} = \frac{n\sqrt{n-1}}{n-2} \frac{\sum_{i=1}^{n}(Z_i - Z_{avg})^3}{\left[\sum_{i=1}^{n}(Z_i - Z_{avg})^2)\right]^{3/2}} \quad \ldots\ldots\ldots\ldots\ldots\ldots (2.22)$$

Each of these roughness parameters has individual strengths and weaknesses in representing a rough surface (Czichos et al. 2006). A single parameter cannot represent a 3D rough surface properly. Two surfaces having similar R_a, R_{rms} and/or R_z can have a different R_{sk}. However, most of the system-specific correlations between hydrodynamic and physical roughness of solid surfaces are based on a single average value like R_a, R_{rms} or R_z (Bons 2010). These models usually neglect the orientation of roughness elements.

A better way to represent the physical roughness of a surface is to use a combination of two statistical parameters instead of one (Flack and Schultz 2010b). For example, Flack and Schultz (2010a) correlated R_{rms} and R_{sk} to k_s:

$$k_s = 4.43 R_{rms} (1 + R_{sk})^{1.37} \quad \ldots\ldots\ldots\ldots\ldots (2.23)$$

The coefficients for this correlation were established by analyzing many data sets for the physical roughness of different solid surfaces, including packed spheres, sandpaper, gravel, honed pipe, commercial steel pipe, closed pack pyramids and scratched plates. Also, the model was successfully used for flat surfaces coated with nanostructured marine anti-fouling agents (Unal et al. 2012). It appears that the Flack and Schultz model should be capable of accurately estimating k_s of rough and viscous coatings, such as the ones produced in the present study. This is described in detail in the next chapter.

It should be mentioned that the physical roughness, i.e., the irregular waves on the interface between a viscous coating layer and flowing water is associated with the interfacial instability due to viscosity stratification (Hooper and Boyd 1987, Kushnir et al. 2014). Such instability is usually a result of interaction of the flows in the two layers, which are connected through the velocity and viscous stresses at the interface (Tilley 1994, Govindarajan and Sahu 2014). The phenomenon can be analyzed theoretically using the concept of Kelvin-Helmholtz instability (Al-Wahaibi and Angeli 2007, Barral et al. 2015). However, this kind of analysis is not likely to be useful in determining the equivalent hydrodynamic roughness produced by the rough interface (Al-Wahaibi 2012, Edomwonyi-Otu and Angeli 2015). Also, current research shows that the interfacial topology is less important than the flow conditions in determining k_s. That is why the instability analysis is beyond the scope of present study, although it can be used to investigate important aspects of roughness formation at the oil-water interface.

CHAPTER 3

A CFD METHODOLOGY TO DETERMINE THE HYDRODYNAMIC ROUGHNESS PRODUCED BY A THIN LAYER OF VISCOUS OIL*

3.1. Background

Water-assisted pipeline transportation is a promising alternative technology for transporting viscous oils like heavy oil and bitumen. Here, the viscous oil flows in the core, and water flows through the annulus. The annular water-film protects the viscous oil from touching the pipe wall and, thereby, acts as a lubricant. The lubricating water is either applied externally or already present in the transporting mixture (Arney et al. 1993, Joseph et al. 1999, McKibben et al. 2000b, Sanders et al. 2004, McKibben and Gillies 2009). This pipeline transportation technology is referred to as lubricated pipe flow (LPF). It requires much lower energy input compared to the transportation of viscous oil alone in the pipeline (Rodriguez et al. 2009, Crivelaro et al. 2009).

A concern for the application of the LPF is that some oil tends to permanently adhere to the pipe wall (Saniere et al. 2004). This phenomenon is called "wall-fouling". Even though frictional pressure loss in a fouled pipe is higher compared to that for similar transportation in an un-fouled pipe, the loss is substantially lower than what would be expected for transporting only heavy oil or bitumen (Arney et al. 1996, Joseph et al. 1999, McKibben et al. 2000b, Schaan et al. 2002, Sanders et al. 2004, Rodriguez et al. 2009, Crivelaro et al. 2009, McKibben and Gillies 2009). It is worth mentioning that the hydrodynamic stability of LPF in a fouled pipe is robust enough to sustain the water lubricated flow regime (Jeseph et al. 1997, Joseph et al. 1999, McKibben and Gillies 2009, Rodriguez et al. 2009).

Formation of wall-fouling layer of oil is practically unavoidable in the industrial-scale applications of LPF technology (McKibben et al. 2000b, Rodriguez et al. 2009, Schaan et al. 2002, Shook et al. 2002). Different degrees of wall-fouling are experienced in various applications of LPF, making it possible to divide LPF into two major categories depending on the extent of fouling: core annular flow (CAF) and continuous water assisted flow (CWAF). CAF primarily denotes a somewhat idealized concept of LPF, as it involves a core of viscous

---

**A version of this chapter has been submitted for publication to the Journal of Hydraulic Engineering. This paper is co-authored by S. Rushd, A. Islam, and S. Sanders.*

oil lubricated with a water annulus in an un-fouled pipe (Arney et al. 1993). In practice, most (if not all) commercial applications of LPF can be categorized as CWAF.

Presently, a reliable model to predict pressure losses in CWAF is not available (Shook et al. 2002, McKibben and Gillies 2009, Hart 2014). While numerous empirical, semi-mechanistic and numerical models have been proposed (e.g., Arney et al.1993, Ho and Li 1994, Joseph et al. 1999, Rodriguez et al. 2009, Crivelaro et al. 2009 and Sakr et al. 2012), all are very limited in applicability. Some are only appropriate for CAF and others are highly system-specific. None of the existing models explicitly addresses the effect of wall-fouling on frictional pressure losses.

Although the layer is relatively thin (compared to the pipe diameter), it is textured or rippled, which can significantly increase the hydrodynamic roughness (Brauner 1963, Picologlou et al. 1980, Shook et al. 2002). The mechanism of roughness increase by the presence of a viscous film on a solid wall has not been sufficiently studied to date. In the present study, we evaluate the hydrodynamic roughness produced by a very viscous coating layer, which is an idealized version of the fouling layer in a CWAF pipeline.

The engineering scale for hydrodynamic roughness is the Nikuradse sand grain equivalent (Flack and Schultz 2010a). This kind of equivalent roughness is used extensively for commercial metal pipes or channels. Similar roughness is also utilized for various unusual rough walls, such as metal walls with uniform roughness, mini-channels or biofilms on a solid wall (Bayazit 1976, Picologlou et al. 1980, Kandlikar et al. 2005). A biofilm, unlike rigid metal roughness, is conformable. Nevertheless, it can substantially increase the hydrodynamic roughness causing a rise in the power required for pumping water through bio-fouled pipes and channels (Andrewartha 2010, Lambert et al. 2009). Higher hydrodynamic roughness due to bio-fouling also significantly increases energy consumption for plying ships with bio-fouled bodies and hulls (Schultz 2007). The thickness and roughness of a biofilm are strongly dependent on the flow conditions; again, different biofilms demonstrate individual roughness characteristics under comparable flow conditions. In other words, the hydrodynamic roughness for a biofilm is determined by flow conditions, physical characteristics and, also, thickness of the film. Interestingly, analogous behavior was also observed in experiments involving the turbulent flow of water over viscous wall-coatings

(Brauner 1963, Shook et al. 2002). However, a detailed study on the roughness caused by a viscous oil film is not presently available in the literature.

Previous experimental studies of equivalent hydrodynamic roughness mostly involved solid surfaces or bio-fouling layers (Kandlikar et al. 2005, Barton et al. 2005, Adams et al. 2012). The experiments were carried out using either a large rectangular flow cell or a pipe. For the rectangular flow tests, the roughness was usually placed on a wall of the cell and three other walls were ensured to be smooth. The velocity profile perpendicular to the rough wall was measured to determine the hydrodynamic roughness on the basis of correlations, such as the law of the wall. The reliability of the measurement was subject to not only the measuring equipment but also to the size of the flow cell. Typically a large cell was used to ensure that the measured velocity profile would not be affected by the walls. On the other hand, pressure gradients were commonly measured for the pipe flow tests. The measurement was used to estimate the hydrodynamic roughness on the basis of correlations, for example Colebrook formula. The prerequisite for using this kind of correlation is uniformity in roughness all over the physical wall. These are not applicable for flow cells with asymmetric wall roughness.

3.2. CFD-based Determination of Hydrodynamic Roughness

In this study, the hydrodynamic roughness associated with a wall-coating of viscous oil was experimentally investigated. A customized rectangular flow cell was used for the experiments. The cell was fabricated so that water, under turbulent flow conditions, could be pumped over a film of oil coated on the bottom wall of the cell. The flow cell was fabricated with a cross-section of 25.4 mm × 15.9 mm. The size of the flow cell did not allow reliable determination of the velocity profile near the coating surface. However, the pressure loss across the flow cell could be measured accurately, but these measured values could not be used to determine equivalent hydrodynamic roughness because the wall roughness in the coated flow cell was not uniform. Thus, existing methodologies were not applicable for the analysis of hydrodynamic roughness associated with the flow conditions studied here. Necessarily a new methodology was used to determine the hydrodynamic roughness. It is a more general approach and not restricted by the size of the flow cell or the uniformity of wall roughness.

The new methodology was developed based on the prediction of measured pressure losses using computational fluid dynamics (CFD) simulations. The flow cell geometry and flow conditions were simulated for this purpose. The unknown hydrodynamic roughness produced by the wall-coating layer of heavy oil was an input parameter for the simulation. The pressure losses were predicted using a trial-and-error procedure that required iterative specification of the roughness and repeated simulations.

We validated the CFD-based approach using the simulation process in three different case studies, which involved analysis of the equivalent hydrodynamic roughnesses produced by walls of the clean flow cell, sandpapers of two grits and four bio-fouling layers. Data were generated as part of the current work for the first two cases. For the third case (bio-fouling), data were collected from Andrewartha (2010). After validation, the CFD approach was used for the wall-fouling layer of the viscous oil. The predicted values of the equivalent roughness were corroborated further by estimating the same values from the measurement of physical roughness with a correlation proposed by Flack and Schultz (2010a).

3.3. Experimental Facilities and Method

The experimental setup used in this study was a 25.4 mm flow loop as shown schematically in Figure 3.1(A). This loop consisted of a water tank, pump-motor set, flexible connector and damper, heat exchanger, flow cell, filter and associated copper/flexible tubing. Water from the tank was circulated through the loop by a pump (Moyno 1000) driven by a VFD and motor (7.5 hp BALDOR INDUSTRIAL MOTOR). The pump speed was set to obtain the desired mass flow rate of water. The flexible connector and dampener minimized unwanted vibration in the loop. The heat exchanger provided isothermal conditions, with all tests conducted at 20°C. The filter (Arctic P2 filter with 34 micron bag) collected oil droplets from the coating layer in the flow cell. A small fraction of the wall-coating oil was stripped from the coating under some operating conditions and the filter prevented recirculation of oil droplets through the loop. A Coriolis mass flow meter (Krohne MFM 4085K Corimass, type 300G+) measured both mass flow rate and temperature.

The flow cell was fabricated from carbon steel and was 2.5 m long and 6 mm thick, with a 25.4 mm × 25.4 mm cross section as shown in Figure 3.1(B). The first 1.5 m of this cell served as the entrance length. A 1.0 m downstream from the entrance was fitted with two viewing windows and is referred to as the flow visualizing section. A 9.5 mm thick stainless steel plate was placed at the bottom of the flow cell. This plate was cut into several segments for the convenience of installation and conducting surface roughness measurements at the end of each test. The flow cell was equipped with a differential pressure transducer (Validyne P61) for online measurement of pressure loss of the flow cell. A more detailed description of the flow cell including an engineering drawing and photographs is included in Appendix 1.

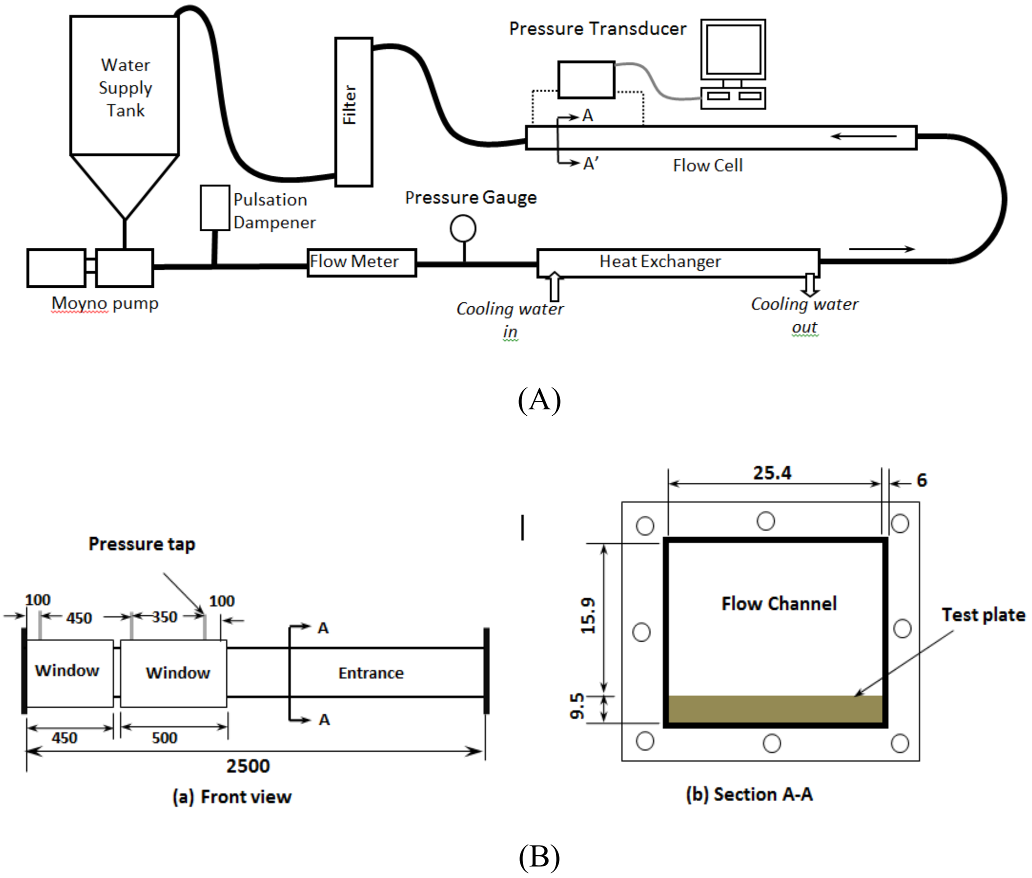

Figure 3.1. Schematic presentation of the experimental setup: (A) Complete flow loop; (B) Details of the flow cell (dimensions are in mm).

A fully automated Mitutuyo Contracer Contour Measuring System (Model CV-3100H4) was used to measure the physical roughness of the clean test plate, sandpaper and oil coating. The Contracer uses a carbide stylus. The weight of this stylus is balanced so that the measuring force (i.e. the effective weight) is only 30 mN. As a result the surface roughness is not altered or damaged by the stylus. When the stylus travels over a surface, its perpendicular movement (i.e. physical roughness) is quantified. The working principle of the Contracer is analogous to that of a standard contact profilometer. A profilometer usually measures roughness at the micron scale (Flack and Schultz 2010a). However, the Contracer can measure roughness over a wider scale, from sub-micron to millimeter. More importantly, a profilometer is suitable for solid surfaces only, while a Contracer can also be used for a softer surface provided a reasonable rigidity is maintained during the measurement. In the present investigation, for example, the oil-coated test plates were in contact with dry ice during Contracer measurements. The Contracer and its use in current work are described in detail in Appendix 4.

Initially, pressure losses were measured with water flowing through the cell over a clean (un-fouled) test plate. Water flow rates were controlled so that the Reynolds number (Re_w) was varied over a range of $10^4 – 10^5$ ($10^4 < Re_w < 10^5$). These tests were carried out to assess the hydrodynamic roughness of the clean walls in the flow cell. Pressure drops were measured under fully developed flow conditions, as the entrance length was more than $60D_h$, where D_h is the hydraulic diameter. Repeatable steady state pressure differences measured across this section also indicated fully developed flow (Appendix 5). The pressure taps for these measurements were located 800 mm apart, over the length of the flow visualizing section. The first tap was 100 mm downstream of the entrance to this section and the second one was 100 mm upstream of the exit from the flow cell. The locations of the pressure taps are illustrated in Figure 3.1(B).

Subsequently, flow tests were conducted with sandpaper and a wall-coating of heavy oil in the flow cell. For the sandpaper tests, the sandpaper was glued on the bottom plate in the flow visualizing section. The plate was made with a single piece of steel bar. A slide caliper was used to measure the thickness of the sandpaper. For the coating experiments, a viscous heavy oil (Husky PG 46-37 300/400A, $\mu_o = 2.13 \times 10^4$ Pa.s @ $T = 20°\text{C}$) was obtained from Husky Oil, Canada. A description of the oil is available in Appendix 2. The bottom wall comprised an assembly of ten plates. Each plate was coated separately with a specific thickness of the viscous oil and placed in the flow cell to form the coating layer of a uniform thickness. The step-by-step coating procedure is given in Appendix 3. The average thickness of the coating layer (t_c) was determined by weighing the test plates without and with coating oil. It should be noted that the coated plates were also weighed before and after the flow test. The difference between the measured weights was usually not large. That is why t_c was considered to be unaffected by the flow rate and, as such, was taken as a controlled parameter. The uncertainty associated with the measurement of t_c was 11% (Appendix 5). The pressure taps for the sandpaper and the wall-coating tests were located 450 mm apart over the flow visualizing section (Figure 3.1B). Repeatable steady state pressure losses were measured over this section.

Examples of calculating coating thickness from measured weights of oil on test plates and measuring pressure gradients are presented here for a specific flow condition. The coating thicknesses before and after a flow test are shown in Table 3.1, while the measured values of pressure gradients (30 s average values) are presented in Figure 3.2. These results demonstrate that changes in the coating thickness and corresponding pressure gradients were almost negligible even after repeating water flow rates over a period of around one and a half hour. Detailed results for all flow conditions are available in Appendix 6.

Table 3.1. An example of coating thickness (t_c = 0.5 mm) determination (Oil density, ρ_o = 1021 kg/m^3; Area of test plate, A_p = 2.54 × 10^{-3} m^2)

Test plate #	Weight of coating oil, m_o (g)		Coating thickness, $t_c = m_o/\rho_o A_p$ (mm)		
	Before flow test	After flow test	Before flow test	After flow test	Average
1	1.3	1.2	0.5	0.5	0.5
2	1.3	1.5	0.5	0.6	
3	1.3	1.4	0.5	0.5	

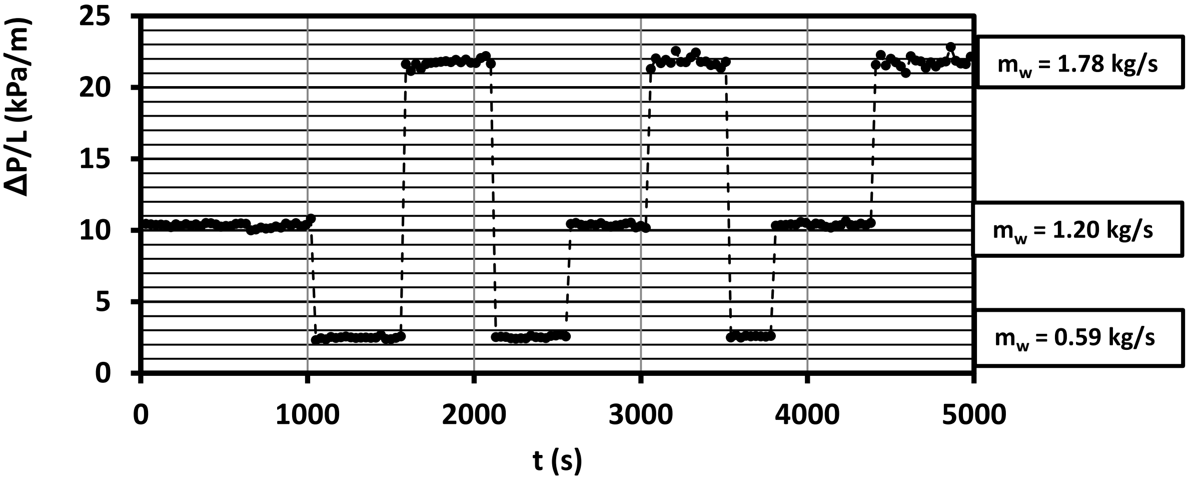

Figure 3.2. Illustration of pressure gradients (*ΔP/L*) measured over time (*t*) for different mass flow rates of water (m_w).

After completing a set of flow tests with a particular wall-coating, the coated plates located in the section between the pressure taps were removed from the flow cell. This process took less than 5 minutes. The test plates were then placed in a freezer maintained at -10°C. It should be noted that at room temperature, the rough surface of the oil coating, which was produced because of the flow past it in the cell, would maintain its shape for more than an hour after a test was completed because the oil viscosity was very high. When contour measurements were to be made, a test plate was removed from the freezer and placed on the top of a container that contained dry ice. The Contracer was then used to measure the topology of the frozen coating. The procedure followed to preserve the roughness on the wall-coating is described in Appendix 3.

The Contracer was used to measure the physical roughness by conducting contour measurements over a large area (xy) of 80 mm × 15 mm. The area selected for measurement was located in the center of each test plate. The roughness in this area was observed to be unaffected in the course of separating the test plate from the flow cell. Figure 3.3 shows schematically the measured area on a test plate. The measured area is much larger (~ 1200 mm^2) than the usual test area for measuring roughness on a solid surface, which is in the scale of $\mu\mathrm{m}^2$ (Flack and Schultz 2010a, Afzal et al. 2013). In addition to assessing roughness over a large area, the measurements were repeated many times: 29 repeated measurements for test plates coated with a 1 mm layer of oil and 11 measurements for test plates coated with a layer that was 0.5 mm thick.

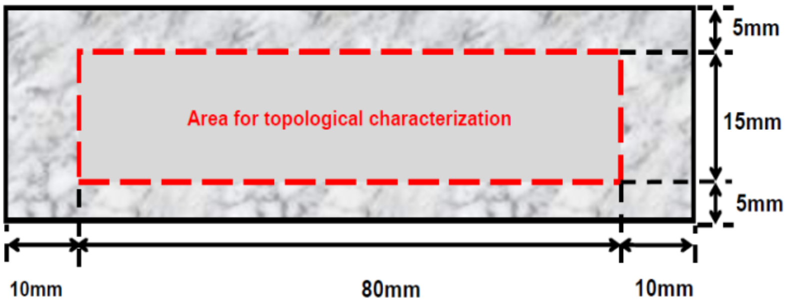

Figure 3.3. Illustration of the test plate area for topological (Contracer) measurements.

3.4. CFD Simulations

The CFD simulations described here were used to determine the hydrodynamic roughness in terms of sand grain equivalent (k_s). The flow conditions in the flow cell were modeled using the CFD software package, ANSYS CFX 13.0. A ω-based Reynolds Stress Model, ω-RSM, was used to model the turbulent flow.

3.4.1. Turbulence model: ω-RSM

The performance of a Reynolds Stress Model (RSM) is generally more accurate, especially in simulating anisotropic flow conditions. The application of RSM for flows in rectangular channels where the geometry induced strong secondary flows was validated by Fletcher et al. (2009) and Amano et al. (2010). Moreover, the superiority of the ω-RSM over the k-ω model for turbulent flows over rough surfaces ($k_s \sim 1$ mm) was demonstrated by Mothe and Sharif (2006). For these reasons, since the present work involves both a rectangular flow cell and a very rough wall, the ω-RSM model was deemed the most appropriate choice. Better performance of *ω*-RSM over *k*-*ω* model in determining k_s produced by a wall-coating layer in the rectangular flow cell is demonstrated in Chapter 2 and in Appendix 7.

The most important features of the ω-RSM are described here. The description is based on Fletcher et al. (2009) and the ANSYS CFX-Solver Theory Guide (2010). In this narrative, the differential equations are presented with index notation[†].

The basic governing equations of turbulent motion for a viscous liquid like water are the Navier–Stokes Equations. Turbulent flow fluctuations are included in the model by a time-averaging concept known as Reynolds Averaging. In the course of this averaging process, additional terms known as the Reynolds stresses appear in the Reynolds-Averaged Navier–Stokes (RANS) equations. It is necessary to model the Reynolds stresses for closure of the RANS equations. The RANS equations of continuity and momentum transport for an incompressible, Newtonian fluid can be presented in their general forms as follows:

Continuity:

$$\frac{\partial U_i}{\partial x_i} = 0 \text{....................} \quad (3.1)$$

Momentum transport:

$$\rho \frac{DU_i}{Dt} = -\frac{\partial}{\partial x_i}\left[p + \frac{2}{3}\mu \frac{\partial U_k}{\partial x_k}\right] + \frac{\partial}{\partial x_j}\left[\mu\left(\frac{\partial U_i}{\partial x_j} + \frac{\partial U_j}{\partial x_i}\right)\right] - \rho \frac{\partial}{\partial x_j}\left(\tau_{ij}\right) + S_i \text{.............} (3.2)$$

[†] In Cartesian coordinate, for example, U_i represents all three components (x, y, z) of the vector U. Likewise, τ_{ij} stands for the nine components (xx, xy, xz, yx, yy, yz, zx, zy, zz) of the tensor τ. The differential operators are denoted similarly. Also, the summation convention is implied.

where p is the static (thermodynamic) pressure, S_i is the sum of body forces and τ_{ij} is the fluctuating Reynolds stress contributions.

A number of models are available in ANSYS CFX 13.0 for the Reynolds stresses (τ_{ij}) in RANS equations. Among the available models, ω-RSM was selected as most suitable for this work. In this model, τ_{ij} is made to satisfy a transport equation. A separate transport equation is solved for each of the six Reynolds stress components of τ_{ij}. The differential transport equation for Reynolds stress is as follows:

$$\rho \frac{D\tau_{ij}}{Dt} = -\rho P_{ij} - \rho \Phi_{ij} + \frac{2}{3}\beta' \rho \omega k \delta_{ij} + \frac{\partial}{\partial x_k}\left[\left(\mu + \frac{\mu_t}{\sigma_k}\right)\frac{\partial \tau_{ij}}{\partial x_k}\right] \ldots\ldots \ (3.3)$$

The Reynolds stress production tensor P_{ij} is given by:

$$P_{ij} = \tau_{ik}\frac{\partial U_j}{\partial x_k} + \tau_{jk}\frac{\partial U_i}{\partial x_k}, P = \frac{1}{2}P_{kk} \ \ldots\ldots\ldots \ (3.4)$$

The constitutive relation for the pressure-strain term Φ_{ij} in Eq. (3.3) is expressed as follows:

$$\Phi_{ij} = \beta' C_1 \rho \omega \left(\tau_{ij} + \frac{2}{3}k\delta_{ij}\right) - \hat{\alpha}(P_{ij} - \frac{2}{3}P\delta_{ij}) - \hat{\beta}(D_{ij} - \frac{2}{3}P\delta_{ij}) - \hat{\gamma}\rho k(S_{ij} - \frac{1}{3}S_{kk}\delta_{ij}) \ldots\ldots\ldots\ldots\ldots (\ 3.5)$$

In this expression, the tensor D_{ij} is given by:

$$D_{ij} = \tau_{ik}\frac{\partial U_k}{\partial x_j} + \tau_{jk}\frac{\partial U_k}{\partial x_i} \ \ldots\ldots\ldots\ldots\ldots \ (3.6)$$

While the model coefficients are the following:

$$\beta' = 0.09; \hat{\alpha} = (8 + C_2)/11; \hat{\beta} = (8C_2 - 2)/11; \hat{\gamma} = (60C_2 - 4)/55; C_1 = 1.8; C_2 = 0.52$$

In addition to the stress equations, the ω-RSM uses the following equations with corresponding coefficients for the turbulent eddy frequency ω and turbulent kinetic energy k:

$$\rho\frac{D\omega}{Dt} = \alpha\rho\frac{\omega}{k}P_k - \beta\rho\omega^2 + \frac{\partial}{\partial x_k}\left[\left(\mu + \frac{\mu_t}{\sigma}\right)\frac{\partial\omega}{\partial x_k}\right] \text{.............. (3.7)}$$

$$\rho\frac{Dk}{Dt} = P_k - \beta'\rho k\omega + \frac{\partial}{\partial x_j}\left[\left(\mu + \frac{\mu_t}{\sigma_k}\right)\frac{\partial k}{\partial x_j}\right] \text{................. (3.8)}$$

In these equations, P_k is given by:

$$P_k = \mu_t\left(\frac{\partial U_i}{\partial x_j} + \frac{\partial U_j}{\partial x_i}\right)\frac{\partial U_i}{\partial x_j} - \frac{2}{3}\frac{\partial U_k}{\partial x_k}\left(3\mu_t\frac{\partial U_k}{\partial x_k} + \rho k\right) \text{............(3.9)}$$

While the coefficients are:

$$\sigma^* = 2; \sigma = 2; \beta = 0.075; \alpha = \frac{\beta}{\beta'} - \frac{\kappa^2}{\sigma(\beta')^{0.5}} = \frac{5}{9}; \kappa = 0.41; \sigma_k = 2$$

In the previously mentioned transport equations, the turbulent viscosity μ_t is defined as:

$$\mu_t = \rho\frac{k}{\omega} \text{............. (3.10)}$$

Usually a wall is treated using the no-slip boundary condition for CFD simulations. Mesh insensitive automatic near wall treatment is available for the ω-RSM in ANSYS CFX 13.0. The treatment is meant to control the smooth transition from the viscous sub-layer to the turbulent layer through the logarithmic zone. Important features of the near wall treatment for ω-RSM are outlined as follows:

(a) In the case of a hydrodynamically smooth wall, the viscous sub-layer is connected to turbulent layer with a log-law region. Velocity profiles for the near wall regions are:

Viscous sub-layer: $u^+ = y^+$ .... (3.11)
Log-law region: $u^+ = (1/\kappa)\ln(y^+) + B - \Delta B$ .... (3.12)

Here,
$u^+ = U_t/u_\tau$; $y^+ = \rho\Delta y u_\tau/\mu = \Delta y u_\tau/\nu$; $u_\tau = (\tau_w/\rho)^{0.5}$

In the log-law, B and ΔB are constants. The value of B is considered as 5.2 and that of ΔB is dependent on the wall roughness. For a smooth wall, $\Delta B = 0$. The term Δy, in the definition of y^+, is calculated as the distance between the first and the second grid points off the wall. Special treatment of y^+ in CFX allows arbitrarily refining the mesh.

(b) For a hydrodynamically rough wall, the roughness is scaled with Nikuradse sand grain equivalent (k_s). The non-dimensional roughness k_s^+ is defined as $k_s u_\tau / \nu$. A wall is treated as hydrodynamically rough when $k_s^+ > 70$. The value of ΔB is empirically correlated to k_s^+:

$$\Delta B = \frac{1}{\kappa} \ln\left(1 + 0.3 k_s^+\right) \ldots\ldots\ldots \text{(3.13)}$$

ΔB represents a parallel shift of logarithmic velocity profile compared to the smooth wall condition.

(c) At the fully rough condition ($k_s^+ > 70$), the viscous sub-layer is assumed to be destroyed. Effect of viscosity in the near wall region is neglected.

(d) The equivalent sand grains are considered to have a blockage effect on the flow. This effect is taken into account by virtually shifting the wall by a distance of $0.5k_s$.

3.4.2. Simulation setup

The CFD simulations were conducted for the following flow scenarios: (a) four walls of the flow cell were smooth and (b) three walls of the cell were smooth and one wall was rough. All computations were performed to obtain steady state solutions. A typical computational time requirement for a single data point was 45 minutes.

Geometry

The general geometry of the 3D computational domain is presented in Figure 3.4. The material filling the domain was water. The physical properties of the water at 20°C were chosen to match the experiments. The dimensions of this geometry are identical to the inner dimensions of the experimental flow cell. The general length (*l*) of all flow domains was 1000 mm. A length of 2000 mm was also tested to confirm the length independence of simulated results. The width (*w*) was equal to that of the flow cell (25.4 mm). The height (*h* =

15.9 – t_c mm) was varied depending on the average thickness (t_c) of oil coating on the bottom wall. The tested values of t_c were 0.1 mm, 0.2 mm, 0.5 mm and 1.0 mm.

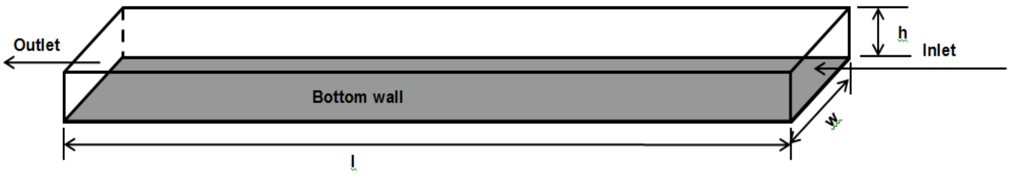

Figure 3.4. Schematic representation of the geometry of the flow domain.

Boundary conditions

As can be seen in Figure 3.4, the computational domain has six distinct boundaries where boundary conditions should be prescribed: the inlet, the outlet and the four walls. At the inlet, the mass flow rate of water and a turbulence intensity of 5% were specified. The same flow rate was also prescribed at the outlet. The no-slip condition was used at the boundaries representing the four walls. These walls were considered to be hydrodynamically smooth for simulating the scenario of the clean flow cell with no wall-coating. Flow situations in the cell with a rough surface (wall-coating layer or sandpaper) were simulated by considering the bottom wall as rough and the three other walls as smooth. Specification of k_s of the rough wall was required for these simulations. The k_s values were unknown for the bottom wall. A trial-and-error procedure was used to determine k_s for a particular rough surface. Starting from a low value, the value of k_s was increased in increments until the difference between the experimental and the simulation results was less than 5%. The final value of k_s was considered to be the hydrodynamic roughness of the corresponding rough wall. A more detailed description of the procedure is available in Chapter 4.

Meshing

The flow geometry was created and meshed with ANSYS ICEM CFD. Since the computational domain was very regular, the software was used to discretize the domain into structured grids. Based on the number of nodes, the meshes tested in the current work can be classified as coarse (nodes < 50,000), intermediate (50,000 < nodes < 500,000) and fine (nodes > 500,000). The total number of nodes considered to be sufficient for grid independence was 670200. A cross-sectional view of the fine mesh is shown in Figure 3.5.

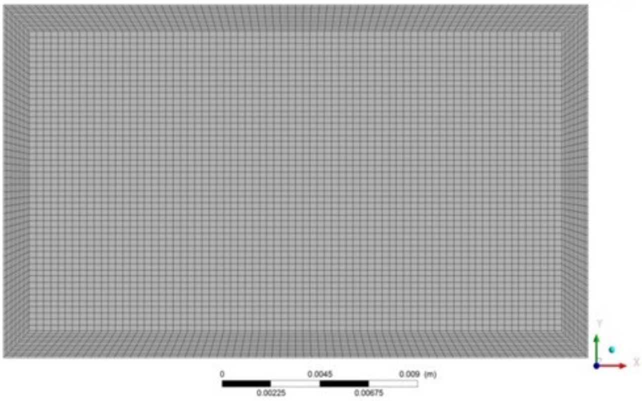

Figure 3.5. Two-dimensional illustration of the fine mesh used for the simulations.

3.5. Validation of the CFD Procedure

The new CFD approach for calculation of equivalent hydrodynamic roughness was validated by applying it to analyze data obtained from three independent sets of experiments:

i) Clean flow cell tests
ii) Sandpaper tests
iii) Bio-fouling tests

The experiments involved both solid and soft rough surfaces, which produced equivalent sand grain roughnesses in the range of 0 – 5 mm. The case studies are presented as follows:

3.5.1. Case study 1: Rectangular flow cell with clean walls

The pressure gradients for the flow tests in the clean flow cell that did not have any wall-coating were measured and the data were analyzed both analytically and numerically. The overall difference between the predicted and measured values was less than 10%. Measured pressure gradients with corresponding predictions are presented in Figure 3.6 as a function of water velocity, which was calculated from the measured mass flow rate and nominal cross sectional area of the flow cell.

Figure 3.6 shows both CFD simulation results and values calculated using the Blasius equation, in a modified form suitable for rectangular flow geometries that can induce secondary flows (Jones 1976). All four walls of the flow domain were considered to be hydrodynamically smooth (k_s = 0) for the simulation. The predicted values of pressure gradients agree quite well with the corresponding measurements for a smooth wall condition.

This agreement confirms that the clean walls of the flow cell were smooth during the experiments. These results also help to validate the ability to predict pressure losses in the rectangular flow cell, which may induce secondary flows, using the CFD simulation procedure described earlier.

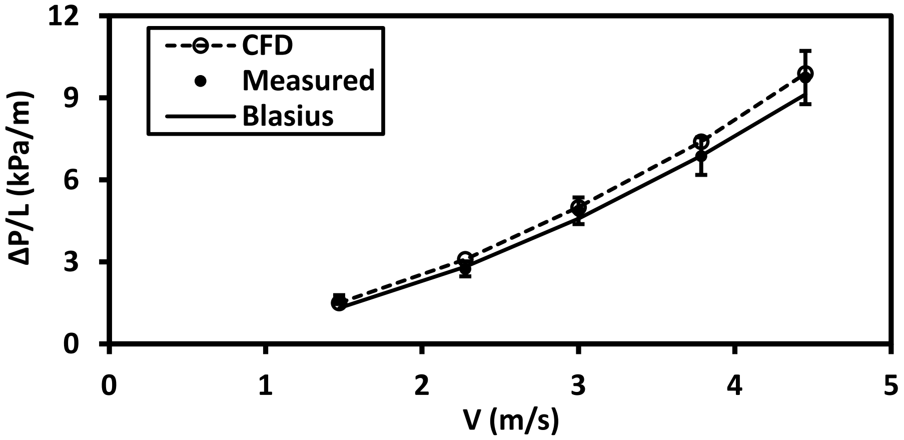

Figure 3.6. Comparison of the measured and predicted pressure gradients for a clean flow cell.

3.5.2. Case study 2: Sandpaper tests

Sandpapers of 80 and 120 grit were used for the experiments. Figure 3.7 shows photographs of the sandpapers. Flow tests were conducted by placing the sandpaper plates in the flow visualizing section of the flow cell. Pressure losses were recorded while water flow rates were varied. Additionally, the physical roughnesses of the sandpapers were measured with the MITUTOYO Contracer. The values from the Contracer measurements were used to determine the equivalent sand grain roughness using a correlation (Eq. 3.14) that was proposed by Flack and Schultz (2010a) on the basis of two statistical parameters, root mean square (R_{rms}) and skewness (R_{sk}):

$k_s = 4.43 R_{rms} (1 + R_{sk})^{1.37}$ ………….. (3.14)

$R_{rms} = \sqrt{\frac{\sum_{i=1}^{n} z_i^2}{n}}$ (z_i: data set of n data points on lateral axis x) ……………. (3.15)

$R_{sk} = \frac{n\sqrt{n-1}}{n-2} \frac{\sum_{i=1}^{n}(z_i - z_{avg})^3}{(\sum_{i=1}^{n}(z_i - z_{avg})^2)^{3/2}}$ (z_{avg}: arithmetic average of z_i) ……………… (3.16)

The rms-value represents the magnitude and skewness shows the spatial variation of roughness (King 1980). The values of k_s with the associated statistical parameters are reported in Table 3.2.

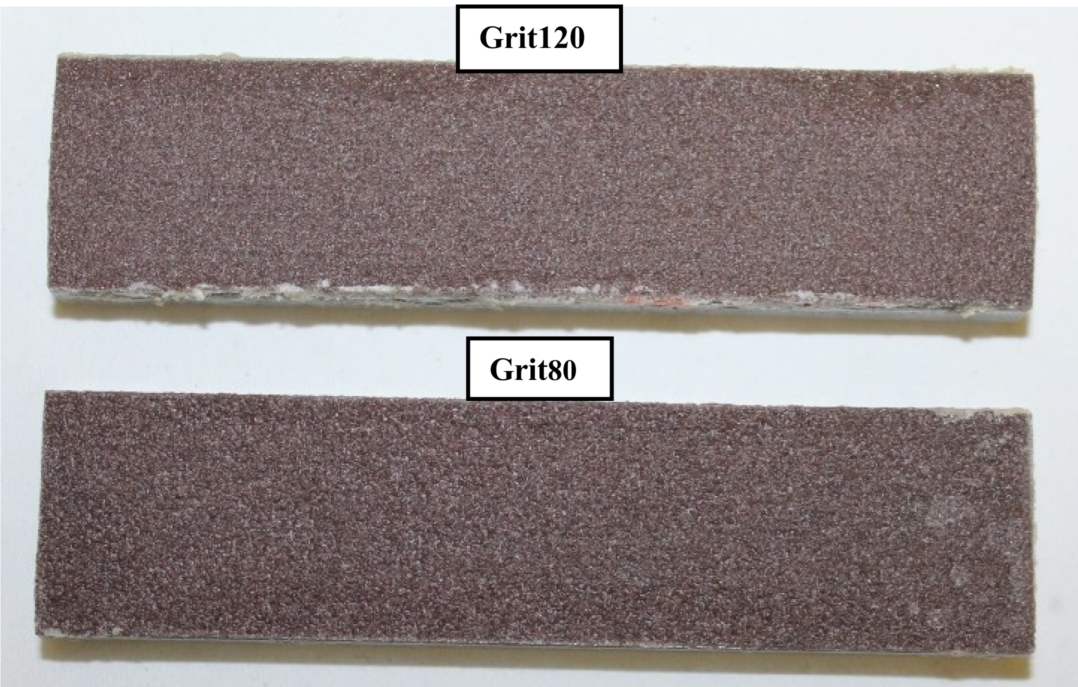

Figure 3.7. Photograph of the sandpapers.

Table 3.2. Hydrodynamic roughness with statistical parameters for the sandpapers

Sandpaper		RMS Roughness R_{rms} (μm)	Skewness of roughness R_{sk}	Sand grain roughness (Flack and Schultz model) k_s (mm)
Grit	Thickness (mm)			
80	0.7	73	0.43	0.5
120	0.9	55	0.19	0.3

For this case study, the estimated values of k_s were used as the boundary conditions to predict the measured pressure gradients following the simulation procedure described in Section 3.4 (CFD Simulation). The measured values of pressure gradients ($\Delta P/L_E$) are compared with the simulation results ($\Delta P/L_P$) in Figure 3.8, which shows the predictions to vary within ±15% of the measurements. The reasonable agreement shown here further validates the new CFD procedure. This agreement also suggests that ω-RSM is capable of simulating flow conditions in a rectangular flow cell having asymmetric wall roughness. Please refer to Appendix 8 for more details of this case study.

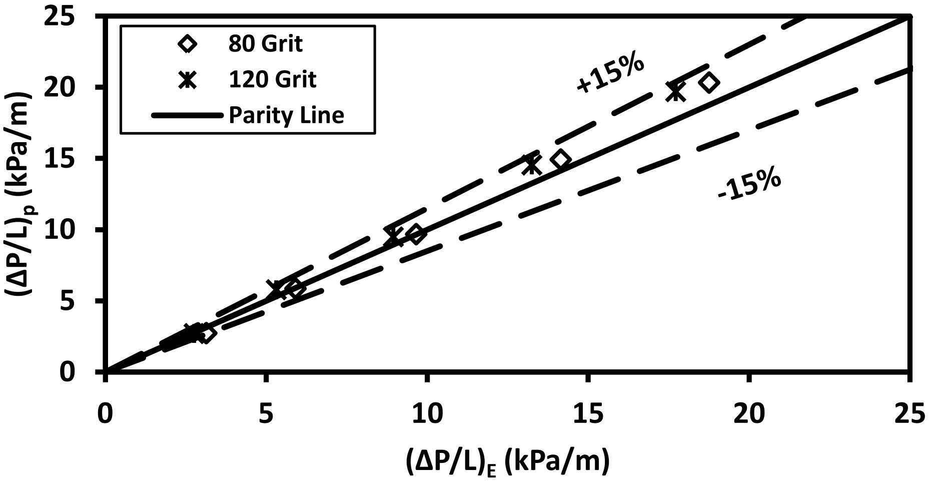

Figure 3.8. Comparison of the measured and predicted pressure gradients for sandpaper tests.

3.5.3. Case study 3: Bio-fouling tests

Andrewartha (2010) conducted experiments using a rectangular flow cell, which was fabricated from Plexiglas and had a cross-sectional area of 200 mm × 600 mm. Three walls of the custom built flow cell were smooth and the fourth wall was coated with a bio-fouling layer. Two separate parameters (velocity profile and drag force) were measured so that two separate calculations of k_s could be made. The velocity profile was measured using both a Pitot tube and Laser Doppler Velocimetry. The drag force was measured directly with a transducer.

Values of k_s, obtained from the velocity profile data (Andrewartha 2010), were then re-calculated using the CFD methodology developed here. In this case study, though, the measured velocity profiles, instead of pressure gradients, were predicted using the simulation results for this case study. Values of k_s for the wall simulating the bio-fouled rough wall were changed iteratively for the simulation. The value that could predict dimensionless velocity (u^+) profile within ±10% of the measured values was considered as the representative k_s for the corresponding bio-fouling layer. Figure 3.9 illustrates an example of the agreement between the measured and predicted velocity profiles.

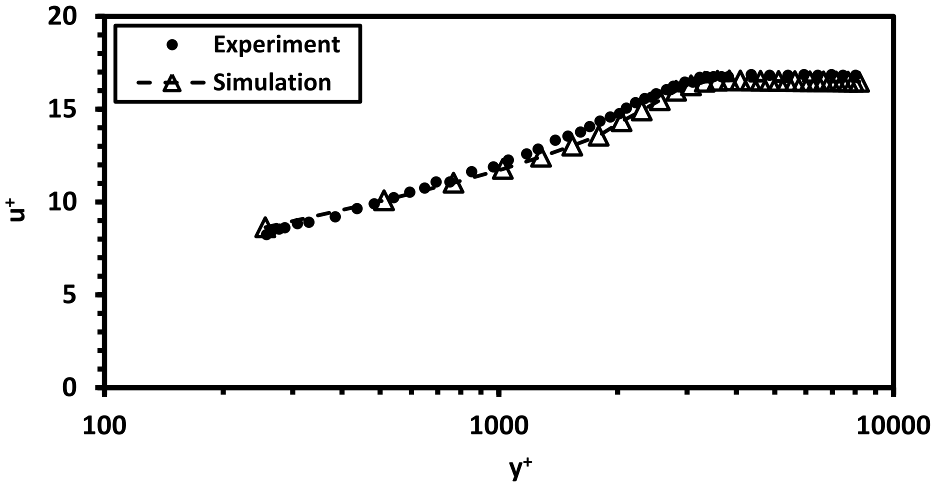

Figure 3.9. Example of the agreement between simulation results and experimental measurements for velocity profile (bio-fouling sample RP2F5).

The experimentally determined values of k_s and the corresponding results of the new CFD-based approach are compared in Table 3.3. The results of k_s determined by Andrewartha (2010) from two separate measurements show that significant uncertainty (as high as 100%) can be involved in such determinations. Interestingly, the results obtained from our CFD approach fall within the range of the experimental measurements. This agreement proves that the methodology used in this work is an effective tool for determining k_s. It is simple and capable of yielding reliable results. More details of this case study are available in Appendix 8.

Table 3.3. Comparison of the experimental hydrodynamic roughness with simulation results for bio-fouling tests

Bio-fouling Sample (Andrewartha 2010)	Hydrodynamic Roughness, k_s (mm)		
	Andrewartha (2010) Experiments		CFD Simulation (Current work)
	Method 1: Drag	*Method 2: Velocity Profile*	
RP1F1	5.73	5.33	5.5
RP1F4	4.47	3.47	4.0
RP2F5	4.37	2.59	3.0
SP1F6	1.03	0.00 (Smooth)	0.0 (Smooth)

3.6. Results and Discussion: Wall-Coating Tests

After validating it with three independent case studies, the CFD approach was used to determine the hydrodynamic roughness produced by the wall-coating layers of the viscous oil. Since similar data are not available in the literature to the best of our knowledge, the values of k_s obtained from the CFD simulations were corroborated further based on the topological measurement of physical roughness.

3.6.1. Hydrodynamic roughness

For the wall-coating tests, the bottom wall of the flow cell in the flow visualizing section was coated with viscous oil. The turbulent flow of water changed the topology of coating surface by producing physical roughness. After an initial period of around 500 s, visible changes of the roughness were negligible and the pressure losses did not change with time. The scenario is illustrated with Figure 3.10 that shows the values of instantaneous pressure gradients as a function of time. Detailed results are presented in Appendix 6.

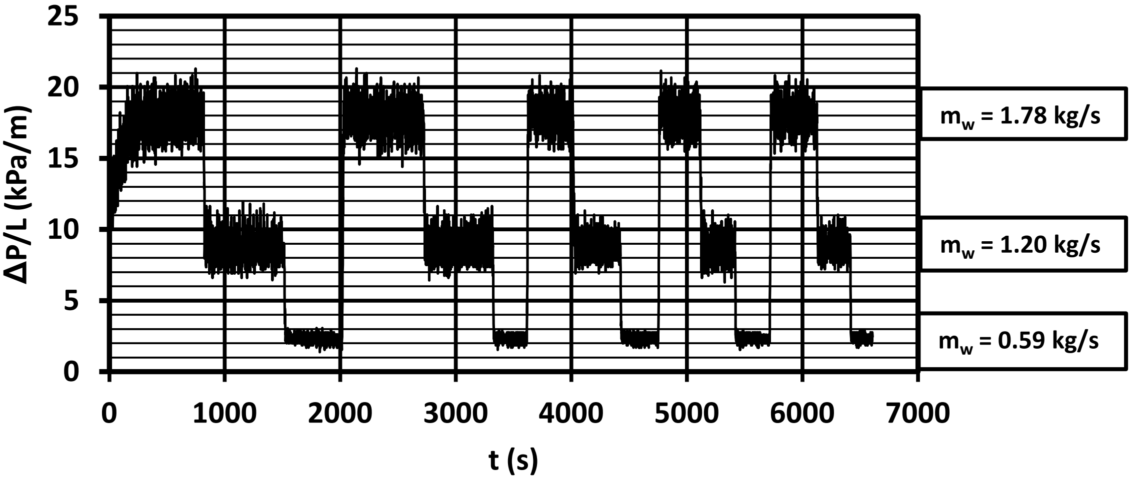

Figure 3.10. Illustration of instantaneous pressure gradients recorded at a time interval of 1 s as a function of time for a coating thickness of 0.2 mm.

Average values of the pressure gradients (as illustrated in Figure 3.10) were predicted by applying the CFD methodology to determine the equivalent hydrodynamic roughness produced by the wall-coating layers. The results are reported in Table 3.4. The values of k_s were quite proportional to the values of t_c. That is, a thicker coating layer could produce higher roughness under comparable flow conditions. The flow rate was not found to affect the hydrodynamic roughness; a single value of k_s could make reasonable predictions of $\Delta P/L$ for different values of m_w while t_c was constant. However, the intuitive expectation was to obtain a distinct equivalent hydrodynamic roughness for a combination of m_w and t_c. The reason for this apparent irregularity was not clear from the pressure loss measurements. This phenomenon was clarified after the measurement of actual physical roughness, which is discussed in the next section.

Table 3.4. Comparison of measurements with simulation results

Measurement			Simulation	
Coating thickness, t_c (mm)	Mass flow rate of water, m_w (kg/s)	Pressure gradient, $\Delta P/L$ (kPa)	Pressure gradient, $\Delta P/L$ (kPa)	Equivalent hydrodynamic roughness, k_s (mm)
0.1	0.59	2.0	2.0	0.1
	1.20	7.6	7.1	
	1.78	15.3	14.7	
0.2	0.59	2.2	2.3	0.4
	1.20	8.7	8.3	
	1.78	17.6	17.2	
0.5	0.59	2.2	2.8	1.5
	1.20	10.2	10.5	
	1.78	21.6	22.2	
1.0	0.59	3.6	3.6	3.5
	1.20	14.0	13.6	
	1.78	28.7	28.9	

3.6.2. Physical roughness

Surface characterization of the clean test plates and the rough wall-coatings was conducted with the MITUTOYO Contracer. Figures 3.11 and 3.12 illustrate respectively the topology of a clean wall and that of a coating layer. Actual roughnesses are demonstrated quantitatively with 3D plots, which were developed using the data obtained from the topological measurements. It should be noted that the clean test plates (no oil coating) behaved as smooth walls and the coating surface behaved as rough wall. The difference in hydrodynamic behavior can be appreciated by inspecting the 3D plots. The average physical roughness of the clean wall ($t_c = 0$) was 2 μm while the roughness of the coating surface ($t_c = 1.0$ mm) was 266 μm. That is, the hydrodynamically rough wall had a physical roughness two orders of magnitude greater than the smooth wall.

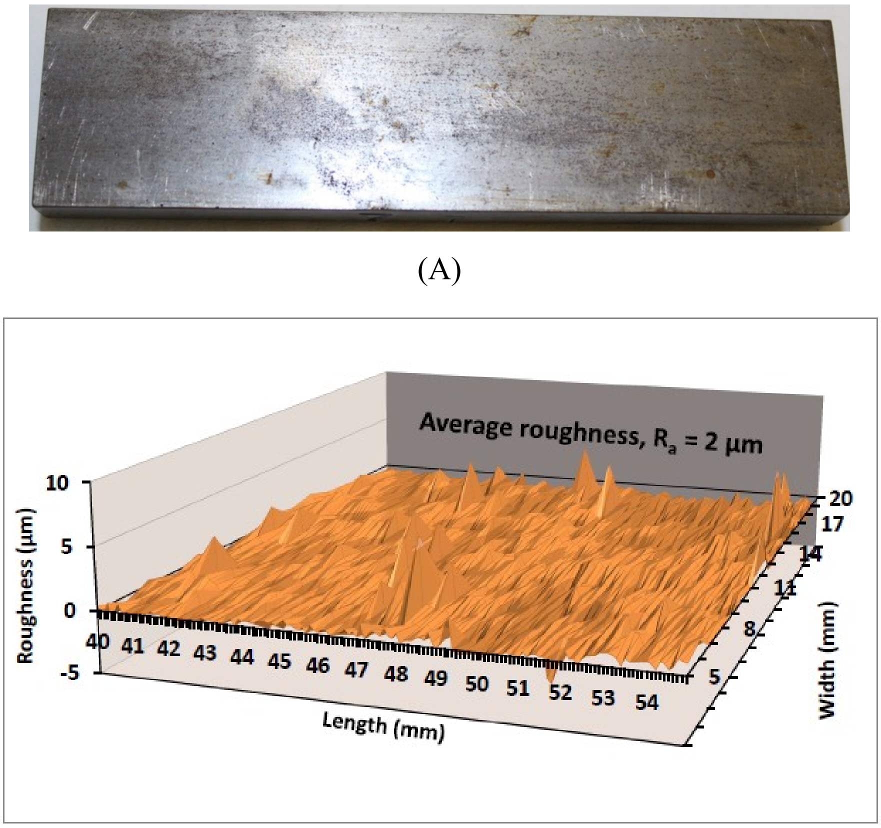

(A)

(B)

Figure 3.11. Illustration of the clean wall of a test plate: (A) Photograph; (B) 3D plot of the measured topology.

It is clear from Figure 3.12 that the roughness of the wall-coating layer was 3D in nature. That is, the variation was not consistent in any direction. The most probable reason for this kind of variation in roughness was the presence of secondary flows in the rectangular flow cell. The topological measurements were conducted over a large area (~ 1200 mm^2) to take the 3D nature of roughness into account. Also, the measurements were replicated a number of times (~ 40). Each of these data sets was comprised of approximately 800 × 15 data points. Examples of the collected data and the procedure used for data analysis are presented in Appendix 4.

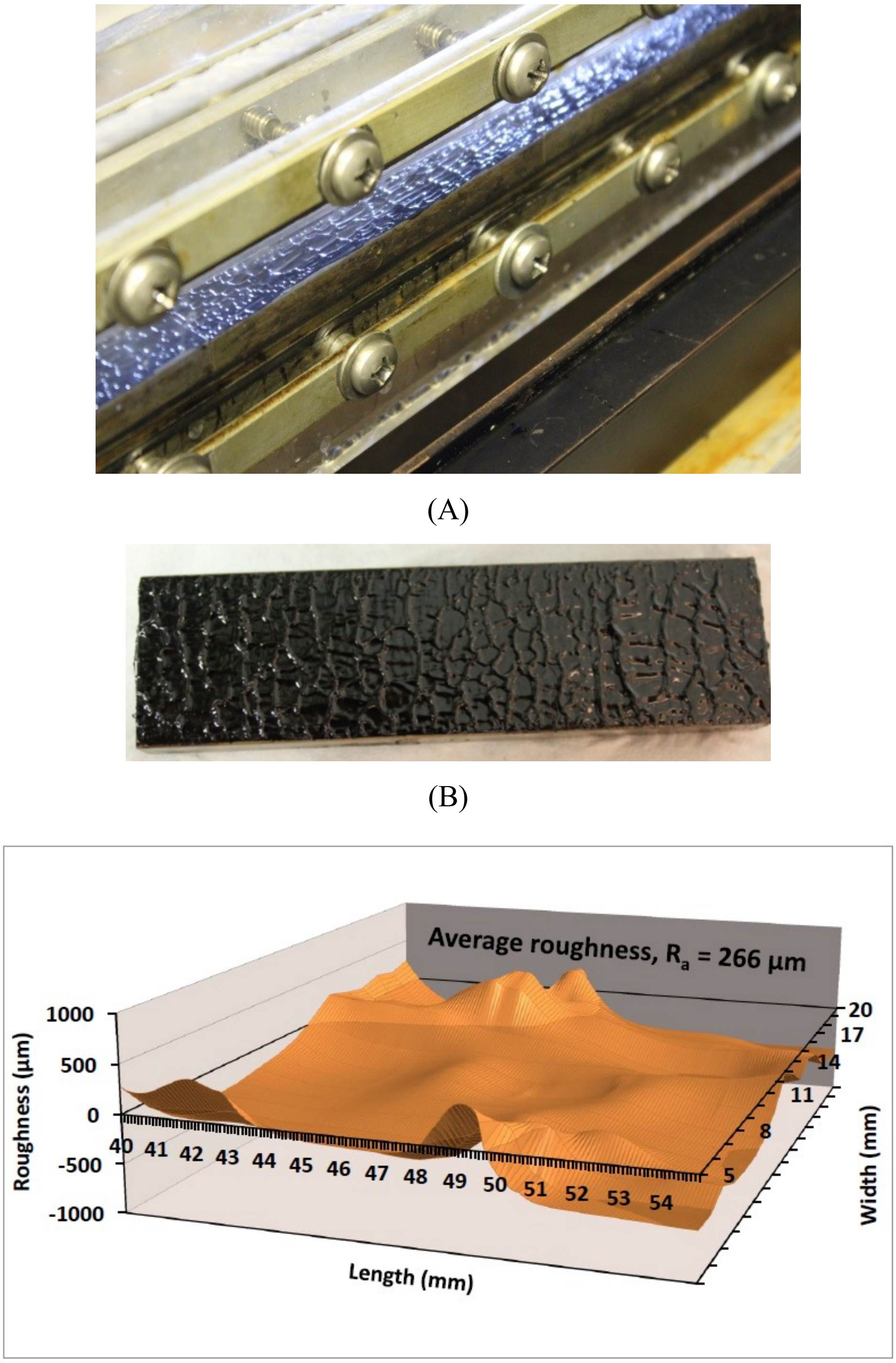

(A)

(B)

(C)

Figure 3.12. Illustration of the rough wall-coating layer (t_c = 1.0mm): (A) Photograph under flow conditions; (B) Photograph of a test plate with frozen coating layer; (C) 3D plot for the measured topology.

The topological data were used to estimate the values of k_s using the correlation (Eq. 3.14) proposed by Flack and Schultz (2010a). Although the model was developed for solid roughness, we applied it for the frozen viscous surface. The reasons for this application are as follows:

(i) A correlation between the equivalent hydrodynamic roughness produced by the physical roughness on a viscous wall-coating is unavailable in the literature.

(ii) Due to the high viscosity of the coating oil ($\mu_o = 2.13 \times 10^4$ Pa.s), no effective change in topology was observed under steady state flow conditions. That is, the roughness on the viscous wall-coating was comparable to a solid surface.

(iii) Most of the system-specific correlations between hydrodynamic and physical roughness on solid surfaces are based on a single average value, like center line average (R_a), root-mean-square average (R_{rms}) or peak-to-valley average (R_z) (Bons 2010). These models are mostly system specific and usually neglect the spatial distribution of roughness elements. Flack and Schultz (2010a) addressed the issue by incorporating skewness (R_{sk}) in their proposed correlation. In doing so the potential field of application for this model is significantly improved.

(iv) There are a few other models available in the literature that take into account the orientation of roughness elements (see, for example, Young et al. 2007); however, those models involve computationally complex parameters. In most cases, these parameters are worth evaluating for small scale measurements of roughness on a small area (~ μm^2). Compared to those models, the applicability of the correlation proposed by Flack and Schultz (2010a) is more comprehensive.

The equivalent roughness values calculated using the Flack and Schultz model are presented in Table 3.5 (see Appendix 5 for details). These results show the effect of flow rate on the roughness. The values of k_s, which are dependent on the rms-value (R_{rms}) and the skewness (R_{sk}) of roughness, tend to decrease with increasing flow rate. Although the variation in the flow rate of water does not change R_{rms} (~ $0.3t_c$) appreciably, the increasing flow rate reduces R_{sk}. In other words, the tested range of water flow rates does not change the magnitude of the roughness significantly, but reduces the spatial variation of roughness to some extent. Thus an approximate uncertainty of 30% is associated with the average values of k_s due to changing water flow rate. This can be considered an acceptable level of uncertainty, because previous researchers found higher uncertainties for the values of equivalent hydrodynamic roughness, for example:

a) The range of uncertainty for the equivalent hydrodynamic roughness produced by a typical solid surface is 20% - 70% (White 1999);

b) The values of k_s for different bio-fouling layers determined using separate experimental measurements (Andrewartha 2010) involved uncertainty of 7% - 100% (*cf.* Table 3.3);

c) Bhatt (2007) showed that the values of k_s calculated using a correlation can involve uncertainty of 20% - 65%.

It is also clear from the last two columns of Table 3.5 that good agreement is obtained between the k_s determined from the surface measurements and the k_s determined from the simulations (reproduced from Table 3.4). That means the values of k_s obtained on the basis of two independent methods agree quite well. This agreement supports the CFD approach used in the current work to determine the values of k_s produced by a viscous layer of wall-coating.

Table 3.5. Hydrodynamic roughness and associated statistical parameters

Coating thickness t_c (mm)	Mass flow rate of water m_w (kg/s)	RMS roughness R_{rms} (μm)		Skewness R_{sk}	Hydrodynamic roughness, k_s (mm)		
					Surface measurement (Flack and Schultz model)		CFD simulation
					Flow dependent	Average	
0.5	0.59	176		0.87	1.8	1.7	1.5
	1.20	181		0.78	1.8		
	1.78	181		0.62	1.5		
1.0	0.59	372		0.91	4.0	3.4	3.5
	1.20	315		0.82	3.2		
	1.78	316		0.73	3.0		

3.7. Summary

The objective of our research was to study the hydrodynamic roughness produced by a film of viscous wall-coating. The atypical roughness was investigated with experiments and numerical simulations. The outcomes of this research are summarized as follows:

(i) The equivalent hydrodynamic roughness produced by a viscous surface can be determined by predicting measured pressure losses with numerical simulation of flow conditions. A CFD-based methodology is validated and applied for this purpose in the current work.

(ii) This study suggests that the CFD-based approach developed here will be useful in determining the hydrodynamic equivalent of any rough surface (e.g., viscous oil, solid and bio-fouling).

(iii) A hydrodynamic roughness correlation (Flack and Schultz 2010a) that was developed for solid surfaces has been applied in this work for the coating layer of viscous oil with success.

CHAPTER 4

A PARAMETRIC STUDY OF THE HYDRODYNAMIC ROUGHNESS PRODUCED BY A WALL-COATING LAYER OF VISCOUS OIL[‡]

4.1. Introduction

The wall-fouling layer in a water lubricated pipeline is a nearly stationary coating film of viscous oil adhered on the pipe wall (Joseph et al. 1999, McKibben et al. 2000b, Shook et al. 2002, Schaan et al. 2002, McKibben et al. 2007, Vuong et al. 2009). This wall-coating layer can produce a very large equivalent hydrodynamic roughness value. The typical equivalent roughness of a commercial steel pipe is about 0.045 mm (White 1999), while a pipeline with a viscous oil layer on the pipe wall can produce a hydrodynamic roughness of 1 mm or more (Brauner 1963, Shook et al. 2002). The roughness is produced primarily through contact between the viscous oil coating and the turbulent water layer that flows over the film while lubricating the oil core. The result is a rippled or rough wall that produce very large hydrodynamic roughness values (Brauner 1963, Picologlou et al. 1980, Shook et al. 2002). While the presence of the coating reduces somewhat the cross-sectional area available for flow, which also causes an increase in pressure loss for a given throughput, the increased hydrodynamic roughness plays a much more important role in this increase.

In the present study, a customized rectangular flow cell was used to perform a parametric investigation of the equivalent hydrodynamic roughness produced by the wall-coatings of different viscous oils. The CFD-based procedure described in Chapter 3 was used to determine the roughness values. The procedure was also applied for a set of pipeloop test results published elsewhere (McKibben et al. 2007; McKibben and Gillies 2009). Based on the results presented here, a new correlation is proposed for the equivalent hydrodynamic roughness produced by a viscous layer of wall-coating in terms of the coating thickness. This correlation can be used to estimate the roughness directly from either a measured or a known value of the physical wall-coating thickness.

[‡‡] *A version of Chapter 4 was published in the proceedings of SPE Heavy Oil Conference 2015: S. Rushd and S. Sanders, 2015. SPE-174485-MS, Society of Petroleum Engineers, SPE Canada Heavy Oil Technical Conference, 09-11 June, Calgary, Alberta, Canada. Another version of the chapter, co-authored by S. Rushd and S. Sanders, has been submitted to the Journal of Petroleum Science.*

4.2. Description and Application of Equipment and Processes

4.2.1. Experimental setup

A 2.5 m long rectangular flow cell was designed and fabricated for the present study. The flow cell consists of a square channel where segmented steel plates comprise the bottom of the cell. These plates were coated with a measured thickness (t_c) of oil prior to the start of each flow experiment. The cross section of the flow channel without wall-coating was 15.9 mm × 25.4 mm. Its entrance length was 1.5 m, which is more than $60D_h$; D_h is the hydraulic diameter defined as $4A/P$, where A is the cross-sectional area and P is the wetted perimeter of the cross-sectional area. The flow cell included two Plexiglas windows in order to observe the shape of oil-water interface. This custom built cell was placed in a 25.4 mm pipeloop as shown in Figure 4.1(A). A photograph of the cell under actual flow condition when physical roughness was developed on the wall-coating layer is included in Figure 4.1(C). A detailed description of the flow cell is available in Appendix 1.

Water from the supply tank was circulated through the loop with a pump (Moyno 1000) driven by a VFD and motor (7.5 hp BALDOR INDUSTRIAL MOTOR). The pump speed was set to obtain the desired mass flow rate of water. The flexible connector and dampener minimized unwanted vibrations resulting from pressure pulses from the pump. The heat exchanger was used to maintain the water temperature at 20°C. The filter (Arctic P2 filter with 34 micron bag) collected any stray oil droplets stripped from the coating layer; however, for the tests reported here coating loss was negligible because of the relatively high oil viscosities used. A coriolis mass flow meter (Krohne MFM 4085K Corimass, type 300G+) measured both mass flow rate and temperature of the flowing water.

The steady state pressure loss across the flow cell was measured with a differential pressure transducer (Validyne P61). The experiments were conducted by varying water flow rates, coating thickness and oil viscosities. Water flowing over the wall-coating layer formed irregular ripples on the oil surface (Figure 4.1C), which increased the equivalent hydrodynamic roughness.

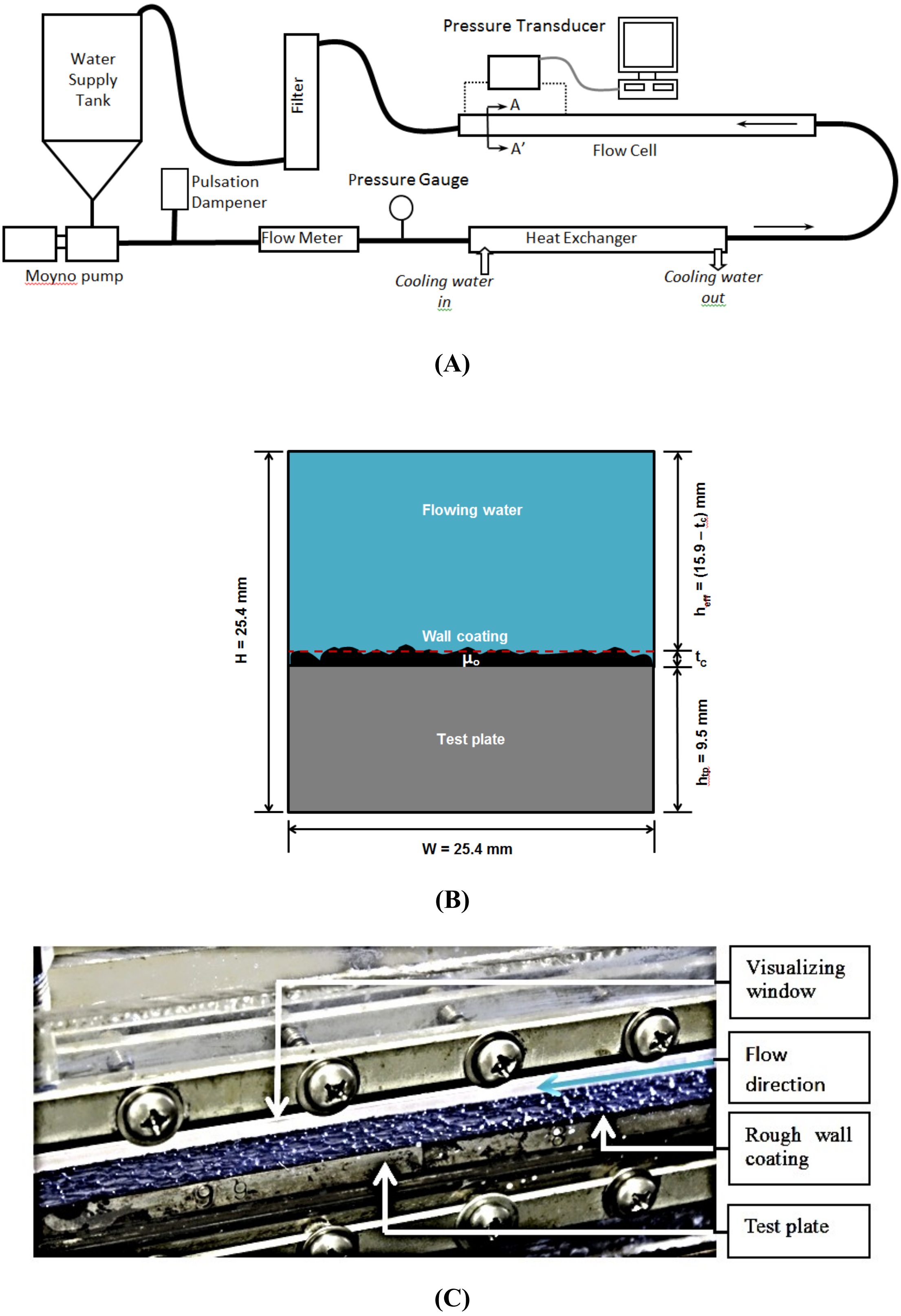

Figure 4.1. Illustration of the experimental facility: (A) Schematic presentation of the flow loop; (B) Cross-sectional view (section A-A') of the flow cell; (C) Photograph showing the actual flow situation.

4.2.2. Experimental parameters

The rectangular flow cell was used to study the hydrodynamic effect of different viscous wall-coatings. The measured variable was the pressure gradient ($\Delta P/L$). The controlled parameters (with corresponding values) are listed in Table 4.1. The most important of these parameters are average thickness (t_c) and viscosity (μ_o) of the coating oil. The bottom wall of the rectangular flow cell was coated with the oil. The sample oils used for the current research are described in greater detail in Appendix 2. These oils were provided by Husky Energy and Syncrude Canada Ltd. The experimental t_c value for an oil was selected depending on oil viscosity (μ_o) and mass flow rate of water (m_w). The value of t_c that could be maintained under the highest flow rate for the lower viscosity oils ($\mu_o \sim 65$ Pa.s & 320 Pa.s) was 0.2 mm. Similarly, the maximum t_c for the higher viscosity oils ($\mu_o \sim 2620$ Pa.s & 21 300 Pa.s) was 1.0 mm. Tested values of t_c for these oils were 0.2 mm, 0.5 mm and 1.0 mm. The overall uncertainty associated with the measurement of t_c in the flow cell was 10% (See Appendix 5 for details). Thus, the coating thickness for the first phase of experiments was selected so that the water flow rate could not change it significantly; experimental evidences for the stability of coating thickness are available in Appendix 6. The purpose of these tests was to evaluate the effects of flow rate and oil viscosity on the hydrodynamic roughness while keeping the coating thickness constant.

Table 4.1. Controlled parameters for the experiments

Controlled Parameter	Values
Thickness of wall-coating (t_c), mm	0.2, 0.5 & 1.0
Viscosity of coating oil (μ_o), Pa.s	65, 320, 2620 & 21 300
Mass flow rate of water (m_w), kg/s	0.59, 0.91, 1.20, 1.52 & 1.78
Flow Temperature (T), °C	20

4.3. CFD Simulations

The CFD simulations were used to determine the unknown equivalent sand-grain roughness of the rough viscous oil-covered bottom wall of the flow cell. This was done by modeling the water flow through the cell over the viscous coating with the CFD software package, ANSYS CFX 13.0. The software solves the governing differential equations which include Reynolds Average Navier-Stokes (RANS) continuity and momentum equations. The Reynolds stress term in RANS was modeled using an omega based Reynolds Stress Model (ω-RSM). The model was described in Chapter 3. Calculated values of pressure gradient were obtained with the simulations by specifying the values of k_s for the walls. However, the values were unknown for the oil-coated bottom wall of the flow cell for any given flow condition. A trial-and-error procedure was adopted to determine the appropriate equivalent hydrodynamic roughness. Starting from a low value, k_s was changed in increments and the simulation was repeated until a reasonable agreement between the measured and predicted pressure loss (maximum 5% difference) was observed. The final value of k_s at which this condition was met was considered to be the equivalent hydrodynamic roughness of the corresponding rough wall. Basic steps of the trial-and-error procedure are illustrated in Figure 4.2.

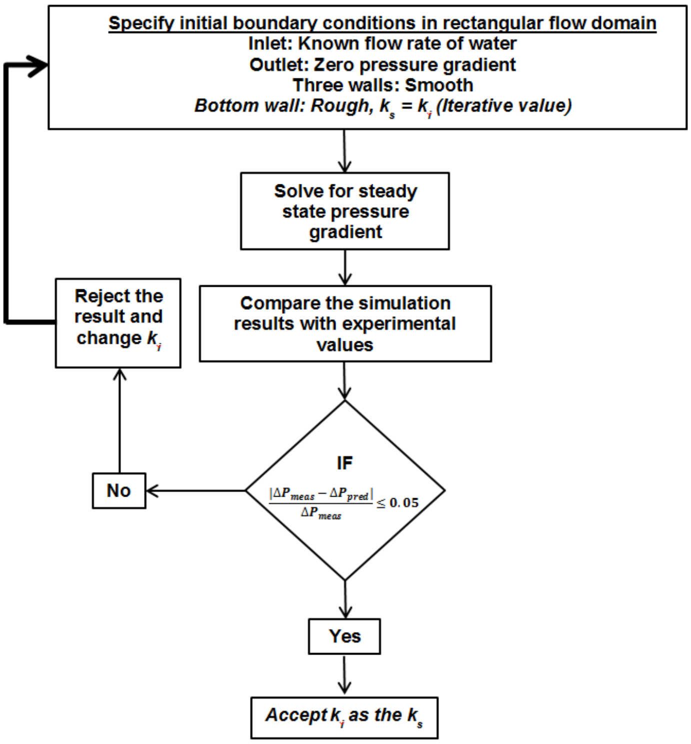

Figure 4.2. Flow chart describing the steps involved in the simulation procedure for computing the equivalent sand-grain roughness (k_s).

4.3.1. Geometry and meshing

Dimensions of the geometry correspond to the inner dimensions of the flow cell. The material filling the computational domain is room temperature water. Although the typical length of the computational flow domain was 1.0 m, a 2.0 m length was also tested to confirm the length independence of simulated results. The flow geometry mesh was generated with ANSYS ICEM CFD. Mesh independence tests of the simulation results were performed. The total number of nodes considered to be enough for grid independence for the rectangular domain was 670 200. Illustrative descriptions of the geometry and mesh are available in Chapter 3.

4.3.2. Boundary conditions

The boundary conditions for the flow domain were prescribed as follows. At the inlet, the experimental mass flow rate of water and a turbulent intensity of 5% were specified. A zero pressure was specified at the outlet. The no-slip condition was used at boundaries representing walls. Two side walls and the upper wall in the rectangular domain were considered hydrodynamically smooth (k_s = 0). Flow conditions with rough wall-coatings were simulated by considering the bottom wall in the rectangular domain as rough ($k_s > 0$). All computations were performed to obtain steady state solutions. Typical computational time requirement was 45 minutes for each test condition modeled.

4.4. Results and Discussion

As mentioned earlier, two hydrodynamic effects were produced by the wall-coating layer: a reduction of the effective flow area and a drastically increased equivalent sand grain roughness. The reduction in the flow area is taken into account through the average thickness of the wall-coating layer, which is a physical parameter that can be measured directly. However, the equivalent roughness cannot be measured directly. It is usually calculated on the basis of multiple measurements, including pressure gradient, flow rate, fluid properties and flow geometry. In this work, the k_s value corresponding to each combination of viscous wall-coating thickness (t_c) and water Reynolds number (Re_w) are determined by conducting CFD simulations to develop a correlation between k_s and t_c.

4.4.1. Rectangular flow cell results

The variation in pressure gradient due to the change in controlled parameters is demonstrated in Figure 4.3(A). It can be seen from the figure that higher flow rates, expressed here as bulk water velocity through the flow cell ($V=m_w/\rho_w A_{eff}$), cause $\Delta P/L$ to increase approximately with V^2, as would be expected for the turbulent flow of water through a channel or pipe. Note, however, that compared to the clean wall condition, $\Delta P/L$ is significantly higher when the wall is coated with oil ($t_c > 0$). The difference is as large as one order of magnitude for the highest flow rate. Clearly, the primary contributor to the measured pressure loss at any velocity is the presence of the oil coating in the flow cell. Another important point to note is that the results are presented for a specific oil. Although four different oils with viscosities ranging from 65 Pa.s to 21 300 Pa.s were tested (see Table 4.1), the results were almost identical to those presented in Figure 4.3(A). In other words, oil viscosity played a negligible role over the range of viscosities tested here. The impact of μ_o on the measured $\Delta P/L$ is demonstrated in Figure 4.3(B).

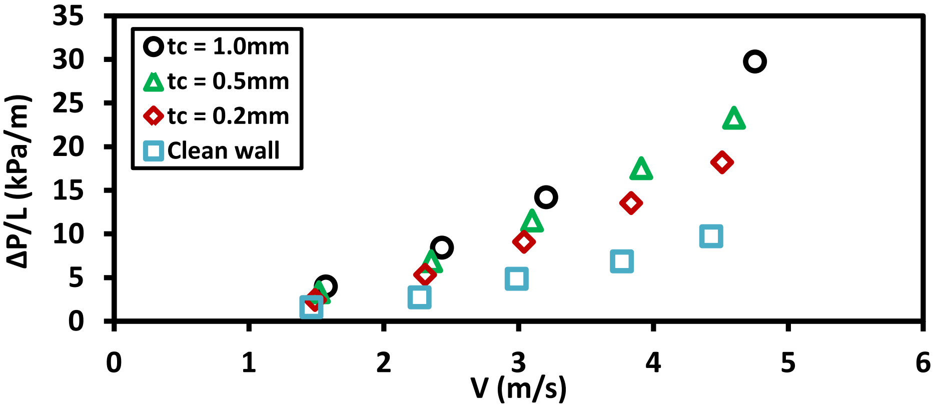

(A)

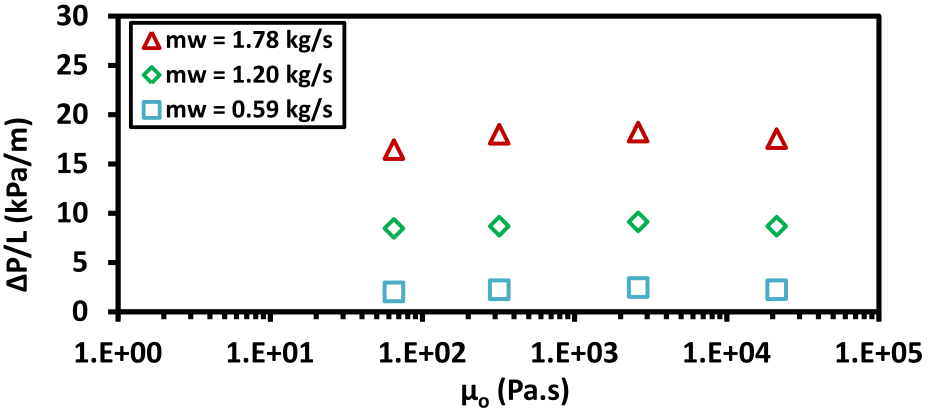

(B)

Figure 4.3. Presentation of experimental results for the rectangular flow cell: (A) Pressure gradients ($\Delta P/L$) as a function of bulk water velocity (V) for varying coating thickness (t_c) and a constant oil viscosity (μ_o = 2620 Pa.s); (B) $\Delta P/L$ as a function of μ_o for varying water flow rate (m_w) and a fixed coating thickness (t_c = 0.2 mm).

4.4.2. Comparison of roughness effects with reduced flow area effects

The wall-coating layers in the flow cell increased pressure gradients by increasing the equivalent hydrodynamic roughness and, also, by reducing the effective flow area. Relative contributions of these effects are compared here. In this regard, the relative changes in pressure loss and hydraulic diameter are considered, below, to better analyze the results presented in the previous section:

a) The reduction in flow area due to wall-coating can be quantified in terms of a percentile reduction in hydraulic diameter ($\%\Delta D_h$):

$$\%\Delta D_h = \frac{D_h^{clean} - D_h^{coat}}{D_h^{clean}} \times 100 \;\ldots\ldots.(4.1)$$

Here, $D_h = 2wh/(w+h)$ and $h = 15.9 - t_c$ mm for the rectangular flow cell; $t_c = 0$ when the wall is clean.

b) The increase in pressure loss due to the wall-coating can be quantified as a percentile increment in pressure gradient ($\%\Delta P/L$):

$$\%\Delta P/L = \frac{\Delta P/L^{coat} - \Delta P/L^{clean}}{\Delta P/L^{clean}} \times 100 \ldots\ldots\ldots\;(4.2)$$

c) In general, $\Delta P/L$ increases as D_h decreases when V is constant. For hydrodynamically smooth wall(s), constant fluid properties and flow rates, $\Delta P/L$ is inversely proportional to $D_h^{1.25}$, i.e., $\Delta P/L \approx CD_h^{-1.25}$ (White, 1999). This relation is derived using Blasius' Law, which was proposed for hydraulically smooth pipes. The relationship for hydraulically rough wall(s) is complex. In such a scenario, $\Delta P/L$ changes exponentially as a function of k_s and D_h.

Using the experimental results, $\%\Delta D_h$ is calculated in the range of 0.3% - 4.0%. If the viscous wall-coatings were hydrodynamically smooth, the corresponding $\%\Delta P/L$ would be in the range of 2% - 16% ($\Delta P/L \approx CD_h^{-1.25}$). However, the range of $\%\Delta P/L$ calculated using measured values of $\Delta P/L$ is 50% - 200%. The significant relative change in pressure gradients demonstrates the dominant effect of hydrodynamic roughness in the flow cell.

A quantitative comparison of the contributions in pressure gradients due to the reduction in flow area and the increase in hydrodynamic roughness is presented in Figure 4.4, which is produced for one of the higher viscosity oils (μ_o ~ 2620 Pa.s) and the highest mass flow rate (m_w = 1.78 kg/s). Evaluation of Figure 4.4 provides the following conclusions:

i) Experimental *%ΔP/L* is much higher compared to the similar estimates obtained by using Blasius' correlation.

ii) Evidently, *%ΔP/L* calculated from the measured values of pressure gradients cannot be explained with respect to the reduction in flow area due to wall-coating only. It can be explained by considering that the viscous wall-coating not only reduces the effective flow area but also increases the equivalent hydrodynamic roughness.

iii) The obvious source for the hydrodynamic roughness produced by the layer of viscous oil on the wall is the rough interface between wall-coating and turbulent water.

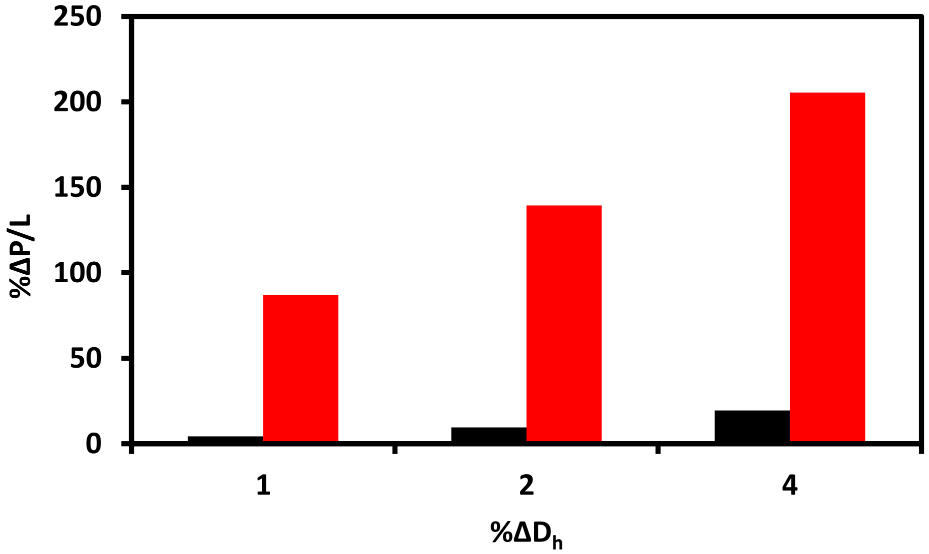

Figure 4.4. Presentation of the increase in pressure gradient (*%ΔP/L*) as a function of the reduction in hydraulic diameter (*%ΔD*$_h$); Black columns: Blasius' estimates; red columns: calculations from measured values (μ_o = 2620 Pa.s, m_w = 1.78 kg/s).

4.4.3. Analysis of hydrodynamic roughness

The respective sand grain equivalent for each experimental coating layer was determined. The procedure to determine the hydrodynamic roughness produced by a wall-coating layer is demonstrated in Figure 4.5, where experimental results are shown in comparison to the simulation results. The detailed results and associated errors are available in Appendix 5.

As demonstrated in Figure 4.5, the simulated pressure gradients (*ΔP/L*) agree well with the corresponding experimental results when the rectangular flow cell is clean, i.e., the conditions where the bottom wall is not coated with oil (t_c = 0). For these simulations all four walls of the rectangular flow cell were considered “smooth”, i.e., $k_s = 0$. This finding was also discussed Chapter 3. Compared to the smooth wall condition ($t_c = 0$), the measured pressure gradients are significantly higher for the coated walls ($t_c > 0$). Clearly, the major contributor to the additional $\Delta P/L$ is the wall coating layer of oil on the bottom wall of the flow cell.

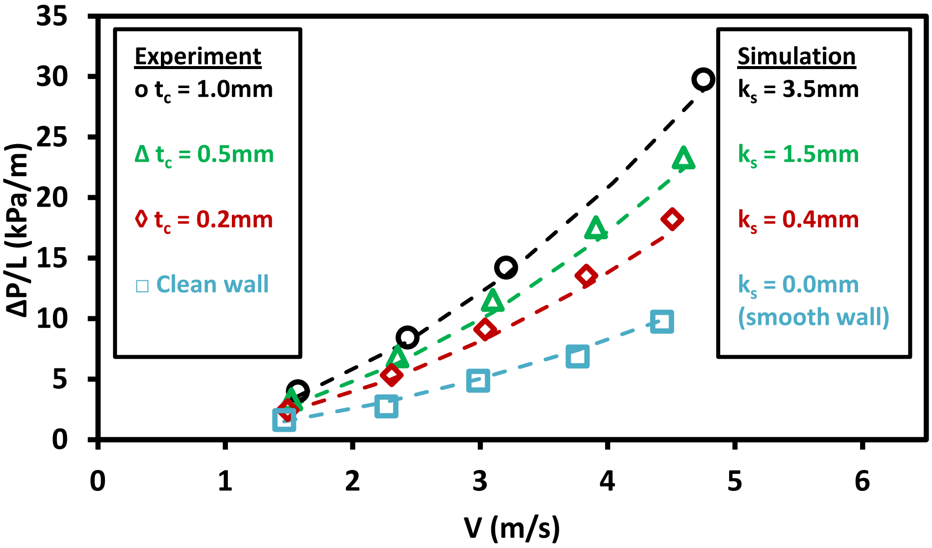

Figure 4.5. Comparison of the simulation and the experimental results for the rectangular flow cell (μ_o = 2620 Pa.s).

The results presented in Figure 4.5 show that the hydrodynamic roughness produced by a coating thickness can be satisfactorily modeled with a single value of k_s for varying water flow rate and oil viscosity over the range of values tested here. That is, k_s is a strong function of t_c and a weak function of μ_o or V. The reasons for this observation can be stated as follows:

(i) Irrespective of μ_o, the t_c was controlled as constant in the flow cell for the tested range of V.

(ii) The physical roughness developed on the coating layer was observed to be independent of μ_o. That is, there was no observable difference for the physical roughness at a fixed V when coating oil was changed. However, it was not possible to measure the physical roughness when the oil viscosity was less than 21 300 Pa.s (see Chapter 3 for details).

The dependence of k_s on t_c in the rectangular flow cell is more clearly demonstrated in Figure 4.6, which also indicates a proportional correlation between k_s and t_c.

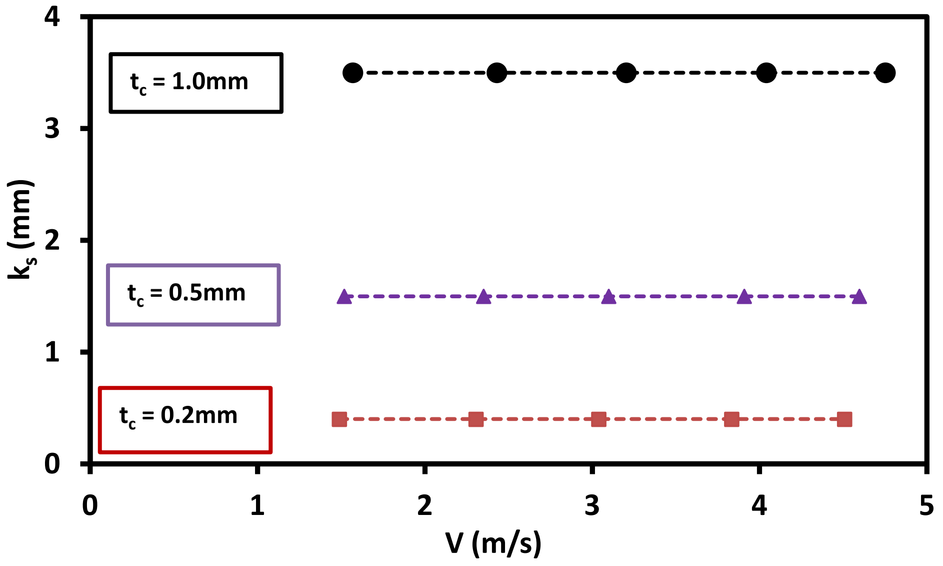

(A)

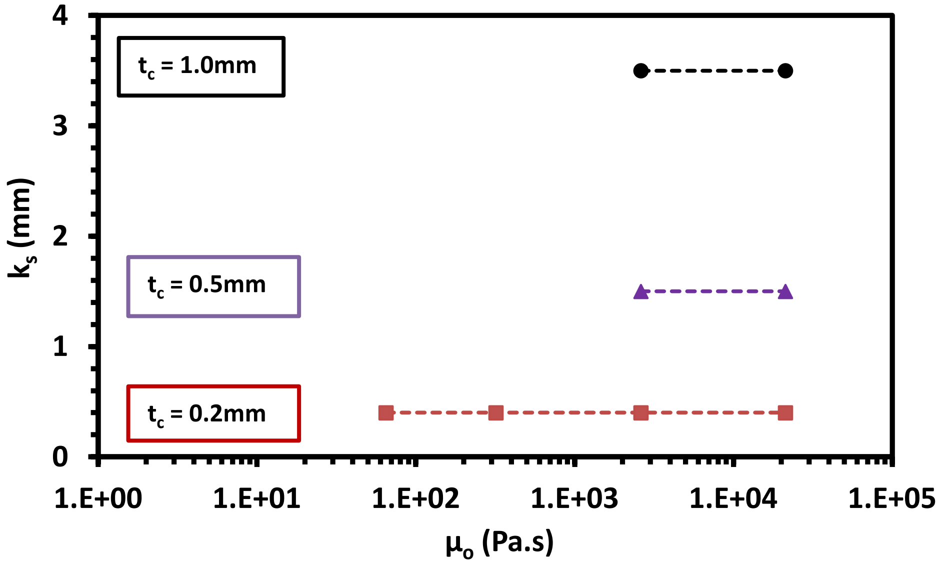

(B)

Figure 4.6. Illustration of hydrodynamic roughness (k_s) for flow cell experiments as a function of: (A) velocity (V); (B) oil viscosity (μ_o).

4.4.4. Application of CFD method to pipeline results

The methodology for determining the equivalent hydrodynamic roughness developed for the flow cell experiments was then applied to determine k_s for comparable tests carried out with a recirculating pipeloop. The pipeline tests were conducted at the Saskatchewan Research Council (SRC) Pipeflow Technology Centre^{TM} (McKibben et al. 2007; McKibben and Gillies 2009).

The experiments utilized a 103.3 mm (ID) pipe where its internal wall was fouled/coated with two different heavy oils (μ_o ~ 3 Pa.s & 27 Pa.s). The wall-coatings were developed in the course of testing lubricated pipe flows. After completing a set of LPF tests, water was pumped through the pipeline to drive out the oil core. The flow scenario for the pipeline testing is shown schematically in Figure 4.7. Pressure loss and wall-coating thickness measurements were made simultaneously at mean (bulk) water velocities of V = 0.5, 1.0, 1.5 and 2.0 m/s. A custom-built double pipe heat exchanger (Schaan et al. 2002) and a "hot film probe" were used to obtain wall-coating thickness measurements. A more detailed description of the apparatus and test procedure is available in Chapter 5. The wall-coating thickness for the pipeline tests decreased with increasing velocity, i.e., t_c values were not independent of V; the coating was partially stripped from the wall as the water velocity was increased.

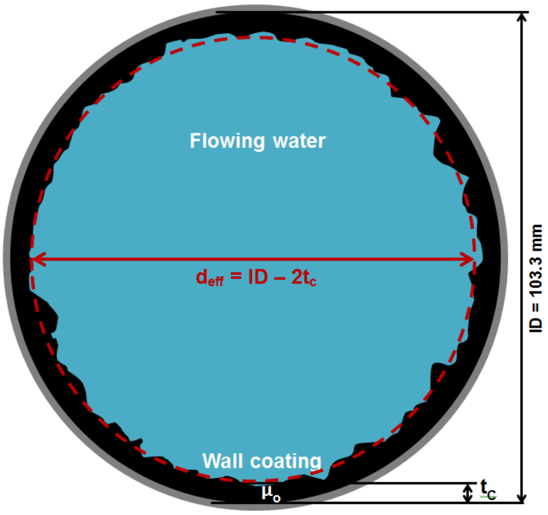

Figure 4.7. Schematic cross-sectional view of test section in the pipeline.

As was done for the rectangular flow cell tests, CFD simulations of the water flush tests were conducted to determine the equivalent hydrodynamic roughness. The typical results of experiments and simulations for the pipeline tests are shown in Figure 4.8. Both k_s and t_c values vary with V and μ_o in the pipeline tests; specifically, k_s is a direct function of t_c and an indirect function of V and μ_o. It should be noted that, even though t_c changes with V for the pipeline tests, the proportional relationship between t_c and k_s is similar to that of the flow cell experiments.

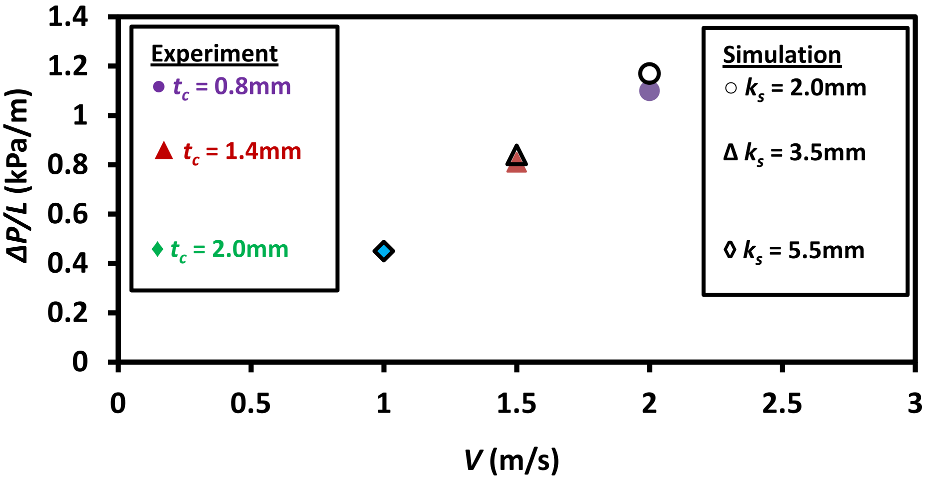

Figure 4.8. Comparison of simulation and experimental results for the pipeline tests conducted at SRC ($\mu_o \sim 27$ Pa.s).

The values of hydrodynamic roughness for the pipeline tests were calculated using two separate, independent methods: by predicting measured pressure losses with CFD simulations conducted using the same procedure used earlier for the rectangular flow cell tests, and by using the Colebrook correlation:

$$\frac{1}{\sqrt{f}} = -2\log_{10}\left(\frac{k_s}{3.7d_{eff}} + \frac{2.51}{Re_w\sqrt{f}}\right),\ 4\times10^3 < Re < 1\times10^8 \text{..........(4.3)}$$

For the pipeline tests, the wall-coating was assumed to be uniform over the wetted perimeter of the pipe, thereby providing the opportunity to calculate directly the hydrodynamic roughness from the measured pressure loss. The values calculated on the basis of the Colebrook formula agree reasonably well with the values obtained using the CFD method. The results are presented in Table 4.2.

Table 4.2. Hydrodynamic roughness for pipeline tests ($\mu_o \sim 27$ Pa.s)

Water Velocity (V) m/s	Wall-Coating Thickness (t_c) mm	Pressure Gradient (ΔP/L) kPa/m	Equivalent Sand Grain Roughness (k_s) Mm	
			Colebrook Correlation	CFD Method
1.0	2.0	0.45	5.9	5.5
1.5	1.4	0.81	4.1	3.5
2.0	0.8	1.10	2.5	2.0

4.4.5. Correlation of k_s with t_c

A correlation between k_s and t_c is proposed here, on the basis of the data obtained from rectangular flow cell tests and the pipe flow tests. The correlation is expressed in Eq. (4.4) and illustrated in Figure 4.9.

$$k_s = 2.76t_c, 0.2\,mm \le t_c \le 2.0\,mm \ldots\ldots\ldots\ldots\ldots (4.4)$$

The proportionality constant of the equation is determined with a regression analysis for which $R^2 = 0.96$. The average uncertainty associated with the predictions of this correlation is ±14%.

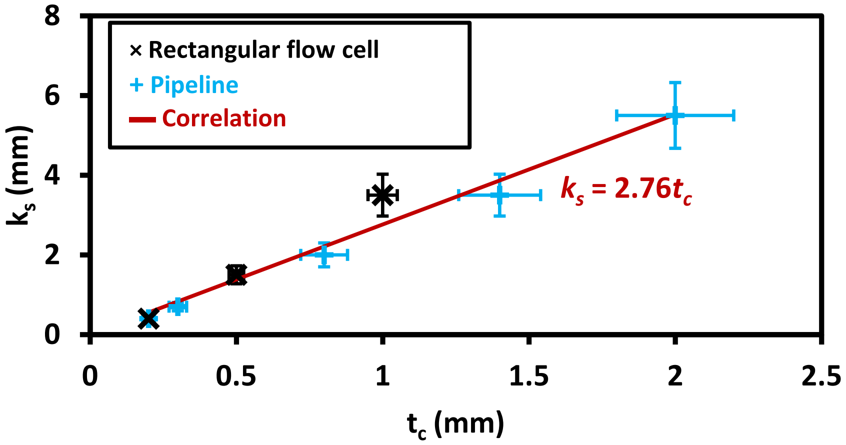

Figure 4.9. Correlation between hydrodynamic roughness (k_s) and coating thickness (t_c).

As shown in Figure 4.9, eight data points are used to develop the correlation. Three of these points are obtained from the experiments conducted with the flow cell and five points are from pipeline tests. Multiple combinations of oil viscosity, water flow rate and coating thickness were used for the flow cell experiments. Therefore, the three data points shown in Figure 4.9 actually correspond to 24 different flow conditions, meaning the correlation is based on 29 distinct flow conditions. The data used for developing the correlation are presented in Table 4.3.

The relationship between k_s and t_c proposed in this work is the first of its kind. To the best of our knowledge, a similar correlation is not available in the literature. An example of its application to the prediction of pressure losses in a fouled/coated pipeline is presented in Appendix 13.

Table 4.3. Data used for developing the correlation between k_s and t_c (Eq. 4.4)

Apparatus	Hydraulic Diameter (D_h) Mm	Oil Viscosity (μ_o) Pa.s	Average Velocity (V) m/s	Coating Thickness (t_c) mm	Hydrodynamic Roughness (k_s) Mm
Flow Cell	20	65, 320, 2620, 21300	1.5	0.2	0.4
			3.1		
			4.5		
		2620, 21300	1.5	0.5	1.5
			3.1		
			4.6		
			1.6	1.0	3.5
			3.2		
			4.8		
Pipeline	100	3	1.0	0.2	0.4
			1.5	0.3	0.7
		27	1.0	0.8	2.0
			1.5	1.4	3.5
			2.0	2.0	5.5

4.5. Summary

The objective of current work is to provide detailed information about the hydrodynamic roughness that a wall-coating of viscous oil produces. The outcome of this study can be summarized as follows:

a) A film of viscous oil causes a significant increase in the frictional pressure loss compared to a clean, smooth wall.

b) The new CFD-based procedure developed to determine equivalent hydrodynamic roughness has been applied successfully for flow cells of different geometries (rectangular flow cell and pipe).

c) The hydrodynamic roughness data obtained from two very different wall-coating tests (rectangular flow cell and pipeline) collapsed, which broadens the potential field of application of the CFD-based procedure used to determine the roughness.

d) Among the tested parameters, oil viscosity and water flow rate did not affect the hydrodynamic roughness produced by different wall-coating layers directly. These parameters influenced the sustainable coating thickness under a specific flow condition. A coating layer's thickness was the determining factor for the resulting equivalent hydrodynamic roughness.

e) A correlation that demonstrates the ratio between equivalent hydrodynamic roughness and wall-coating thickness to be a constant when only water flows over the viscous layer was an important outcome of this project; this new finding leads to study the dependence of a similar ratio between hydrodynamic roughness and wall-fouling thickness in a water lubricated pipeline on the operating conditions.

CHAPTER 5

A NEW APPROACH TO MODEL FRICTIONAL PRESSURE LOSS IN WATER-ASSISTED PIPELINE TRANSPORTATION OF HEAVY OIL AND BITUMEN[§]

5.1. Introduction

A technical challenge to the application of lubricated pipe flow (LPF) is the unavailability of a reliable model to predict pressure losses on the basis of flow conditions (McKibben et al. 2000b, Shook et al. 2002, McKibben and Gillies 2009). The issue is that although a number of empirical, semi-mechanistic and numerical models have been proposed, these models are only appropriate for idealized core-annular flow (CAF) or are highly system-specific. Notable examples of models with limited applicability include those of Arney et al. (1993), Ho and Li (1994), Joseph et al. (1999), McKibben and Gillies (2009), Rodriguez et al. (2009), Crivelaro et al. (2009), de Andrade et al. (2012) and Sakr et al. (2012). Clearly, models developed for CAF cannot be applied to continuous water assisted flow (CWAF) and vice versa. None of the existing models address specifically the effect of wall-fouling on pressure losses.

Pressure loss models for LPF, such as those mentioned above, can be classified as either single-fluid or two-fluid models. The single-fluid models generally take an empirical approach to predict pressure gradient for lubricated pipe flow. Hydrodynamics of the flow system are modeled with respect to the transportation of a hypothetical single-phase fluid under similar process conditions (Arney et al. 1993, Joseph et al. 1999, Rodriguez et al. 2009, McKibben and Gillies 2009). The hydrodynamic effects associated with all physical aspects, including wall-fouling, are usually accounted for in these models through the use of empirical constants. The major limitation of single-fluid models is that they tend to be limited in applicability, i.e., are system-specific.

Two-fluid models are more mechanistic compared to the single-fluid models. However, most of the two-fluid models were proposed for CAF in a smooth pipe; in other words, the hydrodynamic effects of wall-fouling were usually neglected. Consequently, they cannot be used for CWAF. In two-fluid models the governing equations for each liquid are numerically solved using Computational Fluid Dynamics (CFD). The flow in the water

---

[§] *A version of this chapter has been submitted for publication to the Canadian Journal of Chemical Engineering. This paper is co-authored by S. Rushd, M. McKibben and S. Sanders.*

annulus is considered turbulent, whereas the core-flow (containing the viscous oil) is regarded as laminar. The accuracy of this approach depends on the numerical procedure employed, especially in the approach taken to model the turbulence in the water annulus. Three examples of this type of approach are those used by Ho and Li (1994), Crivelaro et al. (2009) and Sakr et al. (2012).

Ho and Li (1994) considered the turbulent water annulus to be the major source of pressure losses in CAF. They modeled turbulence using the Prandtl mixing-length model and considered the core-flow to have no velocity gradient, i.e., plug flow. The Prandtl mixing-length model is known to be inadequate for capturing the physics of most turbulent flows (Doshi and Gill 1970). Crivelaro et al. (2009) and Sakr et al. (2012) followed similar methodologies to simulate CAF. Their modeling approach required correlations to account for interfacial mixing of the two fluids which were not validated for CAF. Also, they did not validate the simulation results for pressure gradients with measured values. To model the turbulent water annulus, they relied on two-equation isotropic models: standard k-ε and k-ω models. However, these models are not suggested for anisotropic turbulent flow and very rough surfaces (Mothe and Sharif 2006, Zhang et al. 2011). The water annulus in a CWAF pipeline involves both anisotropic turbulence and flow over a very rough surface (Joseph et al. 1999, Shook et al. 2002, Rodriguez et al. 2009, McKibben and Gillies 2009).

In the present study, a new approach is developed to predict the pressure losses in water-assisted pipe flow. Instead of solving the flow field for both oil and water (as in the previous two-fluid models), we do so for the turbulent water annulus only. This approach addresses some of the shortcomings of the previous two-fluid models: for example, reduced computational requirements and the fact that no interfacial mixing model is required. It also allows us to incorporate the specific effects of wall-fouling and water hold-up, which can be simply defined as the *in situ* water volume fraction (as opposed to the delivered or input value). The new model is implemented using the commercial CFD package ANSYS CFX 13.0.

5.2. Development of Proposed Modeling Approach

Similar to previous two-fluid models, we assume the pressure losses in continuous water-assisted flow are directly related to the turbulent flow of the water annulus. Figure 5.1 shows a sketch of the approach taken in this study to simulate CWAF. The oil core is assumed to be cylindrical in shape. It is modeled as a moving wall. The velocity of this boundary (V_c) is the average velocity of the oil in the core. This consideration is based on the fact that, in previous works, the oil core was found to flow as a plug with negligible internal velocity gradient (Arney et al. 1993, Ho and Li 1994, Joseph et al. 1999, Herrera et al. 2009, Rodriguez et al. 2009, Crivelaro et al. 2009, de Andrade et al., 2012, Sakr et al. 2012, McKibben and Gillies 2009). The annular domain is assumed to be concentric and consists of water only. In addition to the friction (pressure) losses due to the turbulent flow of the water annulus, a reduction in effective pipe inner diameter and an increase in hydrodynamic roughness due to wall-fouling also contribute significantly to the pressure gradients.

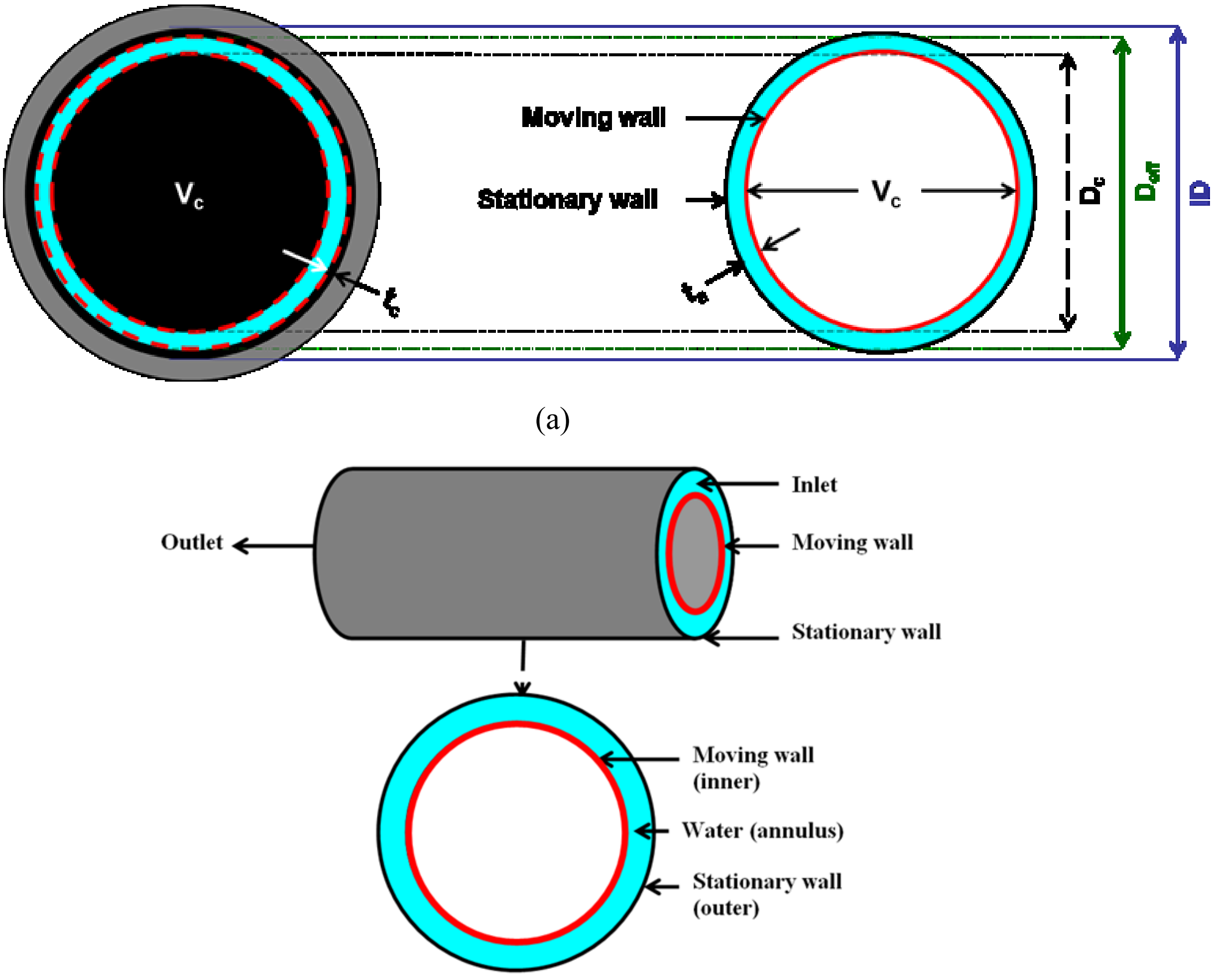

(b)

Figure 5.1. Schematic presentation of flow geometry and boundaries: (a) Cross-sectional view of the idealized flow regime of CWAF and the modeled flow domain; (b) Boundaries of the flow domain: 3D front view and 2D cross sectional view.

The thickness of the lubricating water annulus (t_a) is an important input for the current model. This thickness is calculated on the basis of the holdup ratio (H_w), which represents the *in situ* water fraction in fully developed flow. The calculation is made by using an empirical correlation between H_w and C_w (Arney et al. 1993), where C_w is the lubricating water fraction:

$$H_w = C_w[1 + 0.35(1 - C_w)] \quad \text{.……..………(5.1)}$$

The relationship between H_w and t_a is expressed using three equations:

$$D_{eff} = D - 2t_c \quad \text{……………………………………………….(5.2)}$$

$$H_w = \frac{Vol_{water}}{Vol_{eff}} = \frac{\pi\left(D_{eff}^2 - D_c^2\right)Z}{\pi D_{eff}^2 Z} \Rightarrow D_c = D_{eff}\sqrt{(1 - H_w)} \quad \text{………….(5.3)}$$

$$t_a = \frac{D_{eff} - D_c}{2} \quad \text{……………………………………………….(5.4)}$$

Eq. (5.2) shows the relation between effective diameter (D_{eff}) and internal diameter (D) of the pipe in terms of the average thickness of wall-fouling (t_c), which is a measured parameter. On the basis of the definition of H_w, the core diameter (D_c) is related to D_{eff} and H_w in Eq. (5.3). The annular thickness t_a is calculated from D_{eff} and D_c by using Eq. (5.4).

The boundaries of the flow geometry are also shown in Figure 5.1. At the inlet, the mass flow rate of water (m_w) and a moderate turbulence intensity of 5% were specified. The same m_w was also specified at the outlet. The no-slip condition was used at boundaries representing walls. The inner wall (moving wall) was considered hydrodynamically smooth ($k_s = 0$). Flow situations with a rough wall-fouling layer were simulated by considering the outer wall (stationary wall) as rough ($k_s > 0$). The k_s value for a rough wall must be specified for the simulations. However, the values of k_s produced by the stationary oil-layer on the pipe wall for the given flow conditions were unknown. To determine the appropriate k_s values for a CWAF data set, a trial-and-error procedure was adopted. The details of the procedure are available in Chapters 3 and 4. The boundary conditions are summarized in Table 5.1.

Table 5.1. Range of boundary conditions

Parameter:	Mass flow rate of water (m_w)	Velocity (V)	Hydrodynamic roughness (k_s)	
Boundary:	Inlet/Outlet	Moving wall	Stationary outer wall	Moving inner wall
Value:	2.3 – 35.8 kg/s	1.13 – 2.38 m/s	0.0 – 1.0 mm	0.0 mm (Smooth)

The governing differential equations, the Reynolds Average Navier-Stokes (RANS) equations were solved as part of the CFD simulation. The Reynolds stress term in RANS was modeled using an omega-based Reynolds Stress Model, ω-RSM. This model was demonstrated as effective in modeling the hydrodynamic roughness produced by the wall-coating layers of different heavy oils in Chapters 3 and 4. The typical length of the computational flow domain was 1.0 m; however, a 2.0 m length was also tested to confirm the length independence of simulated results. All computations were performed to obtain steady state solutions. The typical computational time requirement was 45 minutes for a single data point. The flow geometry mesh was generated with ANSYS ICEM CFD. Mesh independence tests of the simulation results were performed. The minimum number of hexahedral mesh elements considered to be enough for grid independence were 350 000. Examples of mesh and post processing results are shown in Figure 5.2.

The basic steps followed in developing current modeling approach are stated below:

1) Determine the values of k_s produced by wall-fouling layers for each set of experimental conditions of a CWAF data set (calibrating data) available in Appendix 9;
2) Analyze the results of k_s and the corresponding flow conditions to ascertain the significant process parameters that determine the hydrodynamic roughness;
3) Conduct a dimensional analysis to correlate k_s to the important process variables;
4) Apply the newly developed correlation to predict the values of k_s for another data set (test data) also available in Appendix 9;
5) Apply the CFD-based simulation methodology to predict pressure gradients of the test data set.

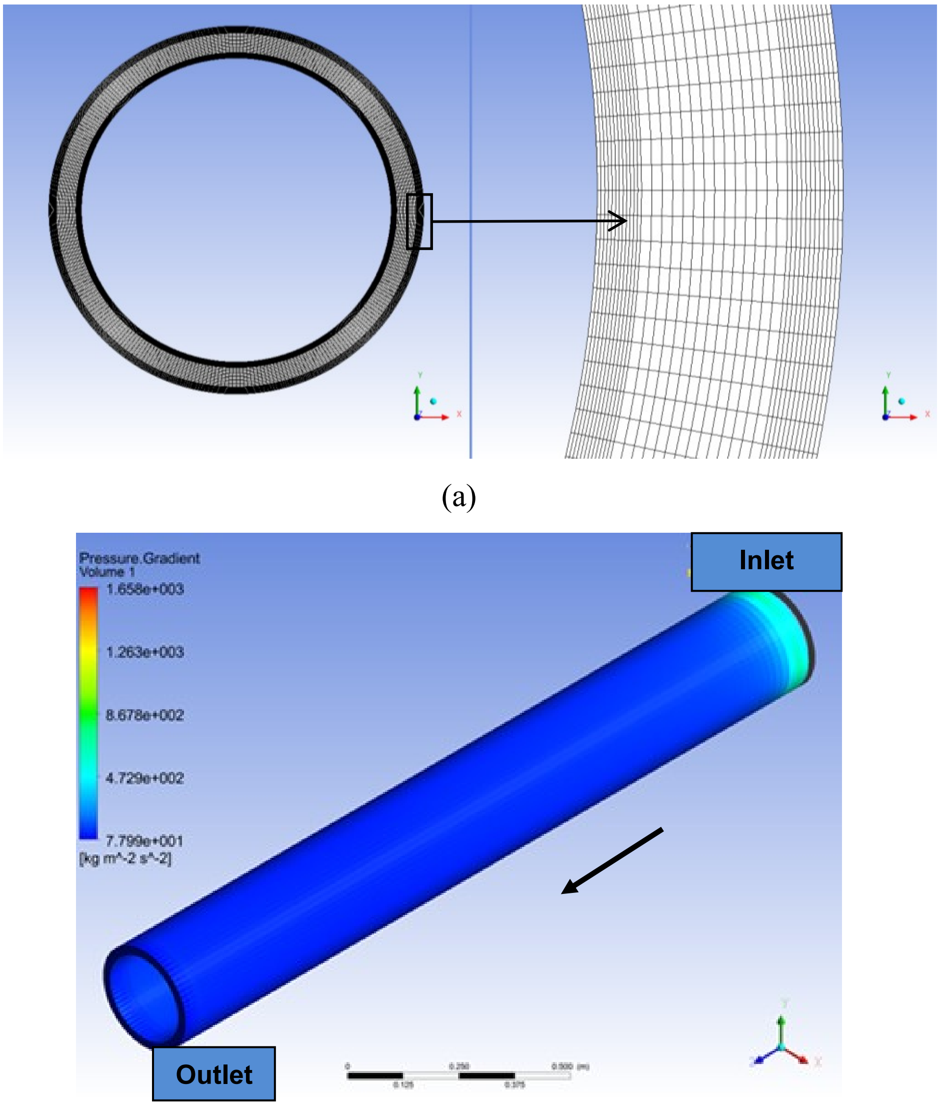

(a)

(b)

Figure 5.2. Samples of simulation results: (a) Meshing (number of mesh elements: 392 200); (b) Steady state post processing results for pressure gradients.

5.3. Experimental Facilities and Results

5.3.1. Source and location

The experiments were conducted at the Saskatchewan Research Council (SRC) Pipe Flow Technology Centre. The following descriptions of the experimental facilities and results are presented in this work with permission from SRC. For additional details on the experimental method, please see McKibben et al. (2007) and McKibben and Gillies (2009).

5.3.2. Facilities and methods

The tests were conducted in SRC's 100 mm and 260 mm pipe flow loops. Initially the loops were loaded with oil from a loading tank, and then a fixed quantity of water was added. After adding water, the oil-water mixture was recirculated in the loop at different flow rates to develop the CWAF regime. The water lubrication was ensured primarily by measuring pressure losses (i.e., pressure gradients) at different locations in the pipe loop. The pressure gradients measured for CWAF were orders of magnitude lower than those measured before the lubricated flow was established. In addition to measuring pressure losses for a specific flow condition, the corresponding average thickness of the wall-fouling layer was also measured. The key features of the flow loops are described below.

100 mm Pipe loop:

(i) A 9.14 m long 103.3 mm diameter horizontal steel pipe was used as the test section for measuring frictional pressure gradients in the CWAF. The measurement was conducted with a Validyne differential pressure transducer.

(ii) Initially two separate Moyno progressing cavity pumps were used for adding oil and water in the loop. The larger of these two pumps was used for oil and the smaller one was used for water. Later the lubricated flow regime was established by recirculating the oil-water mixture in the pipeline. The larger pump was used for the recirculation.

(iii) A special double-pipe heat exchanger was used to indirectly determine the average thickness of fouling on pipe wall (t_c). The details of this apparatus were reported by Schaan et al. (2002). It is a non-invasive device for measuring t_c online. The indirect measurement of t_c by the heat exchanger was validated by measuring the same thickness directly with a hot-film probe.

(iv) There were two ports used for collecting fluid samples during steady state flow conditions. The ports were located before and after the pump station. The collected samples were analyzed to determine the fraction of free water, i.e., lubricating water (C_w) in the CWAF regime.

260 mm Pipe loop:

The design of the 260 mm pipe loop was comparable to the 100 mm loop. Here, a 14.94 m long 264.8 mm diameter horizontal steel pipe was used as the test section for measuring frictional pressure gradients. Two separate Moyno progressive cavity pumps were used for adding heavy oil and water to the pipeline. The thickness of wall-fouling was measured with the hot-film probe only.

5.3.3. Results

The experiments were conducted in the two pipe loops (D ~ 100 and 260 mm) with three different oils (μ_o ~ 1.3, 1.4 and 26.5 Pa.s at 25°C). Properties of these oils are available in Appendix 2. The lubricating water fraction was typically in the range of 24% to 43%, which corresponds to a total or input water fraction of 30% - 50%. A part of the water was emulsified with the oil when the mixture passed through the pump in the recirculating loop. During the flow tests, the pressure gradients and the thickness of the wall-fouling layer were measured while controlling the process temperature (T) and the flow rate, i.e., the average/bulk velocity (V). The data sets used for the current research are reported in Appendix 9. Typical results of $\Delta P/L$ for changing V under different process conditions are presented in Figure 5.3.

It can be seen from Figure 5.3 that higher bulk velocity causes the pressure gradient to increase. This is a standard trend. For the turbulent flow of water through a pipe, $\Delta P/L$ increases approximately with V^2. The results presented in three graphs of the figure are discussed as follows:

(A) Figure 5.3(a) shows the effect of D on $\Delta P/L$ when μ_o and C_w are constant. As expected, smaller D yields higher $\Delta P/L$.

(B) Figure 5.3(b) demonstrates the influence of C_w on $\Delta P/L$ under comparable process conditions. Increasing C_w from 0.25 to 0.40 does not cause any appreciable change in $\Delta P/L$. Previous experimental work demonstrated a similar effect (McKibben et al. 2000; Rodriguez et al. 2009).

(C) Figure 5.3(c) illustrates the consequence of changing μ_o in CWAF. Increasing μ_o increases $\Delta P/L$ under comparable process conditions. This effect differentiates the CWAF from the idealistic CAF system. General understanding of CAF suggests the impact of μ_o on $\Delta P/L$ to be insignificant (Oliemans and Ooms 1986). The most probable reason for the difference is wall-fouling, which is usually neglected in analysis of CAF. The present experiments demonstrate that μ_o has a significant influence on the wall-fouling and, as a result, on $\Delta P/L$ in CWAF.

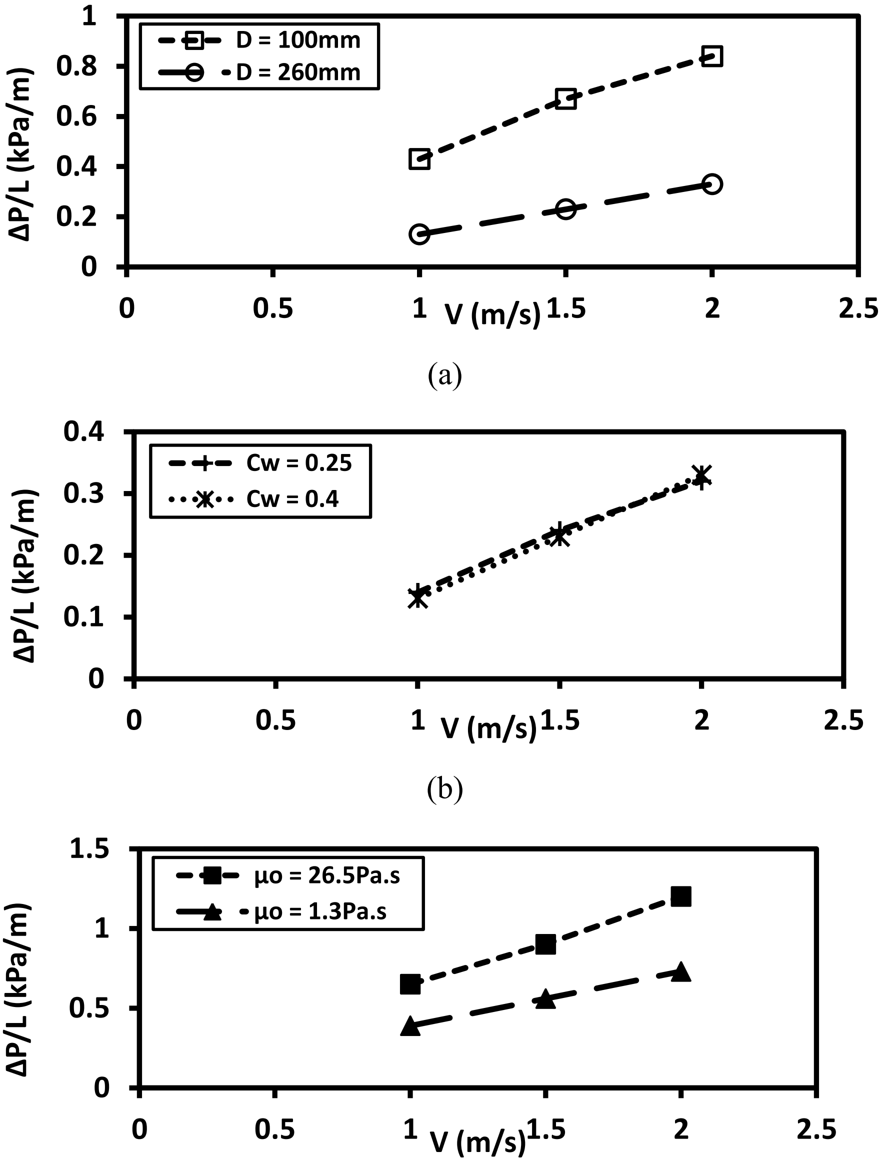

(a)

(b)

(c)

Figure 5.3. Measured pressure gradients (Δ*P/L*) as a function of average velocity (*V*) under comparable process conditions for the following variables: (a) Pipe diameter, *D* (μ_o = 1.4 Pa.s, C_w = 0.4); (b) Lubricating water fraction, C_w (μ_o = 1.4 Pa.s, D = 260 mm); (c) Oil viscosity, μ_o (C_w = 0.3, D = 100 mm).

The dependence of t_c of wall-fouling on different process variables (V, μ_o, D and C_w) is illustrated in Figure 5.4. This illustration shows an inverse effect of V on t_c. That is, higher flow rates produce in lower values of t_c. Figure 5.4(a) demonstrates the effect of μ_o on t_c. Increasing μ_o increases t_c under comparable flow conditions. Similar effect of D on t_c is shown in Figure 5.4(b). However, increasing D made the effect of V on t_c almost negligible. Figure 5.4(c) shows that C_w does not have a strong influence on t_c.

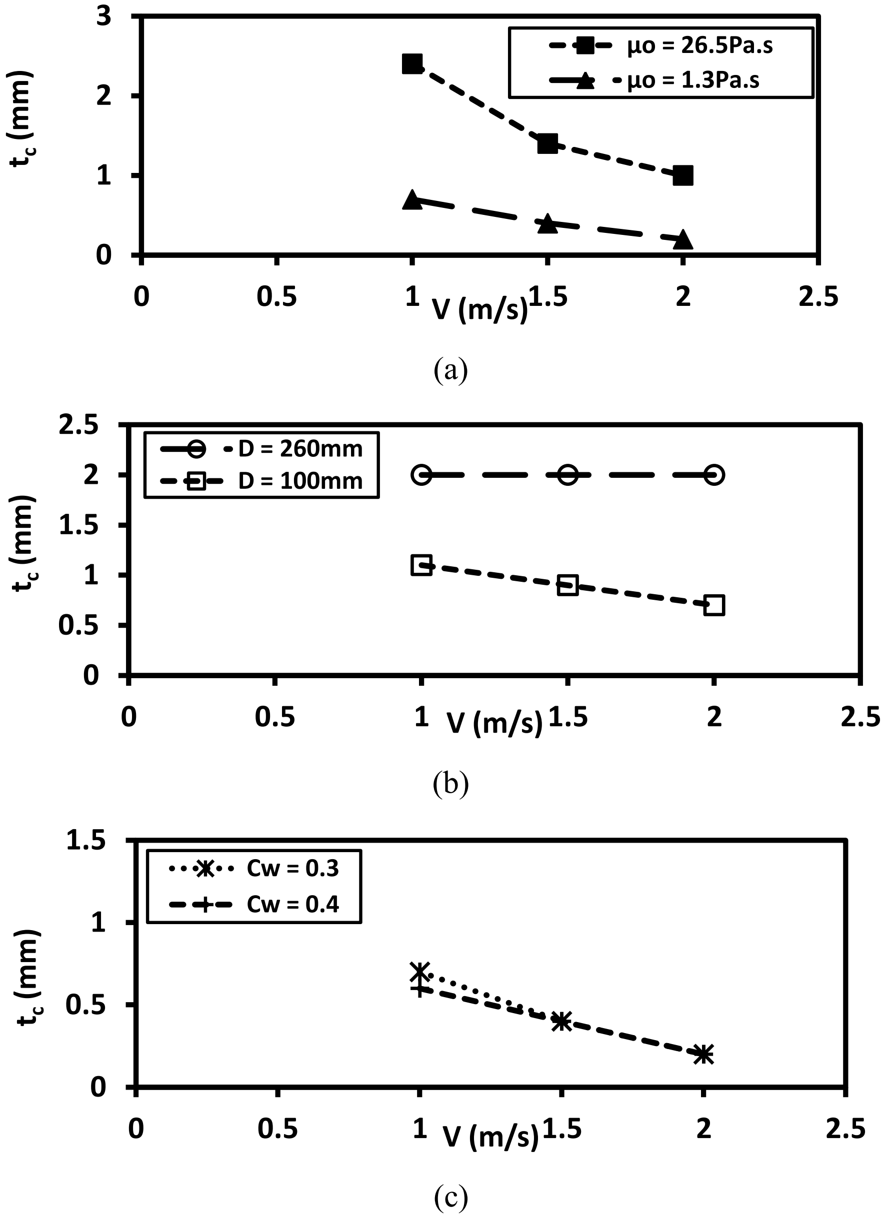

Figure 5.4. Average thickness of wall-fouling (t_c) as a function of average velocity (V) for following variables: (a) Oil viscosity, μ_o ($C_w = 0.3$, D = 100 mm); (b) Pipe diameter, D (μ_o = 1.4 Pa.s, $C_w = 0.4$); (c) Lubricating water fraction, C_w (μ_o = 1.3 Pa.s, D = 100 mm).

5.4. Determination and Analysis of Hydrodynamic Roughness

The technique to determine the hydrodynamic roughness produced by a wall coating layer is illustrated in Figure 5.5. In Figure 5.5(a), the measured values of pressure gradients are shown in comparison to the simulation results as a function of mixture average velocity. The difference between the simulation results and the measurement was less than ± 5%. The values of k_s required to produce the simulation results of Figure 5.5 (a) are presented in Figure 5.5(b).

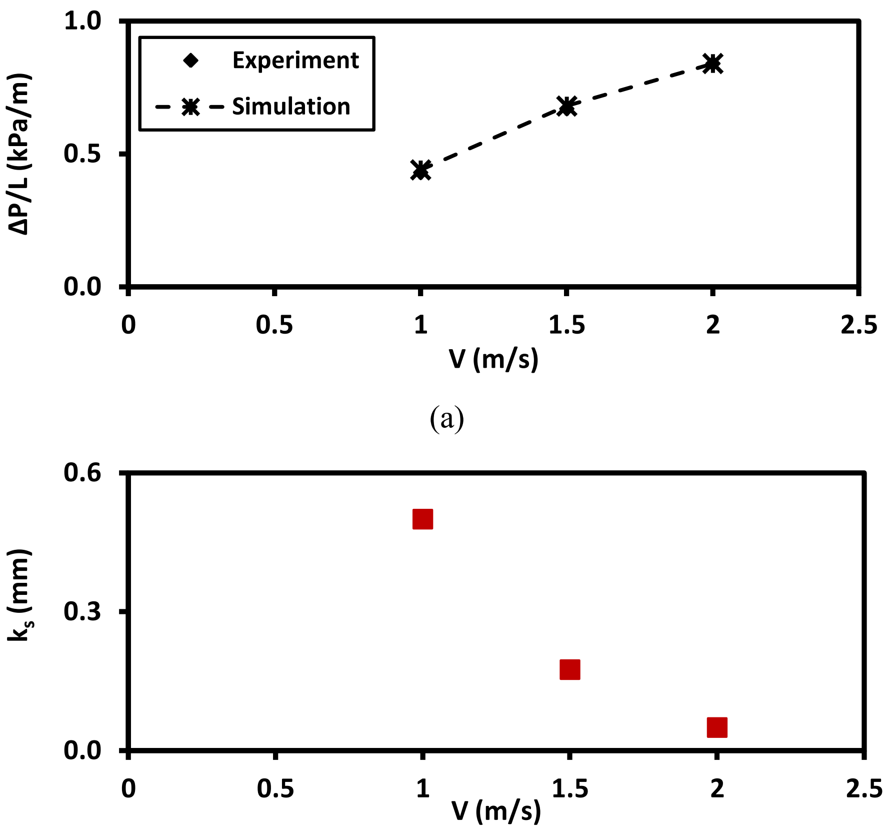

(a)

(b)

Figure 5.5. Illustration of the procedure used to determine equivalent hydrodynamic roughness (μ_o = 1.4 Pa.s, D = 100 mm, C_w = 0.4): (a) comparison of simulation results with measured values; (b) the values of k_s (mm) used for the simulation.

The hydrodynamic roughness produced by the wall-fouling in CWAF was found to be primarily dependent on the average velocity. The dependence is illustrated in Figure 5.5, which shows that the value of k_s decreases with increasing V. A similar inverse relationship between k_s and V is also demonstrated in Figure 5.6 for other experimental conditions. This figure shows the effects of C_w, μ_o, and D on the k_s determined for each set of flow conditions. Decreasing any of these three parameters leads to a corresponding decrease in k_s. It should be noticed that the effect of these process parameters (C_w, μ_o and D) on k_s is most significant at lower velocities. The wall-fouling layer tends to behave like a smooth wall (k_s ~ 0) irrespective of other flow conditions at sufficiently high velocity. Thus, the current analysis demonstrates that k_s is dependent on V, C_w, μ_o, and D.

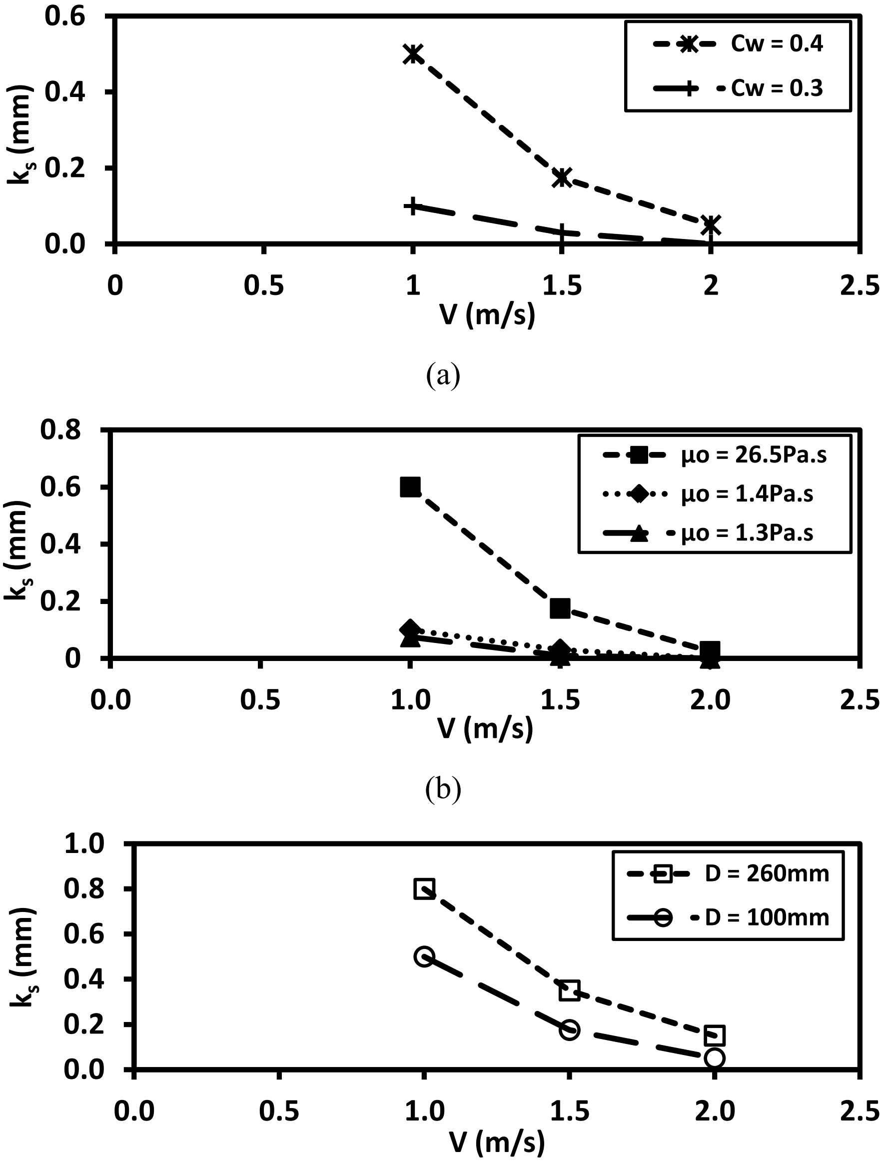

(a)

(b)

(c)

Figure 5.6. Dependence of hydrodynamic roughness (k_s) on average velocity (V) and the following parameters in the CWAF pipeline: (a) Lubricating water fraction, C_w (D = 100 mm, μ_o = 1.4 Pa.s); (b) Oil viscosity, μ_o (D = 100 mm, C_w = 0.3); (c) Pipe diameter, D (C_w = 0.4, μ_o = 1.4 Pa.s).

In addition to the hydrodynamic roughness produced by the wall-fouling layer, its average thickness is also a dependent variable. The relationship between k_s, t_c and the flow parameters was studied earlier by conducting idealized experiments with only water flowing over wall coating layers of multiple viscous oils (see Chapters 3 and 4). The results of those experiments demonstrated a proportional correlation between k_s and t_c. However, this correlation is found to be absent in case of CWAF. The relation between k_s and t_c for the calibrating data set is shown in Figure 5.7, where the value of k_s is presented as a function of t_c for different flow conditions. It is evident that k_s in CWAF is not proportional to t_c; a similar magnitude of t_c under different flow conditions results in quite different values of k_s. This is because the values of k_s and t_c are separately influenced by the process conditions, i.e., the independent variables (V, C_w, μ_o, and D).

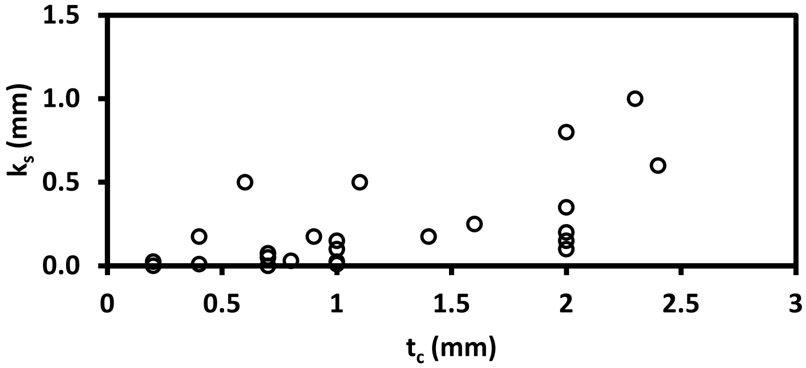

Figure 5.7. Hydrodynamic roughness (k_s) as a function of wall-fouling thickness (t_c) for the following flow conditions: V =1, 1.5 & 2 m/s, C_w = 0.25, 0.30 & 0.42, μ_o = 1.3, 1.4 & 26.5 Pa.s and D = 100 & 260 mm.

The current analysis of the CWAF data and previously conducted wall-coating experiments indicate that the interrelation among the significant process variables is subject to the mechanism that sustains wall-fouling. The mechanism, which was reported in the literature (see, for example, Joseph et al. 1999, Schaan et al. 2002, Shook et al. 2002, Vuong et al. 2009 and McKibben et al. 2007), can be described as follows:

a) The lubricating water annulus is turbulent in the continuous water-assisted flow regime.
b) The turbulent water annulus causes irregular waves on the surface of the oil core and the wall-fouling layer.
c) Crests of the waves are torn away to form oil droplets in the turbulent water annulus.
d) The turbulence in the water annulus also causes a fraction of the oil droplets to be deposited on the surfaces of the wall-fouling layer and the oil core.
e) At steady state conditions, a dynamic equilibrium exists between oil droplets being sheared away from and deposited onto the wall-fouling layer in a CWAF pipeline.

A schematic to explain the complex scenario is shown in Figure 5.8, where the shearing and the deposition of oil droplets only on the wall-fouling layer are illustrated.

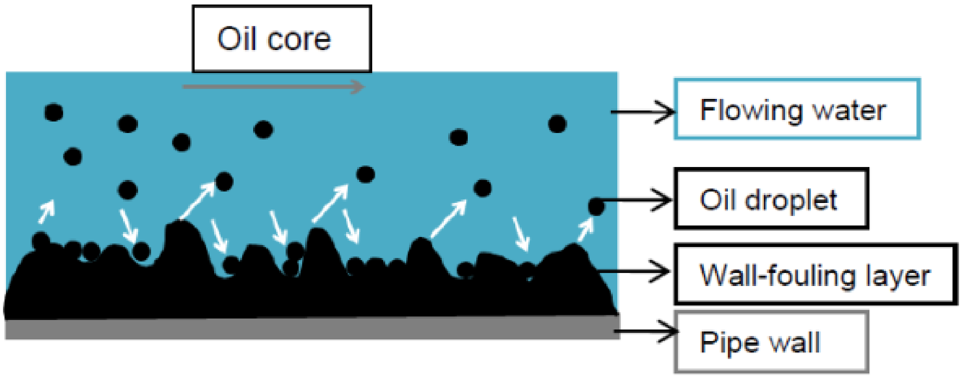

Figure 5.8. Illustration of the postulated mechanism that develops and sustains wall-fouling in a CWAF pipeline: oil drops being sheared and deposited on the wall-fouling layer.

The postulated mechanism helps to visualize the development of physical roughness over the wall-fouling layer in a CWAF pipeline. Previous experimental studies, as presented in Chapters 3 and 4, proved the degree of physical roughness on a wall-fouling layer to essentially limit the magnitude of the corresponding hydrodynamic roughness. In those experiments, the turbulent water produced irregular waves, i.e., physical roughness on the oil surface. The turbulent water also sheared the oil droplets from the wave crests to yield a steady state value of coating thickness for a given flow rate. However, there was no deposition of oil droplets on the rough surface. In contrast, the physical roughness on the wall-fouling layer in a CWAF pipeline results from a balanced shearing-deposition mechanism. The mechanism is understandably controlled by the independent process variables, *viz.*, V, μ_o, D and C_w. These variables limit the scale of physical roughness and, as such, the magnitude of k_s. Reasonably, the independent variables also play an important role in determining t_c. For example, a higher flow rate increases turbulence in the water annulus. Increased turbulence magnifies both shearing and deposition of oil droplets but clearly moves the dynamic equilibrium where shearing (removal) of oil becomes more dominant than it was at lower flow rates. The most probable result is the reduction in physical roughness on the wall-fouling layer and its thickness. That is why increased velocities reduce both k_s and t_c (*cf.* Figures 5.4 and 5.6). The predictions of k_s obtained from two different correlations developed for the flow conditions discussed here are compared in Appendix 14.

5.5. Dimensional Analysis

Based on the analysis presented in previous section, the significant parameters with respective dimensions are identified as follows:

Dependent variables: k_s (L), t_c (L)
Independent variables: V (LT^{-1}), D (L), ρ_w (ML^{-3}), μ_w ($ML^{-1}T^{-1}$), μ_o ($ML^{-1}T^{-1}$), C_w ($M^0L^0T^0$)

It should be noted that C_w is a dimensionless parameter. Also two additional independent variables, water density (ρ_w) and water viscosity (μ_w) are taken into account here. Due to the fixed temperature, these secondary variables were constant for the data set analyzed earlier. However, both of these fluid properties are expected to vary with temperature.

According to the Buckingham Π Theorem, the variables (k_s, t_c, V, D, ρ_w, μ_w and μ_o) can be grouped into dimensionless Π groups as follows:

Dependent Group:

Dimensionless hydrodynamic roughness, $k_s^+ = k_s/t_c$ ……… (5.5)

Independent Groups:

Equivalent water Reynolds number, $Re_w = DV\rho_w/\mu_w$ ……… (5.6)
Viscosity ratio, $\mu^+ = \mu_o/\mu_w$ ………………………… (5.7)

That is, the current analysis results in one dependent (k_s^+) and two independent (Re_w and μ^+) dimensionless groups. One more independent non-dimensional parameter, C_w was identified earlier. The functional relation of the dimensionless parameters is presented as follows:

$k_s^+ = \mathrm{f}(Re_w, \mu^+, C_w)$………………(5.8)

In Eq. (5.8), the dependent non-dimensional parameter k_s^+ represents the relative roughness where k_s is scaled with t_c. The first independent group Re_w is an equivalent water Reynolds number. In Re_w, length scale is D, velocity scale is V and fluid properties are the properties of lubricating water, ρ_w and μ_w. The second independent group μ^+ can be considered as the viscosity ratio or relative viscosity where μ_o is scaled with μ_w. The final independent non-dimensional parameter is C_w. Please refer to Appendix 10 for additional details of the dimensional analysis.

It should be noted that interfacial tension, which is an independent variable, has not been considered for the dimensional analysis. The reasons for the exclusion are as follows:

a) An order of magnitude analysis demonstrates that importance of interfacial tension is almost negligible compared to viscosity and velocity for the current study. Details of the analysis are available in Appendix 10.
b) The flow system under consideration involves heavy oil and water. For such a specific system, the interfacial tension is likely to be a strong function of oil viscosity (Schonhorn 1967, Queimada et al. 2003, Isehunwa and Olubukola 2012). Since viscosity was not found to affect the hydrodynamic roughness (Chapter 4 and Appendix 11), interfacial tension was also considered not to have a significant influence on the k_s produced by the wall-fouling layer in a CWAF pipeline.

5.6. Development of a Correlation for Hydrodynamic Roughness

By adapting the methodology suggested by Bhagoria et al. (2002), the calibrating data were regressed to find a best fit correlation for the dependency expressed in Eq. (5.8). The final correlation is expressed as

$$k_s^+ = \mathrm{A}(Re_w)^x(C_w)^y(\mu^+)^z \text{.............}(5.9)$$

The values of the coefficients considered to yield best fit for the analyzed data are:

$\mathrm{A} = 1.6 \times 10^6$, $x = -1.042$, $y = 3.435$, $z = 0$

Using those values of the coefficients, Eq. (5.9) can be rewritten as:

$$k_s^+ = \frac{1.6\times10^6}{(Re_w)^{1.042}}(C_w)^{3.435} \text{ ....}(5.10)$$

It should be noted that the effect of relative viscosity (μ^+) on the relative roughness (k_s^+) turned out to be insignificant in course of data regression for model fitting. Similar inconsequential effect of oil viscosity on the equivalent roughness was also observed in the idealized wall-coating experiments (Chapter 4). The significant parameters that influence k_s^+ are C_w and Re_w. The experimental ranges of these parameters are $10^5 < Re_w < 10^6$ and $0.20 < C_w < 0.45$.

The regression analysis, which was used to obtain optimum values of the coefficients in the correlation (Eq. 5.10), produced a R^2 value of 0.74. The prediction capability of the correlation is presented in Figure 5.9, where the predictions of k_s^+ are shown as a function of the results obtained from experimental data. The predicted values are quite evenly distributed across the parity line. The symmetry of results suggests the model is capable of providing a reasonable estimate for k_s. However, further fine tuning of the coefficients with respect to a wider variation of process conditions is required to enhance its accuracy. Detailed steps of the model development are available in Appendix 11.

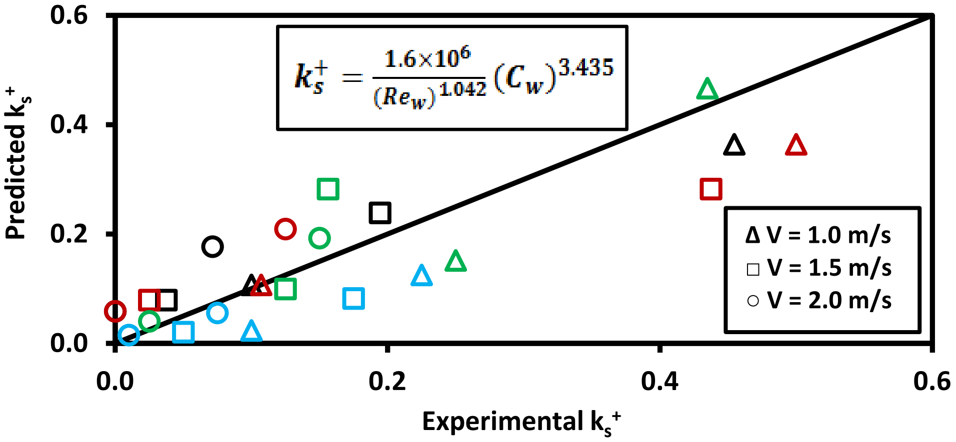

Figure 5.9. Prediction capability of the correlation (Eq. 5.10); range of C_w: 0.24 – 0.43; marker colors: Blue D = 260 mm & μ_o = 1.4 Pa.s, Black D = 100 mm & μ_o = 1.4 Pa.s, Dark red D = 100 mm & μ_o = 1.3 Pa.s, Green D = 100 mm & μ_o = 26.5 Pa.s.

5.7. Application of the New Modeling Approach

Applicability of the new modeling approach proposed in this work is tested by predicting pressure gradients of two data sets: the test data and the calibrating data. The calibrating data (T = 25°C) were used in developing the new correlation for k_s (Eq. 5.10). The test data (T = 35°C) were preserved for testing the new modeling approach. For the application, the values for respective independent dimensionless groups (Re_w, C_w *and* μ^+) are calculated first. Then the dependent parameter k_s^+ is determined by applying the correlation

(Eq. 5.10). The estimated values of k_s are used to compute $\Delta P/L$ by applying the previously described CFD methodology. The application of the current modeling approach is illustrated with an example (calculation provided) in Appendix 13. The predicted results for all data points are presented as a function of the experimental measurements in Figure 5.10. This presentation shows that the current modeling methodology is capable of predicting pressure losses with reasonable accuracy (*cf.* Figures 2.1 and 2.3).

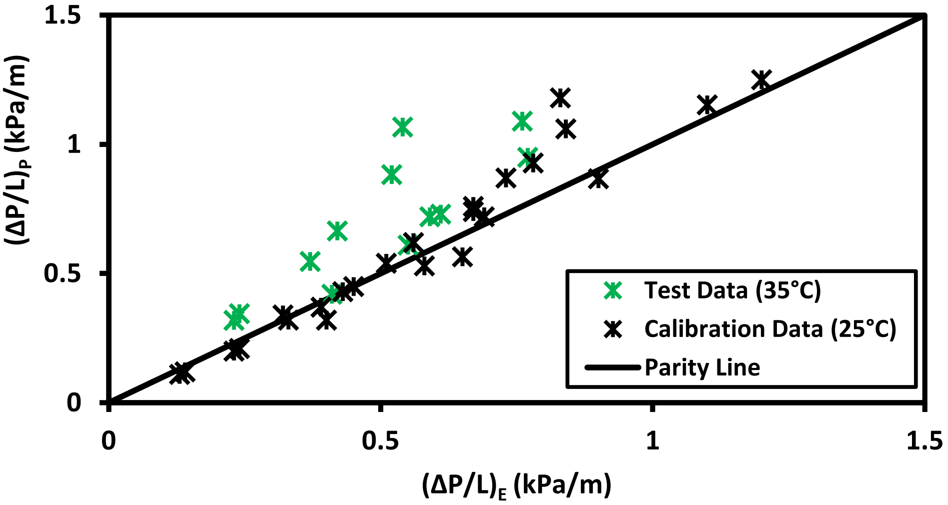

Figure 5.10. Prediction capability of the proposed approach to model CWAF pressure loss; Test data: D = 100 mm, C_w = 0.20 – 0.40, μ_o = 1.2 & 16.6 Pa.s, V = 1.0, 1.5, 2.0 m/s; Calibration data: D = 100, 260 mm, C_w = 0.25 – 0.40, μ_o = 1.3, 1.4 & 26.5 Pa.s, V = 1.0, 1.5, 2.0 m/s.

The performance of current model is tested further against that of five existing models in Table 5.2, where the error ($\Delta P/L_{pred} - \Delta P/L_{meas}$) associated with each model is reported with three statistical parameters, Root Mean Square (RMS), %Average and %Maximum:

$$RMS = \sqrt{\frac{\sum_{i=1}^{n}(Prediction - Measurement)_i^2}{n}} \text{................(5.11)}$$

$$\%Average = \pm\frac{\sum_{i=1}^{n}(\frac{Prediction - Measurement}{Measurement}\times 100)_i}{n} \text{................(5.12)}$$

$$\%Maximum = \pm Max\left|(\frac{Prediction - Measurement}{Measurement}\times 100)_i\right| \text{................(5.13)}$$

Positive values of % average/maximum are over predictions and negative values are under predictions by the corresponding model. The current model is more effective as it produces better predictions compared to the existing models in predicting measured values of pressure gradients. This is because previous models were not developed by focusing on the distinct phenomena associated with the continuous water-assisted flow system.

Table 5.2. Comparison of the proposed modeling approach with existing models

Model	Error		
	RMS (kPa/m)	% Average	% Maximum
Current model	0.16	15	98
Rodriguez & Bannwart (2009)	0.24	-36	-71
Ho & Li (1994)	0.32	-51	-76
Arney et al (1993)	0.42	-70	-86
McKibben and Gillies (2009)	0.70	74	345
Joseph et al (1999)	3.45	531	1065

As mentioned earlier, the models proposed by Arney et al. (1993) and Ho and Li (1994) were developed by analyzing the experimental results of core-annular flow (CAF). They used deliberate measures to reduce wall-fouling. On the other hand, Rodriguez et al. (2009) developed their empirical model based on lab- and pilot-scale CAF experiments. The wall-fouling was rigorously controlled in the laboratory; however, the fouling was impossible to avoid in the pilot-scale field applications. This model was developed using CAF data with and without wall-fouling. The negative values of % average/maximum error for the three CAF models suggest that these are under predicting the measured values of pressure gradients in CWAF pipelines, i.e., the CAF models cannot take the effects of wall-fouling into account. McKibben and Gillies (2009) proposed their model on the basis of a large data set that was produced by conducting both intermittent and continuous water-assisted flow experiments. Joseph et al. (1999) developed their model using data of an intermittent water-assisted flow system, known as the self-lubricated flow of bitumen froth. Since the intermittent water-assist involves sporadic, direct contact between the oil core and the pipe wall, pressure losses are usually higher compared to those measured for CWAF. As a result, these models over predict the pressure gradients in CWAF pipelines. Although the current model also over predicts the pressure losses, it does so to a much lesser degree than the other models. Thus, the performance of this model can be said to provide the most accurate predictions of any model currently available in the literature for CWAF pipelines. However, we are in the early stages of water-assisted flow technology development. The proposed methodology of modeling frictional pressure loss is one of the first efforts to explicate the hydrodynamics of CWAF. This modeling approach in its current form is only a convenient means to carry out preliminary assessments; whenever possible, actual pipe flow data should be sought for the specific mixtures to be transported.

5.8. Summary

The objective of the current work is to develop a new approach to model frictional pressure loss in the water-assisted pipeline transportation of heavy oil and bitumen. The important outcomes of this study are summarized as follows:

a) A convenient CFD approach is developed to predict the frictional pressure loss in a CWAF pipeline. The model, even in its nascent form, is capable of producing better predictions than the existing models. The hydrodynamic effects of wall-fouling are specifically addressed in this new model. It also takes into account the effects of important process parameters, such as water fraction, pipe diameter and mixture flow rate, on the pressure loss.

b) A new correlation is proposed to determine the hydrodynamic roughness produced by the wall-fouling layer under operating condition in a CWAF pipeline. It provides estimates of the hydrodynamic roughness based on key operating parameters, e.g., the mixture flow rate, water fraction and thickness of wall-fouling layer. At the present time, a similar model is not available in the literature.

CHAPTER 6
CONCLUSIONS AND RECOMMENDATIONS

6.1. General Summary

It is evident from the literature and a few commercial successes that continuous water assisted flow (CWAF) is a viable method for the long distance transportation of heavy oil and bitumen. One of the most important barriers to broad commercial implementation of this flow technology is the lack of a reliable model for frictional pressure losses as a function of operating parameters, e.g., pipe diameter, flow rates, fluid properties and water fraction. It is important to develop a new modeling approach, one that is specifically capable of dealing with the hydrodynamic effects produced by the "wall-fouling" layer in a CWAF pipeline. Even though wall-fouling is an important and unavoidable characteristic of this pipeline transportation technology, it has not been properly investigated to date. Therefore, the research for this dissertation was focused on the investigation of the hydrodynamic effects produced by the wall-fouling layer. The exploration began with a comprehensive, idealized lab-scale investigation and ended with the modeling of large-scale pipe flow experiments. The outcomes of the current work are summarized in this section.

The laboratory component of the research involved an innovative set of experiments. The objective was to study the hydrodynamic behavior of the wall-fouling layer under controlled flow conditions. The fouling layer was replicated by coating a wall of a customized flow cell with a thin layer of viscous oil. Important achievements and new understanding resulting from the lab-studies include the following:

(i) A new apparatus and procedure were developed to study the hydrodynamic effects produced by a viscous oil layer coating on a wall. The response of the wall-coating layer to the turbulent flow of water ($10^4 < Re < 10^5$) over its surface was investigated with visual observation and measurement of pressure loss in a customized flow cell. In the course of the experiments, turbulent water flowed over stationary layers of different viscous oils coated on the bottom wall of the flow cell. The oil layers reduced the effective flow area by less than 10%, which was not expected to cause a substantial increase in pressure loss compared to the loss in the clean flow cell under comparable flow conditions. However, the measured pressure losses in a flow cell with a wall-coating were significantly higher than the losses in a clean flow cell without any wall-coating.

The difference between the measured values of pressure losses was approximately 200% at the highest flow rate ($Re_w \sim 9 \times 10^4$). This experimental observation suggested that the wall-coating layer not only reduced the effective flow area but more importantly produced a significantly larger equivalent hydrodynamic roughness compared to the hydrodynamic roughness associated with the clean wall.

(ii) Conventional methods of quantifying equivalent hydrodynamic roughness typically involve complex flow visualization experiments. In the present study, a new approach using CFD simulations was developed as an alternative. The method was validated using data from the literature (bio-fouling) and experiments conducted at the University of Alberta using materials of fixed roughness (sandpaper).

(iii) The actual (or physical) roughness of the wall-coating, produced during tests conducted with a very viscous oil ($\mu_o = 2.13 \times 10^4$ Pa.s), was measured using a Contracer Contour Measurement System. The measured values were used to estimate the corresponding hydrodynamic roughness. The estimated values agreed reasonably well with the predictions obtained using the CFD methodology.

(iv) Using the measurements of pressure losses from the present study (rectangular flow cell) and the literature (pipe flow), a novel data set was generated for the wall-coating thickness (0.2 mm $\leq t_c \leq$ 2.0 mm) and the corresponding hydrodynamic roughness (0.4 mm $\leq k_s \leq$ 5.5 mm) for six different heavy oils (2.90×10^0 Pa.s $\leq \mu_o \leq 2.13\times10^4$ Pa.s). The hydrodynamic roughness produced by an oil layer was a strong function of the corresponding coating thickness, while the thickness was dependent on the oil viscosity and the water flow rate. Based on the data set, a correlation was proposed to predict the equivalent hydrodynamic roughness produced by a viscous wall-coating when only water flowed over the coating layer.

After the laboratory study was completed, a data set collected from actual CWAF tests in large pipelines ($D \sim$ 100 mm and 260 mm) was analyzed. The goal was to develop a new methodology to model frictional pressure losses that could address the characteristic phenomena associated with this transportation technology, such as wall-fouling and water holdup. The outcomes of the data analysis can be summarized as follows:

(i) The equivalent hydrodynamic roughness produced by the wall-fouling layer in a CWAF pipeline was quantified following the CFD procedure developed during the laboratory investigations.

(ii) A dimensional analysis was conducted to identify the flow parameters that most directly influenced the hydrodynamic roughness produced by a wall-fouling layer. Based on the analysis, a new correlation was developed to predict the hydrodynamic roughness produced by a wall-fouling layer in a CWAF pipeline.

(iii) A new CFD-based methodology was developed to predict frictional pressure losses in a CWAF pipeline. This approach addresses the following phenomena:

- Reduction in effective pipe diameter due to wall-fouling
- Increase in equivalent hydrodynamic roughness produced by the wall-fouling layer
- Water hold-up, i.e., *in situ* volume fraction of water
- Reduced requirement of computational time

The new model implemented using a commercial CFD package ANSYS CFX 13.0 requires approximately 45 minutes for simulating a single data point. Similar simulation with the existing CFD method (Crivelaro et al. 2009, de Andrade et al. 2012, Sakr et al. 2012) needs more than 24 hours.

6.2. Novel Contributions

A new CFD-based modeling approach to predict frictional pressure losses in the continuous water assisted flow of heavy oil and bitumen

A novel CFD approach was developed to model the frictional pressure loss in a CWAF pipeline. The model accounts for many important process parameters, such as extent of wall-fouling, water fraction and pipe diameter. The inputs required for the CFD simulation are calculated directly from these flow conditions. Compared to existing CFD models, the current model is a considerable improvement as it produces more accurate predictions and requires significantly fewer computing resources. This new model also produces more satisfactory predictions than the existing empirical or semi-mechanistic models. For a CWAF data set, the average error in predicting pressure losses produced by this model (15%) is significantly less than the average error produced by existing models (35% - 531%). It is a physics-based approach, which will be beneficial for the design, scale-up and operation of any water-assisted pipeline system.

A correlation to predict the hydrodynamic roughness produced by the wall-fouling layer in the water assisted pipeline transportation of heavy oil and bitumen

The equivalent hydrodynamic roughness produced by a wall-fouling layer under different flow conditions in CWAF pipelines was quantified for the first time. These values were used to correlate the roughness to the flow conditions on the basis of dimensional analysis. In this new correlation, the equivalent hydrodynamic roughness is a function of specific operating parameters, such as the thickness of the wall-fouling layer, mixture flow rate, pipe diameter, water density, water viscosity and lubricating water fraction. It estimates the equivalent roughness produced by the wall-fouling under actual CWAF operating conditions. The values of the roughness are essential to the prediction of CWAF pressure losses according to the modeling approach developed in the current study.

A new CFD methodology to determine the unknown hydrodynamic roughness produced by a rough surface

A CFD-based methodology was developed to determine the equivalent hydrodynamic roughness produced by the wall-coating layers of different heavy oils. Experimentally measured pressure gradients were predicted by simulating the flow conditions for each test case. The new approach was developed because the existing methods, such as measuring velocity profile above the rough surface and using correlations like Colebrook or Churchill formula, could not be used for the conditions tested in the current project. Although developed for the specific purpose of determining the equivalent hydrodynamic roughness produced by a wall-coating layer of viscous oil, the new method was applied to determine the hydrodynamic roughness produced by a variety of rough surfaces: solid walls, sandpapers, bio-fouling layers and wall-coating layers. This CFD approach is applicable for flow of water or other liquids over any rough surface.

A novel correlation to predict the hydrodynamic roughness produced by a layer of viscous oil on a wall

A new correlation was developed for the equivalent hydrodynamic roughness produced by a viscous layer of wall-coating in terms of the coating thickness. This correlation can be used to estimate the equivalent hydrodynamic roughness from either a measured or a known value of the physical thickness of the wall-coating layer. The estimated value will be an input parameter for CFD simulation. It will also be necessary to calculate frictional pressure loss on the basis of a correlation like Colebrook or Churchill equation and a phenomenological formula like Darcy-Weisbach equation. The new correlation is applicable to estimate pressure losses in flow situations where turbulent water flows on viscous wall-coating layer, e.g., water flushing a pipeline fouled with viscous oil.

6.3. Uncertainties and Challenges

The uncertainties and challenges associated with this research include the following:

a) A source of imprecision for the results obtained from the laboratory experiments was the size of the rectangular flow cell. Its aspect ratio (height : width) was ~ 1 : 1.6. The measured parameters, i.e., pressure gradient and physical roughness are likely to be influenced by the secondary flows induced by the geometry of the flow cell. The contribution of secondary flows to the measured values was not determined in the course of the current research, which leaves an unaccounted for factor in the results presented earlier. However, the effect of secondary flows was taken into account in this research by using an anisotropic Reynolds stress model (ω-RSM) for modeling turbulent flow conditions in the flow cell. Moreover, it was possible to combine the flow cell data with the pipe flow data, which indicates that secondary flow was not necessarily a dominant factor affecting the presented results. Nonetheless, additional experiments, perhaps using actual pipe flows, should be conducted.

b) It was challenging to deal with the time requirements for the experiments. The average time required to complete a set of wall-coating experiments was three weeks. This time constraint did not allow us to produce a large number of data points by varying the controlled parameters over wider ranges. As a result, the experimental trends were concluded on the basis of a limited number of data points. This is a limitation of the current work.

c) The uncertainties associated with the new methodology to model the frictional pressure loss in a CWAF pipeline stemmed primarily from the modeling assumptions. The oil core in the pipe was assumed to be concentric. In reality, it is likely to be eccentric (off-centered). The surface of the oil core was assumed smooth, although the surface has been shown to be rough. Also, the lubricating annulus in a CWAF pipeline was assumed to be water alone. However, the annular region is filled with a mixture of water, oil droplets and fine particles. These realities, if taken into account properly, will almost certainly have an impact on the predicted values of frictional pressure losses. Clearly, future work is required to develop a more comprehensive model following the approach introduced in this work.

6.4. Recommendations

The research for this dissertation falls within two separate subjects in the field of pipeline hydraulics:

i) Hydrodynamic roughness produced by a viscous layer of wall-coating
ii) Modeling frictional pressure losses in the continuous water assisted flow (CWAF) of heavy oil and bitumen

Additional studies should be done to generalize some of the results of this study. The future work that would further each of the current research subjects is discussed below.

6.4.1. Hydrodynamic roughness

The effect of secondary flows on the hydrodynamic roughness produced by a wall-coating layer of viscous oil can be investigated by changing the aspect ratio of the flow cell(s). The flow tests of this research should be repeated using new cells having different aspect ratios, such as 1:1, 1:5 and 1:10. It will allow the determination of the effect of secondary flows on the hydrodynamic roughness from an experimental perspective. The new setup should be designed so that it is possible to measure the velocity profile just above the wall-coating layer, which is the standard practice for evaluating hydrodynamic roughness. By adding this experimental capability, the CFD approach can be validated more rigorously.

Another interesting research topic is the influence of oil droplets present in the turbulent water on the mechanism of generating physical roughness on the wall-coating layer. The oil droplets are likely to have a significant impact on the physical roughness and, as such, the equivalent hydrodynamic roughness. A setup similar to the one used for the current research can be used for the experiments. Instead of tap water, the flowing fluid should be an oil-in-water emulsion. This study will provide a better understanding of the hydrodynamic roughness produced by the wall-fouling layer in a CWAF pipeline.

An interesting new study can be initiated based on the measurement of physical roughness discussed in Chapter 3. For the purpose, a solid structure would be reproduced with the measured topology of viscous oil. Flow tests would be conducted using the solid rough surface. These tests will help to better understand the contribution of physical roughness to the pressure loss, i.e., the equivalent hydrodynamic roughness. Based on such flow tests, CFD simulation can be developed and validated using the reproduced topology as a boundary condition. The validated simulation will be useful in studying the effect of physical roughness by varying the topology over a wide range.

6.4.2. Modeling CWAF pressure losses

A limitation of the model presented in this work is the idealized consideration of a concentric oil core. Future work is required to incorporate the effect of eccentricity in this model because previous studies suggest the oil core in the fully developed CWAF in a horizontal pipe to be eccentric (Oliemans and Ooms 1986, McKibben et al. 2000a, Benshakhria et al. 2004, Herrera et al. 2009, Sotgia et al. 2008, Strazza et al. 2011). The effect of the core location on the pressure gradient has not been studied in detail to date (see, for example, Benshakhria et al. 2004). The experimental investigation of the effect of eccentricity can be done by using an apparatus similar to the one used by Polderman et al. (1986). They used an axially movable rubber string inside a steel pipe. Water was pumped in the annulus between the string and the pipe's inner wall to replicate core annular flow. The position and outer diameter of the string can be adjusted to control the thickness and the eccentricity of water annulus. The CFD approach introduced in this research to model CWAF will be useful to simulate the flow conditions in an eccentric core annular flow system.

It would be interesting to conduct a study focusing on the oil core itself, specifically, the relationship between surface roughness and CWAF behavior. Similar to the wall-fouling layer, the surface of the oil core in a CWAF pipeline is likely to be rough under steady state flow conditions (Joseph et al. 1999, Sotgia et al. 2008, Strazza et al. 2011). However, the hydrodynamic effects of this roughness have not been studied to date. In the current work, the interface between the oil core and the water annulus is simulated as a moving wall. Although the physical roughness on the interface should have been modeled with the equivalent hydrodynamic roughness, we assumed the surface to be hydrodynamically smooth for the purpose of simplicity. Larger values of oil core hydrodynamic roughness will almost certainly change the frictional pressure losses.

The annular fluid that lubricates the oil core in the CWAF was considered as water in the current research. In reality the lubricating fluid is likely to be a mixture of two major components, water and oil droplets (Sotgia et al. 2008; Vuong et al. 2009; Strazza et al. 2011). However, the hydrodynamic effect of oil droplets in a lubricating water annulus is yet to be studied. A possible effect would be changing the apparent viscosity of the lubricating fluid. The apparent viscosity would depend on various factors, such as volumetric fraction of oil and size/shape of oil droplets. A detailed analysis would be required to appreciate the hydrodynamic effects of oil droplets in a lubricating water annulus.

Current pressure loss model is potential for engineering scale up as it was developed on the basis of CWAF data obtained by using significantly different diameter pipes: 4 inch and 10 inch. The data set was divided into two parts on the basis of operating temperature, calibration data (T ~ 25°C) and test data (T ~ 35°C). The calibration data set was used to develop a correlation, while the test data set was meant to test the performance of the newly developed model. It would be interesting to divide the CWAF data on the basis pipe diameter (instead of temperature), i.e., to use the 4 inch pipe data for the calibration and 10 inch pipe data for the test. The model should also be tested for other pipe diameters. In this way, the performance of current model in scale up can be better understood.

The oil core touching the pipe wall in a large water-assisted pipeline is an unaddressed phenomenon. The model proposed in this thesis is not capable of addressing the issue. Experiments conducted at SRC suggest that this phenomenon is significant for intermittent water-assist when the bulk velocity is less than 1 m/s and the water fraction is less than 30% (McKibben et al. 2007 and McKibben and Gillies, 2009). Dedicated future works are necessary to ascertain the contribution of intermittent core/wall contact to the frictional pressure loss.

Another unaddressed issue is the hydrodynamic effects of the solids in a CWAF pipeline. The solids embedded on the surfaces of wall-fouling layer and oil core can have impact on the equivalent hydrodynamic roughness. Also, the solids (fine particles) in the lubricating fluid may change its apparent viscosity and the nature of the contact between the oil-covered wall and the oil core (see Joseph et al. 1999 for additional details). Future work would help to characterize the effects of solid fraction on the pressure losses in CWAF pipelines.

REFERENCES

Adams, T., Grant, C. and Watson, H., 2012. A simple algorithm to relate measured surface roughness to equivalent sand-grain roughness, *International Journal of Mechanical Engineering and Mechatronics*, **1(1)**, pp. 66-71, Avestia Publishing, Journal ISSN: 2929-2724, Article ID: 008, DOI: 10.11159/ijmem.2012.008.

Afzal, N., Seena, A. and Bushra, A., 2013. Turbulent flow in a machine honed rough pipe for large Reynolds numbers: General roughness scaling laws, *Journal of Hydro-environment Research*, **7**, pp. 81 – 90.

Al-Wahaibi, T. and Angeli, P., 2007. Transition between stratified and non-stratified horizontal oil–water flows, Part I: stability analysis, *Chem. Eng. Sci.*, **62**, pp. 2915 – 2928.

Al-Wahaibi, T., 2012. Pressure gradient correlation for oil–water separated flow in horizontal pipes, *Experimental Thermal and Fluid Science*, **42**, pp. 196 – 203.

Amano, R. S., Guntur, K. and Lucci J. M., 2010. Computational study of gas turbine blade cooling channel, Proceedings of the 14th International Heat Transfer Conference, IHTC14-22920, August 8 – 13, 2010, Washington, DC, USA.

Andrewartha, J. M., 2010. The Effect of Freshwater Biofilms on Turbulent Boundary Layers and the Implications for Hydropower Canals. PhD thesis, University of Tasmania, Australia.

ANSYS CFX-Solver Theory Guide, 2010. Release 13.0, ANSYS, Inc., Southpointe, 275 Technology Drive, Canonsburg, PA 15317, pp. 77 – 140.

Andrewartha, J. M., Sargison, J. E. and Perkins, K. J., 2008. The influence of freshwater biofilms on drag in hydroelectric power schemes, *WSEAS TRANSACTIONS on FLUID MECHANICS*, **3(3)**, pp. 201-206, ISSN: 1790-5087.

Antonia, R. A. and Krogstad, P. A., 2001. Turbulence structure in boundary layers over different types of surface roughness. *Fluid Dynamics Research*, **28**, pp. 139 – 157.

Arney, M. S., Bai, R., Guevara, E., Joseph, D. D. and Liu, K., 1993. Friction Factor and Holdup Studies for Lubricated Pipelining – I, Experiments and Correlations, *Int. J. Multiphase Flow*, **19(6)**, pp. 1061-76.

Arney, M. S., Ribeiro, G. S., Guevara, E., Bai, R. and Joseph, D. D., 1996. Cement-lined pipes for water lubricated transport of heavy oil, *Int. J. Multiphase Flow*, **22(2)**, pp. 207 – 221.

Ashrafi, M., Souraki, Y., Karimaie, H., Torsaeter, O. and Bjorkvik, B. J. A., 2011. Experimental PVT Property Analyses for Athabasca Bitumen, Canadian Unconventional Resources Conference, Calgary, Alberta, Canada.

Aupoix, B., Arnal, D., Bezard, H., Chaouat, B., Chedenergne, F., Deck, S., Gleize, V., Grenard, P. and Laroche, E., 2011. Transition and turbulence modeling. *Journal AerospaceLab*, **2**, AL02-01, pp. 1 – 13.

Bannwart, A. C., Rodriguez, O. M. H., de Carvalho, C. H. M., Wang, I. S. and Vara, R. M. O., 2004. Flow patterns in heavy crude oil – water flow. *Journal of Energy Resources Technology (Transactions of ASME)*, **126**, pp. 184 – 189, DOI: 10.1115/1.1789520.

Bannwart, A. C., Rodriguez, O. M. H., Biazussi, J. L., Martins, F. N., Selli, M. F. and de Carvalho, C. H. M., 2012. Water-assisted flow of heavy oil in a vertical pipe: pilot-scale experiments, *International Journal of Chemical Reactor Engineering*, **10**, Article A32, DOI: 10.1515/1542-6580.2965.

Barral, A. H., Ebenezer, A. and Angeli, P., 2015. Investigations of interfacial waves at the inlet section in stratified oil–water flows, *Experimental Thermal and Fluid Science*, 60, pp. 115 – 122.

Barton, A. F., Wallis, M. R., Sarglson, J. E., Bula, A. and Walker, G. J., 2008. Hydraulic roughness of biofouled pipes, biofilm character, and measured improvements from cleaning, *J. Hydraul. Eng.*, **134**, pp. 852-857.

Barton, A. F., Sargison, J. E., Walker, G. J., Osborn, J. E. and Brandner, P. A., 2005. A baseline study of the effect of freshwater biofilms in hydraulic conduits, *XXXI IAHR CONGRESS*, Sept. 11 – 16, 2005, Seoul, Korea, pp. 992-1002.

Bayazit, M., 1976. Free surface flow in a channel of large relative roughness, *Journal of Hydraulic Research*, **14(2)**, pp. 115-126.

B. C. MacDonald & Co (BCM). Surface Finish 101: Basic Components and Elements of Surface Topography. http://www.bcmac.com/pdf_files/surface%20finish%20101.pdf (retrieved at 05 December 2015).

Beer, D. D., Stoodley, P. and Lewandowski, Z., 1994. Liquid flow in heterogeneous biofilms, *Biotechnology and Bioengineering*, John Willey & Sons, Inc., **44**, pp. 636-641, CCC 0006-3592/94/050636-06.

Bensakhria, A., Peysson, Y., Antonini, G., 2004. Experimental study of the pipeline lubrication for heavy oil transport. *Oil & Gas Science and Technology – Rev. IFP.*, **59(5)**, pp. 523 – 533.

Bergstrom, D. J., Kotey, N. A. and Tachie, M. F., 2002. The effects of surface roughness on the mean velocity profile in a turbulent boundary layer, *Journal of Fluids Engineering*, Transactions of the ASME, **124**, pp. 664-670, DOI: 10.1115/1.1493810.

Bhagoria, J. L., Saini, J. S. and Solanki, S. C., 2002. Heat transfer coefficient and friction factor correlations for rectangular solar air heater duct having transverse wedge shaped rib roughness on the absorber plate. *Renewable Energy*, **25**, pp. 341 – 369.

Bhatt, C. P., 2007. Assessment of uncertainty in equivalent sand grain roughness methods. MSc Thesis, The University of Alabama, Birmingham, Alabama, USA.

Bird, R.B., Stewart, W.E. and Lightfoot, E.N., 2001. Transport Phenomena (Second Edition ed.). John Wiley & Sons, New York.

Bjørnseth, F., 2013. Heavy Oil Production Technology Challenges and the Effect of Nano Sized Metals on the Viscosity of Heavy Oil: A literature review and an experimental study. MSc Thesis, Department of Petroleum Engineering and Applied Geophysics, Norwegian University of Science and Technology.

Bonkdari, H., Lipeme-kouyi, G. And Asawa, G. L., 2014. Developing turbulent flows in rectangular channels: A parametric study. *Journal of Applied Research in Water and Wastewater*, **1(2)**, pp. 53 – 58.

Bons, J. P., 2010. A review of surface roughness effects in gas turbines. *Journal of Turbomachinery*, **132**, pp. 021004-1 – 16, DOI: 10.1115/1.3066315.

Brauner, H., 1963. Flow Resistance in Pipes with Ripple Roughness, *Chemische Zeitung (Chemist Review Eng)*, **87**, pp. 199 – 210.

Canadian Association of Petroleum production (CAPP), "Crude Oil: Forecast, Market and Transportation", 2015. [cited October 2015], www.capp.ca.

Charles, M. E., Govier, G. W. and Hodgson, G. W., 1961. The pipeline flow of equal density oil water mistures, *Can. J. Chem. Eng.*, **39**, 27 – 36.

Crivelaro, K. C. O., Damacena, Y. T., Andrade, T. H. F., Lima, A. G. B. and Farias Neto, S. R., 2009. Numerical simulation of heavy oil flows in pipes using the core-annular flow technique, *WIT Transactions on Engineering Sciences,* **63**, pp. 193 – 203.

Czichos, H., Saito, T. and Smith, L., Eds., 2006. Springer Handbook of Materials Measurement Methods. Springer-Verlag: Berlin and Heidelberg, Germany, pp. 268 – 270, ISBN: 978-3-540-30300-8.

Davidson, L., 2011. An introduction to turbulence models. Publication 97/2, Department of Thermo and Fluid Dynamics, Chalmers University of Technology, Goteborg, Sweden.

de Andrade, T. H. F., Crivelaro, K. C. O., de F. Neto, S. R. and de Lima, A. G. B., 2012. Numerical Study of Heavy Oil Flow on Horizontal Pipe Lubricated by Water, A. Ochsner *et al.* (eds.), *Materials with Complex Behaviour II*, *Advanced Structured Materials 16*, Springer-Verlag Berlin Heidelberg 2012, pp. 99 – 118, DOI: 10.1007/978-3-642-22700-4_6.

Doshi, M. R. and Gill, W. N., 1970. A note on the mixing length theory of turbulent flow. *AIChE Journal*, **16(5)**, pp. 885 – 888.

Edomwonyi-Otu, L. C. and Angeli, P., 2015. Pressure drop and holdup predictions in horizontal oil–water flows for curved and wavy interfaces, *Chemical Engineering Research and Design*, **93**, pp. 55 – 65.

Farshad, F. F., Rieke, H. H. and Mauldin, C., 2002. Flow test validation of direct measurement methods used to determine surface roughness in pipes (OCTG), *SPE 76768*, Society of Petroleum Engineering Inc., SPE Western Regional/AAPG Pacific Section Joint Meeting, Anchorage, Alaska, USA, 20-22 May 2002.

Flack, K. and Schultz, M. P., 2010a. Roughness scaling parameters in the fully-rough regime, Nickels (ed.), *IUTAM Symposium on The Physics of Wall-Bounded Turbulent Flows on Rough Walls*, IUTAM Bookseries 22, Springer Science + Business Media B. V., pp. 99-104, DOI 10.1007/978-90-481-9631-9_14.

Flack, K. A. and Schultz, M. P., 2010b. Review of hydraulic roughness scales in the fully rough regime, *Journal of Fluids Engineering*, **132**, Transactions of the ASME, pp. 041203.

Fletcher, D. F., Geyer, P. E. and Haynes, B. S., 2009. Assessment of the SST and omega-based Reynolds stress models for the prediction of flow and heat transfer in a square-section u-bend, *Computational Thermal Sciences*, **1**, pp. 385 – 403.

Gadelha, A. J. F., de Farias Neto, S. R., Swarnakar, R. and de Lima, A. G. B., 2013. Thermo-hydrodynamics of core-annular flow of water, heavy oil and air using CFX, *Advances in Chemical Engineering and Science*, **3**, pp. 37 – 45.

Govindarajan, R. and Sahu, K. C., 2014. Instabilities in viscosity-stratified flow. Annu. Rev. Fluid Mech., 2014, **46**, pp. 331–53

Guevara, E., Gonzalez, J. and Nunez, G., 1998. Highly Viscous Oil Transportation Methods in the Venezuela Oil Industry, [8]4, *Proceedings of the 15th World Petroleum Congress,* John Wiley & Sons, Beijing, China, pp. 495 – 502.

Hart A., 2014. A review of technologies for transporting heavy crude oil and bitumen via pipelines. *J Petrol Explor Prod Technol*, **4**, pp. 327 – 336.

Herrera J. R., Mena B., Romo C. A. and Manero O., 2009. Lubricated pipe transport of heavy crude oils. *Petroleum Science and Technology*, **27(13)**, pp. 1466 – 1479.

Ho W. S. and Li N. N., 1994. Core-Annular Flow of liquid membrane emulsion, *AIChE Journal*, **40(12)**, pp. 1961 – 1968.

Holland F. A. and Bragg R., 1995. Fluid flow for chemical engineers, 2nd Edition, Elsevier.

Hooper, A. P. and Boyd, W. G. C., 1987. Shear-flow instability due to awall and a viscosity discontinuity at the interface, *J. Fluid Mech.* **179**, pp. 201 – 25.

Huang A., Christodoulou C. and Joseph D. D., 1994. Friction factor and holdup studies for lubricated pipelining – II: Laminar and k-ε models for eccentric core flow, *Int. J. Multiphase Flow*, **20(3)**, pp. 481 – 491.

International Energy Agency (IEA), "World energy outlook 2013". www.iea.org.

Isaacs, J.D., Speed, J.B., 1904. Method of Piping Fluids. US Patent No. 759374.

Isehunwa, S.O. and Olubukola, O., 2012. Interfacial tension of crude oil-brine systems in the niger delta, *IJRRAS*, **10(3)**, pp. 460 – 465.

Jean F. G., Sébastien G., Guy M. and Armelle S., 2005. Prospective Analysis of the Potential Non-conventional World Oil Supply: Tar Sands, Oil Shales and Non-conventional Liquid Fuels from Coal and Gas, Institute for Prospective Technological Studies, European Commission, Technical Report EUR 22168 EN, Printed in Spain.

Jones O. C., 1976. An Improvement in the Calculation of Turbulent Friction in Rectangular Ducts, *Journal of Fluids Engineering*, June 1976, pp. 173 – 180.

Joseph D. D., Bai R., Chen K. P. and Renardy Y. Y., 1997. Core-Annular Flows, *Annu. Rev. Fluid Mech.*, **29**, pp. 65 – 90.

Joseph D. D., Bai R., Mata C., Sury K. and Grant C., 1999. Self-lubricated transport of bitumen froth, *Journal of fluid mechanics*, **386**, pp. 127 – 148.

Kandlikar S. G., Schmitt D., Carrano A. L. and Taylor J. B., 2005. Characterization of surface roughness effects on pressure drop in single-phase flow in minichannels, *Phys. Fluids*, American Institute of Physics, **17**, pp. 100606, DOI 10.1063/1.1896985.

King T. G., 1980. rms, skew and kurtosis of surface profile height distributions: some aspects of sample variation, *Precis Eng*, **2(4)**, pp. 207 – 215.

Kushnir, R., Segal, V., Ullmann, A. and Brauner, N., 2014. Inclined two-layered stratified channel flows: Long wave stability analysis of multiple solution regions, *Int. J. Multiphase Flow*, **62**, pp. 17 – 29.

Lambert, M. F., Edwards, R. W. J., Howie, S. J., Gilio, B. B. D. and Quinn, S. P., 2009. The impact of biofilm development on pipe roughness and velocity profile, *World*

Environmental and Water Resources Congress 2009, Great Rivers, ASCE, pp. 122-134.

Langelandsvik, L. I., Kunkel, G. J. and Smits, A. J., 2008. Flow in a commercial steel pipe, *J. Fluid Mech.*, **595**, pp. 323-339.

Launder, B. E. and Spaulding, D. B., 1972. Mathematical Models of Turbulence, Academic Press, New York.

Martínez-Palou, R., de Lourdes Mosqueira, M., Zapata-Rendón, B., Mar-Juárez, E., Bernal-Huicochea, C. and de la Cruz Clavel-López, J., Aburto, J., 2011. Transportation of heavy and extra-heavy crude oil by pipeline: A review, *Journal of Petroleum Science and Engineering*, **75**, 274–282.

McKibben, M. J., Gillies, R. G. and Shook, C. A., 2000a. A laboratory investigation of horizontal well heavy oil – water flows, *The Canadian Journal of Chemical Engineering*, **78**, 743 – 751.

McKibben, M. J., Gillies, R. G. and Shook, C. A., 2000b. Predicting pressure gradients in heavy oil-water pipelines, *The Canadian Journal of Chemical Engineering*, **78**, 752 – 756.

McKibben, M., Gillies, R. and Sanders, S., 2007. Water-assisted pipeline transportation of Bitumen/Heavy Oils and co-produced sand: 2006 Annual Report, *SRC Publication No. 11716-1C07, PTRC No. 001-00086-SRC (Year 2),* Petroleum Technology Research Centre, Regina, SK, Canada.

McKibben, M. and Gillies, R., 2009. Water-assisted pipeline transportation of Bitumen/Heavy Oils and co-produced sand: 2008 Annual Report, *SRC Publication No. 11716-1C09, PTRC No. 001-00086-SRC (Year 3),* Saskatchewan Research Council Pipeflow Technology Centre, Saskatoon, SK, Canada.

Mothe, K. K. and Sharif, M. A. R., 2006. Assessment of the omega based models in the prediction of incompressible turbulent flows over flat rough surfaces. *Collection of Technical Papers – 44th AIAA Aerospace Sciences Meeting*, Reno, Nevada, American Institute of Aeronautics and Astronautics, **12**, pp. 8707 – 8715/AIAA 2006 – 0718.

Nikuradse, J., 1950. Laws of flow in rough pipes. *National Advisory Committee for Aeronautics (NACA)*, Technical Memorandum 1292. (Translation of “Strömungsgesetze in rauhen Rohren”. VDI-Forschungsheft 361. Beilage zu “Forschung auf dem Gebiete des Ingenieurwesens” Ausgabe B Band 4, July/August 1933.)

Nunez, G. A., Rivas, H. J. and Joseph, D. D., 1998. Drive to produce heavy crude prompts variety of transportation methods, *Oil & Gas Journal*, **96(43)**, 59 – 63.

Oliemans, R. V. A. and Ooms, G., 1986. Core-Annular flow of oil and water through a pipeline. *Multiphase Science and Technology*, **2**, pp. 427 – 476.

Oliemans, R. V. A., Ooms, G., Wu, H. L. and Duijvestijn, A., 1987. Core-annular oil/water flow: The turbulent-lubricating-film model and measurements in a 5 cm pipe loop, *Int. J. Multiphase Flow*, **13(1)**, pp. 23 – 31.

Ooms, G., Segal, A., Van der Wees, A. J., Meerhoff, R. and Oliemans, R. V. A., 1984. A theoretical model for core-annular flow of a very viscous oil core and a water annulus through a horizontal pipe, *Int. J. Multiphase Flow*, **10(1)**, pp. 41 – 60.

Polderman, H. G., Velraeds, G. and Knol, W., 1986. Turbulent lubrication flow in an annular channel. *Journal of Fluids Engineering*, **108**, pp. 185 – 192.

Pope, S. B., 2000. Turbulent Flows. Cambridge, United Kingdom Cambridge University Press, ISBN 0 521 59886 9.

Picologlou, B. F., Characklis, W. G. and Zelver, N., 1980. Biofilm growth and hydraulic performance, *Journal of the Hydraulics Division*, **106(5)**, pp. 799-746.

Queimada, A. J., Marrucho, I. M., Stenby, E. H. and Coutinho, J. A. P., 2003. Generalized Relation Between Surface Tension and Viscosity: a Study on Pure and Mixed n-alkanes, Fifteenth Symposium on Thermophysical Properties, June 22 – 27, 2003, Boulder, Colorado, USA.

Rodriguez, O. M. H., Bannwart, A. C. and de Carvalho, C. H. M., 2009. Pressure loss in core-annular flow: Modeling, experimental investigation and full-scale experiments, *Journal of Petroleum Science and Engineering*, **65**, pp. 67 – 75.

Sanders, R. S., Ko, T., Bai, R. and Joseph, D. D., 2004. Factors governing friction losses in self lubricated transport of bitumen froth: 1. water release, *The Canadian Journal of Chemical Engineering*, **82**, pp. 735 – 742.

Sakr, A. L., Sultan, G. I., Safan, M. G. And Tolba, M. M., 2012. Flow structure development due to injection water into the annulus of heavy oil pipe flow, *SPE Journal*, SPE 151402.

Saniere, A., Henaut, I. and Argillier, J. F., 2004. Pipeline transportation of heavy oils, a strategic, economic and technological challenge, *Oil & Gas Science and Technology – Rev. IFP*, **59**, 455 – 466.

Schaan, J., Sanders, R. S., Litzenberger, C., Gillies, R. G. and Shool, C. A., 2002. Measurement of heat transfer coefficients in pipeline flow of Athabasca Bitumen froth, *BHR Group 2002 Multiphase Technology*, pp. 25 – 38.

Schonhorn, H., 1967. Surface tension – viscosity relationship for liquids, *Journal of Chemical and Engineering Data*, **12(4)**, pp. 524 – 525.

Schultz, M. P. and Swain, G. W., 2000. The influence of biofilms on skin friction drag, *Biofouling: The Journal of Bioadhesion and Biofilm Research*,Taylor & Francis, **15:1-3**, pp. 129-139, DOI: 10.1080/08927010009386304.

Schultz, M. P., 2007. Effects of coating roughness and biofouling on ship resistance and powering, *Biofouling: The Journal of Bioadhesion and Biofilm Research*, Taylor & Francis, **23:5**, pp. 331-341, DOI: 10.1080/08927010701461974.

Schultz, M. P. and Flack, K. A., 2003. Turbulent boundary layers over surfaces smoothed by sanding, *Journal of Fluids Engineering*, Transactions of the ASME, **125**, pp. 863-870, DOI: 10.1115/1.1598992.

Shockling, M. A., Allen, J. J. and Smits, A. J., 2006. Roughness effects in turbulent pipe flow, *J. Fluid Mech.*, **564**, pp. 267-285.

Shook, C. A., Gillies, R. G. and Sanders, R. S., 2002. Pipeline hydrotransport with applications in the oil sand industry, *SRC Publication No. 11508-1E02*, Saskatchewan Research Council Pipeflow Technology Centre, Saskatoon, SK, Canada.

Sodja, J. and Podgornik, R., 2007. Turbulence Models in CFD. Department of Physics, University of Ljubljana, Ljubljana, Slovenia.

Sotgia, G., Tartarini, P. and Stalio, E., 2008. Experimental analysis of flow regimes and pressure drop reduction in oil-water muxtures. *International Journal of Multiphase Flow*, **34(12)**, pp. 1161-1174, doi:10.1016/j.ijmultiphaseflow.2008.06.001.

Strazza, D., Grassi, B., Demori, M., Ferrari, V. and Poesio, P., 2011. Core-annular flow in horizontal and slightly inclined pipes: Existence, pressure drops, and hold-up. *Chemical Engineering Science*, **66**, pp. 2853 – 2863.

Taitel, Y. and Dukler, A. E., 1979. A model for predicting flow regime transitions in horizontal and near horizontal gas-liquid flow, *AIChE Journal*, **22 (1)**, pp. 47 – 55.

Tilley, B. S., Davis, S. H. and Bankoff, S. G., 1994. Linear stability of two-layer fluid flow in an inclined channel, *Phys. Fluids*, **6**, pp. 3906 – 3922.

Unal, U. O., Unal, B. and Atlar, M., 2012. Turbulent boundary layer measurements over flat surfaces coated by nanostructured marine antifoulings. *Exp Fluids*, **52**, pp. 1431 – 1448, DOI: 10.1007/s00348-012-1262-z.

Vuong, D. H., Zhang, H. Q., Sarcia, C. and Li, M., 2009. Experimental study on high viscosity oil/water flow in horizontal and vertical pipes, *SPE 124542, SPE Annual Technical Conference and Exhibition,* New Orleans, Louisiana, USA.

Wallin, S., 2000. Engineering turbulence modelling for CFD with a focus on explicit algebraic Reynolds stress models. PhD Thesis, Department of Mechanical Engineering, Royal Institute of Technology, Stockholm, Sweden.

White, F. M., 1999. Fluid Mechanics, 4th Edition, McGraw-Hill, Boston, Mass., USA, pp. 349.

Young, P. L., Brackbill, T. P. and Kandlikar, S. G., 2007. Estimating roughness paramters resulting from various machining techniques for fluid flow applications, *Proceedings of the Fifth International Conference on Nanochannels, Microchannels and Minichannels*, ICNMM2007, June 18-20, 2007, Puebla, Mexico, ASME, ICNMM2007-30033.

Zhang, X. W., Jin, X. L., Wang, Y., Deng, K. and Ren, Z. M., 2011. Comparison of standard k-ε model and RSM on three dimensional turbulent flow in the SEN of slab continuous caster controlled by slide gate. *ISIJ International*, **51(4)**, pp. 581 – 587.

APPENDIX 1
THE DESCRIPTION OF THE CUSTOMIZED FLOW CELL

Experiments were conducted using an existing pipeloop at the University of Alberta. A detailed description of the loop is available in Razzaque *et al*. (2003). It was a 35 m long horizontal loop made of 25.4 mm ID copper tube. Water was pumped from a tank with a Moyno 1000 progressing cavity pump (Model No. A2FCDQ 3AAA). The pump was driven by a 7.5 hp motor (BALDOR INDUSTRIAL MOTOR, Model No. M3710T). The pipeloop was equipped with a coriolis mass flow meter (Krohne MFM 4085K Corimass, type 300G+) and a 4 m long double pipe heat exchanger. The flow meter was used to measure the mass flow rate and the temperature, while the heat exchanger was used to maintain a steady state temperature of flowing water (20±2°C). The experiments were conducted by adding a custom built rectangular flow cell to the pipeloop. Two flexible 26.5 mm hoses were used to join the flow cell with the pipeline. After exited from the flow cell, water was filtered through a 34 micron high performance filter bag (3M Purification 100 Series). The filter bag was housed in an Arctic P2 Filter (Part No. FHS02-004SE-N32-501S).

Engineering drawing:

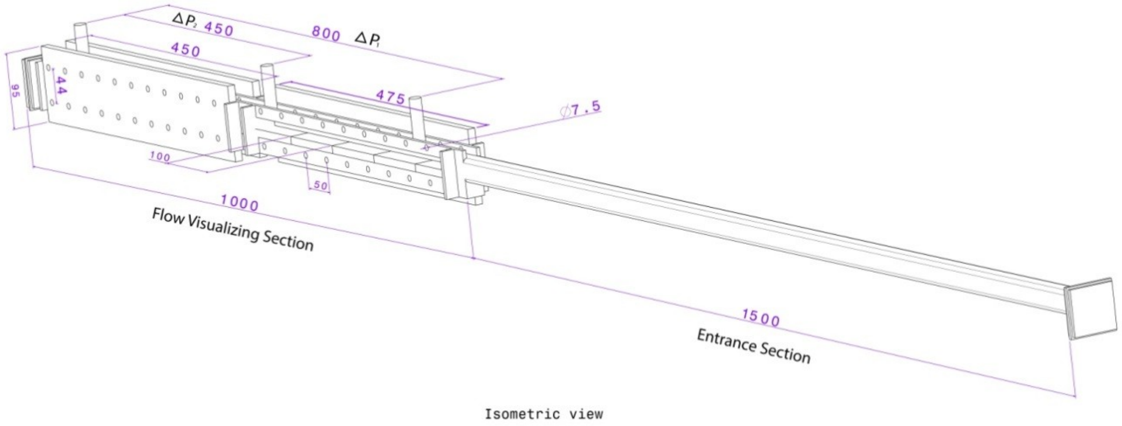

Figure A1.1. Basic engineering drawing of the flow cell (the dimensions are in mm).

Photographs:

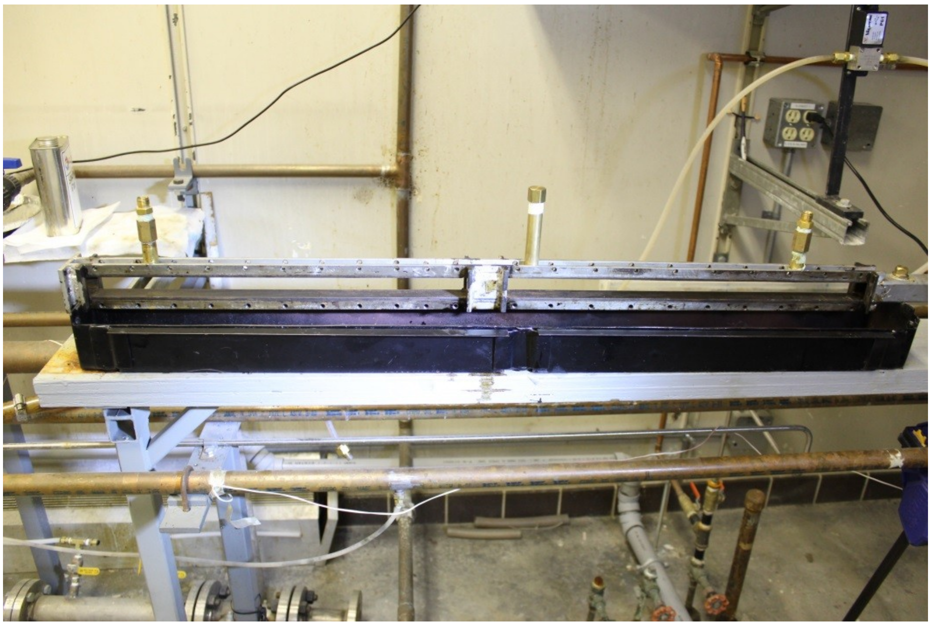

(a)

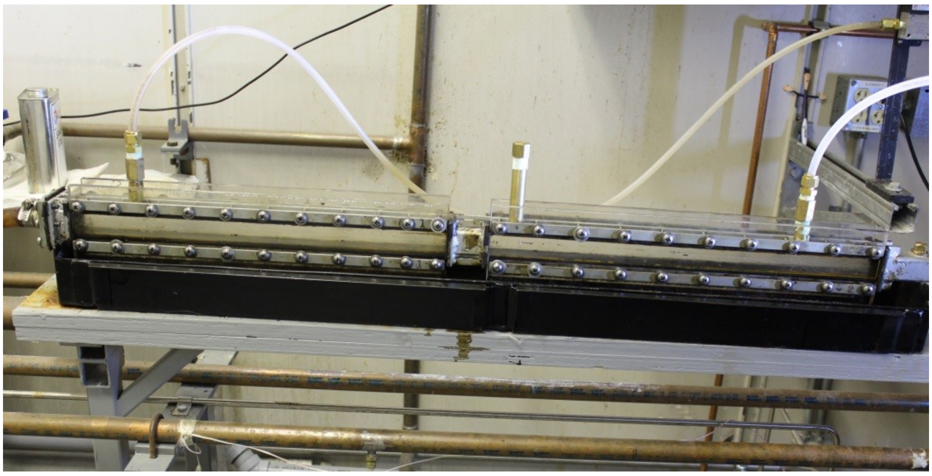

(b)

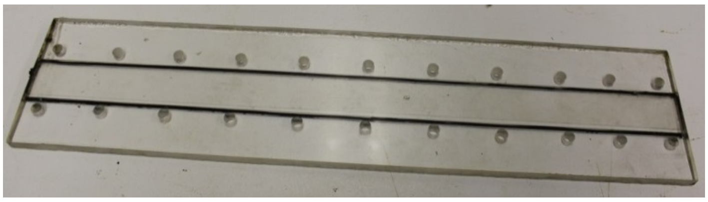

(c)

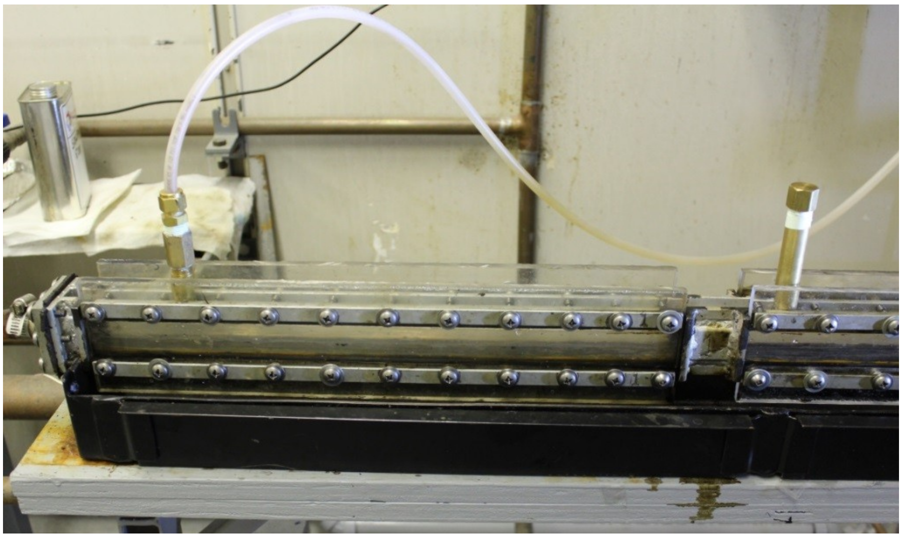

(d)

(e)

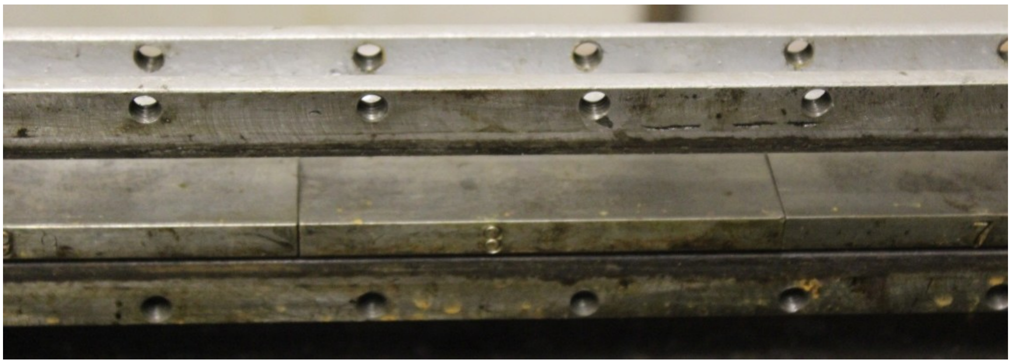

(f)

(g)

Figure A1.2. Photographs showing the flow cell: (a) Flow visualizing section without viewing windows and test plates; (b) Flow visualizing section with mounted Plexiglas windows: only water flowing in the channel; (c) A Plexiglas window with o-ring; (d) Test section for the wall-coating experiments with mounted Plexiglas windows; (e) Flow visualizing section with coated bottom wall; (f) Test plates without wall-coating; (g) Test plates with wall-coating.

APPENDIX 2

DESCRIPTIONS OF THE SAMPLE OILS

Sample 1:

It was a performance graded asphalt binder (PG 46-37, 300/400A). Husky Energy, Canada provided this oil from the refinery in Lloydminster, AB. The properties of this sample as provided from plant were as follows:

Density @ 15°C: 1021 kg/m^3

Dynamic viscosity @ 135°C: 0.155 Pa.s

Dynamic viscosity @ 60°C: 66 Pa.s

A viscosity, μ (Pa.s) vs. temperature, T (°C) graph was also supplied. It is a semi-logarithmic graph. Following power law correlation was derived by using the data points from that graph:

$$\mu = 2\times10^{12}T^{-6.128}$$

This correlation yields the room temperature viscosity:

Dynamic viscosity @ 20°C: 21297 Pa.s ~ 21 300 Pa.s

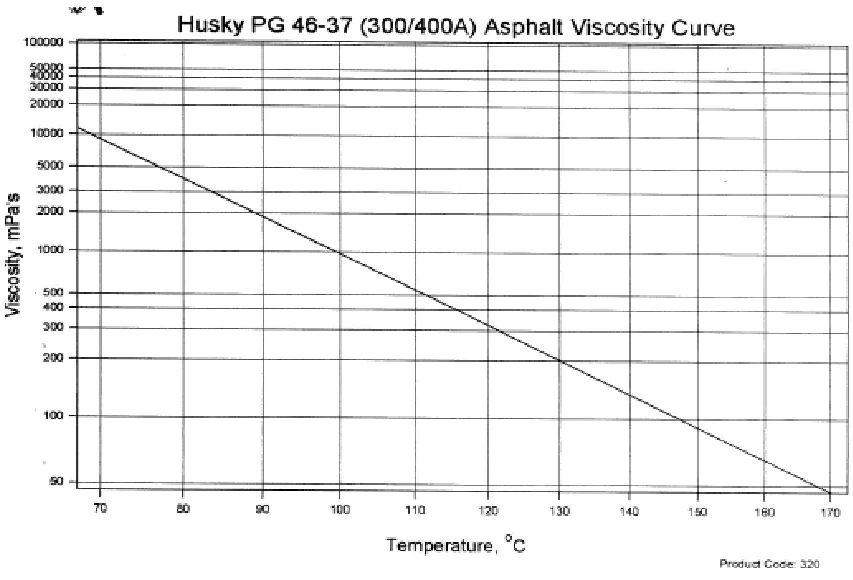

Figure A2.1. The viscosity vs. temperature graph provided by Husky Energy.

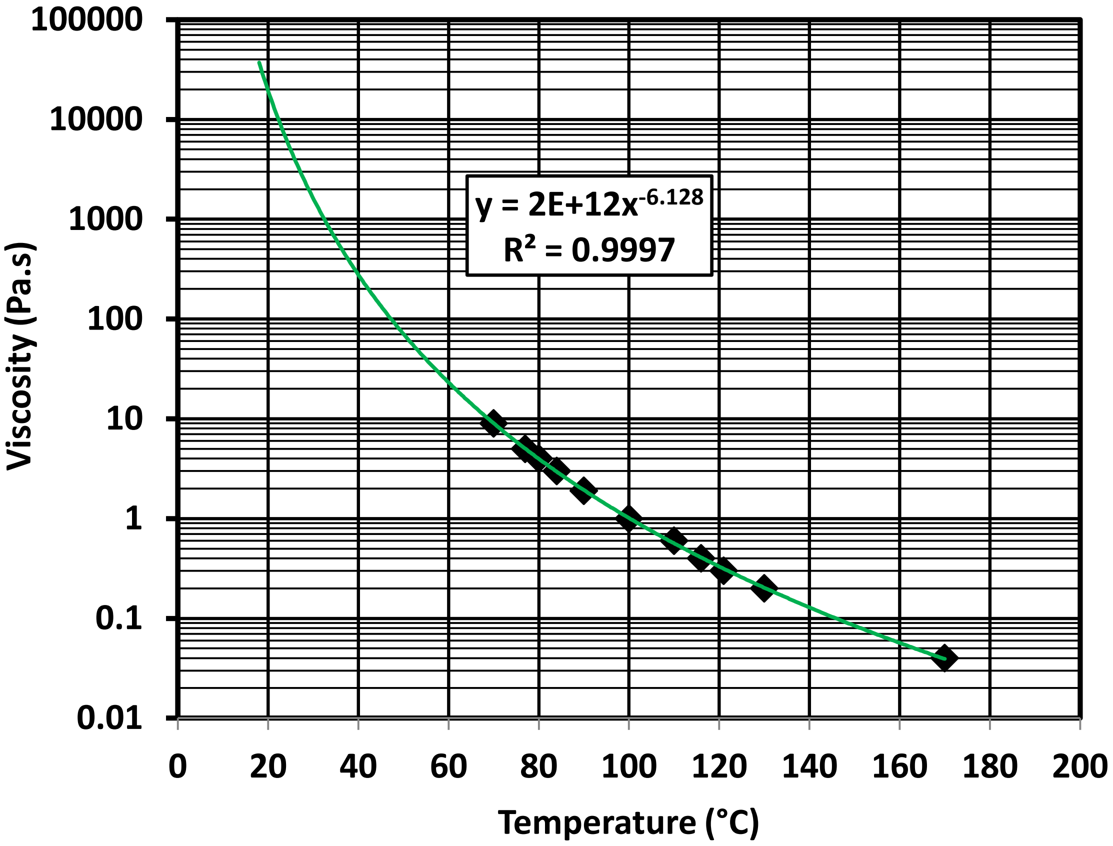

Figure A2.2. The graph used to develop a correlation between oil viscosity and temperature.

Sample 2:

It was a mixture of 80% bitumen and 20% gas oil. The bitumen and the gas oil were provided by SynCrude, Canada from the laboratory in Edmonton, AB. The viscous mixture was characterized in the Saskatchewan Research Council, Saskatoon, SK. The measured properties of this oil were as follows:

Density @ 20°C: 1000 kg/m^3

Dynamic viscosity @ 20°C: 2619 Pa.s ~ 2620 Pa.s

A Haake Rheo-stress Viscometer RS150 was used for the measurements. The measured data were as follows:

Table A2.1. Viscometer data for Sample 2.

Temperature T (°C)	Density ρ (kg/m^3)	Spindle speed Ω (rpm)	Torque T (μNm)
20.0	1000	0.03	28493
		0.04	33967
		0.04	40035
		0.05	45540
		0.06	50900
		0.06	56138
		0.07	61990
		0.07	67027
		0.08	72266
		0.09	78197
		0.09	84549
		0.10	90598
		0.10	94963
		0.11	97959
		0.11	99654
		0.11	100163
		0.11	99513
		0.11	97821
		0.11	95453
		0.10	92477
		0.10	88740
		0.09	84159

Sample 3:

It was a mixture of 60% bitumen and 40% gas oil. The bitumen and the gas oil were provided by SynCrude, Canada from the laboratory in Edmonton, AB. The viscous mixture was characterized in the Saskatchewan Research Council, Saskatoon, SK. The measured properties of this oil were as follows:

Density @ 20°C: 1000 kg/m^3
Dynamic viscosity @ 20°C: 320 Pa.s

A Haake RS150 Viscometer and a Haake RS6000 Rotational Rheometer were used for the measurements. The measured data were as follows:

Table A2.2. Viscometer data for Sample 3.

RS150				RS6000			
Temperature T (°C)	Density ρ (kg/m^3)	Spindle speed Ω (rpm)	Torque T (μNm)	Temperature T (°C)	Density ρ (kg/m^3)	Spindle speed Ω (rpm)	Torque T (μNm)
20.1	1000	0.12	13313	20.0	1000	1.00	114184
		0.14	14922			0.21	23921
		0.24	26479			0.46	53210
		0.37	40794			0.85	96998
		0.51	56591			0.09	10845
		0.65	71835			0.39	44576
		0.80	88420			0.84	95958
		0.96	105631			1.24	141162
		1.11	120867				
		1.25	135700				
		1.34	144503				
		1.34	144504				
		1.34	144500				
		1.29	139719				
		1.20	129492				
		1.07	115007				
		0.92	99762				
		0.78	83850				
		0.62	67455				
		0.47	50732				
		0.32	34055				
		0.17	17864				

Sample 4:

It was a mixture of 40% bitumen and 60% gas oil. The bitumen and the gas oil were provided by SynCrude, Canada from the laboratory in Edmonton, AB. The viscous mixture was characterized in the Saskatchewan Research Council, Saskatoon, SK. The measured properties of this oil were as follows:

Density @ 20°C: 1000 kg/m^3
Dynamic viscosity @ 20°C: 65 Pa.s

A Haake RS6000 Rotational Rheometer was used for the measurements. The measured data were as follows:

Table A2.3. Rheometer data for Sample 4.

Temperature T (°C)	Density ρ (kg/m^3)	Spindle speed Ω (rpm)	Torque T (μNm)
20.0	1000	0.99	22671
		1.99	45342
		2.98	67967
		3.97	90468
		4.97	112897
		5.97	135221
		6.96	157392
		7.96	179589
		7.04	158491
		5.08	114867
		2.98	67724
		2.01	45753
		1.00	22888

Sample 5:

It was the lube oil supplied by Shell Canada to the Saskatchewan Research Council Pipe Flow Technology Centre, Saskatoon, SK. Its commercial name was Shellflex 810. The measured properties of this oil were as follows (McKibben et al. 2007):

Table A2.4. Properties of Shellflex 810.

Temperature, T (°C)	Density, ρ (kg/m^3)	Temperature, T (°C)	Viscosity, μ (Pa.s)
15	895	20	2.10
		25	1.30
		35	0.75
		40	0.53

Sample 6:

The commercial name of this lube oil was Catenex S 779. It was supplied by Shell, Canada to the Saskatchewan Research Council Pipe Flow Technology Centre, Saskatoon, SK. The measured properties of this oil were as follows (McKibben and Gillies 2009):

Table A2.5. Properties of Catenex S 779.

Temperature, T (°C)	Viscosity, μ (Pa.s)	Density, ρ (kg/m^3)
20	2.042	890.9
25	1.369	-
30	0.947	885.3
35	0.660	-
40	0.475	879.5
45	0.348	-
50	0.262	874.4

Sample 7:

It was a crude oil. Husky Energy, Canada provided this oil from Forest Bank to the Saskatchewan Research Council Pipe Flow Technology Centre, Saskatoon, SK. The measured properties of this oil were as follows (McKibben et al. 2007):

Table A2.6. Properties of Forest Bank crude oil (Husky Energy).

Temperature, T (°C)	Density, ρ (kg/m^3)	Temperature, T (°C)	Viscosity, μ (Pa.s)
15	987	20	31.4
		50	1.86

The method of linear interpolation was used to calculate the viscosity at 25°C and 35°C as ~ 26.5 Pa.s and ~ 16.6 Pa.s, respectively.

Sample 8:

It was a crude oil. Canadian Natural Resources Ltd. (CNRL) provided this oil from their Lone Rock facilities to the Saskatchewan Research Council Pipe Flow Technology Centre, Saskatoon, SK. The measured properties of this oil were as follows (McKibben and Gillies 2009):

Table A2.7. Properties of Lone Rock crude oil (CNRL).

Temperature, T (°C)	Density, ρ (kg/m^3)	Temperature, T (°C)	Viscosity, μ (Pa.s)
-	961	20	3.66
		35	1.22
		50	0.49

The method of linear interpolation was used to know the viscosity at 25°C as ~ 2.85 Pa.s.

APPENDIX 3

IMPORTANT EXPERIMENTAL PROCEDURES

A. Coating Procedure:

a) If the sample oil is not mobile enough for taking in a disposable syringe at room temperature, heat the oil. The temperature of the heater should not be more than 100°C.

b) Determine the weight of oil required for the intended thickness (t_c) of coating layer:

- Volume, V (m^3) = $0.1 \times 0.025 \times t_c = 0.0025t_c$
- Weight, W_1 (g) = V (m^3) $\times \rho_o$ (kg/m^3) $\times 1000g/1kg = 2.5t_c\rho_o$

c) Weigh the 100mm test plate on a scale: W_2 (g).

d) Take the volume of oil (~ $2500t_c$ ml) required for the coating layer in a disposable syringe.

e) Place the test plate on a digital scale.

f) Slowly inject the oil on the test plate and carefully follow the increment of scale reading.

g) As the scale reading reaches W_1+W_2, stop injecting oil on the test plate.

h) Following procedure should be followed for creating an uniform coating thickness:

   i) If the oil is mobile enough for taking in a disposable syringe at room temperature, leave the test plate with sample oil in the RFC. The oil will spread itself uniformly on the test plate with in 2 – 3 hours.

   ii) If the oil is not mobile enough for taking in a disposable syringe at room temperature, press the oil with fingers to spread it as uniformly as possible on the test plate. Then, leave the coated plates in the RFC over night. The oil will uniformly spread itself.

   iii) Prior to touching the viscous oil with fingers, it is necessary to wear disposable hand gloves and wet the gloves with ordinary oil. The ordinary oil acts as a barrier between the glove and the sample oil.

Figure A3.1. Photograph of a coated plate with frozen wall-coating prior to the flow tests.

B. Preserving the roughness on wall-coating layer:

It was challenging to preserve the rough morphology developed on the wall-coating layer of heavy oil. The preservation was necessary for the topographic measurement. Steps followed for preserving the rough morphology on the viscous surface are pointed as follows:

(i) Stop the flow by shutting the pump off.
(ii) Drain off the water in the pipeloop.
(iii) Unscrew the Plexiglas window.
(iv) Carefully withdraw the test plates from the flow-cell.
(v) If required, use soft tissue papers to suck water droplets on the rough surface of wall-coating.
(vi) Place the test plates in a freezer. Refrigerate the test plates with rough wall-coating overnight.
(vii) Take the refrigerated test plates with rough coating of viscous oil to the contracer for topographic measurements.
(viii) Place enough dry ice all over the rough wall-coating; however, maintain a narrow passage clean of dry ice for the movement of the stylus.
(ix) Refill the dry ice regularly.

Figure A3.2. Photograph of a frozen wall-coating layer after the flow tests.

APPENDIX 4
DESCRIPTION OF MITUTOYO CONTRACER

Apparatus:

The model of the MITUTOYO contracer used for measuring the surface roughness is CV-3100H4. It is a powerful system for automatic measurement with high precision. Significant features of the instrument are pointed as follows:

i) The contracer has a motorized Z axis.

ii) Measured values in X and Z axis can be recorded digitally.

iii) There is an USB interface for rapid data transmission to the connected computer.

iv) The operation of the contracer can be controlled and programed with the software, FORMPAK.

v) Measuring range in X axis is 100 mm and that in Z axis is 50 mm

vi) Resolution in X axis is 0.05 µm and that in Z axis is 0.2 µm.

vii) Measurement accuracy in X axis is ±(1+0.01L) µm and that in Z axis is ±(2+|4H|/100) µm.

Figure A4.1. Photograph showing basic parts of the MITUTOYO Contracer.

Steps for programming in FORMPAK:

- (i) Position the test piece. [Stylus should be in up position ALWAYS]
- (ii) Create a folder
- (iii) New program (for HOME POSITION)
  - a) Register the position by clicking the icon 'move' on right hand side.
    - i) Label name (e.g., HOME POSITION)
    - ii) Click on 'Read Position'
    - iii) State of stylus:
      - Move after raising
    - iv) Check 'Register in part program'
    - v) Check 'Absolute'
    - vi) Start 'Movement'
    - vii) Save in the folder
- (iv) New program (for MAIN PROGRAM: x-macro/x-unit program)
  - a) Register the position by clicking the icon 'move' on right hand side.
    - i) Label Name (e.g., MAIN POSITION)
    - ii) State of stylus:
      - Move after raising
    - iii) Check 'Register in part program'
    - iv) Check 'Absolute'
    - v) Start 'Movement'
  - b) Settings: 'Set measuring conditions'
    - i) Meas. length: (e.g., 5mm)
    - ii) Meas. pitch: (e.g., 3)
    - iii) Auto return:
      - Return to meas. start position
      - Stylus status: Return with stylus raising
    - iv) Click 'OK'
  - c) Settings: 'Set run condition of the part program''
    - i) Click 'Output results'
    - ii) Check 'Output measured point data (Text)'
    - iii) File name setting
      - Assign name automatically: Folder name: (e.g., Browse)
    - iv) Click 'OK'

d) Click ‘Measure’

e) Save in folder (e.g., as Main)

(v) New program (for CREATING N-PARTS: loop)

a) File: New of N-Parts

b) Part program:

  i) Register loop start:

    - Label name: (e.g., Loop)
    - Number of ___(e.g., 3)
    - Step & Repeat
    - Step: Y-axis step:___ (e.g., 2mm)

c) Part program:

  i) Register part program:

    - Browse: (e.g., Main)

d) Part program:

  i) Register loop end

e) Part program

  i) Register part program:

    - Browse: (e.g., Home)

f) File: Save part program for N-parts (e.g., Test_Loop)

g) Part program:

  i) Mode change: N-parts part program Run Mode

h) Run N-P (data will be saved in folder)

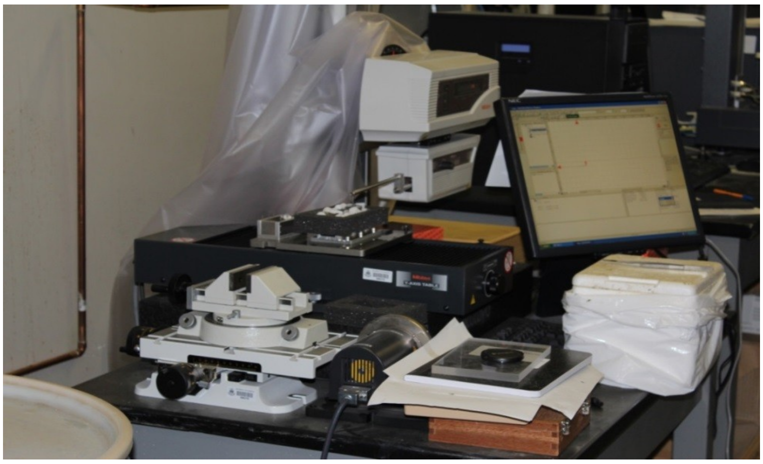

(a)

(b)

Figure A4.2. Photographs showing the roughness measurement with MITUTOYO Contracer: (a) Complete setup of Contracer in operation; (b) The stylus moving over the oil surface frozen with dry ice.

Steps for the measurements:

1) Turn on the FORMPAK module.
2) Set the test plate in the designated holder.
3) If required, surround the test plate with enough dry ice.
4) Click on the 'Run N-P' button in the FORMPAK module.
5) Allow uninterrupted functioning of the contracer for around 45 minutes.
6) Take off the test plate from the holder.

Steps for data analysis:

The raw data are recorded in CSV format. Each file contains the absolute values of (X, Z) for a specific Y. Considering Y = 0 (mm) for the edge of a test plate, typically Y = 6:1:20 (mm). The resolution on X-axis is 0.1mm. As a result, X = 0 : 0.1 : X_{max} (mm); typical value of X_{max} is 60mm. The values of Z, i.e., the roughness are measured for every X. Following steps are followed for analyzing the data.

1) Extract the CSV data files corresponding to 10 values of Y in a spreadsheet. The values of (X, Z) should be arranged for every Y.
2) Subtract the initial absolute value of X for every Y from all values of X. The subtraction should provide the relative values of X (e.g., X = 0:0.1:60 mm).
3) Plot the absolute values of Z as the function of relative values of X and draw a linear trendline.

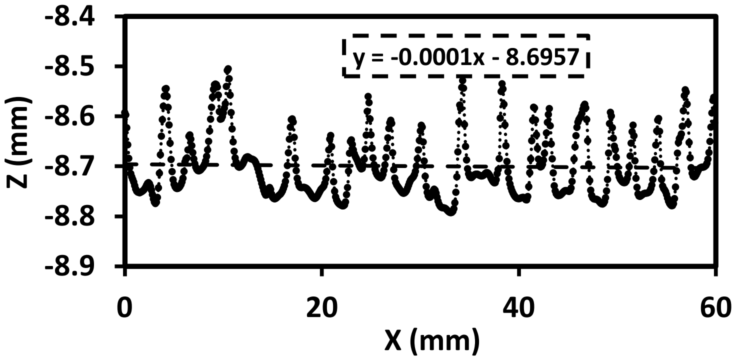

Figure A4.3. Graph showing the measured roughness with the corresponding trendline.

4) Subtract the absolute values of Z from the corresponding values of the trendline to obtain the relative values of Z.
5) Plot the relative values of Z with respect to the corresponding relative values of X.

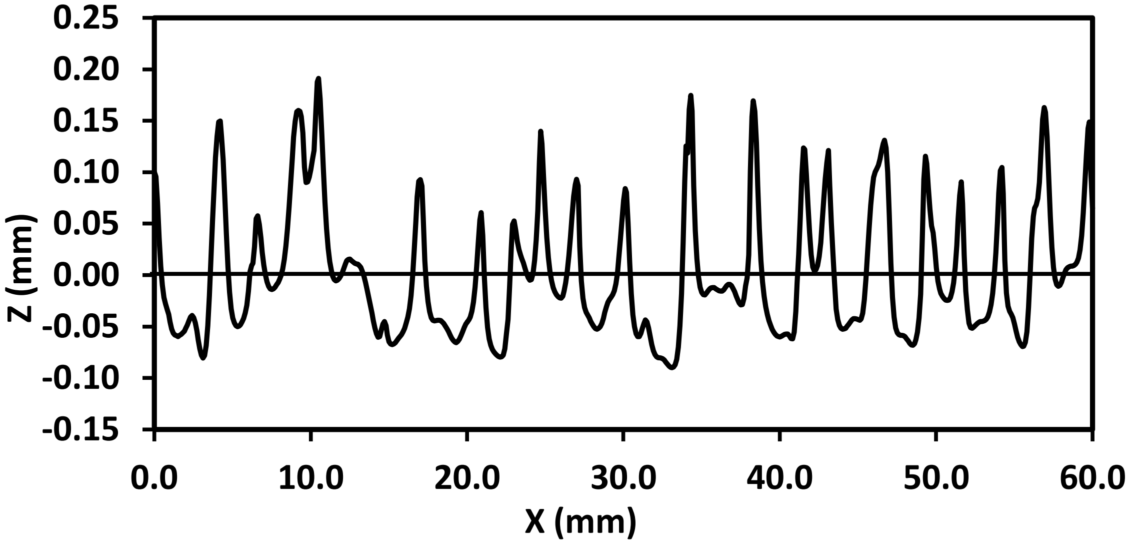

Figure A4.4. Graph showing the relative values of roughness.

6) Use the relative values of Z for calculating the statistical parameters, like R_a, R_{rms} and R_{sk}.

Table A4.1. An example of the data sets from MITUTOYO Contracer

Absolute Values		Relative Values	
X (mm)	Z (mm)	X (mm)	Z (mm)
20.4381	-8.5926	0.0	0.1003
20.5383	-8.5972	0.1	0.09573
20.639	-8.623	0.2	0.06996
20.7398	-8.657	0.3	0.035991
20.8429	-8.6842	0.4	0.008821
20.9452	-8.7027	0.5	-0.00965
21.047	-8.7147	0.6	-0.02162
21.1481	-8.7211	0.7	-0.02799
21.2483	-8.7263	0.8	-0.03316
21.3482	-8.7315	0.9	-0.03833
21.4481	-8.7387	1.0	-0.0455
21.5486	-8.7455	1.1	-0.05227
21.6495	-8.7497	1.2	-0.05644
21.75	-8.7516	1.3	-0.05831
21.8502	-8.7522	1.4	-0.05888
21.9502	-8.753	1.5	-0.05965
22.0506	-8.7519	1.6	-0.05852
22.1505	-8.7509	1.7	-0.05749
22.2506	-8.7495	1.8	-0.05606
22.3506	-8.7479	1.9	-0.05443
22.4508	-8.7453	2.0	-0.0518
22.5509	-8.7421	2.1	-0.04857
22.6509	-8.7379	2.2	-0.04434
22.7505	-8.7343	2.3	-0.04071
22.8497	-8.7327	2.4	-0.03908
22.9488	-8.7349	2.5	-0.04125
23.0483	-8.7401	2.6	-0.04642
23.148	-8.7478	2.7	-0.05409
23.2482	-8.7566	2.8	-0.06286
23.3487	-8.7653	2.9	-0.07153
23.4496	-8.7717	3.0	-0.0779
23.5508	-8.7745	3.1	-0.08067
23.6523	-8.7719	3.2	-0.07804
23.754	-8.7623	3.3	-0.06841
23.8558	-8.7431	3.4	-0.04917
23.9571	-8.7139	3.5	-0.01994
24.0571	-8.6769	3.6	0.017086
24.1556	-8.6398	3.7	0.054215
24.2535	-8.6068	3.8	0.087245
24.3512	-8.5798	3.9	0.114274
24.4491	-8.5594	4.0	0.134703
24.5465	-8.5454	4.1	0.148733
24.6426	-8.5445	4.2	0.149661
24.7396	-8.56	4.3	0.13419
24.8387	-8.5822	4.4	0.11202
24.9376	-8.6173	4.5	0.07695
25.0393	-8.6538	4.6	0.04048
25.1415	-8.6864	4.7	0.007911
25.2442	-8.7107	4.8	-0.01636
25.3465	-8.7269	4.9	-0.03253
25.4482	-8.7361	5.0	-0.0417
25.5491	-8.7409	5.1	-0.04647
25.6496	-8.7437	5.2	-0.04924
25.75	-8.7445	5.3	-0.05001
25.8502	-8.7441	5.4	-0.04958
25.9505	-8.7427	5.5	-0.04815
26.0507	-8.7401	5.6	-0.04552
26.1509	-8.7365	5.7	-0.04189
26.2512	-8.7313	5.8	-0.03666
26.3518	-8.724	5.9	-0.02933
26.4531	-8.7102	6.0	-0.0155
26.5523	-8.6912	6.1	0.003534
26.6489	-8.6855	6.2	0.009263
26.7498	-8.6833	6.3	0.011494
26.8531	-8.6671	6.4	0.027724
26.9522	-8.64	6.5	0.054854
27.0457	-8.6373	6.6	0.057582
27.1442	-8.6457	6.7	0.049212
27.2441	-8.6587	6.8	0.036242
27.3446	-8.6727	6.9	0.022272
27.4455	-8.6852	7.0	0.009802
27.5465	-8.6948	7.1	0.000233
27.6474	-8.7017	7.2	-0.00664
27.7481	-8.7061	7.3	-0.01101
27.8486	-8.7085	7.4	-0.01338
27.949	-8.7091	7.5	-0.01395
28.0492	-8.7085	7.6	-0.01332
28.1494	-8.7071	7.7	-0.01189
28.2495	-8.7047	7.8	-0.00946
28.3494	-8.7025	7.9	-0.00723
28.4496	-8.6995	8.0	-0.0042
28.5498	-8.6955	8.1	-0.00017

Continued (Table A4.1)

Absolute Values		Relative Values			Absolute Values		Relative Values	
X (mm)	Z (mm)	X (mm)	Z (mm)		X (mm)	Z (mm)	X (mm)	Z (mm)
28.6502	-8.6894	8.2	0.005964		32.7487	-8.6825	12.3	0.014093
28.7509	-8.6802	8.3	0.015194		32.8482	-8.6813	12.4	0.015323
28.8514	-8.6672	8.4	0.028224		32.948	-8.6811	12.5	0.015553
28.9519	-8.6501	8.5	0.045354		33.0477	-8.6825	12.6	0.014183
29.0521	-8.6293	8.6	0.066184		33.1478	-8.6839	12.7	0.012813
29.1519	-8.6058	8.7	0.089714		33.248	-8.6851	12.8	0.011643
29.2509	-8.5821	8.8	0.113444		33.3481	-8.6857	12.9	0.011073
29.3493	-8.5615	8.9	0.134073		33.448	-8.6863	13.0	0.010503
29.4474	-8.5461	9.0	0.149503		33.5479	-8.6875	13.1	0.009333
29.5454	-8.5369	9.1	0.158732		33.6476	-8.6895	13.2	0.007363
29.6438	-8.5355	9.2	0.160162		33.7473	-8.6933	13.3	0.003593
29.7433	-8.5367	9.3	0.158992		33.8472	-8.698	13.4	-0.00108
29.8418	-8.5416	9.4	0.154121		33.947	-8.7044	13.5	-0.00745
29.9388	-8.5576	9.5	0.13815		34.0471	-8.7116	13.6	-0.01462
30.0385	-8.5907	9.6	0.10508		34.1473	-8.7192	13.7	-0.02219
30.1445	-8.6059	9.7	0.089912		34.2476	-8.7266	13.8	-0.02956
30.2471	-8.6051	9.8	0.090743		34.3478	-8.7342	13.9	-0.03713
30.3473	-8.6007	9.9	0.095173		34.4481	-8.7414	14.0	-0.0443
30.4478	-8.5932	10.0	0.102703		34.5484	-8.7484	14.1	-0.05127
30.5477	-8.5836	10.1	0.112333		34.649	-8.754	14.2	-0.05684
30.6492	-8.5748	10.2	0.121163		34.7498	-8.7577	14.3	-0.06051
30.7529	-8.5403	10.3	0.155694		34.8511	-8.7571	14.4	-0.05988
30.8489	-8.5082	10.4	0.187823		34.9519	-8.7508	14.5	-0.05355
30.9408	-8.505	10.5	0.191051		35.0511	-8.7448	14.6	-0.04752
31.0368	-8.5249	10.6	0.17118		35.1498	-8.7425	14.7	-0.04519
31.1363	-8.5575	10.7	0.138609		35.2483	-8.7464	14.8	-0.04906
31.2375	-8.5927	10.8	0.10344		35.348	-8.7556	14.9	-0.05823
31.3395	-8.6253	10.9	0.07087		35.4493	-8.762	15.0	-0.0646
31.4419	-8.6511	11.0	0.045101		35.5502	-8.7643	15.1	-0.06687
31.544	-8.67	11.1	0.026232		35.6505	-8.7651	15.2	-0.06764
31.6456	-8.6832	11.2	0.013062		35.7508	-8.7645	15.3	-0.06701
31.7468	-8.6916	11.3	0.004693		35.8509	-8.7631	15.4	-0.06558
31.8475	-8.6973	11.4	-0.00098		35.9509	-8.7611	15.5	-0.06355
31.9481	-8.7007	11.5	-0.00435		36.0508	-8.7589	15.6	-0.06132
32.0487	-8.7019	11.6	-0.00552		36.1507	-8.7571	15.7	-0.05949
32.149	-8.7013	11.7	-0.00489		36.2507	-8.7555	15.8	-0.05786
32.2491	-8.6999	11.8	-0.00346		36.3509	-8.7527	15.9	-0.05503
32.3493	-8.6973	11.9	-0.00083		36.451	-8.7492	16.0	-0.0515
32.4494	-8.6943	12.0	0.002203		36.5512	-8.7442	16.1	-0.04647
32.5495	-8.6899	12.1	0.006633		36.6514	-8.7386	16.2	-0.04084
32.6492	-8.6857	12.2	0.010863		36.752	-8.7303	16.3	-0.03251

Continued (Table A4.1)

Absolute Values		Relative Values			Absolute Values		Relative Values	
X (mm)	Z (mm)	X (mm)	Z (mm)		X (mm)	Z (mm)	X (mm)	Z (mm)
36.8529	-8.7176	16.4	-0.01978		40.9531	-8.7107	20.5	-0.01165
36.954	-8.6985	16.5	-0.00065		41.0537	-8.6907	20.6	0.008385
37.0544	-8.673	16.6	0.024885		41.1534	-8.6672	20.7	0.031915
37.1535	-8.6458	16.7	0.052115		41.2512	-8.6457	20.8	0.053444
37.2515	-8.6219	16.8	0.076044		41.3455	-8.6384	20.9	0.060772
37.3483	-8.6067	16.9	0.091273		41.4393	-8.6607	21.0	0.0385
37.445	-8.6052	17.0	0.092802		41.5395	-8.7011	21.1	-0.00187
37.542	-8.6115	17.1	0.086531		41.6438	-8.7308	21.2	-0.03154
37.6379	-8.6421	17.2	0.05596		41.7464	-8.75	21.3	-0.05071
37.7395	-8.6839	17.3	0.01419		41.8483	-8.7612	21.4	-0.06188
37.8445	-8.7087	17.4	-0.01058		41.9493	-8.7676	21.5	-0.06825
37.9463	-8.7241	17.5	-0.02595		42.0498	-8.7716	21.6	-0.07222
38.0477	-8.7336	17.6	-0.03542		42.1502	-8.7742	21.7	-0.07479
38.1487	-8.7396	17.7	-0.04139		42.2504	-8.776	21.8	-0.07656
38.2495	-8.7421	17.8	-0.04386		42.3505	-8.7772	21.9	-0.07773
38.3498	-8.7427	17.9	-0.04443		42.4505	-8.7784	22.0	-0.0789
38.4499	-8.7425	18.0	-0.0442		42.5507	-8.7792	22.1	-0.07967
38.5498	-8.7423	18.1	-0.04397		42.651	-8.779	22.2	-0.07944
38.6498	-8.7421	18.2	-0.04374		42.7516	-8.7774	22.3	-0.07781
38.7496	-8.7427	18.3	-0.04431		42.853	-8.7713	22.4	-0.07168
38.8495	-8.7437	18.4	-0.04528		42.9541	-8.7567	22.5	-0.05705
38.9494	-8.7454	18.5	-0.04695		43.0547	-8.7425	22.6	-0.04282
39.0493	-8.7478	18.6	-0.04932		43.1574	-8.7099	22.7	-0.01018
39.1493	-8.7506	18.7	-0.05209		43.2557	-8.6739	22.8	0.025845
39.2494	-8.7534	18.8	-0.05486		43.351	-8.6505	22.9	0.049274
39.3494	-8.7568	18.9	-0.05823		43.446	-8.6472	23.0	0.052602
39.4496	-8.7598	19.0	-0.0612		43.5443	-8.6563	23.1	0.043532
39.5499	-8.7622	19.1	-0.06357		43.6451	-8.6671	23.2	0.032762
39.6501	-8.7638	19.2	-0.06514		43.7462	-8.675	23.3	0.024892
39.7505	-8.7644	19.3	-0.06571		43.8468	-8.6802	23.4	0.019723
39.8509	-8.7632	19.4	-0.06448		43.9471	-8.6842	23.5	0.015753
39.951	-8.761	19.5	-0.06225		44.0471	-8.6882	23.6	0.011783
40.0512	-8.7576	19.6	-0.05882		44.147	-8.6934	23.7	0.006613
40.1511	-8.7538	19.7	-0.05499		44.2473	-8.6984	23.8	0.001643
40.2509	-8.75	19.8	-0.05116		44.3477	-8.7026	23.9	-0.00253
40.3507	-8.7464	19.9	-0.04753		44.4484	-8.7052	24.0	-0.0051
40.4503	-8.7442	20.0	-0.0453		44.5494	-8.7044	24.1	-0.00427
40.5503	-8.7422	20.1	-0.04327		44.6507	-8.6985	24.2	0.001664
40.6506	-8.7396	20.2	-0.04064		44.752	-8.6859	24.3	0.014294
40.7513	-8.734	20.3	-0.03501		44.8533	-8.666	24.4	0.034225
40.8521	-8.7251	20.4	-0.02608		44.9551	-8.6376	24.5	0.062655

Continued (Table A4.1)								
Absolute Values		Relative Values			Absolute Values		Relative Values	
X (mm)	Z (mm)	X (mm)	Z (mm)		X (mm)	Z (mm)	X (mm)	Z (mm)
45.0557	-8.5902	24.6	0.110085		49.1511	-8.7434	28.7	-0.04189
45.1481	-8.5604	24.7	0.139913		49.2509	-8.738	28.8	-0.03646
45.2383	-8.5727	24.8	0.12764		49.3507	-8.7326	28.9	-0.03103
45.3374	-8.6054	24.9	0.09497		49.4502	-8.728	29.0	-0.0264
45.4397	-8.637	25.0	0.0634		49.5497	-8.7252	29.1	-0.02357
45.5419	-8.6636	25.1	0.036831		49.6496	-8.7232	29.2	-0.02154
45.644	-8.6833	25.2	0.017162		49.7498	-8.7208	29.3	-0.01911
45.7457	-8.6969	25.3	0.003592		49.8502	-8.7168	29.4	-0.01508
45.8468	-8.7061	25.4	-0.00558		49.9508	-8.7101	29.5	-0.00835
45.9476	-8.7126	25.5	-0.01205		50.0515	-8.6996	29.6	0.002184
46.0481	-8.7168	25.6	-0.01622		50.152	-8.6849	29.7	0.016914
46.1485	-8.7196	25.7	-0.01899		50.2521	-8.6672	29.8	0.034644
46.2487	-8.7214	25.8	-0.02076		50.3517	-8.6483	29.9	0.053574
46.3489	-8.7226	25.9	-0.02193		50.4505	-8.6292	30.0	0.072704
46.4493	-8.723	26.0	-0.0223		50.5474	-8.618	30.1	0.083933
46.5499	-8.7212	26.1	-0.02047		50.6424	-8.6217	30.2	0.080261
46.6506	-8.7164	26.2	-0.01564		50.7383	-8.6514	30.3	0.05059
46.7511	-8.7081	26.3	-0.00731		50.8397	-8.6895	30.4	0.01252
46.8515	-8.6972	26.4	0.003624		50.943	-8.72	30.5	-0.01795
46.9521	-8.6823	26.5	0.018554		51.0458	-8.7405	30.6	-0.03842
47.0523	-8.6637	26.6	0.037184		51.1478	-8.7523	30.7	-0.05019
47.1519	-8.6431	26.7	0.057814		51.249	-8.7592	30.8	-0.05706
47.2503	-8.6243	26.8	0.076644		51.3499	-8.762	30.9	-0.05983
47.348	-8.6131	26.9	0.087873		51.4506	-8.7618	31.0	-0.0596
47.4458	-8.608	27.0	0.093002		51.5512	-8.7588	31.1	-0.05657
47.5396	-8.6142	27.1	0.08683		51.6513	-8.7537	31.2	-0.05144
47.635	-8.6731	27.2	0.027959		51.7509	-8.7488	31.3	-0.04651
47.7436	-8.7067	27.3	-0.00561		51.85	-8.7458	31.4	-0.04348
47.8463	-8.7236	27.4	-0.02248		51.9488	-8.7478	31.5	-0.04545
47.9479	-8.7326	27.5	-0.03145		52.0481	-8.7537	31.6	-0.05132
48.0487	-8.7372	27.6	-0.03602		52.1481	-8.7619	31.7	-0.05949
48.149	-8.7402	27.7	-0.03899		52.2486	-8.7699	31.8	-0.06746
48.249	-8.743	27.8	-0.04176		52.3494	-8.7759	31.9	-0.07343
48.349	-8.746	27.9	-0.04473		52.45	-8.7796	32.0	-0.0771
48.4492	-8.7488	28.0	-0.0475		52.5504	-8.7818	32.1	-0.07927
48.5493	-8.7514	28.1	-0.05007		52.6507	-8.7828	32.2	-0.08024
48.6496	-8.7534	28.2	-0.05204		52.7508	-8.783	32.3	-0.08041
48.75	-8.754	28.3	-0.05261		52.8507	-8.7832	32.4	-0.08058
48.8503	-8.7532	28.4	-0.05178		52.9506	-8.7838	32.5	-0.08115
48.9505	-8.7514	28.5	-0.04995		53.0504	-8.7852	32.6	-0.08252
49.0508	-8.7484	28.6	-0.04692		53.1504	-8.7872	32.7	-0.08449

Continued (Table A4.1)								
Absolute Values		Relative Values			Absolute Values		Relative Values	
X (mm)	Z (mm)	X (mm)	Z (mm)		X (mm)	Z (mm)	X (mm)	Z (mm)
53.2505	-8.7894	32.8	-0.08666		57.3482	-8.7142	36.9	-0.01023
53.3507	-8.7912	32.9	-0.08843		57.4481	-8.717	37.0	-0.013
53.4509	-8.7924	33.0	-0.0896		57.548	-8.7202	37.1	-0.01617
53.5511	-8.7928	33.1	-0.08997		57.648	-8.7246	37.2	-0.02054
53.6514	-8.7922	33.2	-0.08934		57.7484	-8.7282	37.3	-0.02411
53.7519	-8.79	33.3	-0.08711		57.8486	-8.7312	37.4	-0.02708
53.8528	-8.7849	33.4	-0.08198		57.9491	-8.733	37.5	-0.02885
53.9544	-8.7729	33.5	-0.06995		58.0499	-8.7328	37.6	-0.02862
54.056	-8.752	33.6	-0.04901		58.1513	-8.7269	37.7	-0.02269
54.158	-8.7211	33.7	-0.01808		58.2517	-8.7148	37.8	-0.01056
54.2599	-8.6712	33.8	0.031847		58.3514	-8.7066	37.9	-0.00233
54.3579	-8.6121	33.9	0.090976		58.4577	-8.6846	38.0	0.019706
54.4496	-8.5775	34.0	0.125603		58.5616	-8.6036	38.1	0.100737
54.5456	-8.5844	34.1	0.118732		58.6536	-8.5505	38.2	0.153865
54.6532	-8.5422	34.2	0.160965		58.7439	-8.535	38.3	0.169392
54.7436	-8.5286	34.3	0.174592		58.8384	-8.5454	38.4	0.15902
54.8344	-8.5439	34.4	0.159319		58.9359	-8.576	38.5	0.128449
54.9315	-8.6165	34.5	0.086748		59.0362	-8.6172	38.6	0.087279
55.0402	-8.6603	34.6	0.042981		59.1385	-8.6588	38.7	0.04571
55.1429	-8.6874	34.7	0.015911		59.2419	-8.6904	38.8	0.014141
55.2453	-8.705	34.8	-0.00166		59.3447	-8.7111	38.9	-0.00653
55.347	-8.7151	34.9	-0.01173		59.4462	-8.725	39.0	-0.0204
55.4481	-8.7203	35.0	-0.0169		59.5472	-8.7353	39.1	-0.03067
55.5488	-8.7224	35.1	-0.01897		59.6479	-8.743	39.2	-0.03834
55.6492	-8.7226	35.2	-0.01914		59.7485	-8.7488	39.3	-0.04411
55.7495	-8.7208	35.3	-0.01731		59.8489	-8.7534	39.4	-0.04868
55.8494	-8.7186	35.4	-0.01508		59.9491	-8.7572	39.5	-0.05245
55.9492	-8.717	35.5	-0.01345		60.0494	-8.7602	39.6	-0.05542
56.049	-8.716	35.6	-0.01242		60.1497	-8.7624	39.7	-0.05759
56.1488	-8.7158	35.7	-0.01219		60.2499	-8.764	39.8	-0.05916
56.2487	-8.7158	35.8	-0.01216		60.3501	-8.7646	39.9	-0.05973
56.3485	-8.717	35.9	-0.01333		60.4502	-8.7648	40.0	-0.0599
56.4487	-8.718	36.0	-0.0143		60.5504	-8.7644	40.1	-0.05947
56.5487	-8.7188	36.1	-0.01507		60.6504	-8.7634	40.2	-0.05844
56.6489	-8.7194	36.2	-0.01564		60.7503	-8.7626	40.3	-0.05761
56.7491	-8.7192	36.3	-0.01541		60.8502	-8.7622	40.4	-0.05718
56.8492	-8.7182	36.4	-0.01438		60.9499	-8.7624	40.5	-0.05735
56.9494	-8.7164	36.5	-0.01255		61.0496	-8.7642	40.6	-0.05912
57.0493	-8.7142	36.6	-0.01032		61.1498	-8.7668	40.7	-0.06169
57.1489	-8.7128	36.7	-0.00889		61.2508	-8.7672	40.8	-0.06206
57.2486	-8.7128	36.8	-0.00886		61.3531	-8.7605	40.9	-0.05533

Continued (Table A4.1)								
Absolute Values		Relative Values			Absolute Values		Relative Values	
X (mm)	Z (mm)	X (mm)	Z (mm)		X (mm)	Z (mm)	X (mm)	Z (mm)
61.3531	-8.7605	40.9	-0.05533		65.4495	-8.7497	45.0	-0.0433
61.4554	-8.7407	41.0	-0.03549		65.5497	-8.7503	45.1	-0.04387
61.5557	-8.713	41.1	-0.00776		65.6504	-8.7491	45.2	-0.04264
61.6552	-8.6853	41.2	0.019965		65.7517	-8.7436	45.3	-0.03711
61.7561	-8.6489	41.3	0.056395		65.8532	-8.7304	45.4	-0.02388
61.8546	-8.6078	41.4	0.097525		65.9541	-8.7105	45.5	-0.00395
61.9488	-8.5819	41.5	0.123453		66.0541	-8.6857	45.6	0.020885
62.0415	-8.5834	41.6	0.121981		66.153	-8.6612	45.7	0.045414
62.1385	-8.6076	41.7	0.09781		66.2515	-8.6388	45.8	0.067844
62.2396	-8.6371	41.8	0.06834		66.3495	-8.6221	45.9	0.084573
62.3414	-8.6641	41.9	0.041371		66.4476	-8.6118	46.0	0.094903
62.4437	-8.6857	42.0	0.019802		66.5465	-8.6065	46.1	0.100233
62.5464	-8.6976	42.1	0.007932		66.6462	-8.6033	46.2	0.103462
62.6481	-8.7014	42.2	0.004163		66.7464	-8.6001	46.3	0.106692
62.7491	-8.7002	42.3	0.005393		66.847	-8.5942	46.4	0.112623
62.8497	-8.6962	42.4	0.009423		66.947	-8.5862	46.5	0.120653
62.9506	-8.6877	42.5	0.017954		67.0462	-8.5791	46.6	0.127782
63.0515	-8.6741	42.6	0.031584		67.1444	-8.5759	46.7	0.131012
63.1521	-8.6555	42.7	0.050214		67.2412	-8.5832	46.8	0.123741
63.2519	-8.6334	42.8	0.072344		67.3377	-8.6066	46.9	0.10037
63.3506	-8.6122	42.9	0.093574		67.4362	-8.6489	47.0	0.058099
63.4487	-8.5964	43.0	0.109403		67.5386	-8.6956	47.1	0.01143
63.5439	-8.5846	43.1	0.121232		67.6431	-8.7286	47.2	-0.02154
63.636	-8.619	43.2	0.086859		67.7463	-8.7479	47.3	-0.04081
63.7392	-8.6552	43.3	0.05069		67.8482	-8.7583	47.4	-0.05118
63.8412	-8.6851	43.4	0.020821		67.9493	-8.7631	47.5	-0.05595
63.9423	-8.7132	43.5	-0.00725		68.0499	-8.7651	47.6	-0.05792
64.0446	-8.739	43.6	-0.03302		68.1501	-8.7657	47.7	-0.05849
64.1483	-8.7492	43.7	-0.04319		68.2502	-8.7657	47.8	-0.05846
64.2489	-8.755	43.8	-0.04896		68.35	-8.7661	47.9	-0.05883
64.3496	-8.7577	43.9	-0.05163		68.4498	-8.7671	48.0	-0.0598
64.4499	-8.7587	44.0	-0.0526		68.5497	-8.7691	48.1	-0.06177
64.5502	-8.7583	44.1	-0.05217		68.6497	-8.7713	48.2	-0.06394
64.6502	-8.7577	44.2	-0.05154		68.7499	-8.7737	48.3	-0.06631
64.7504	-8.7561	44.3	-0.04991		68.8502	-8.7751	48.4	-0.06768
64.8504	-8.7541	44.4	-0.04788		68.9505	-8.7755	48.5	-0.06805
64.9503	-8.7519	44.5	-0.04565		69.051	-8.7741	48.6	-0.06662
65.0502	-8.7499	44.6	-0.04362		69.1516	-8.7705	48.7	-0.06299
65.1499	-8.7487	44.7	-0.04239		69.2526	-8.763	48.8	-0.05546
65.2496	-8.7485	44.8	-0.04216		69.354	-8.7494	48.9	-0.04183
65.3495	-8.7489	44.9	-0.04253		69.457	-8.7264	49.0	-0.01879

Continued (Table A4.1)								
Absolute Values		Relative Values			Absolute Values		Relative Values	
X (mm)	Z (mm)	X (mm)	Z (mm)		X (mm)	Z (mm)	X (mm)	Z (mm)
69.5603	-8.6736	49.1	0.034037		73.6501	-8.7518	53.2	-0.04294
69.6572	-8.6146	49.2	0.093066		73.7505	-8.7492	53.3	-0.04031
69.7472	-8.5921	49.3	0.115593		73.8509	-8.7448	53.4	-0.03588
69.8408	-8.5995	49.4	0.108221		73.9515	-8.7377	53.5	-0.02875
69.94	-8.6228	49.5	0.084951		74.0523	-8.7266	53.6	-0.01762
70.0421	-8.6437	49.6	0.064081		74.1533	-8.7099	53.7	-0.00089
70.1441	-8.6598	49.7	0.048012		74.2541	-8.6872	53.8	0.021845
70.2452	-8.6667	49.8	0.041142		74.3543	-8.6575	53.9	0.051575
70.3433	-8.682	49.9	0.025872		74.4526	-8.6294	54.0	0.079704
70.444	-8.7006	50.0	0.007302		74.5493	-8.6077	54.1	0.101433
70.5461	-8.7138	50.1	-0.00587		74.6429	-8.6045	54.2	0.104661
70.6475	-8.7213	50.2	-0.01334		74.736	-8.6302	54.3	0.078989
70.7481	-8.7257	50.3	-0.01771		74.8355	-8.695	54.4	0.014219
70.8485	-8.7285	50.4	-0.02048		74.9448	-8.7265	54.5	-0.01725
70.9486	-8.7309	50.5	-0.02285		75.0474	-8.7395	54.6	-0.03022
71.0489	-8.7324	50.6	-0.02432		75.1488	-8.7446	54.7	-0.03529
71.1492	-8.7328	50.7	-0.02469		75.2489	-8.7472	54.8	-0.03786
71.2495	-8.7324	50.8	-0.02426		75.3485	-8.7508	54.9	-0.04143
71.35	-8.7299	50.9	-0.02173		75.4482	-8.7566	55.0	-0.0472
71.4507	-8.7245	51.0	-0.0163		75.5483	-8.7636	55.1	-0.05417
71.5515	-8.7156	51.1	-0.00737		75.6489	-8.7698	55.2	-0.06034
71.6526	-8.7008	51.2	0.007464		75.7495	-8.7742	55.3	-0.06471
71.7534	-8.6793	51.3	0.028995		75.8499	-8.777	55.4	-0.06748
71.8531	-8.6538	51.4	0.054524		75.9502	-8.7788	55.5	-0.06925
71.9511	-8.6309	51.5	0.077454		76.0509	-8.7786	55.6	-0.06902
72.0458	-8.6178	51.6	0.090582		76.152	-8.7748	55.7	-0.06519
72.1376	-8.6391	51.7	0.06931		76.2538	-8.7647	55.8	-0.05506
72.237	-8.689	51.8	0.01944		76.3562	-8.7415	55.9	-0.03182
72.3429	-8.724	51.9	-0.01553		76.4568	-8.7092	56.0	0.000506
72.4461	-8.7421	52.0	-0.0336		76.5551	-8.6738	56.1	0.035935
72.5475	-8.7553	52.1	-0.04677		76.6506	-8.6527	56.2	0.057064
72.6496	-8.7596	52.2	-0.05104		76.7477	-8.6446	56.3	0.065193
72.7501	-8.7602	52.3	-0.05161		76.8473	-8.6416	56.4	0.068223
72.8503	-8.759	52.4	-0.05038		76.9487	-8.6355	56.5	0.074353
72.9503	-8.7574	52.5	-0.04875		77.0513	-8.6199	56.6	0.089984
73.0502	-8.756	52.6	-0.04732		77.1529	-8.589	56.7	0.120914
73.1501	-8.7546	52.7	-0.04589		77.2502	-8.5587	56.8	0.151244
73.2499	-8.754	52.8	-0.04526		77.3447	-8.547	56.9	0.162972
73.3498	-8.7538	52.9	-0.04503		77.4404	-8.5518	57.0	0.158201
73.4498	-8.7536	53.0	-0.0448		77.5369	-8.5756	57.1	0.13443
73.55	-8.753	53.1	-0.04417		77.6364	-8.6144	57.2	0.095659

Continued (Table A4.1)			
Absolute Values		Relative Values	
X (mm)	Z (mm)	X (mm)	Z (mm)
77.7388	-8.6525	57.3	0.05759
77.8417	-8.6829	57.4	0.027221
77.9446	-8.7028	57.5	0.007352
78.0467	-8.714	57.6	-0.00382
78.148	-8.7196	57.7	-0.00939
78.2488	-8.7212	57.8	-0.01096
78.3494	-8.7202	57.9	-0.00993
78.4497	-8.717	58.0	-0.0067
78.5497	-8.713	58.1	-0.00267
78.6495	-8.7088	58.2	0.001563
78.7491	-8.7052	58.3	0.005193
78.8487	-8.7033	58.4	0.007123
78.9485	-8.7023	58.5	0.008153
79.0484	-8.7017	58.6	0.008783
79.1483	-8.7019	58.7	0.008613
79.2485	-8.7013	58.8	0.009243
79.3487	-8.6999	58.9	0.010673
79.4488	-8.6981	59.0	0.012503
79.5495	-8.694	59.1	0.016633
79.6504	-8.6859	59.2	0.024764
79.7517	-8.6725	59.3	0.038194
79.853	-8.6503	59.4	0.060424
79.9532	-8.6216	59.5	0.089155
80.0519	-8.5934	59.6	0.117384
80.1491	-8.5682	59.7	0.142613
80.2402	-8.5621	59.8	0.148741
80.3337	-8.6129	59.9	0.097969
80.4414	-8.6465	60.0	0.064401

APPENDIX 5

ERROR ANALYSES

A. Mass Flow Rate (MFR):

(i) MFR is measured with a Coriolis Mass Flowmeter, Krohne MFC 085 Smart.

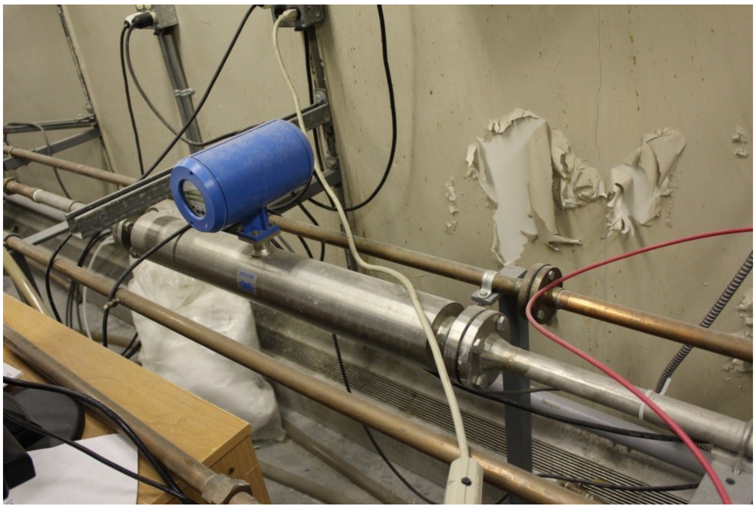

Figure A5.1. Coriolis Mass Flowmeter (Krohne MFC 085 Smart) in the flow loop.

(ii) The data (kg/s) are recorded manually with respect to specific pump powers: 10, 15, 20, 25 and 30 Hz.

(iii) The data (kg/s) are recorded over a period of December 2012 to November 2013.

(iv) 3 decimal points are considered significant for recording the data.

(v) Two major components are identified while analyzing the error:

  a. Machine Error, ME (bias or systematic uncertainty): 0.25% of Full Scale (FS)
  b. Precision Error, PE (random uncertainty): Standard deviation of the data recorded in course of the experiments

(vi) The Total Error (TE) is calculated as the RMS value of the aforementioned error components.

$$TE\ (\pm) = \sqrt{(ME^2 + PE^2)}\ unit$$

$$\%TE = \frac{TE}{Average\ MFR} \times 100$$

(vii) The Overall Error (OE) is the arithmetic average of the individual TE for all measurements.

$$\%OE = \frac{\sum_{i}^{n} TE_i\,(\%)}{n}$$

(viii) The TE ranges within 0.5% - 1.2%. While the OE is less than 1%. As a result, the error in measuring MFR can be considered as negligible.

Table A5.1. The recorded mass flow rates of water[**]

Mass flow rates, m_{wi} (kg/s)									
Pump-motor power (Hz)					***Pump-motor power (Hz)***				
10	***15***	***20***	***25***	***30***	***10***	***15***	***20***	***25***	***30***
0.572	0.893	1.179	1.498	1.764	0.596	0.924	1.206	1.524	1.788
0.573	0.894	1.18	1.499	1.765	0.597	0.925	1.207	1.525	1.789
0.574	0.895	1.181	1.500	1.766	0.598	0.926	1.208	1.526	1.790
0.575	0.896	1.184	1.501	1.767	0.599	0.927	1.209	1.527	1.791
0.576	0.897	1.185	1.502	1.768	0.600		1.21	1.528	1.792
0.577	0.898	1.186	1.505	1.769	0.601		1.211	1.529	1.793
0.578	0.906	1.187	1.506	1.77	0.602		1.212	1.530	1.794
0.579	0.907	1.188	1.507	1.771	0.605		1.213	1.531	1.795
0.580	0.908	1.190	1.508	1.772	0.606		1.214	1.532	1.796
0.581	0.909	1.191	1.509	1.773	0.607		1.215	1.533	1.797
0.582	0.91	1.192	1.51	1.774	0.608		1.217		1.798
0.583	0.911	1.193	1.511	1.775	0.610		1.218		1.799
0.584	0.912	1.194	1.512	1.776	0.611		1.219		1.800
0.585	0.913	1.195	1.513	1.777	0.612		1.22		1.801
0.586	0.914	1.196	1.514	1.778	0.613		1.221		1.802
0.587	0.915	1.197	1.515	1.779			1.222		1.803
0.588	0.916	1.198	1.516	1.78			1.223		1.804
0.589	0.917	1.199	1.517	1.781			1.224		1.805
0.590	0.918	1.200	1.518	1.782			1.225		1.806
0.591	0.919	1.201	1.519	1.783			1.226		1.807
0.592	0.92	1.202	1.52	1.784			1.227		1.808
0.593	0.921	1.203	1.521	1.785			1.228		1.809
0.594	0.922	1.204	1.522	1.786			1.229		1.81
0.595	0.923	1.205	1.523	1.787					1.811

Table A5.2. Average mass flow rates and associated errors

Pump-motor power (Hz)	Average Mass flow rate, m_w (kg/s)	Total Error (%)	Overall Error (%)
10	0.587	1.0	0.8
15	0.912	1.2	
20	1.202	0.6	
25	1.516	0.6	
30	1.783	0.5	

[**] The repetitions are discarded, only the unique values are incorporated in this table.

B. Temperature:

(i) Temperature T (°C) is measured with a Coriolis Mass Flowmeter, Krohne MFC 085 Smart.

(ii) The data (°C) are manually recorded in course of the experiments over a period of December 2012 to November 2013.

(iii) 1 decimal point is considered significant for recording the data.

(iv) Two major components are identified while analyzing the error:

   a. Machine Error ME (bias or systematic uncertainty): 0.25% of Full Scale (FS)
   b. Precision Error PE (random uncertainty): Standard deviation of the data recorded in course of the experiments

(v) The Total Error (TE) is calculated as the RMS value of the aforementioned error components.

$$TE\ (\pm) = \sqrt{(ME^2 + PE^2)}\ unit$$

$$\%TE = \frac{TE}{Average\ T} \times 100$$

(vi) The measured temperature is ~20°C with a TE of ~9%: 20±2°C.

Table A5.3. Measured temperatures and associated error

Temperature, T (°C)					
Date	Highest	Lowest	Date	Highest	Lowest
21-Dec-12	19.5	18.6	25-Sep-13	19.9	18.3
8-Jan-13	20.0	18.8	26-Sep-13	19.1	18.0
10-Jan-13	18.9	18.8	27-Sep-13	22.4	19.8
15-Jan-13	19.9	19.1	30-Sep-13	22.4	21.8
17-Jan-13	20.0	19.2	1-Oct-13	20.6	20.0
24-Jan-13	19.8	19.2	2-Oct-13	21.5	20.3
7-Feb-13	19.5	19.2	3-Oct-13	19.2	18.0
11-Feb-13	19.8	19.3	7-Oct-13	21.3	20.2
13-Feb-13	19.6	19.0	8-Oct-13	21.6	19.8
15-Feb-13	19.8	16.4	9-Oct-13	21.8	19.9
20-Feb-13	20.8	18.7	10-Oct-13	20.9	19.4
25-Feb-13	19.7	18.6	11-Oct-13	21.7	19.7
13-Mar-13	20.1	19.6	16-Oct-13	20.8	18.8
25-Mar-13	19.8	18.6	17-Oct-13	20.4	19.4
10-Apr-13	19.4	17.8	18-Oct-13	20.1	19.4
18-Apr-13	20.9	18.0	21-Oct-13	20.1	19.6
22-Apr-13	19.5	18.1	22-Oct-13	19.7	19.0
23-Apr-13	20.0	18.9	23-Oct-13	20.3	19.9
24-Apr-13	20.0	18.4	24-Oct-13	20.5	20.3
25-Apr-13	20.7	19.0	25-Oct-13	21.0	18.8
30-Apr-13	20.6	18.3	28-Oct-13	20.1	17.8
1-May-13	19.9	18.8	30-Oct-13	21.0	19.7
2-May-13	21.6	18.8	31-Oct-13	18.5	17.0
3-May-13	20.8	19.4	1-Nov-13	20.4	19.9
17-May-13	21.1	18.7	4-Nov-13	20.1	19.2
20-May-13	21.4	18.5	5-Nov-13	20.8	19.2
23-May-13	21.0	18.7	Average temperature, T (°C): 19.7±1.8 ≈ 20±2 Total Error (%): 9		
24-May-13	22.2	18.1			
5-Jun-13	21.4	18.4			
6-Jun-13	21.6	18.5			
7-Jun-13	20.6	18.7			
17-Jun-13	20.9	18.3			
18-Jun-13	20.8	19.3			
19-Jun-13	21.1	19.9			
18-Sep-13	20.4	19.8			
19-Sep-13	20.1	19.7			
23-Sep-13	19.8	19.6			
24-Sep-13	19.5	18.7			

C. Coating thickness:

(i) The procedure followed to prepare a coating layer of a particular thickness is as follows:

   a. Determine the weight of oil required for x_i mm thick coating-layer on a test plate:

$$\text{Volume, } V\,(\mathrm{m}^3) = A_{test\ plate} \times 0.00x_i$$

$$\text{Weight, } W_1\,(\mathrm{g}) = V\,(\mathrm{m}^3) \times \rho_{oil}\,(\mathrm{kg/m}^3) \times 1000\mathrm{g}/1\mathrm{kg} = A_{test\ plate}\rho_{oil}$$

   b. Weigh the 100mm test plate on a scale: W_2 (g).

   c. Add oil with a syringe or reduce oil from test plates with a spatula as required to ensure weight of the test plate to be $W_1 + W_2$ (g).

   d. If required, heat the plate with oil at 80°C - 100°C for around 30 minutes and ensure that the sample is evenly spread on a plate.

   e. Re-weigh to ensure the weight to be $W_1 + W_2$ (g).

(ii) The procedure followed for measuring thickness of oil on a 100mm test plate is as follows:

   a. Use a precision balance, Talent TE6101 (SARTORIUS), to weigh a clean 100mm test plate without oil.

   b. Use the same precision balance, Talent TE6101 (SARTORIUS), to weigh a 100mm test plate coated with oil.

   c. Difference between the measured weights is the weight/mass of coating oil (m_{oil}).

   d. The thickness of oil coating (t_c) is calculated as follows:

$$t_c = m_{oil}/(\rho_{oil} \times A_{test\ plate})$$

(iii) The densities of the sample oils (ρ_{oil}) used for measuring t_c were either supplied by the producer or measured in the SRC. The error associated with the densities was considered negligible, as ρ_{oil} for the heavy oil is not highly sensitive to temperature.

(iv) Similarly, nominal dimensions for a test plate (i.e. 25mm × 100mm) were used for calculating the area, $A_{test\ plate}$. Repeated measurements of these dimensions yielded less than 1% StDev. Hence, the error associated with $A_{test\ plate}$ was considered negligible.

(v) There is no Machine Error, ME (i.e., bias or systematic uncertainty) associated with the measurement of m_{oil}, as it is the difference between two measurements of the same precision balance, Talent TE6101 (SARTORIUS).

(vi) Although it was not feasible to weigh an oil-coated test plate repeatedly in course of the experiments, the clean test plates were weighed a number of times. The StDev of the measurements was less than 1%. Also, the same coated plate was weighed in different times on a single day. This kind of repeated measurement yielded similar results. Therefore, the Precision Error, PE (random uncertainty) for measuring m_{oil} on a 100mm test plate was considered negligible.

(vii) The plates in the flow visualizing section of the flow-cell were numbered from 1 to 10. Plates 1 to 5 were in the flow developing zone, 6 to 9 were in the developed flow zone and 10 was close to the outlet. As a result, 4 plates numbered 6, 7, 8 and 9 were considered as the test plates.

(viii) Experiments were started with exactly the same m_{oil} (i.e., initial coating thickness, t_{ci}) on all plates. After a flow test, the measured values of m_{oil} (i.e., final coating thickness, t_{cf}) for different test plates (i.e., 6, 7, 8 and 9) differed by 0 – 25% of the average value. The final coating thickness after the first flow test was considered as the initial value for the second flow test. Similar consideration was applied for successive flow tests. A complete set of experiment for a particular coating-layer involved up to five flow tests. Each flow test involved changing pump power from 10Hz to 30Hz. Every flow test caused a minor change in average thickness of the coating layer. Therefore, the coating thickness (t_c) for a flow test was considered as the arithmetic average of initial and final values (i.e., t_{ci} and t_{cf}).

(ix) The coating thickness was not necessarily uniform along the bed in lateral direction during the flow test. That is, there was an uncertainty in thickness along the coating bed. This uncertainty is quantified as the Standard Deviation (StDev) of t_c for different test plates (i.e. 6, 7, 8 and 9).

(x) For every experiment, coating thicknesses on the test plates were determined before and after a flow test. The corresponding StDev was also calculated. The arithmetic average of initial and final values was considered as the StDev for a particular flow test. As mentioned earlier, one experiment involved up to five successive flow tests, that is, six consecutive measurements of m_{oil}.

(xi) The major error related to the measurement of t_c is the StDev in its lateral distribution along the coating bed in test section.

(xii) A specific average thickness (e.g. 0.2mm) of the coating-oil is the arithmetic average of several measurements. Each measurement involves measuring m_{oil} (i.e., t_c) on different test plates for two times.

(xiii) On an average, the Overall Error, OE (or Overall StDev) for measuring coating thickness of oil on test plates is 11%.

Data used for determining the average coating thickness of Sample 1:

Table A5.4. Average coating thickness (t_c) = 0.1mm for Sample 1

Date	Plate #	Weight of the plates		Coating thickness t_{ci} (mm)	Average coating thickness t_c (mm)	StDev (%)
		Oil coated (g)	Clean (g)			
29-Oct-13	6	186.7	186.4	0.12	0.1	14
	7	186.7	186.4	0.12		
	8	186.6	186.3	0.12		
	9	186.6	186.3	0.12		
30-Oct-13	6	186.7	186.4	0.12		
	7	186.8	186.4	0.16		
	8	186.7	186.3	0.16		
	9	186.7	186.3	0.16		
31-Oct-13	6	186.7	186.4	0.12		
	7	186.8	186.4	0.16		
	8	186.7	186.3	0.16		
	9	186.7	186.3	0.16		

Table A5.5. Average coating thickness (t_c) = 0.2mm for Sample 1

Date	Plate #	Weight of the plates		Coating thickness t_{ci} (mm)	Average coating thickness t_c (mm)	StDev (%)
		Oil coated (g)	Clean (g)			
24-Oct-13	6	187	186.4	0.24	0.2	9
	7	187	186.4	0.24		
	8	186.9	186.3	0.24		
	9	186.9	186.3	0.24		
25-Oct-13	6	187.1	186.4	0.24		
	7	187	186.4	0.24		
	8	186.9	186.3	0.24		
	9	186.9	186.3	0.24		
28-Oct-13	6	187	186.4	0.24		
	7	187	186.4	0.24		
	8	186.9	186.3	0.24		
	9	186.9	186.3	0.24		
28-Oct-13	6	186.9	186.4	0.20		
	7	186.9	186.4	0.20		
	8	186.8	186.3	0.20		
	9	186.8	186.3	0.20		
29-Oct-13	6	186.9	186.4	0.20		
	7	186.9	186.4	0.20		
	8	186.8	186.3	0.20		
	9	186.8	186.3	0.20		
29-Oct-13	6	186.9	186.4	0.20		
	7	186.9	186.4	0.20		
	8	186.8	186.3	0.20		
	9	186.8	186.3	0.20		

Table A5.6. Average coating thickness (t_c) = 0.5mm for Sample 1

Date	Plate #	Weight of the plate		Coating thickness t_{ci} (mm)	Average coating thickness t_c (mm)	StDev (%)
		Oil coated (g)	Clean (g)			
16-May-13	7	187.8	186.4	0.55	0.5	5
	8	187.8	186.4	0.55		
	9	187.8	186.4	0.55		
17-May-13	7	187.8	186.4	0.55		
	8	187.8	186.4	0.55		
	9	187.8	186.4	0.55		
20-May-13	7	187.8	186.4	0.55		
	8	187.8	186.4	0.55		
	9	187.8	186.4	0.55		
23-May-13	7	187.8	186.4	0.55		
	8	187.8	186.4	0.55		
	9	187.8	186.4	0.55		
24-May-13	7	187.8	186.4	0.55		
	8	187.7	186.4	0.51		
	9	187.8	186.4	0.55		
27-May-13	7	187.8	186.4	0.55		
	8	187.7	186.4	0.51		
	9	187.8	186.4	0.55		
29-May-13	7	187.7	186.4	0.51		
	8	187.7	186.4	0.51		
	9	187.7	186.4	0.51		
14-Jun-13	7	187.7	186.4	0.51		
	8	187.6	186.3	0.51		
	9	187.7	186.4	0.51		
18-Jun-13	7	187.6	186.4	0.47		
	8	187.8	186.3	0.59		
	9	187.8	186.4	0.55		
19-Jun-13	7	187.6	186.4	0.47		
	8	187.6	186.3	0.51		
	9	187.8	186.4	0.55		
20-Jun-13	7	187.6	186.4	0.47		
	8	187.7	186.3	0.55		
	9	187.8	186.4	0.55		

Table A5.7. Average coating thickness (t_c) = 0.9mm for Sample 1

Date	Plate #	Weight of the plates		Coating thickness t_{ci} (mm)	Average coating thickness t_c (mm)	StDev (%)
		Oil coated (g)	Clean (g)			
16-May-13	7	189	186.4	1.02	0.9	12
	8	188.9	186.3	1.02		
	9	188.9	186.3	1.02		
5-Jun-13	7	188.9	186.4	0.98		
	8	188.8	186.3	0.98		
	9	188.8	186.3	0.98		
6-Jun-13	7	188.9	186.4	0.98		
	8	188.5	186.4	0.82		
	9	188.4	186.4	0.78		
7-Jun-13	7	188.4	186.4	0.78		
	8	188.6	186.4	0.86		
	9	188.2	186.4	0.71		

Data used for determining the average coating thickness of Sample 2:

Table A5.8. Average coating thickness (t_c) = 0.2mm for Sample 2

Date	Plate #	Weight of the plates		Coating thickness, t_{ci} (mm)	Average coating thickness, t_c (mm)	StDev (%)
		Oil coated (g)	Clean (g)			
9-Oct-13	6	186.9	186.4	0.20	0.2	9
	7	186.9	186.4	0.20		
	8	186.8	186.3	0.20		
	9	186.8	186.3	0.20		
9-Oct-13	6	187	186.4	0.24		
	7	187	186.4	0.24		
	8	186.9	186.3	0.24		
	9	186.8	186.3	0.20		
10-Oct-13	6	187	186.4	0.24		
	7	186.9	186.4	0.20		
	8	186.9	186.3	0.24		
	9	186.8	186.3	0.20		
10-Oct-13	6	187	186.4	0.24		
	7	186.9	186.4	0.20		
	8	186.8	186.3	0.20		
	9	186.8	186.3	0.20		
10-Oct-13	6	187	186.4	0.24		
	7	186.9	186.4	0.20		
	8	186.9	186.3	0.24		
	9	186.8	186.3	0.20		
11-Oct-13	6	186.9	186.4	0.20		
	7	186.9	186.4	0.20		
	8	186.8	186.3	0.20		
	9	186.8	186.3	0.20		

Table A5.9. Average coating thickness (t_c) = 0.5mm for Sample 2

Date	Plate #	Weight of the plates		Coating thickness, t_{ci} (mm)	Average coating thickness, t_c (mm)	StDev (%)
		Oil coated (g)	Clean (g)			
14-Oct-13	6	187.7	186.4	0.52	0.5	5
	7	187.7	186.4	0.52		
	8	187.6	186.3	0.52		
	9	187.6	186.3	0.52		
16-Oct-13	6	187.8	186.4	0.56		
	7	187.7	186.4	0.52		
	8	187.5	186.3	0.48		
	9	187.7	186.3	0.56		
16-Oct-13	6	187.7	186.4	0.52		
	7	187.7	186.4	0.52		
	8	187.6	186.3	0.52		
	9	187.7	186.3	0.56		
17-Oct-13	6	187.6	186.4	0.48		
	7	187.6	186.4	0.48		
	8	187.6	186.3	0.52		
	9	187.7	186.3	0.56		

Table A5.10. Average coating thickness (t_c) = 1.0mm for Sample 2

Date	Plate #	Weight of the plates		Coating thickness, t_{ci} (mm)	Average coating thickness, t_c (mm)	StDev (%)
		Oil coated (g)	Clean (g)			
17-Oct-13	6	188.9	186.4	1.00	1.0	11
	7	188.9	186.4	1.00		
	8	188.8	186.3	1.00		
	9	188.8	186.3	1.00		
18-Oct-13	6	188.8	186.4	0.96		
	7	188.6	186.4	0.88		
	8	188.5	186.3	0.88		
	9	188.6	186.3	0.92		
18-Oct-13	6	188.5	186.4	0.84		
	7	188.5	186.4	0.84		
	8	188.3	186.3	0.80		
	9	188.4	186.3	0.84		
18-Oct-13	6	189.2	186.4	1.12		
	7	189.2	186.4	1.12		
	8	189.1	186.3	1.12		
	9	189.1	186.3	1.12		
21-Oct-13	6	189	186.4	1.04		
	7	189	186.4	1.04		
	8	188.9	186.3	1.04		
	9	188.9	186.3	1.04		
21-Oct-13	6	188.9	186.4	1.00		
	7	188.8	186.4	0.96		
	8	188.7	186.3	0.96		
	9	188.5	186.3	0.88		
21-Oct-13	6	188.7	186.4	0.92		
	7	188.5	186.4	0.84		
	8	188.3	186.3	0.80		
	9	188.3	186.3	0.80		

Data used for determining the average coating thickness of Sample 3:

Table A5.11. Average coating thickness (t_c) = 0.2mm for Sample 3

Date	Plate #	Weight of the plates		Coating thickness, t_{ci} (mm)	Average coating thickness, t_c (mm)	StDev (%)
		Oil coated (g)	Clean (g)			
25-Sep-13	7	186.9	186.4	0.20	0.2	17
	8	186.9	186.4	0.20		
	9	186.9	186.4	0.20		
26-Sep-13	7	187.0	186.4	0.24		
	8	187.1	186.4	0.28		
	9	187.0	186.4	0.24		
26-Sep-13	7	187.1	186.4	0.28		
	8	186.8	186.4	0.16		
	9	187.0	186.4	0.24		
27-Sep-13	7	187.0	186.4	0.24		
	8	186.9	186.4	0.20		
	9	187.0	186.4	0.24		
27-Sep-13	7	186.9	186.4	0.20		
	8	186.9	186.4	0.20		
	9	187.0	186.4	0.24		
30-Sep-13	7	186.9	186.4	0.20		
	8	186.8	186.4	0.16		
	9	187.0	186.4	0.24		
30-Sep-13	7	186.8	186.4	0.16		
	8	186.8	186.4	0.16		
	9	186.9	186.4	0.20		

Data used for determining the average coating thickness of Sample 4:

Table A5.12. Average coating thickness (t_c) = 0.2mm for Sample 4

Date	Plate #	Weight of the plates		Coating thickness, t_{ci} (mm)	Average coating thickness, t_c (mm)	StDev (%)
		Oil coated (g)	Clean (g)			
19-Sep-13	7	186.9	186.4	0.20	0.2	18
	8	186.8	186.3	0.20		
	9	186.8	186.3	0.20		
23-Sep-13	7	186.8	186.4	0.16		
	8	186.7	186.3	0.16		
	9	186.7	186.3	0.16		
22-Oct-13	6	187.0	186.4	0.24		
	7	187.0	186.4	0.24		
	8	186.9	186.3	0.24		
	9	187.0	186.4	0.24		
22-Oct-13	6	186.9	186.4	0.20		
	7	186.9	186.4	0.20		
	8	186.8	186.3	0.20		
	9	186.9	186.4	0.20		
23-Oct-13	6	186.7	186.4	0.12		
	7	186.8	186.4	0.16		
	8	186.7	186.3	0.16		
	9	186.8	186.4	0.16		
23-Oct-13	6	187.0	186.4	0.24		
	7	187.0	186.4	0.24		
	8	186.9	186.3	0.24		
	9	187.0	186.4	0.24		
23-Oct-13	6	187.0	186.4	0.24		
	7	186.9	186.4	0.20		
	8	186.8	186.3	0.20		
	9	186.9	186.4	0.20		
24-Oct-13	6	186.8	186.4	0.16		
	7	186.8	186.4	0.16		
	8	186.7	186.3	0.16		
	9	186.8	186.4	0.16		

D. Pressure drops:

(i) Pressure drops are measured with a pressure transducer, Validyne P61.

Figure A5.2. Photograph of the pressure transducer (Validyne P61).

(ii) The data (psig) are recorded automatically with respect to specific pump powers: 10, 15, 20, 25 and 30 Hz. Most of the measurements are done at the powers of 10Hz, 20Hz and 30Hz. However, 15Hz and 25Hz are also used in some cases.

(iii)The data are recorded at a particular pump power (i.e. flow rate) for 100 sec to 7000 sec. Steady state condition is ensured for recording the data.

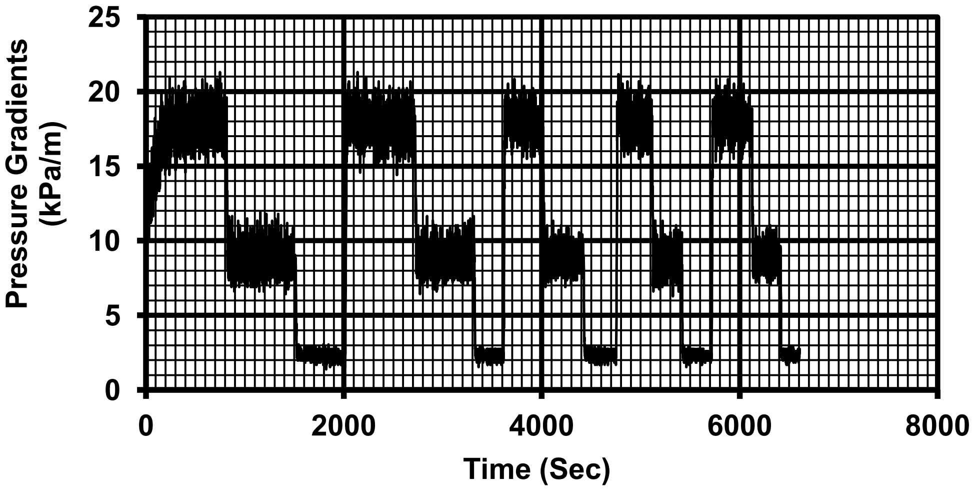

Figure A5.3. An illustration of instantaneous pressure gradients (Sample 1; $t_c = 0.2$mm; Pump Power: 10, 20, 30Hz)

(iv) A LabView program is used to record the data in excel files. The instantaneous pressure drops recorded for every second are converted into 30s averages. These values are averaged further to know the average pressure drops.

(v) The pressure gradients (kPa/m) are calculated as the ratio of pressure drops and distance between the pressure taps.

(vi) The center-to-center distance between the pressure taps is 450mm for the wall-coating tests. Similar distance for the tests with clean flow-cell is 800mm. The common radius of the taps is 5mm. As a result, the maximum error in the measurement of distance between the taps can be 5*100/450 ~ 1.1% or 5*100/800 ~ 0.6%. This error is considered negligible.

(ix) The main source of error is the measurement of pressure drops with Validyne P61 transducer. Two major components are identified while analyzing the error:

   a. Machine Error, ME (bias or systematic uncertainty): 0.25% of Full Scale (FS)
   b. Precision Error, PE (random uncertainty): Standard deviation of the data recorded in course of the experiments

(x) The Total Error (TE) is calculated as the RMS value of the aforementioned error components.

$$TE\ (\pm) = \sqrt{(ME^2 + PE^2)}\ unit$$

$$\%TE = \frac{TE}{Average\ Pressure\ Drop} \times 100$$

(xi) The Overall Error (OE) is the arithmetic average of the individual TE for all measurements.

$$\%OE = \frac{\sum_i^n TE_i\ (\%)}{n}$$

(xii) The data (kPa/m) are recorded over a period of December 2012 to November 2013.

(xiii) The OE for measuring pressure drops is 5%.

Clean wall: No wall-coating:

Table A5.13. 30s Average pressure drops (kPa) for average coating thickness, t_c = 0.0mm (Clean wall)

Pump-motor power (Hz)											
10		***15***		***20***			***25***		***30***		
1.09	1.48	2.01	2.51	3.29	3.79	4.17	5.17	5.79	7.14	7.65	8.27
1.12		2.07	2.54	3.32	3.80	4.18	5.18	5.96	7.20	7.67	8.28
1.13		2.09	2.57	3.33	3.81	4.19	5.19	5.98	7.22	7.69	8.29
1.14		2.10		3.34	3.82	4.20	5.23	5.99	7.26	7.71	8.30
1.15		2.11		3.35	3.83	4.21	5.24	6.02	7.28	7.72	8.32
1.16		2.12		3.36	3.84	4.22	5.28	6.04	7.29	7.78	8.32
1.17		2.13		3.39	3.85	4.23	5.30	6.06	7.30	7.81	8.33
1.18		2.14		3.40	3.86	4.24	5.31	6.11	7.31	7.82	8.35
1.19		2.15		3.41	3.87	4.25	5.34	6.15	7.33	7.84	8.38
1.20		2.16		3.42	3.88	4.26	5.35	6.16	7.34	7.90	8.39
1.21		2.17		3.43	3.90	4.27	5.36	6.20	7.35	7.92	8.41
1.22		2.18		3.44	3.91	4.28	5.37		7.36	7.94	8.42
1.23		2.19		3.45	3.92	4.29	5.38		7.37	7.95	8.43
1.24		2.20		3.46	3.93	4.30	5.39		7.38	7.98	8.46
1.25		2.21		3.47	3.96	4.31	5.40		7.39	7.99	8.48
1.26		2.21		3.50	3.97	4.33	5.41		7.40	8.00	8.49
1.27		2.22		3.51	3.98	4.34	5.43		7.41	8.01	8.50
1.29		2.23		3.52	3.99		5.44		7.42	8.04	8.51
1.30		2.24		3.53	4.00		5.45		7.43	8.05	8.52
1.31		2.25		3.56	4.01		5.46		7.44	8.07	8.53
1.32		2.26		3.57	4.02		5.47		7.45	8.09	8.56
1.33		2.27		3.58	4.03		5.48		7.46	8.11	8.58
1.34		2.28		3.59	4.04		5.49		7.47	8.12	8.59
1.35		2.29		3.60	4.04		5.50		7.49	8.13	
1.36		2.30		3.61	4.05		5.51		7.51	8.14	
1.37		2.31		3.67	4.06		5.52		7.52	8.15	
1.38		2.33		3.68	4.07		5.53		7.53	8.16	
1.39		2.34		3.69	4.08		5.54		7.54	8.18	
1.40		2.37		3.70	4.09		5.55		7.55	8.19	
1.41		2.43		3.71	4.10		5.56		7.56	8.20	
1.42		2.44		3.72	4.12		5.58		7.57	8.21	
1.43		2.45		3.73	4.13		5.59		7.58	8.22	
1.44		2.47		3.73	4.14		5.60		7.59	8.23	
1.45		2.48		3.74	4.15		5.62		7.63	8.24	
1.46		2.50		3.76	4.16		5.66		7.64	8.26	

Wall-coating of Sample 1:

Table A5.14. 30s Average pressure drops (kPa) for average coating thickness, t_c = 0.1mm (Sample 1)

Pump-motor power (Hz)			
10	***20***	***30***	
0.89	3.03	6.59	7.00
0.90	3.29	6.60	7.01
0.91	3.31	6.62	7.02
0.92	3.32	6.65	7.04
0.93	3.33	6.66	7.05
0.94	3.36	6.68	7.10
0.95	3.37	6.70	7.38
0.96	3.38	6.72	
0.97	3.39	6.73	
0.98	3.40	6.74	
	3.41	6.75	
	3.42	6.76	
	3.43	6.77	
	3.44	6.78	
	3.45	6.79	
	3.46	6.80	
		6.81	
		6.82	
		6.83	
		6.84	
		6.85	
		6.86	
		6.87	
		6.88	
		6.89	
		6.90	
		6.91	
		6.92	
		6.93	
		6.94	
		6.95	
		6.96	
		6.97	
		6.98	
		6.99	

Table A5.15. 30s Average pressure drops (kPa) for average coating thickness, t_c = 0.2mm (Sample 1)

Pump-motor power (Hz)				
10	***20***		***30***	
0.94	3.45	4.07	7.45	8.00
0.95	3.62		7.47	8.01
0.96	3.65		7.49	8.02
0.97	3.66		7.51	8.03
0.98	3.67		7.52	8.04
1.00	3.68		7.53	8.05
1.01	3.69		7.57	8.06
1.02	3.70		7.58	8.07
1.03	3.71		7.59	8.08
1.04	3.72		7.60	8.09
1.05	3.75		7.61	8.10
1.06	3.76		7.62	8.11
1.07	3.78		7.64	8.12
	3.80		7.65	8.13
	3.82		7.68	8.15
	3.84		7.69	8.16
	3.85		7.70	8.24
	3.86		7.71	8.33
	3.88		7.72	8.55
	3.89		7.75	8.62
	3.90		7.77	
	3.91		7.79	
	3.92		7.80	
	3.93		7.81	
	3.94		7.84	
	3.95		7.85	
	3.96		7.87	
	3.97		7.90	
	3.98		7.92	
	3.99		7.93	
	4.00		7.94	
	4.01		7.96	
	4.02		7.97	
	4.03		7.98	
	4.05		7.99	

Table A5.16. 30s Average pressure drops (kPa) for average coating thickness, t_c = 0.5mm (Sample 1)

Pump-motor power (Hz)						
10	***20***			***30***		
0.88	4.17	4.58	5.04	9.03	9.62	10.01
0.90	4.18	4.59	5.10	9.07	9.63	10.02
0.91	4.20	4.60		9.17	9.66	10.06
0.92	4.21	4.61		9.18	9.67	10.09
0.93	4.24	4.62		9.21	9.68	10.10
0.94	4.25	4.63		9.25	9.69	10.13
0.95	4.26	4.64		9.26	9.70	10.15
0.97	4.30	4.65		9.27	9.71	10.20
0.98	4.31	4.66		9.28	9.72	10.27
0.99	4.32	4.67		9.29	9.73	10.36
1.00	4.33	4.68		9.31	9.74	10.37
1.01	4.34	4.69		9.32	9.75	10.39
1.02	4.35	4.70		9.33	9.76	10.43
1.03	4.36	4.71		9.35	9.77	10.45
1.04	4.37	4.72		9.37	9.78	10.46
1.05	4.38	4.73		9.38	9.79	10.47
1.06	4.39	4.74		9.40	9.80	10.50
1.07	4.40	4.76		9.41	9.81	10.51
1.08	4.41	4.78		9.42	9.82	10.54
1.09	4.42	4.79		9.43	9.83	10.59
1.10	4.43	4.80		9.44	9.84	10.61
1.11	4.44	4.82		9.45	9.86	10.67
1.12	4.45	4.83		9.46	9.87	10.78
1.13	4.46	4.84		9.47	9.89	
1.14	4.47	4.86		9.48	9.90	
1.15	4.48	4.89		9.49	9.91	
1.16	4.49	4.90		9.50	9.92	
1.17	4.50	4.91		9.51	9.93	
1.18	4.51	4.92		9.52	9.94	
1.20	4.52	4.93		9.53	9.95	
1.21	4.53	4.96		9.56	9.96	
	4.54	4.97		9.58	9.97	
	4.55	4.98		9.59	9.98	
	4.56	5.00		9.60	9.99	
	4.57	5.03		9.61	10.00	

Table A5.17. 30s Average pressure drops (kPa) for average coating thickness, t_c = 1.0mm (Sample 1)

Pump-motor power (Hz)						
10	***20***			***30***		
1.41	5.79	6.26	6.69	12.19	12.81	13.23
1.42	5.84	6.27	6.70	12.29	12.82	13.24
1.44	5.87	6.28	6.72	12.30	12.84	13.25
1.45	5.88	6.29	6.73	12.31	12.85	13.26
1.46	5.91	6.29	6.74	12.32	12.86	13.27
1.47	5.93	6.30	6.76	12.39	12.87	13.29
1.48	5.94	6.31	6.81	12.43	12.90	13.31
1.49	5.95	6.32	6.90	12.46	12.91	13.33
1.50	5.96	6.33	6.94	12.47	12.92	13.35
1.51	5.97	6.34		12.48	12.93	13.36
1.52	5.98	6.36		12.50	12.94	13.37
1.53	5.99	6.38		12.51	12.95	13.40
1.54	6.00	6.39		12.53	12.96	13.41
1.55	6.01	6.40		12.54	12.97	13.42
1.56	6.03	6.41		12.55	12.98	13.49
1.57	6.04	6.43		12.56	12.99	13.50
1.58	6.05	6.44		12.57	13.00	13.53
1.59	6.06	6.46		12.58	13.02	13.56
1.60	6.07	6.47		12.59	13.03	13.70
1.61	6.08	6.48		12.60	13.04	13.82
1.62	6.09	6.50		12.61	13.05	13.92
1.63	6.10	6.51		12.62	13.08	13.93
1.64	6.11	6.52		12.63	13.09	13.94
1.65	6.12	6.53		12.65	13.10	13.95
1.66	6.14	6.54		12.66	13.11	13.96
1.67	6.15	6.55		12.69	13.12	
1.68	6.16	6.56		12.70	13.13	
1.69	6.17	6.58		12.72	13.15	
	6.18	6.60		12.73	13.16	
	6.19	6.61		12.74	13.17	
	6.20	6.63		12.75	13.18	
	6.21	6.64		12.77	13.19	
	6.22	6.66		12.78	13.20	
	6.23	6.67		12.79	13.21	
	6.24	6.68		12.80	13.22	

Wall-coating of Sample 2:

Table A5.18. 30s Average pressure drops (kPa) for average coating thickness, $t_c = 0.2$mm (Sample 2)

Pump-motor power (Hz)					
10	***15***	***20***	***25***	***30***	
0.97	2.22	3.91	5.80	7.96	8.35
0.98	2.25	3.97	5.85	7.97	8.37
0.99	2.27	3.96	5.91	7.89	8.39
1.00	2.29	3.99	5.92	7.90	8.40
1.01	2.30	4.01	5.96	7.96	8.41
1.02	2.32	4.02	5.97	7.98	8.42
1.03	2.33	4.03	5.99	7.99	8.52
1.04	2.34	4.04	6.00	8.02	8.63
1.05	2.35	4.05	6.01	8.03	
1.06	2.36	4.06	6.02	8.04	
1.07	2.37	4.07	6.03	8.05	
1.08	2.38	4.09	6.04	8.06	
1.09	2.39	4.10	6.07	8.07	
1.10	2.40	4.11	6.08	8.09	
1.12	2.41	4.12	6.09	8.10	
1.13	2.42	4.13	6.10	8.11	
1.14	2.43	4.15	6.11	8.12	
1.15	2.44	4.16	6.12	8.13	
1.16	2.46	4.17	6.13	8.14	
1.21	2.47	4.18	6.14	8.16	
1.23	2.48	4.19	6.15	8.17	
1.24	2.52	4.20	6.16	8.19	
1.25	2.57	4.21	6.17	8.20	
1.28	2.58	4.22	6.18	8.21	
	2.59	4.23	6.19	8.22	
	2.60	4.25	6.20	8.24	
	2.65	4.27	6.22	8.25	
	2.66	4.34	6.24	8.26	
		4.36	6.25	8.27	
		4.38	6.28	8.28	
		4.41	6.29	8.29	
			6.30	8.30	
			6.31	8.31	
			6.32	8.33	
			6.33	8.34	

Table A5.19. 30s Average pressure drops (kPa) for average coating thickness, t_c = 0.5mm (Sample 2)

Pump-motor power (Hz)							
10	***15***	***20***		***25***		***30***	
1.26	2.55	4.76	5.66	7.32	8.83	9.70	10.97
1.31	2.79	4.93	5.79	7.40		9.81	10.98
1.32	2.80	4.97	5.83	7.41		9.85	10.99
1.34	2.81	5.01		7.42		9.87	11.00
1.35	2.82	5.02		7.44		9.88	11.04
1.36	2.83	5.03		7.46		9.89	11.13
1.37	2.85	5.05		7.47		9.90	11.17
1.38	2.86	5.06		7.49		9.93	11.18
1.39	2.88	5.07		7.52		9.96	11.21
1.40	2.89	5.09		7.57		10.00	
1.41	2.90	5.10		7.66		10.01	
1.42	2.92	5.11		7.81		10.16	
1.43	3.02	5.12		7.84		10.19	
1.45	3.05	5.13		7.85		10.25	
1.46	3.06	5.14		7.88		10.39	
1.47	3.07	5.15		7.92		10.40	
1.49	3.08	5.16		7.95		10.43	
1.50	3.10	5.19		7.96		10.46	
1.51	3.11	5.20		7.97		10.50	
1.52	3.12	5.23		7.98		10.52	
1.53	3.13	5.24		8.00		10.53	
1.54	3.14	5.31		8.01		10.54	
1.56	3.15	5.32		8.03		10.56	
1.57	3.17	5.37		8.04		10.58	
1.58	3.18	5.38		8.08		10.60	
1.59	3.19	5.39		8.09		10.66	
1.60	3.20	5.44		8.12		10.68	
1.61	3.21	5.47		8.13		10.70	
1.62	3.22	5.49		8.14		10.73	
1.63	3.23	5.51		8.19		10.74	
1.65	3.24	5.54		8.22		10.79	
1.66	3.30	5.55		8.25		10.80	
1.68	3.31	5.57		8.35		10.86	
		5.58		8.36		10.93	
		5.64		8.48		10.96	

Table A5.20. 30s Average pressure drops (kPa) for average coating thickness, t_c = 1.0mm (Sample 2)

Pump-motor power (Hz)			
10	***20***		***30***
1.59	5.55	7.06	11.69
1.60	5.56	7.07	11.74
1.66	5.58	7.14	11.79
1.67	5.60	7.18	11.81
1.68	5.64		11.88
1.71	5.83		12.00
1.72	5.85		12.28
1.73	5.90		12.29
1.74	6.00		12.33
1.75	6.01		12.49
1.76	6.03		12.52
1.77	6.04		12.57
1.78	6.07		12.78
1.79	6.10		12.90
1.82	6.11		13.66
1.83	6.15		13.66
1.85	6.19		13.72
1.87	6.33		13.85
1.88	6.35		13.88
1.91	6.44		13.89
1.92	6.46		13.89
1.93	6.51		13.99
1.94	6.63		14.06
1.97	6.65		14.13
1.98	6.70		14.18
2.02	6.77		14.27
	6.81		14.29
	6.82		14.33
	6.83		14.42
	6.84		14.46
	6.88		14.57
	6.91		14.57
	6.93		14.62
	6.94		14.71
	7.03		14.78

Wall-coating of Sample 3:

Table A5.21. 30s Average pressure drops (kPa) for average coating thickness, t_c = 0.2mm (Sample 3)

Pump-motor power (Hz)				
10	***20***		***30***	
0.76	3.16	4.14	7.19	8.36
0.77	3.22	4.16	7.24	8.38
0.78	3.24	4.18	7.25	8.39
0.80	3.34	4.19	7.26	8.40
0.81	3.36	4.23	7.28	8.41
0.82	3.44	4.24	7.39	8.43
0.83	3.53	4.28	7.61	8.45
0.84	3.59	4.30	7.67	8.46
0.87	3.65	4.67	7.70	8.65
0.88	3.66		7.72	8.74
0.89	3.72		7.74	8.80
0.90	3.77		7.75	9.31
0.92	3.78		7.80	
0.95	3.79		7.81	
0.97	3.86		7.82	
0.99	3.87		7.86	
1.00	3.88		7.91	
1.01	3.89		8.03	
1.02	3.91		8.05	
1.03	3.92		8.06	
1.04	3.93		8.07	
1.05	3.96		8.08	
1.06	3.97		8.10	
1.07	3.98		8.11	
1.08	3.99		8.12	
1.09	4.00		8.13	
1.10	4.01		8.16	
1.11	4.02		8.20	
1.12	4.03		8.22	
1.13	4.04		8.25	
1.17	4.06		8.26	
	4.08		8.27	
	4.09		8.28	
	4.10		8.29	
	4.11		8.35	

Wall-coating of Sample 4:

Table A5.22. 30s Average pressure drops (kPa) for average coating thickness, t_c = 0.2mm (Sample 4)

Pump-motor power (Hz)		
10	***20***	***30***
0.78	3.16	6.96
0.79	3.28	7.00
0.80	3.40	7.01
0.81	3.42	7.06
0.82	3.44	7.09
0.83	3.47	7.10
0.84	3.48	7.14
0.85	3.51	7.17
0.86	3.53	7.18
0.87	3.55	7.22
0.88	3.57	7.29
0.89	3.62	7.31
0.90	3.65	7.33
0.91	3.68	7.36
1.00	3.71	7.39
1.03	3.77	7.40
1.04	3.79	7.43
1.05	3.80	7.45
1.06	3.81	7.49
1.07	3.83	7.51
1.08	3.87	7.52
1.09	3.88	7.54
1.10	3.89	7.55
1.12	3.90	7.59
1.15	3.91	7.61
1.16	3.95	7.66
1.20	3.96	7.69
1.22	3.99	7.70
1.23	4.02	7.71
	4.05	7.74
	4.12	7.75
	4.76	7.76
		7.84
		7.87
		7.99

Table A5.23. Average pressure drops and associated errors

Coating oil	Coating thickness, t_c (mm)	Pump-motor power (Hz)	Average pressure drops, ΔP (kPa)	Total Error (%)	Overall Error (%)
No wall-coating; clean flow-cell	0.0	10	1.3	8	5
		15	2.2	5	
		20	3.9	8	
		25	5.5	4	
		30	7.8	5	
Sample 1	0.1	10	0.9	3	
		20	3.4	2	
		30	6.9	2	
	0.2	10	1.0	3	
		20	3.9	3	
		30	7.9	3	
	0.5	10	1.0	7	
		20	4.6	4	
		30	9.7	4	
	1.0	10	1.6	4	
		20	6.3	4	
		30	12.9	3	
Sample 2	0.2	10	1.1	7	
		15	2.4	4	
		20	4.1	3	
		25	6.1	2	
		30	8.2	2	
	0.5	10	1.5	7	
		15	3.1	6	
		20	5.2	4	
		25	7.9	4	
		30	10.5	4	
	1.0	10	1.8	5	
		20	6.4	8	
		30	13.4	8	
Sample 3	0.2	10	1.0	11	
		20	3.9	7	
		30	8.1	5	
Sample 4	0.2	10	0.9	15	
		20	3.8	7	
		30	7.4	3	

E. Hydrodynamic roughness (Simulation results):

(i) The determination of hydrodynamic roughness (k_s) by simulating experimental pressure gradients ($\Delta P/L$) is dependent on the following major parameters:

- Pressure gradient ($\Delta P/L$)
- Coating thickness (t_c)
- Mass flow rate of water (m_w)

(ii) Since determination of k_s is dependent on $\Delta P/L$, t_c and m_w, the error associated with this parameter is calculated as follows:

a. The Total Error (TE) is calculated as the RMS value of the error components.

$$\%TE\ k_s\ (\pm) = \sqrt{[(\%TE\ \Delta P/L)^2 + (\%TE\ t_c)^2 + (\%TE\ m_w)^2]}$$

b. The Overall Error (OE) is the arithmetic average of the individual TE for all measurements.

$$\%OE = \frac{\sum_i^n TE_i\ (\%)}{n}$$

(iii) The Overall Error (OE) in the determination of k_s is 12.3%.

Table A5.24. Hydrodynamic roughness (k_s) and associated errors (Rectangular Flow Cell)

Coating oil	Coating thickness, t_c (mm)	Hydrodynamic roughness, k_s (mm)	Total Error (%)	Overall Error (%)
No wall-coating; clean flow-cell	0.0	0.0 (Smooth)	6.1	12.3
Sample 1	0.1	0.1	14.2	
	0.2	0.4	9.5	
	0.5	1.5	7.1	
	0.9	3.5	13.2	
Sample 2	0.2	0.4	14.1	
	0.5	1.5	7.1	
	1.0	3.5	13.1	
Sample 3	0.2	0.4	18.7	
Sample 4	0.2	0.4	19.9	

F. Physical roughness:

(ii) Physical roughnesses of the heavy oil coated on 100 mm long steel plates are measured by using a contracer, Mitutoyo CV-3100H4.

(iii) The Mitutoyo Contracer is a sophisticated equipment for measuring surface roughness automatically.

   a. The Contracer uses a stylus and a completely automated system for characterizing the topography of a hard surface.
   b. The Contracer is programed to measure the surface roughness in same co-ordinates (x, y, z) with respect to its fixed position.
   c. The inclination (θ) of the Contracer cannot be fixed automatically; rather it is necessary to fix the θ-position of the stylus manually. That is why in many occasions it was not possible to ensure complete horizontality of the stylus. As a result, the original data involved some unexpected inclination.
   d. It is standard practice to calculate roughness parameters by subtracting the arithmetic average from the fluctuating topographic data. This practice is based on the pre-requirement of perfectly horizontal measurements. However, as our measurements involved some unknown inclinations, linear trendline values, instead of the arithmetic average, are used for calculating the roughness parameters.

(iv) There is no Machine Error, ME (i.e., bias or systematic uncertainty) associated with the measurement of physical roughness, as the data used for calculating roughness parameters are obtained by subtracting the original readings from the corresponding trendline values or arithmetic average.

(v) The major error related to the measurement of physical roughness/topography is the StDev of the same roughness parameter determined in course of the experiments by using various samples in different times.

(vi) An empirical formula proposed by Flack and Schultz (2010a) is used for calculating the Nikuradse sand grain equivalent or hydrodynamic roughness (k_s):

$$k_s = 4.43R_{rms}(1+R_{Sk})^{1.37}$$

Since calculation of k_s involves R_{rms} and R_{Sk}, StDev or error associated with this parameter is calculated as follows:

a. The Total Error (TE) is calculated as the RMS value of the error components.

$$TE\ (\pm) = \sqrt{[(StDev\ R_{rms})^2 + (StDev\ R_{Sk})^2) + (StDev\ k_s)^2]}$$

$$\%TE = \frac{TE}{Average\ k_s} \times 100$$

b. The Overall Error (OE) is the arithmetic average of the individual TE for all measurements.

$$\%OE = \frac{\sum_i^n TE_i\ (\%)}{n}$$

(xiv) The data presented here were recorded over a period of December 2012 to November 2013. The detailed procedure for the data collection is presented in Appendix 4.

(xv) In addition to error, the data presented here also demonstrate the negligible effect of the flow rates on the corresponding roughness.

Table A5.25. Statistical parameters, hydrodynamic roughness and associated error

Coating thickness, t_c (mm)	Mass flow rate of water, m_w (kg/s)	Plate #	Average roughness, R_a (µm)	RMS roughness, R_{rms} (µm)	Skewness of roughness, R_{sk}	Hydrodynamic roughness, k_s (mm)	TE (%)	OE (%)
0.5	0.587	7	172	214	0.94	2.36	1	1
		7	123	152	0.81	1.52		
		8	128	163	0.86	1.70		
		9	140	175	0.85	1.80		
	1.202	8	151	193	0.82	1.95		
		9	140	176	0.89	1.87		
		9	145	173	0.64	1.51		
	1.783	7	154	193	0.68	1.75		
		8	161	196	0.55	1.58		
		8	138	172	0.64	1.50		
		9	130	161	0.60	1.36		
1	0.587	6	255	316	0.81	3.17	2	
		9	321	403	0.95	4.47		
		7	271	406	0.75	3.89		
		8	316	329	1.14	4.13		
		9	332	408	0.92	4.43		
	0.912	7	295	374	0.90	4.00		
		8	272	366	1.25	4.94		
		9	341	427	0.84	4.36		
	1.202	7	314	406	0.99	4.61		
		8	234	293	0.94	3.22		
		9	267	324	0.68	2.92		
		7	223	278	0.92	3.01		
		8	226	276	0.89	2.93		
		9	269	333	0.87	3.48		
		7	263	313	0.70	2.87		
		8	225	296	0.86	3.07		
		9	280	344	0.67	3.07		
		8	237	288	0.72	2.69		
	1.516	6	225	225	0.84	2.29		
		7	278	278	0.92	3.00		
		8	264	264	1.30	3.67		
		9	240	240	1.02	2.79		
	1.783	6	297	372	0.63	3.22		
		7	271	330	0.77	3.20		
		8	224	274	0.57	2.25		
		9	258	325	0.90	3.47		
		7	238	308	0.75	2.94		
		8	217	270	0.77	2.61		
		9	271	335	0.73	3.13		

APPENDIX 6

EXPERIMENTAL EVIDENCE FOR THE STABILITY OF COATING THICKNESS

In the flow tests with wall-coating on the bottom plate, the mass flow rates of water (m_w) were changed over a range of 0.587 kg/s – 1.783 kg/s. The experimental m_w correspond to the range of 1.4 m/s – 4.2 m/s for the average velocity (V). Within this range, the coating thickness (t_c) was found to be independent of water flow-rate. The independence was experimentally ensured by measuring the weight of oil on the segmented plates before and after the flow tests. There were 10 such plates which comprised the bottom plate in the flow visualizing section of the flow cell. These plates were numbered from 1 to 10. Plate 1 was placed at the entrance to the flow visualizing section, while Plate 10 was placed near the outlet. The plates numbered 6, 7, 8 and 9 were positioned in between the pressure taps, i.e., the test section. These plates are the test plates. The following tables show weights of oil on the test plates measured under different flow conditions. There were negligible differences between the initial and the final measurement. Corresponding examples of instantaneous pressure gradient vs time graphs for different scenario are also included here. These graphs demonstrate the development of steady state pressure gradients in course of the experiments.

Table A6.1. Measured weights of tests plates for Sample 1

Average thickness of wall-coating, t_c (mm)	Plate #	Weight of oil coated test plates (g)			Number of conducted test sets
		Initial	Final	Mass change (%)	
0.1	7	0.3	0.4	-33	3
	8	0.3	0.4	-33	
	9	0.3	0.4	-33	
0.2	7	0.6	0.6	0	3
	8	0.6	0.6	0	
	9	0.6	0.6	0	
	7	0.5	0.5	0	3
	8	0.5	0.5	0	
	9	0.5	0.5	0	
0.5	7	1.4	1.3	+7	7
	8	1.4	1.3	+7	
	9	1.4	1.3	+7	
	7	1.3	1.2	-8	3
	8	1.3	1.4	+8	
	9	1.3	1.4	+8	
1	7	2.6	2.0	-23	3
	8	2.6	2.2	-15	
	9	2.6	1.8	-31	

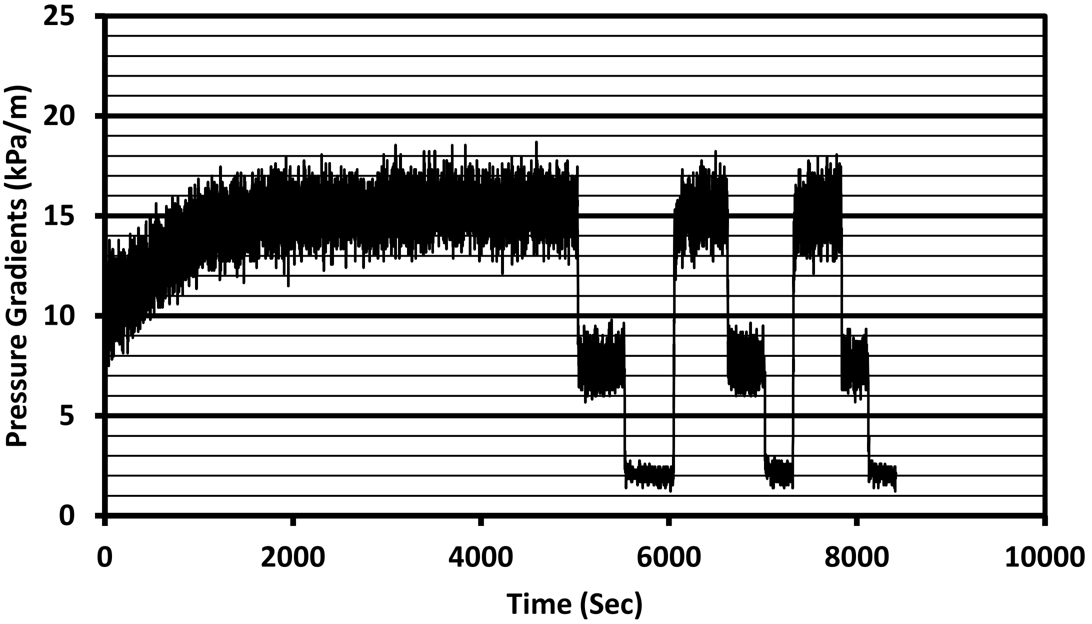
Pressure Gradients (kPa/m)
25
20
15
10
5
0
0
2000
4000
6000
8000
10000
Time (Sec)

(a)

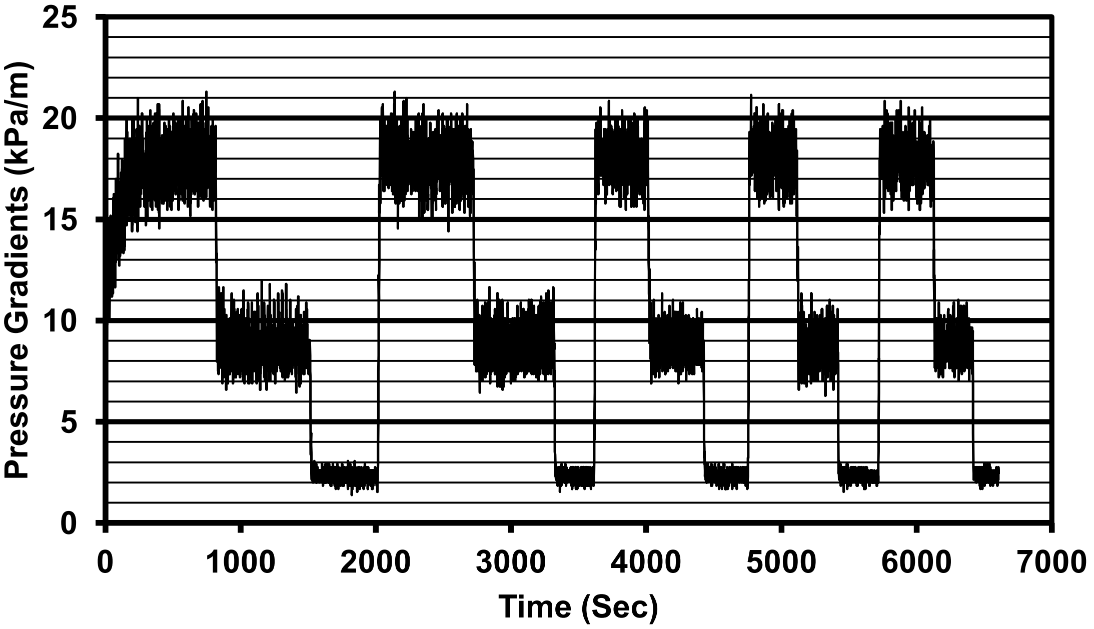
Pressure Gradients (kPa/m)
25
20
15
10
5
0
0
1000
2000
3000
4000
5000
6000
7000
Time (Sec)

(b)

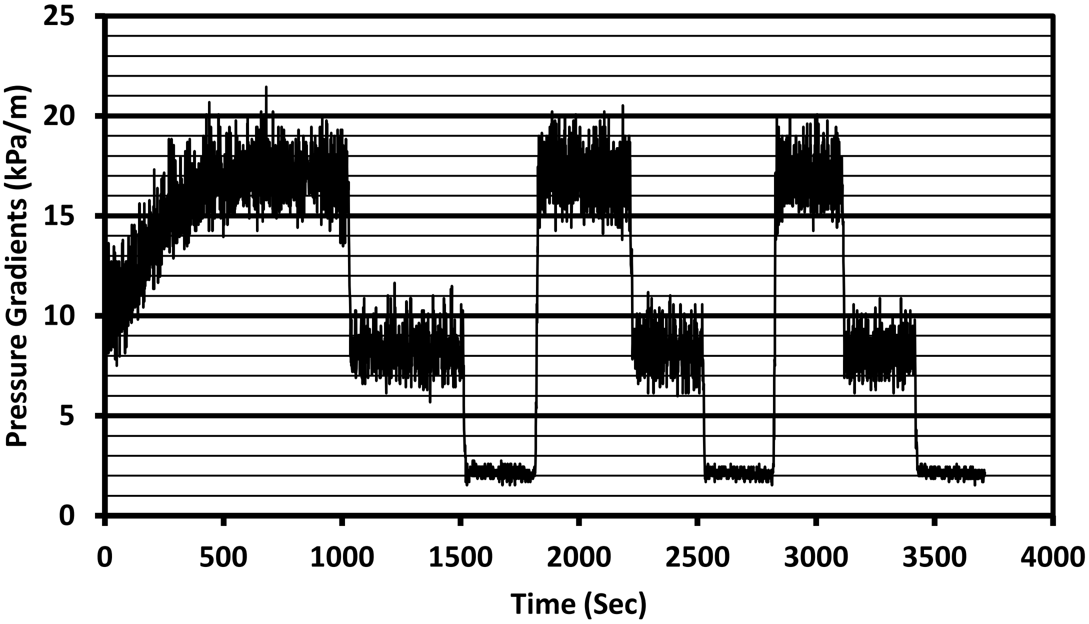

(c)

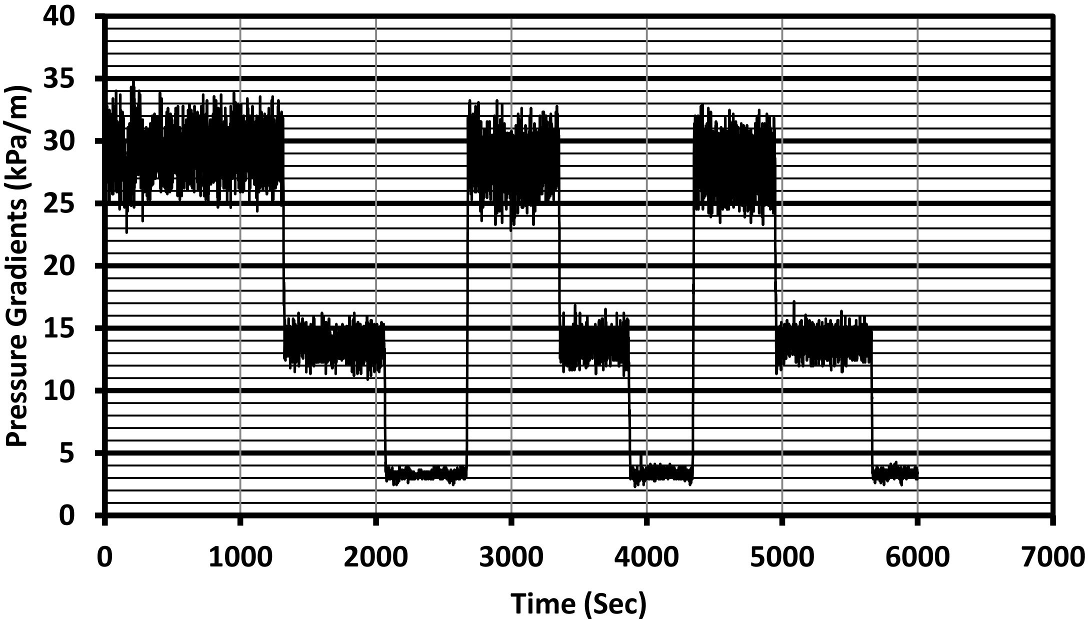

(d)

Figure A6.1. Instantaneous pressure gradients vs time graphs for Sample 1: (a) $t_c = 0.1$ mm; (b) $t_c = 0.2$ mm; (c) $t_c = 0.5$ mm; (d) $t_c = 1.0$ mm.

Table A6.2. Measured weights of tests plates for Sample 2

Average thickness of wall-coating, t_c (mm)	Plate #	Weight of oil coated test plates (g)			Number of conducted test sets
		Initial	Final	Mass change (%)	
0.2	6	0.5	0.5	0	5
	7	0.5	0.5	0	
	8	0.5	0.5	0	
	9	0.5	0.5	0	
0.5	6	1.3	1.2	-8	4
	7	1.3	1.2	-8	
	8	1.3	1.3	0	
	9	1.3	1.4	+8	
1	6	2.5	2.1	-16	3
	7	2.5	2.1	-16	
	8	2.5	2.0	-20	
	9	2.5	2.1	-16	
	6	2.8	2.3	-18	3
	7	2.8	2.1	-25	
	8	2.8	2.0	-29	
	9	2.8	2.0	-29	

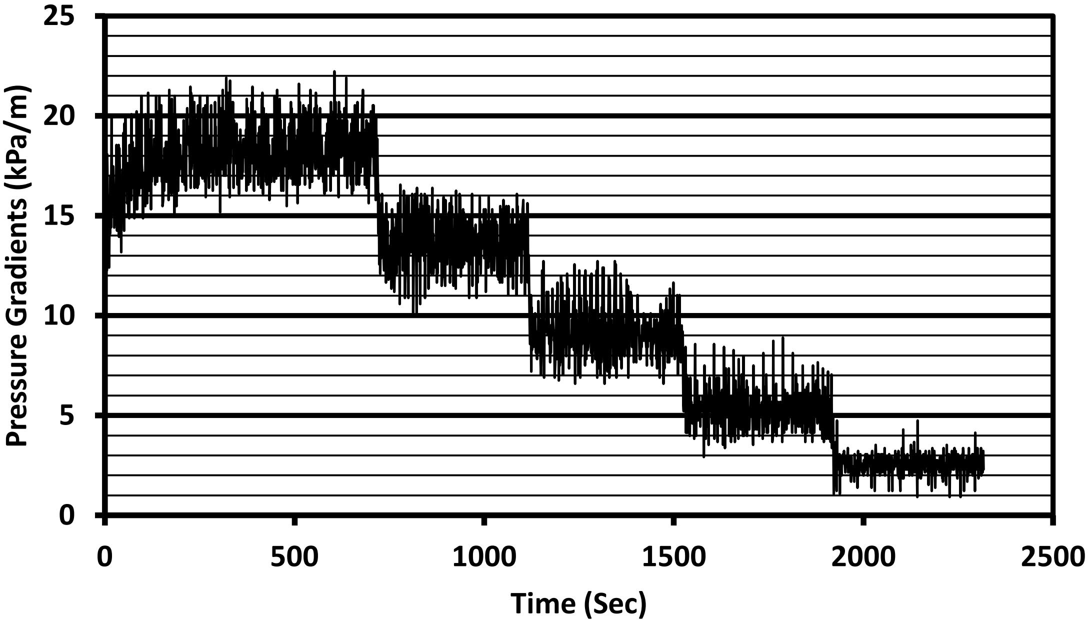
Pressure Gradients (kPa/m)
25
20
15
10
5
0
0
500
1000
1500
2000
2500
Time (Sec)

(a1)

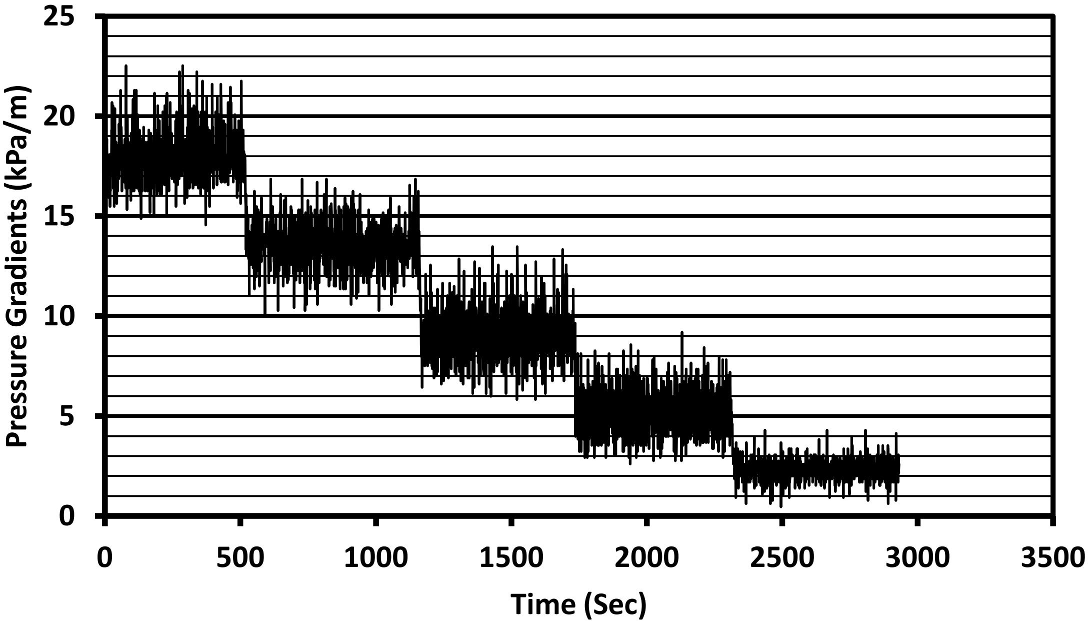
Pressure Gradients (kPa/m)
25
20
15
10
5
0
0
500
1000
1500
2000
2500
3000
3500
Time (Sec)

(a2)

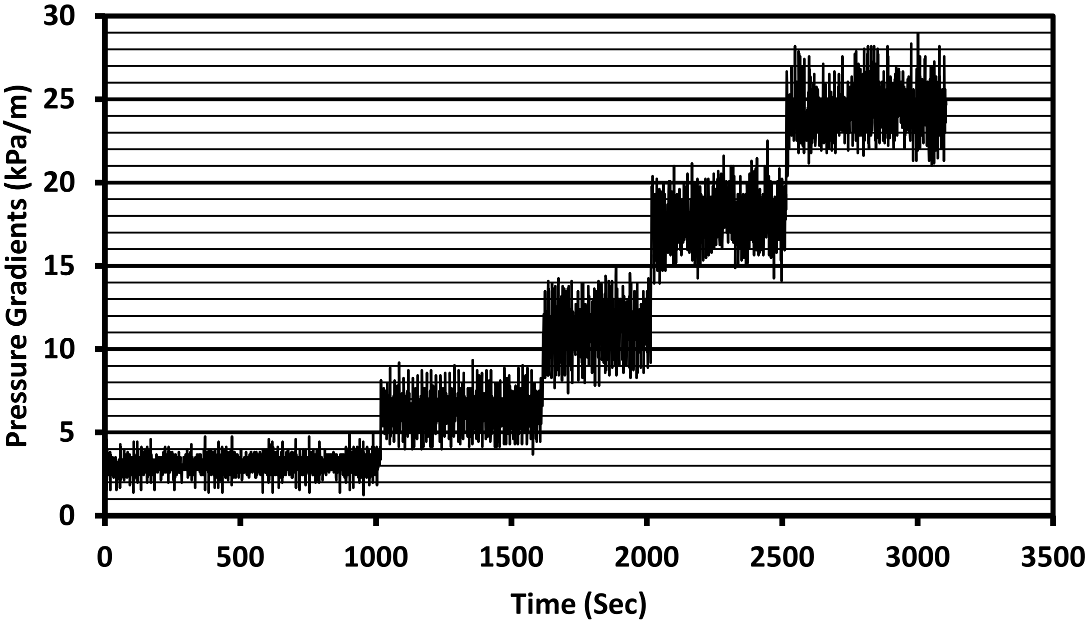
Pressure Gradients (kPa/m)
0
5
10
15
20
25
30
0
500
1000
1500
2000
2500
3000
3500
Time (Sec)

(b1)

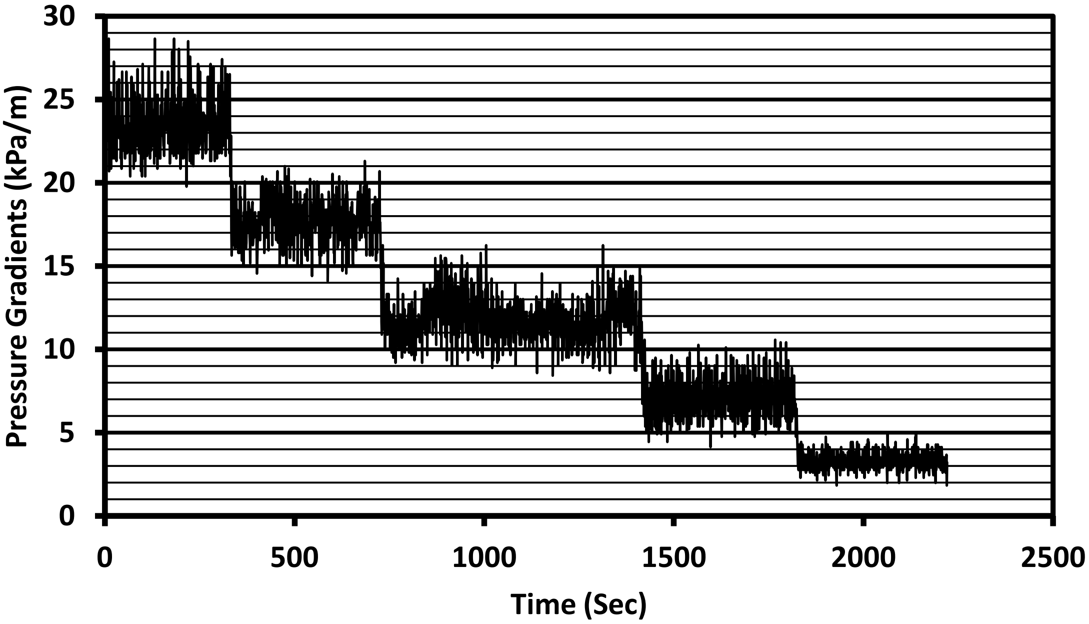
Pressure Gradients (kPa/m)
0
5
10
15
20
25
30
0
500
1000
1500
2000
2500
Time (Sec)

(b2)

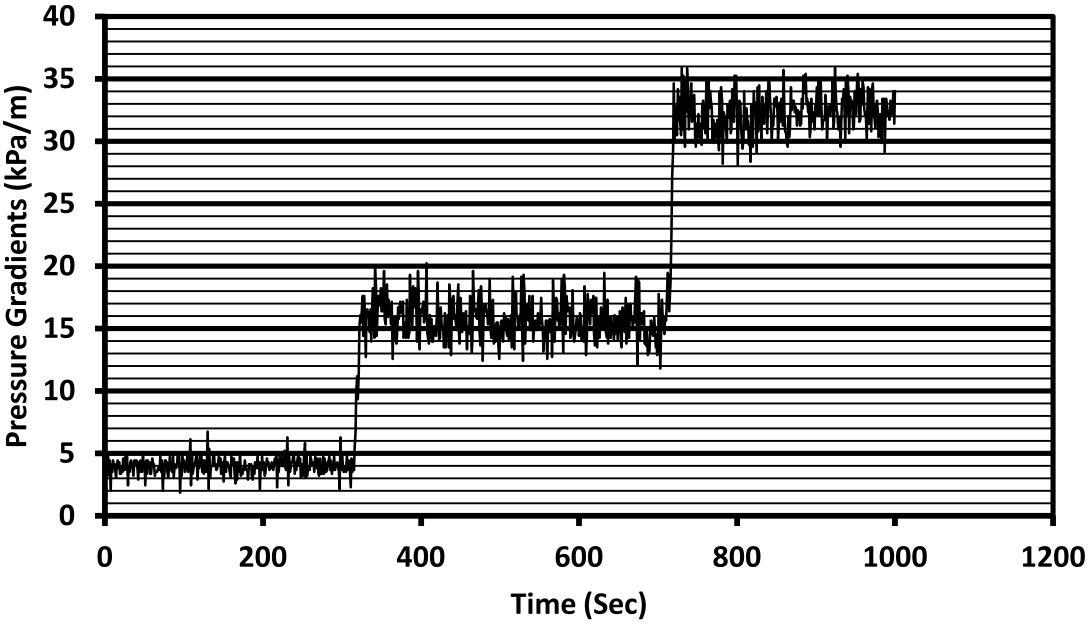

(c1)

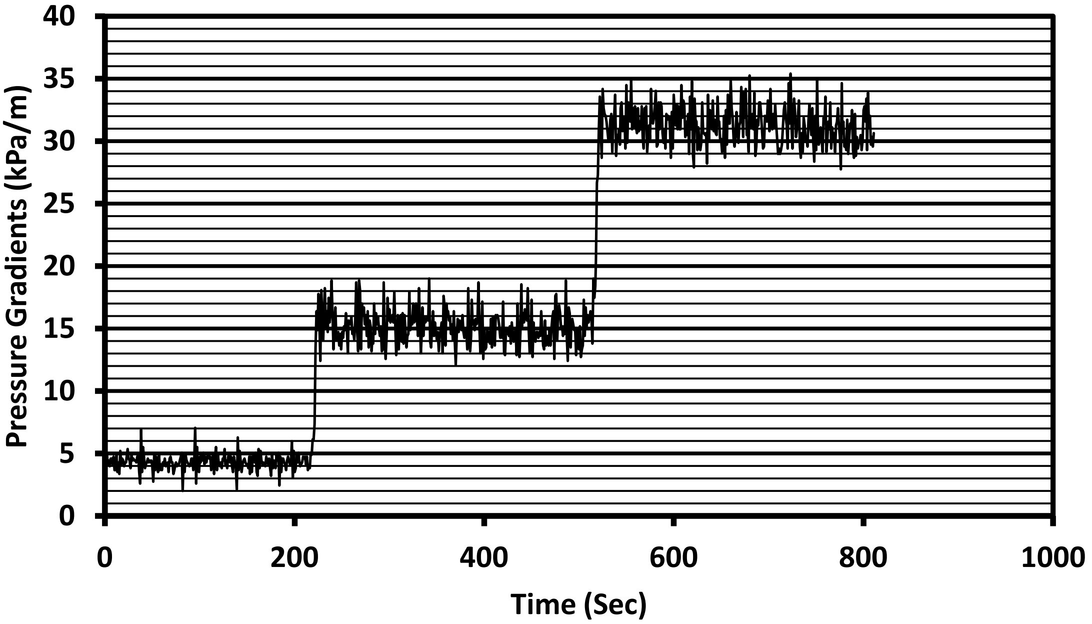

(c2)

Figure A6.2. Instantaneous pressure gradients vs time graphs for Sample 2 recorded during different test set: (a1, a2) t_c = 0.2 mm; (b1, b2) t_c = 0.5 mm; (c1, c2) t_c = 1.0 mm.

Table A6.3. Measured weights of tests plates for Sample 3

Average thickness of wall-coating, t_c (mm)	Plate #	Weight of oil coated test plates (g)			Number of conducted test sets
		Initial	Final	Mass change (%)	
0.2	7	0.5	0.4	-20	6
	8	0.5	0.4	-20	
	9	0.5	0.5	0	

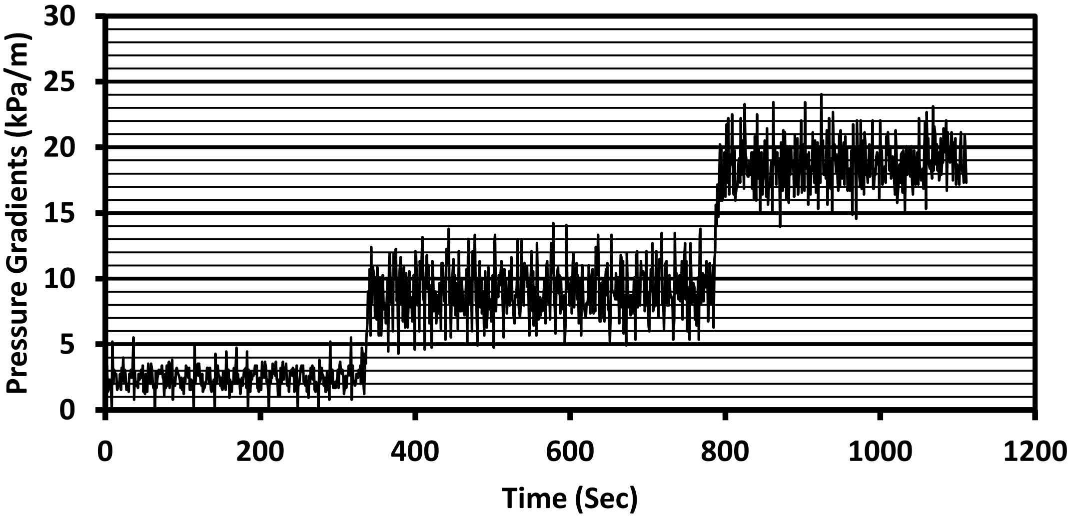

(a1)

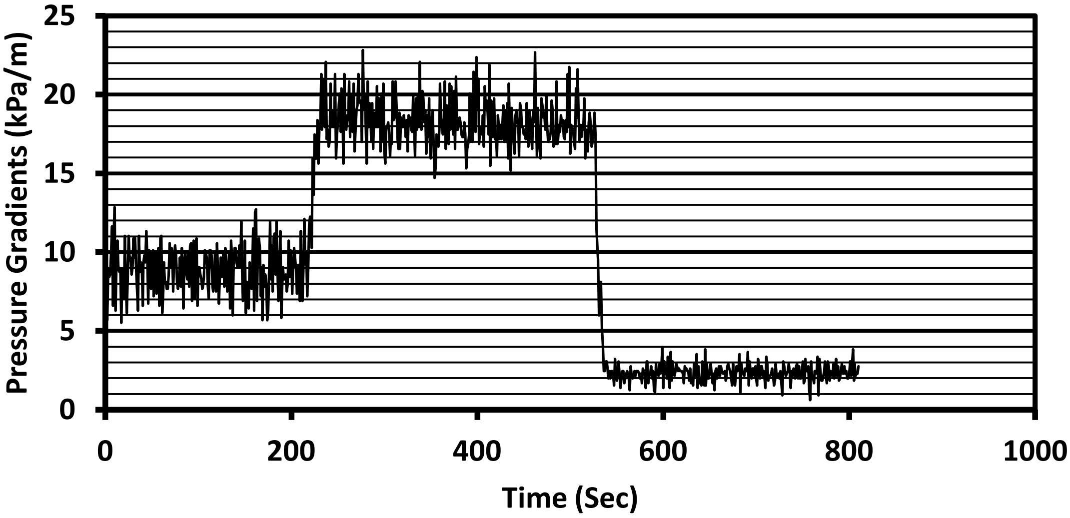

(a2)

Figure A6.3. Instantaneous pressure gradients vs time graphs for Sample 3 (t_c = 0.2 mm) recorded during two different set of experiments.

Table A6.4. Measured weights of test plates for Sample 4

Average thickness of wall-coating, t_c (mm)	Plate #	Weight of oil coated test plates (g)			Number of conducted test sets
		Initial	Final	Mass change (%)	
0.2	7	0.5	0.4	-20	1
	8	0.5	0.4	-20	
	9	0.5	0.4	-20	
	6	0.6	0.4	-33	4
	7	0.6	0.4	-33	
	8	0.6	0.4	-33	
	9	0.6	0.4	-33	

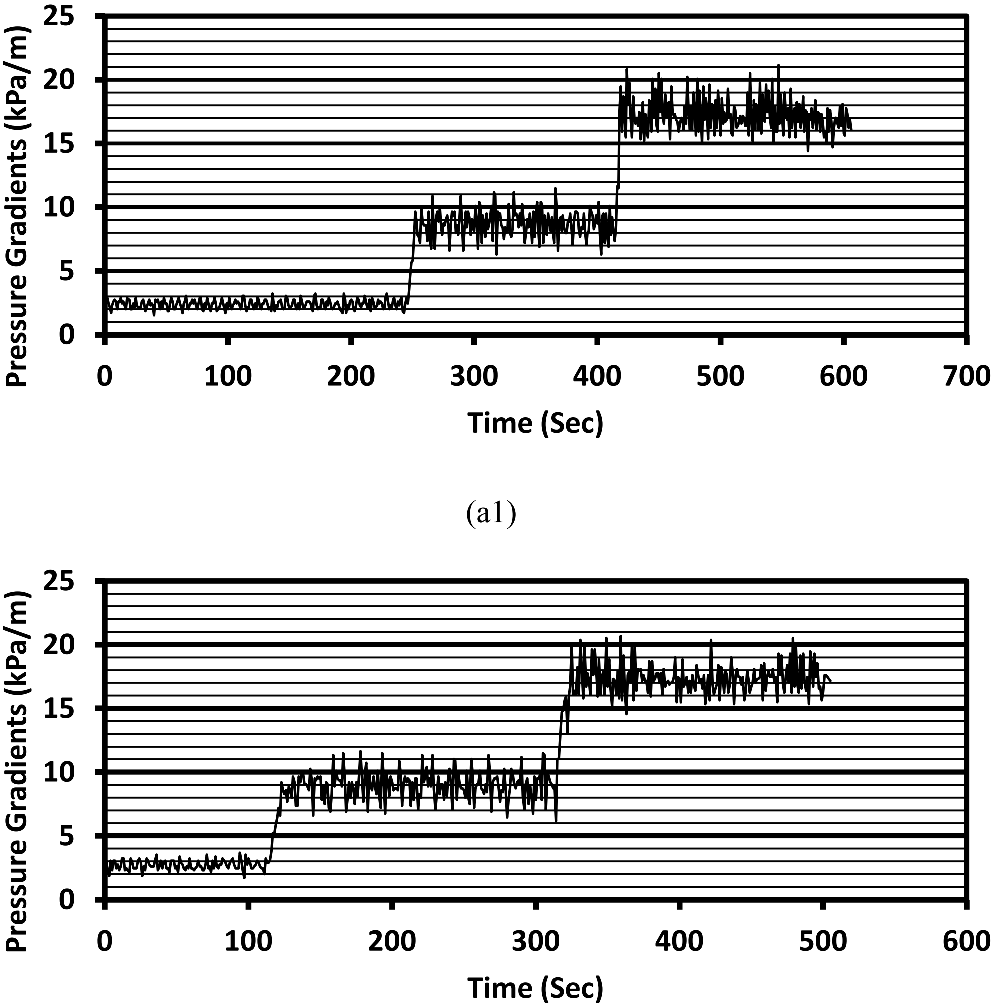

(a1)

(a2)

Figure A6.4. Instantaneous pressure gradients vs time graphs for Sample 4 (t_c = 0.2 mm) recorded during two different set of experiments.

APPENDIX 7

TURBULENCE MODEL SELECTION

The turbulence model used for the current work is a Reynolds Stress Model, ω-RSM. This modeling approach originates from the work by Launder and Spalding (1974). The ω-RSM is a second-order closure model that solves seven transport equations. It takes into account the anisotropy (direction dependence) of turbulence. Its performance is superior compared to the isotropic two equation models, such as k-ε and k-ω model, especially in simulating anisotropic flow conditions with high strain rate (Wilcox, 2006). This kind of flow condition can be generated by a rough wall having high equivalent hydrodynamic roughness (k_s). Appropriateness of ω-RSM over k-ω model for turbulent flows on rough surfaces ($k_s \sim 1$ mm) is demonstrated by Mothe and Sharif (2006). They attribute the superiority of the ω-RSM to its capability of addressing the anisotropy (direction dependence) of turbulence. The primary reason to select this model for current work was its capability to yield more reliable values for hydrodynamic roughness.

In Figure A7.1, the measured values of pressure gradients when average wall-coating thickness (t_c) was 1.0 mm are compared with the corresponding simulation results. Two different turbulence models, namely k-ω and ω-RSM, and two values of hydrodynamic roughness (k_s) were used for the simulation works. The results produced by the ω-RSM when k_s = 3.5 mm agree well with the experimental measurements of pressure gradients. Interestingly, the value of k_s obtained from the measurement of physical roughness was 3.4 mm (Chapter 3/Appendix 4). That is, the turbulence model, ω-RSM is capable of yielding reliable results for k_s.

On the other hand, the k-ω model under predicts the experimental results when k_s = 3.5 mm. This turbulence model can yield acceptable agreement with measurements if $k_s > 8$ mm. However, this value of k_s is unacceptable as the effective height of the flow cell is 14.9 mm when t_c = 1.0 mm.

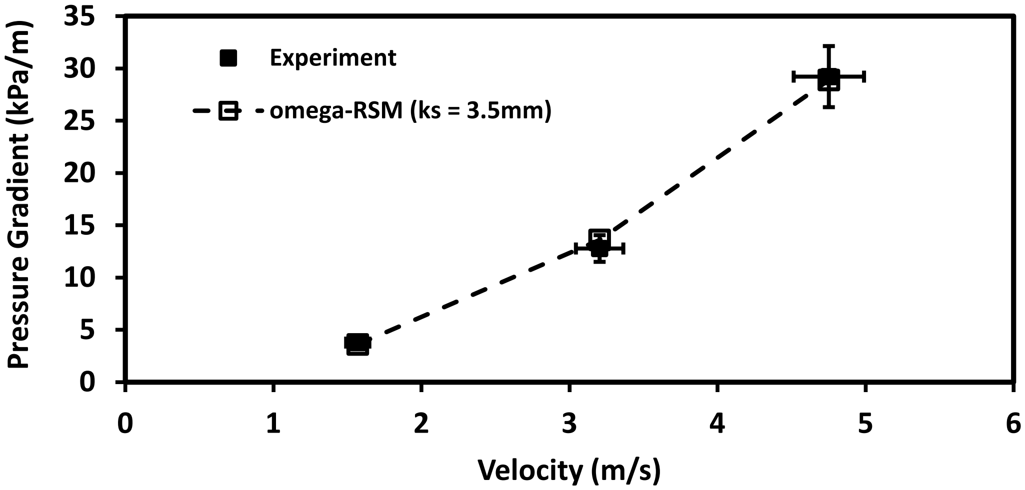

(a)

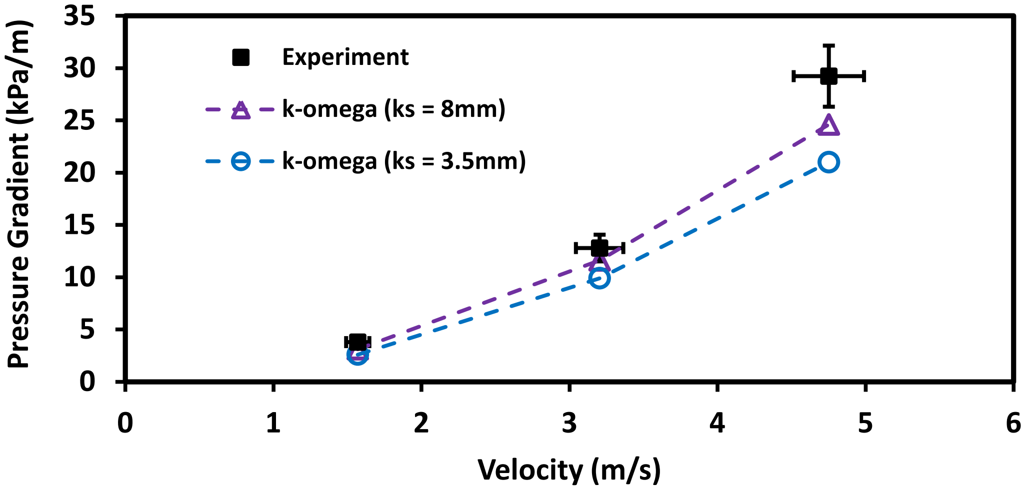

(b)

Figure A7.1. Comparison of experimental pressure gradients with simulation results (average coating thickness, t_c = 1.0 mm): (a) ω-RSM; (b) k-ω.

APPENDIX 8

VALIDATION OF THE CFD METHODOLOGY TO DETERMINE UNKNOWN HYDRODYNAMIC ROUGHNESS

A new methodology for determining unknown equivalent hydrodynamic, i.e., sand grain roughness is developed as part of the current research. The validation of this method is conducted on the basis of two completely different experimental works. One was carried out by the current researcher and the other was done by Andrewartha (2010). Both of these works used rectangular flow cells. However, the dimensions were substantially different. The hydrodynamic roughness was produced in the current work by sandpapers, while Andrewartha (2010) used different biofilms to produce the roughness.

A. Sandpapers

(i) Sandpapers of two different grits, 80 and 120 were selected for the experiments.

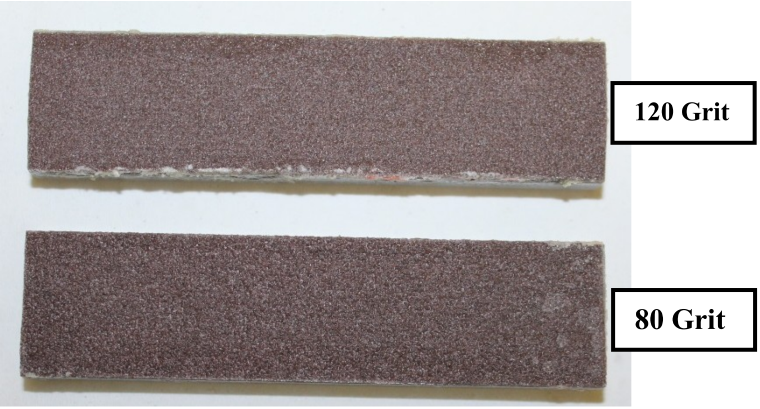

Figure A8.1. Photographs of the sandpapers.

(ii) Physical roughness of the sandpapers was measured with the MITUTOYO Contracer. The measurements for both sandpapers were conducted for three times. The results were used to determine two statistical parameters, RMS roughness (R_{rms}) and skewness of the roughness (R_{sk}). The determined values of the parameters were used for calculating the equivalent sand grain roughness (k_s) using the correlation proposed by Flack and Schultz (2010a) was used for the calculation.

(iii) The sandpapers were glued on two separate steel plates. These plates were placed in the flow visualizing section of the flow-cell. As a result, water could be pumped over the sandpaper. It should be mentioned that the original height of the flow-cell was 25.4mm.

A 9.5mm high steel plate was inserted into the cell and placed on its bottom wall. This plate reduced the effective height of the clean flow-cell to 15.9mm. It was segmented into two major parts. One segment was permanently fixed in the entrance section of the flow cell. The other segment was for the flow visualizing section. It was the sandpaper plate for the current experiments.

(iv) The thicknesses of the sandpaper plates were measured with a digital caliper. The measurements were conducted in multiple sections of the plate. The arithmetic average was considered as the representative thickness, t_{sp}. The measurement was used for calculating the effective height of the flow visualizing section with the sandpaper plates. This height was equal to $(25.4 - t_{sp})$ mm.

(vii) Water was pumped into the flow-cell at different pump-powers, i.e., mass flow rates and the corresponding pressure drops were measured with the pressure transducer, Validyne P61. The data were recorded for more than 1000s to ensure the steady state condition. The overall error for the measurement is around 1%.

(v) The measured pressure gradients are numerically simulated by using the methodology described in Chapter 3. The simulation results in comparison to the experimental measurements are presented here. The results are also plotted. Simulated values are within ±15% of the measurements. The agreement is reasonable.

Table A8.1. Hydrodynamic roughness with associated statistical parameters

Sandpaper grit	RMS Roughness, R_{rms} (μm)	Skewness of roughness, R_{sk}	Flack & Schultz (2010)	
			Sand grain roughness, k_s (mm)	Average k_s (mm)
80	75	0.41	0.53	0.53
	73	0.45	0.53	
	72	0.43	0.52	
120	56	0.20	0.32	0.31
	55	0.20	0.31	
	53	0.16	0.29	

Table A8.2. Thickness of sandpaper plates

80 Grit			120 Grit		
Measurements, t_{spi} (mm)		Average, t_{sp} (mm)	Measurements, t_{spi} (mm)		Average, t_{sp} (mm)
10.10	10.36	10.2	10.14	10.53	10.4
10.11			10.21	10.54	
10.16			10.23	10.55	
10.17			10.25	10.57	
10.18			10.26	10.58	
10.19			10.29	10.59	
10.20			10.30	10.60	
10.21			10.31	10.63	
10.22			10.33		
10.23			10.34		
10.25			10.35		
10.26			10.38		
10.27			10.40		
10.28			10.41		
10.29			10.46		
10.30			10.48		
10.31			10.49		
10.32			10.50		
10.33			10.51		
10.35			10.52		
Nominal thickness of the steel plate: 9.5mm					

Table A8.3. 30s Average pressure drops (kPa)

Sandpaper grit	***Pump-motor power (Hz)***				
	10	***15***	***20***	***25***	***30***
80	1.39	2.59	4.23	6.19	8.31
	1.40	2.62	4.24	6.24	8.34
	1.41	2.63	4.29	6.29	8.40
	1.42	2.64	4.30	6.30	8.41
	1.43	2.65	4.33	6.32	8.42
		2.66	4.34	6.33	8.43
		2.68	4.35	6.36	8.45
		2.69	4.38	6.37	8.46
		2.70	4.39	6.38	8.49
		2.71	4.40	6.39	8.50
			4.41	6.40	8.52
			4.42	6.43	8.54
			4.43	6.44	8.55
			4.44	6.47	8.60
				6.48	8.61
				6.52	8.62
					8.64
120	1.19	2.38	3.87	5.90	7.81
	1.20	2.39	3.95	5.92	7.86
	1.21	2.34	3.98	5.96	7.88
	1.22	2.35	4.00	5.98	7.89
	1.23	2.42	4.03	6.00	7.90
	1.25		4.07	6.01	7.92
	1.28		4.08		7.93
			4.16		7.94
			4.22		8.01
					8.02
					8.06
					8.07
					8.12
					8.11

Table A8.4. Error analysis

Sandpaper grit	Pump-motor power (Hz)	Average pressure drops, ΔP (kPa)	Total Error (%)	Overall Error (%)
80	10	1.4	1	1.2
	15	2.7	1	
	20	4.4	1	
	25	6.4	1	
	30	8.5	1	
120	10	1.2	2	
	15	2.4	1	
	20	4.0	2	
	25	6.0	1	
	30	8.0	1	

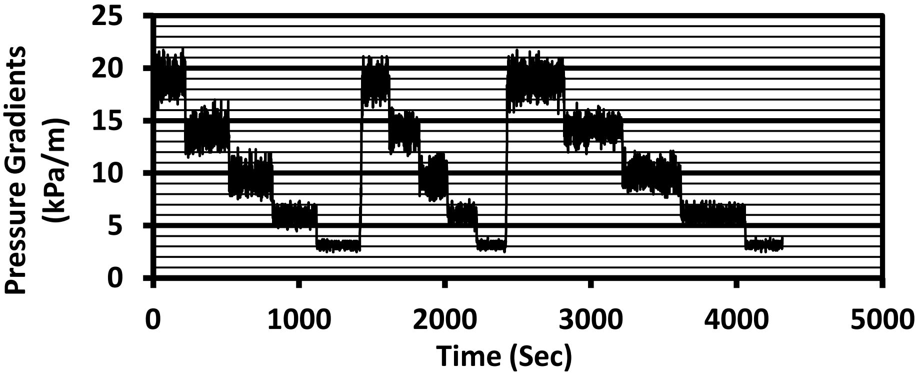

(a)

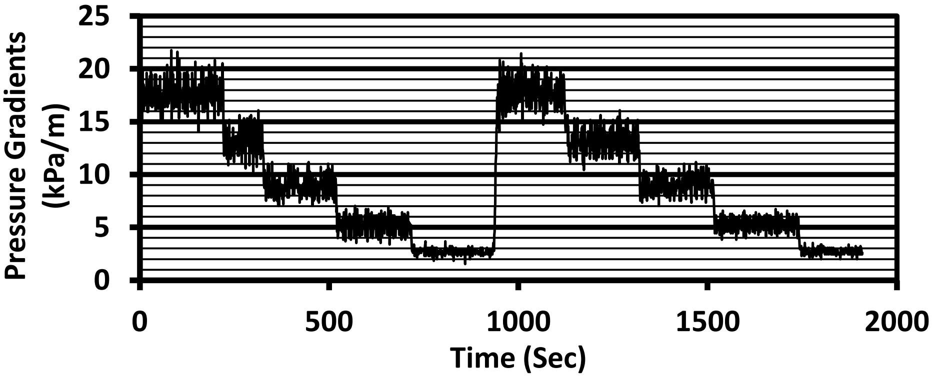

(b)

Figure A8.2. Instantaneous pressure gradients vs time graphs: (a) Sandpaper grit 80 & (b) Sandpaper grit 120.

Table A8.5. Comparison of simulation results with experimental measurements of pressure gradients

Sandpaper grit	Mass flow rate of water, m_w (kg/s)	Pressure gradients, ΔP/L (kPa/m)		Hydrodynamic roughness, k_s (mm)
		Experiment	Simulation	
80	0.589	3.1	2.7	0.53
	0.912	5.9	5.9	
	1.202	9.7	9.7	
	1.516	14.2	14.9	
	1.783	18.8	20.3	
120	0.589	2.8	2.7	0.31
	0.912	5.3	5.8	
	1.202	8.9	9.5	
	1.516	13.3	14.5	
	1.783	17.7	19.7	

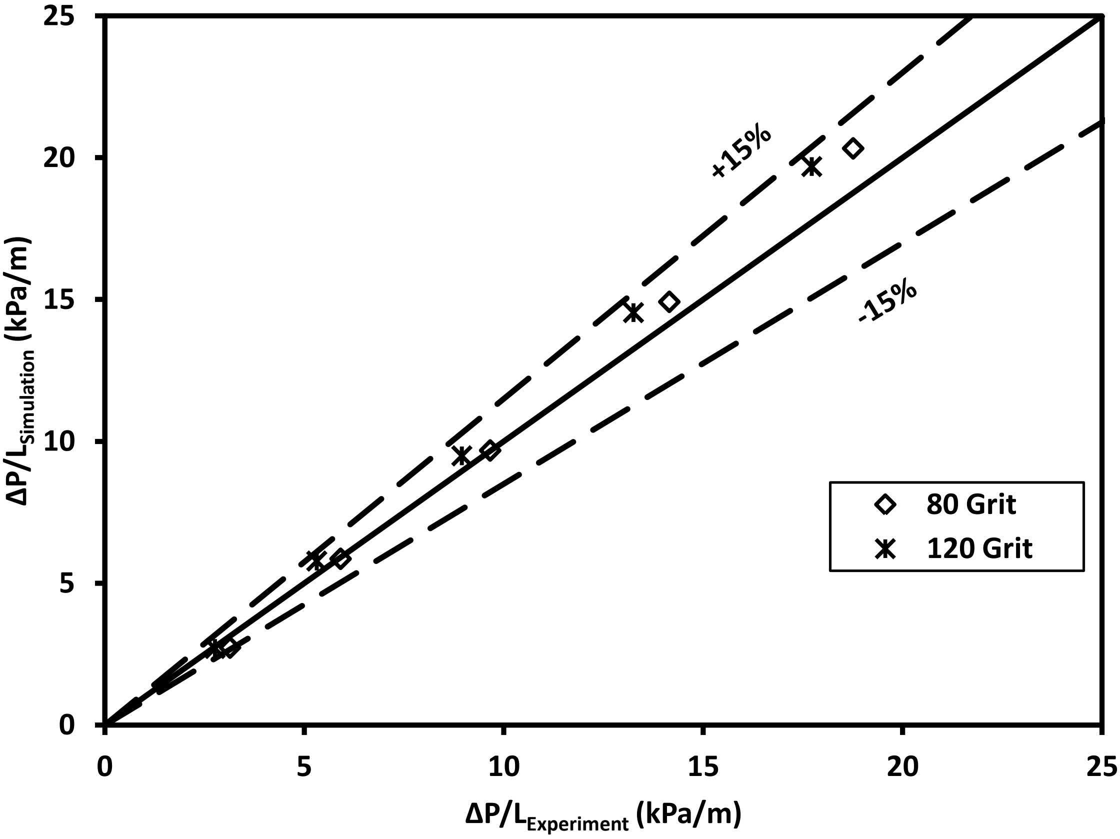

Figure A8.3. Graph showing the simulation results for pressure gradients as a function of corresponding experimental measurements

B. Bio-fouling

(i) The CFD method for determining hydrodynamic roughness was validated by using a set of experimental data involving bio-fouling on a wall. The work was conducted by Andrewartha (2010). A rectangular flow-cell with the dimensions of h × l × w = 200mm × 600mm × 1000mm was used for the experiments. It was fabricated with Perspex. Among the four walls of the cell, three were smooth and the rest was coated with bio-fouling layer. The custom built flow-cell, i.e., the 'work station' was connected to a considerably large water tunnel. The complete flow-loop is presented with following figures.

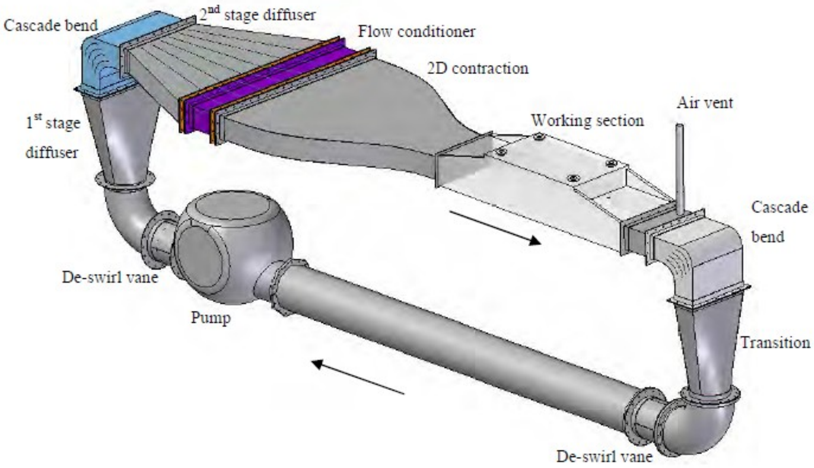

Figure A8.4. Schematic presentation of the flow-loop[††]

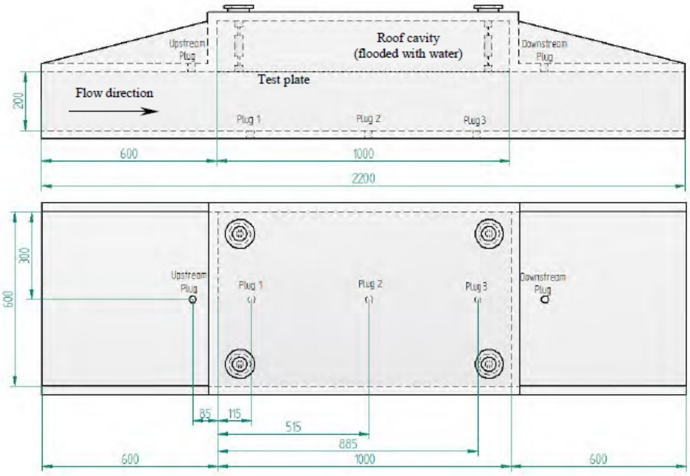

Figure A8.5. Schematic presentation of the working section (dimensions are in mm)[‡‡]

[††] Figure 4.1 in Andrewartha (2010).

[‡‡] Figure 4.2 in Andrewartha (2010).

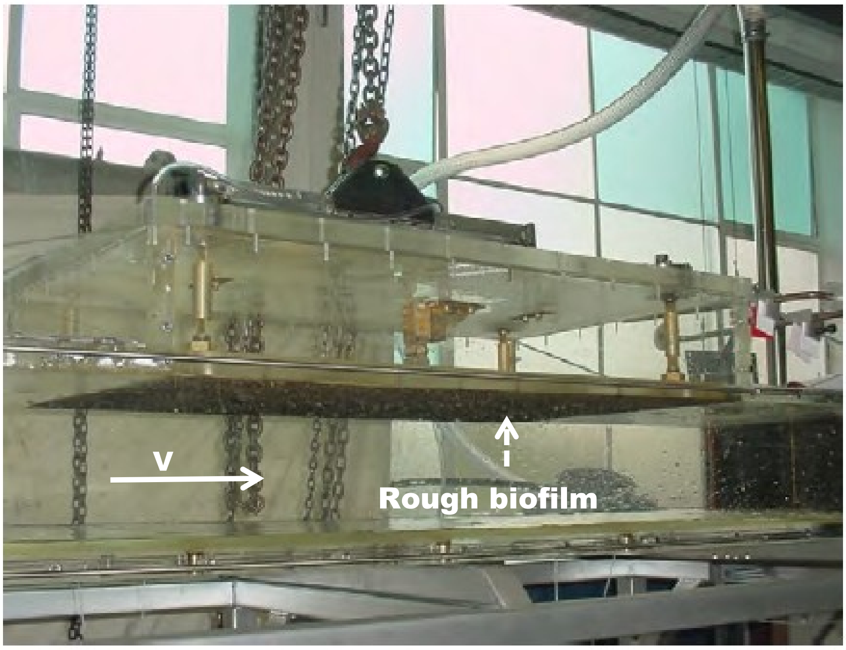

Figure A8.6. Photograph of the working section loaded with bio-fouled wall[§§]

(ii) Two separate parameters, namely the velocity profile perpendicular to bio-fouled wall and the axial drag on the fouled plate were measured. The velocity profile was measured by using both Pitot tube and Laser Doppler Velocimeter. The drag force was measured directly with a transducer. The measurements were used for estimating the hydrodynamic roughness, i.e., the equivalent sand grain roughness (k_s). Please refer to Chapter 5 and Chapter 6 in the reference for the details of the complex procedures used for the calculation.

(iii) We determined the same k_s values by applying the CFD methodology described in Chapter 3. The experimental velocity profiles were simulated with the specification of k_s for the bio-fouled rough wall. The value that can satisfactorily reproduce the measured profile was considered as the representative k_s for the corresponding bio-fouling layer.

(iv) Main purpose of this analytic work is to test the applicability of our CFD procedure in a different context. It helps developing confidence on the simulation technique used to know the unknown k_s for a complicated rough surface.

[§§] Figure 5.17 in Andrewartha (2010).

Table A8.6. Comparison of the experimental hydrodynamic roughness with simulation results.

Bio-fouling Sample	Hydrodynamic Roughness, k_s (mm)		
	Experiment (Andrewartha, 2010)		CFD Simulation (Current work)
	Drag	*Velocity Profile*	
RP1F1	5.73	5.33	5.50
RP1F4	4.47	3.47	4.00
RP2F5	4.37	2.59	3.00
SP1F6	1.03	0.00 (Smooth)	0.00 (Smooth)

(v) The experimentally determined values of k_s and the corresponding results obtained from the CFD simulations are compared here. The simulated results are decided on the basis of the agreement with measured velocity profile. An example of such agreement is represented with following figure.

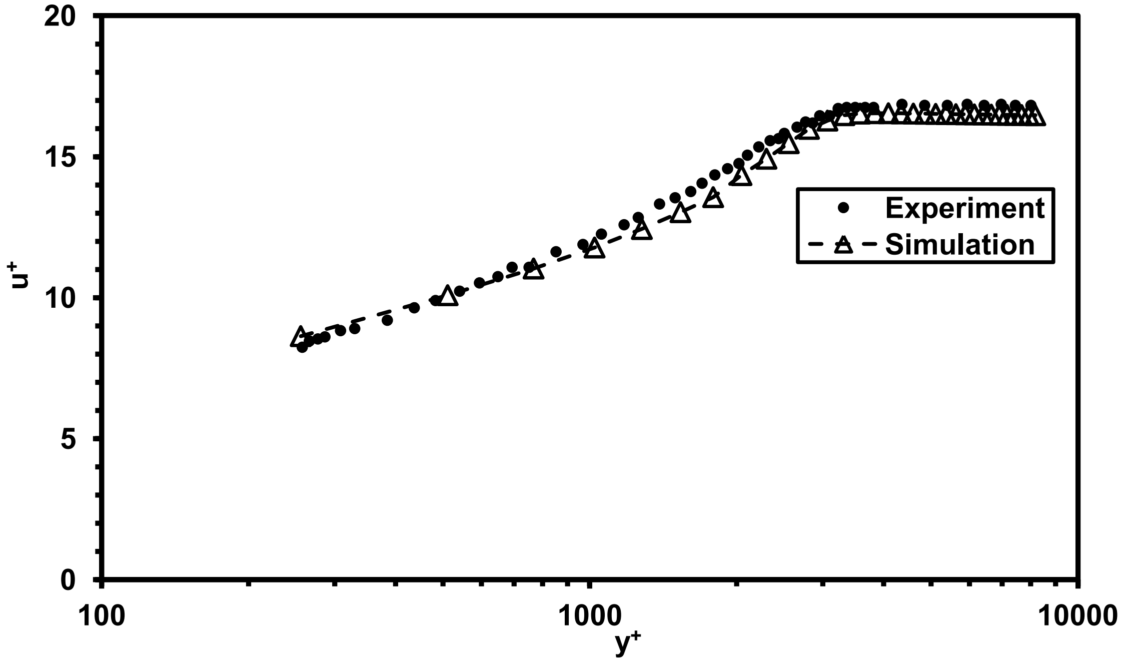

Figure A8.7. Example of the agreement between experimental measurements and simulation results

(vi) The experimental data of k_s for bio-fouling layer show that a conformable layer of wall-fouling can generate high roughness under a turbulent flow condition. This situation is comparable to our experiments where wall-coating layers of a viscous oil yield high roughness. The viscous wall-coating can also be considered as conformable.

(vii) The level of uncertainty involved in the determination of k_s for an unusual rough surface, like a bio-fouling layer is evident from the experimental results. The experimental results determined on the basis of two different measured parameters differ noticeably from each other. It should be mentioned that the parameters were measured in parallel under the same process conditions for the same sample.

(viii) Simulation results are obtained by reproducing the velocity profiles. For that reason the values of simulated k_s agree better with the similar experimental values estimated using the velocity profiles. The simulation results also match well with the k_s obtained by measuring drag. The results are actually within the range of experimental measurements. This agreement proves that the CFD method is an effective tool for determining $\mathrm{k_s}$. It is simple and capable of yielding reliable results.

(ix) The agreement between experimental and simulated velocity profile for the appropriate hydrodynamic roughness is appreciable. This kind of compliance demonstrates the option of reproducing a measured parameter with CFD simulation if $\mathrm{k_s}$ for the walls are specified properly. Thus, it implicitly supports the procedure of determining $\mathrm{k_s}$ by simulating other measured parameters, like pressure gradient.

APPENDIX 9

EXPERIMENTAL DATA AND SIMULATION RESULTS FOR THE SRC TESTS

Table A9.1. Calibration data set (Temperature, $T \sim 25°C$)

Data Point #	ID (mm)	Experimental data					Simulation results	
		Average Velocity, V (m/s)	Lubricating water fraction, C_w	Wall-fouling thickness, t_c (mm)	Pressure gradient, $\Delta P/L$ (kPa/m)	Oil viscosity, μ_o (Pa.s)	Pressure Gradient, $\Delta P/L$ (kPa/m)	Equivalent sand grain roughness, k_s (mm)
1	103.3	1.0	0.28	0.7	0.39	~ 1.3	0.38	0.075
2		1.5	0.29	0.4	0.56		0.60	0.010
3		2.0	0.29	0.2	0.73		0.73	0.000
4		1.0	0.4	0.6	0.40		0.37	0.300
5		1.5	0.42	0.4	0.58		0.57	0.175
6		2.0	0.42	0.2	0.69		0.67	0.025
7		1.0	0.31	2.4	0.65	~ 26.5	0.68	0.600
8		1.5	0.31	1.4	0.90		0.92	0.175
9		2.0	0.26	1.0	1.20		1.20	0.025
10		1.0	0.43	2.3	0.51		0.52	1.000
11		1.5	0.42	1.6	0.78		0.78	0.250
12		2.0	0.41	1.0	1.10		1.05	0.150
13		1.0	0.40	1.1	0.43	~ 1.4	0.44	0.500
14		1.5	0.40	0.9	0.67		0.68	0.175
15		2.0	0.40	0.7	0.84		0.84	0.050
16		1.0	0.28	1.0	0.45		0.43	0.100
17		1.5	0.29	0.8	0.67		0.67	0.030
18		2.0	0.29	0.7	0.83		0.80	0.000
19	264.8	1.0	0.39	2	0.13		0.12	0.450
20		1.5	0.39	2	0.23		0.22	0.350
21		2.0	0.38	2	0.33		0.33	0.150
22		1.0	0.24	2	0.14		0.14	0.200
23		1.5	0.26	2	0.24		0.23	0.100
24		1.0	0.39	2	0.13		0.12	0.450

Table A9.2. Test data set (Temperature, $T \sim 35°\text{C}$)

Data Point #	ID (mm)	Experimental data					Prediction	
							Correlation	CFD Simulation
		Average Velocity, V (m/s)	Lubricating water fraction, C_w	Wall-fouling thickness, t_c (mm)	Pressure gradient, $\Delta P/L$ (kPa/m)	Oil viscosity, μ_o (Pa.s)	Equivalent sand grain roughness, k_s (mm)	Pressure Gradient, $\Delta P/L$ (kPa/m)
1	103.3	1.0	0.17	1.0	0.55	~ 16.60	0.02	0.61
2		1.5	0.28	0.8	0.61		0.06	0.73
3		2.0	0.32	0.7	0.76		0.07	1.09
4		1.0	0.41	1.2	0.41		0.54	0.42
5		1.5	0.41	1.0	0.59		0.29	0.72
6		2.0	0.42	0.5	0.77		0.12	0.95
7		1.0	0.25	0.5	0.24	~ 1.22	0.04	0.34
8		1.5	0.24	0.3	0.42		0.01	0.66
9		2.0	0.25	0.4	0.54		0.02	1.07
10		1.0	0.39	0.5	0.23		0.19	0.32
11		1.5	0.39	0.3	0.37		0.07	0.55
12		2.0	0.39	0.4	0.52		0.07	0.88

Density of water at 35°C, $\rho_w = 994$ kg/m^3 (Kestin et al. 1978)

Viscosity of water at 35°C, $\mu_w = 0.7225$ mPa.s (Kestin et al. 1978)

Source of experimental data: Mckibben et al. (2007) and McKibben and Gillies (2009)

APPENDIX 10
DIMENSIONAL ANALYSIS

Step by step determination of the Π-groups

i. Dependent variable: k_s (L), t_c (L)

Number of variables: 2

Number of basic dimensions: 1

Number of Π-groups: 1

Determination of Π-groups:

$\Pi_1 = k_s(t_c^{a1}) \equiv L(L)^{a1} = L^0$

$L: 1 + a_1 = 0 \Rightarrow a_1 = -1$

$\Pi_1 = k_s/t_c = k_s^+$

ii. Independent variables: V (LT^{-1}), D (L), ρ_w (ML^{-3}), μ_w ($ML^{-1}T^{-1}$), μ_o ($ML^{-1}T^{-1}$)

Number of variables: 5

Number of basic dimensions: 3

Number of Π-groups: 2

Repeating variable: D, ρ_w, μ_w

Determination of Π-groups:

$\Pi_2 = V(D^{a2}\rho_w{}^{b2}\mu_w{}^{c2}) \equiv LT^{-1}(L)^{a2}(ML^{-3})^{b2}(ML^{-1}T^{-1})^{c2} = M^0L^0T^0$

$T: -1 - c_2 = 0 \Rightarrow c_2 = -1$

$M: b_2 + c_2 = 0 \Rightarrow b_2 = +1$

$L: 1 + a_2 - 3b_2 - c_2 = 0 \Rightarrow a_2 = +1$

$\Pi_2 = DV\rho_w/\mu_w = Re_w$

$\Pi_3 = \mu_o(D^{a3}\rho_w{}^{b3}\mu_w{}^{c3}) \equiv ML^{-1}T^{-1}(L)^{a3}(ML^{-3})^{b3}(ML^{-1}T^{-1})^{c3} = M^0L^0T^0$

$T: -1 - c_3 = 0 \Rightarrow c_3 = -1$

$M: 1 + b_3 + c_3 = 0 \Rightarrow b_3 = 0$

$L: -1 + a_3 - 3b_3 - c_3 = 0 \Rightarrow a_3 = 0$

$\Pi_3 = \mu_o/\mu_w = \mu^+$

iii. Result:

$\Pi_1 = f(\Pi_2, \Pi_3, C_w) \Rightarrow k_s^+ = f(Re_w, \mu^+, C_w)$

In addition to the variables mentioned previously, interfacial tension (σ_{ow}) between oil and water phase is also an independent variable. However, this parameter was considered insignificant for the current work based on an order of magnitude analysis that was conducted using two dimensionless groups: Capillary number (Ca) and Weber number (We).

Capillary number, $Ca = \mu_o V/\sigma_{ow}$ = Viscous force/Interfacial force

Weber number, $We = \rho_w V^2 D/\sigma_{ow}$ = Inertial force/Interfacial force

Orders of magnitude for the variables in these groups are:

$\mu_o \sim 10$ (Pa.s), $V \sim 1$ (m/s), $D \sim 0.1$ (m), $\rho_w \sim 1000$ (kg/m^3) $\sigma_{ow} \sim 0.01$ (N/m)

That is,

$Ca \sim 10^3$ and $We \sim 10^4$

Clearly, viscous and inertial forces in the CWAF system under consideration are much more significant than the interfacial force. That is why the interfacial tension (σ_{ow}) was not included in previous dimensional analysis.

APPENDIX 11

DEVELOPMENT OF THE CORRELATION

The procedure followed to develop the correlation is adopted from Bhagoria et al. (2002). The steps are described as follows.

Step 1

Figure A11.1 shows the relative roughness (k_s^+) as a function of the equivalent Reynolds number (Re_w). Following power law relation between k_s^+ and Re_w is obtained by fitting a power law curve in MS Excel.

$$k_s^+ = A_1 Re_w^{x1}$$

The values of the coefficients A_1 and x_1 are subject to the other independent dimensional groups and final regression analysis.

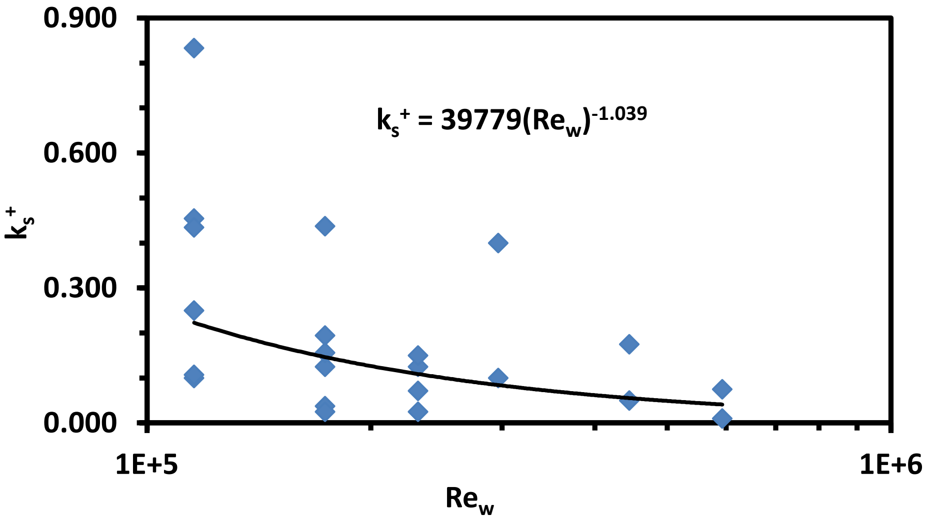

Figure A11.1. A plot of k_s^+ vs. Re_w.

Step 2

Taking the volumetric fraction of lubricating water (C_w) into account, the values of $k_s^+ Re_w^{-x1}$ are plotted against the corresponding values of C_w in Figure A11.2. Following power law relation is obtained by fitting a curve through the points.

$$k_s^+ Re_w^{-x1} = A_2 C_w^{y1}$$

The constants in this equation are reliant on further analysis.

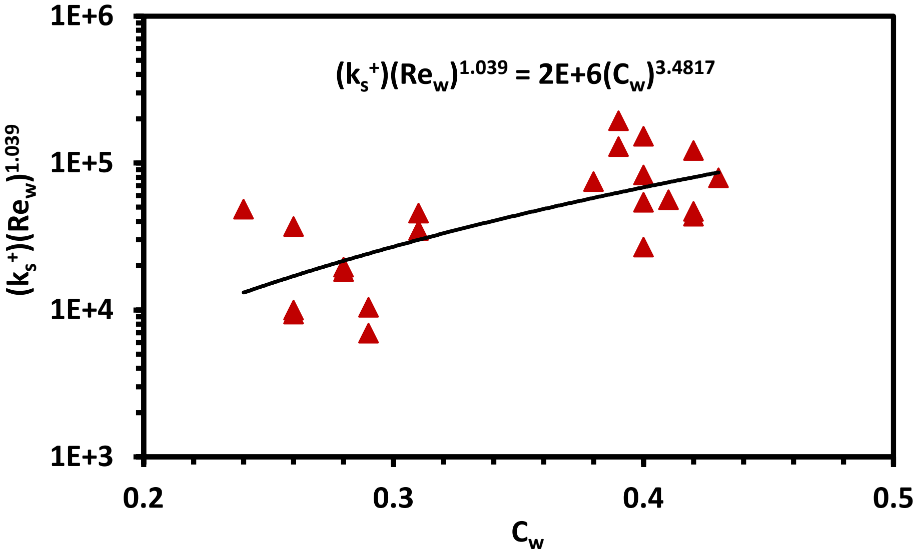

Figure A11. 2. Plot of $(k^+)(Re_w)^{1.039}$ vs. C_w.

Step 3

The values of $k_s^+ Re_w^{-x1} C_w^{-y1}$ are plotted with respect to the corresponding values of the relative viscosity (μ^+). The results are shown in Figure A11.3. Curve fitting through the points yields a power law relation as follows.

$$k_s^+ Re_w^{-x1} C_w^{-y1} = A_3(\mu^+)^{z1}$$

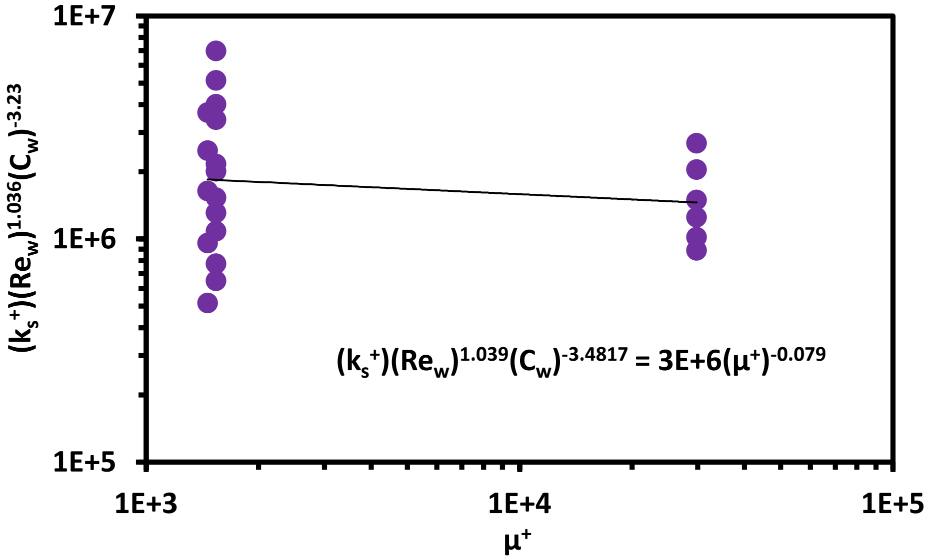

Figure A11. 3. Plot of $(k^+)(Re_w)^{1.039}(C_w)^{-3.4817}$ vs. μ^+.

It is evident from Figure A11.3 that $f(k^+, Re_w, C_w)$ does not necessarily depend on μ^+. The coefficient of μ^+ is 2 orders of magnitude less than those of Re_w and C_w. On the basis of this observation, the $f(k^+, Re_w, C_w)$, i.e., $k_s^+ Re_w^{-x1} C_w^{-y1}$ is considered to be independent of μ^+. That is, the coefficient of μ^+ is assumed as zero.

Step 4

The final equation obtained in Step 3 can be rearranged as follows.

$$k_s^+ = \mathrm{A}(Re_w)^{\mathrm{x}}(C_w)^{\mathrm{y}}(\mu^+)^{\mathrm{z}}$$

The values for the coefficients in this equation are as follows:

A = 1.6 × 10^6
x = -1.042
y = 3.435
z = 0

These are the optimum values for A, x, y and z obtained with regression analysis. The objective of the analysis is to maximize the coefficient of determination, R^2. It is a statistical parameter. The numeric value of R^2 is a measure of the extent to which the dependent parameter(s) is correlated to the independent parameter(s). The perfect correlation is presented by $R^2 = 1.00$. Current regression analysis yields a R^2 value of 0.72. Any value of R^2 less than 1.00 indicates the existence of discrepancy between the experimental results and the results predicted by the regression model.

Statistical definition of R^2:

$$R^2 = 1 - {}^{SS_{res}}\!/_{SS_{tot}}$$

Where,
Residual sum of squares, $SS_{res} = \sum_i (y_i - f_i)^2$
Total sum of squares, $SS_{tot} = \sum_i \left(y_i - y_{avg}\right)^2$

In these definitive equations y_i represents the results of k_s^+ obtained from experimental data and f_i corresponds to the modeled values.

The values of the statistical parameters are presented in Table A11.1.

Table A11.1. Values for the regression analysis

Predicted	Experimental	Average	S_{total}	SS_{total}	S_{res}	SS_{res}
f_i	y_i	y_{avg}	$(y_i-y_{avg})^2$	$\sum(y_i-y_{avg})^2$	$(f_i-y_i)^2$	$\sum(f_i-y_i)^2$
0.08	0.18	0.16	0.0004	0.36	0.0086	0.10
0.06	0.08		0.0064		0.0004	
0.02	0.10		0.0030		0.0058	
0.02	0.05		0.0111		0.0009	
0.01	0.01		0.0211		2.60E-05	
0.36	0.45		0.0896		0.0082	
0.24	0.19		0.0015		0.0020	
0.18	0.07		0.0070		0.0111	
0.11	0.10		0.0030		4.78E-05	
0.08	0.04		0.0138		0.0017	
0.11	0.11		0.0023		5.18E-08	
0.08	0.03		0.0170		0.0029	
0.28	0.44		0.0797		0.0241	
0.21	0.13		0.0009		0.0071	
0.15	0.25		0.0090		0.0097	
0.10	0.13		0.0009		0.0007	
0.04	0.03		0.0169		0.0002	
0.47	0.43		0.0782		0.0010	
0.28	0.16		1.15E-06		0.0158	
0.19	0.15		2.68E-05		0.0018	

APPENDIX 12

PARAMETRIC INVESTIGATION: ECCENTRICITY OF OIL CORE

The investigation is conducted on the basis of data point # 12 in Table A9.2. Details of the point are presented as follows.

Flow regime: Continuous water-assisted flow
Temperature (°C): 35
Pipe ID (mm): 103.3
Average velocity (m/s): 2.0
Lubricating water fraction: 0.39
Wall-fouling thickness (mm): 0.4
Oil viscosity (Pa.s): 1.22
Density of water (kg/m^3): 994 (Kestin et al. 1978)
Viscosity of water (mPa.s): 0.7225 (Kestin et al. 1978)

The effect of the eccentricity of the oil core on pressure gradient is analyzed by using the CFD methodology described in Section 5.2. An eccentric annular system is characterized using two parameters (Uner et al. 1989):

i) Eccentricity ratio or eccentricity (%), $R_e = 100C/(R - R_c)$
ii) Radius ratio, $R_r = R_c/R$

Where R_c is the radius of inner cylinder (oil core), R is that of the outer cylinder (pipe wall), and C is the distance between the centers of outer and inner cylinders. These parameters for an eccentric annulus have been presented in the following figure.

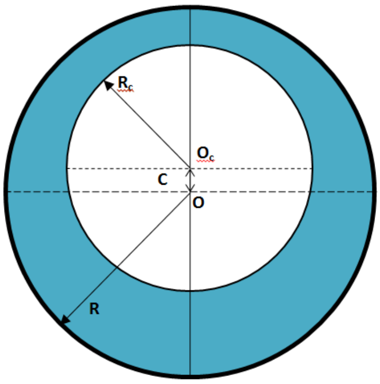

Figure A12.1. Schematic presentation of the eccentricity parameters (based on Figure 1 in Uner et al., 1989).

In addition to R_e (%) and R_r, another parameter is introduced here for presenting the simulation results. It is the Pressure Gradient Reduction (PGR %), which represents the percentile reduction in pressure gradient due to eccentricity of the core.

$$PGR\ (\%) = \frac{PG\ (Concentric) - PG\ (Eccentric)}{PG\ (Concentric)} \times 100$$

Details of simulation:

- Geometry:
  - Length (L) = 2 m
  - Radius of outer cylinder (R) = 51.25 mm
  - Radius of inner cylinder (R_c) = 37.2 mm
  - Distances between the centers (C) = 0, 2, 4, 6, 8, 10, 12 mm
- Boundary conditions:
  - Inlet/Outlet: calculated mass flow rate, m_w = 6.498 kg/s
  - Moving inner wall:
    - Calculated velocity, V_c = 2.35 m/s
    - Assumed wall roughness, k_s = 0 μm (Smooth)
  - Stationary outer pipe wall:
    - Assumed wall roughness, k_s = 0 μm (Smooth)
- Meshing:
  - Number of mesh elements: 1113552

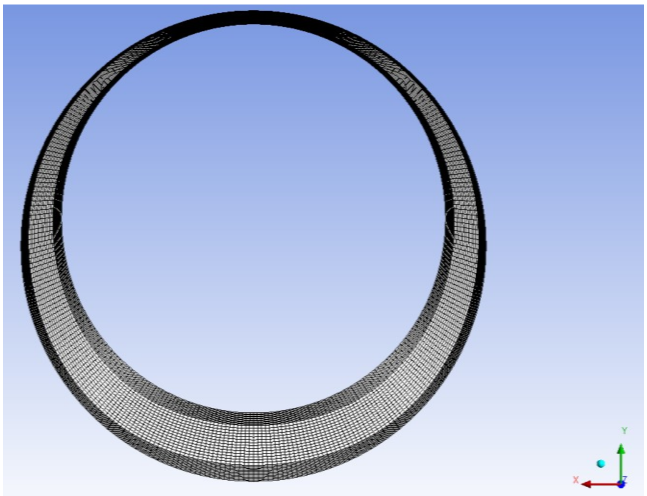

Figure A12.2. Example of meshing an eccentric annulus; total number of mesh elements 1113552.

Table A12.1. Simulation results for different eccentricity

Radius Ratio, R_r	Eccentricity, R_e (%)	Pressure Gradient, PG (kPa/m)	Pressure Gradient Reduction (%)
0.73	0	0.89	0
	14	0.89	0
	28	0.86	8
	43	0.86	8
	57	0.78	30
	71	0.73	43
	85	0.73	43

As can be seen from Table A12.1., less than 40% eccentricity (R_e) does not cause any appreciable change to the pressure gradients. However, the PG decreases for the R_e above 40%. The PG is reduced by more than 20% for $R_e > 50\%$.

APPENDIX 13

SAMPLE CALCULATIONS

A) Application of the correlation presented in Chapter 4

An example illustrating the application of the proposed correlation ($k_s = 2.76t_c$) is presented here. The correlation is used to predict the frictional pressure loss for a specific pipe flow case, and then the predicted value is compared with the measured value. The data for this example are reported by McKibben and Gillies (2009).

Measured/known parameters:

a) Internal diameter of the pipeline (D): 103.3 mm

b) Average water velocity (V): 1.0 m/s

c) Density of water (ρ_w): 997 kg/m^3

d) Viscosity of water (μ_w): 0.001 Pa.s

e) Average thickness of wall-coating/fouling (t_c) (measured): 2.0 mm

Calculations:

a) Effective diameter [D_{eff}]: $D_{eff} = D - 2t_c = 99.3\ mm$

b) Effective velocity [V_{eff}]: $V_{eff} = V\left(\frac{D}{D_{eff}}\right)^2 = 1.1\ m/s$

c) Reynolds number [Re_w]: $Re_w = \frac{D_{eff}V_{eff}\rho_w}{\mu_w} = 1.1 \times 10^5$

d) Equivalent hydrodynamic roughness [k_s]: $\boldsymbol{k_s = 2.76t_c = 5.52\ mm}$

e) Darcy friction factor [f], obtained using the Swamee-Jain correlation:

$$f = 0.25\left[log\left(\frac{\boldsymbol{k_s}}{3.7D_{eff}} + \frac{5.74}{Re_w^{0.9}}\right)\right]^{-2} = 0.0756$$

Prediction:

a) Pressure gradient [ΔP/L]: Darcy Weisbach equation:

$$\frac{\Delta P}{L} = f\frac{\rho_w V_{eff}^2}{2D_{eff}} = \boldsymbol{0.44\ kPa/m}$$

Measurement:

a) Pressure gradient [ΔP/L]: **0.45 kPa/m**

B) Application of the modeling methodology presented in Chapter 5

An example illustrating the application of the proposed modeling approach is presented here. The data for this example are taken from Appendix 9.

Measured/known parameters:

a) Internal diameter of the pipeline (D): 103.3 mm
b) Average velocity (V): 1.5 m/s
c) Temperature (T): 35°C
d) Density of water (ρ_w): 994 kg/m^3
e) Viscosity of water (μ_w): 0.0007225 Pa.s
f) Average thickness of wall-fouling (t_c): 0.8 mm
g) Lubricating water fraction (C_w): 0.28
h) Pressure gradient ($\Delta P/L$): 0.6 kPa/m

Calculations:

a) Hold-up ratio (H_w): 0.35 (Eq. 5.1)
b) Effective diameter (D_{eff}): 101.7 mm (Eq. 5.2)
c) Core diameter (D_c): 82.0 mm (Eq. 5.3)
d) Annular thickness (t_a): 9.9 mm (Eq. 5.4)
e) Equivalent water Reynolds number (Re_w): $Re_w = \frac{DV\rho_w}{\mu_w} = 2.1 \times 10^5$
f) Dimensionless hydrodynamic roughness (k_s^+): 0.057 (Eq. 5.5)
g) Hydrodynamic roughness/Equivalent sand grain roughness (k_s): $k_s = 0.057t_c = 0.046 \text{ mm}$
h) Average velocity of oil core, $V_c = \frac{V(\pi D^2/4)(1-C_w)}{\pi D_c^2/4} = V(D/D_c)^2(1-C_w) = 1.7\ m/s$

CFD simulation steps:

a) Generate a 9.9 mm thick and at least 1 m long annular flow domain; outer dia., $D_{out} = D_{eff}$ = 101.7 mm and inner dia., $D_{in} = D_c$ = 82.0 mm
b) Mesh the flow geometry; the region near the wall should be finer than the bulk region
c) Bring the flow geometry in CFD solver (ANSYS CFX 13.0) and fill the flow domain with 35°C water
d) Select the turbulence model, ω-RSM
e) Specify the boundary conditions as follows:

Outer stationary boundary: wall roughness, $k_s = 0.046$ mm

Inner moving boundary: velocity in flow direction, $v_z = V_c = 1.7$ m/s; smooth wall, $k_s = 0$

f) Solve for steady state solution

g) Calculate the length independent pressure gradient in the fully developed flow section

Predicted pressure gradient (ΔP/L): 0.7 kPa/m

Measured pressure gradient (ΔP/L): 0.6 kPa/m

APPENDIX 14

COMPARISON OF PROPOSED CORRELATIONS

In the current work, two novel correlations were proposed for two specific flow conditions:

Correlation 1: $\frac{k_s}{t_c} = k_s^+ = 2.76$

Correlation 2: $k_s^+ = \frac{1.6\times10^6}{(Re_w)^{1.042}}(C_w)^{3.435}$

Where k_s is the equivalent hydrodynamic roughness, t_c is the thickness of wall-coating or –fouling layer, Re_w is the water equivalent Reynolds number and C_w is the lubricating water fraction in a CWAF pipeline.

Correlation 1 was developed to predict the value of k_s produced by a wall-coating layer of viscous oil when only water flowed over the layer in turbulent condition. According to this correlation, the value of k_s^+ (k_s/t_c) is a constant independent of water flow rate (i.e., Re_w). In comparison to a CWAF pipeline, $C_w = 1$ under this specific flow condition.

Correlation 2 was proposed to predict k_s produced by the wall-fouling layer in a CWAF pipeline under operating condition. Here k_s^+ is dependent on Re_w and C_w. Performance of this correlation is shown in Figure A14.1(A), where predicted values of k_s^+ are presented as a function of C_w for the limiting values of Re_w. Most of the data points fall within the prediction lines.

In Figure A14.1(B), predictions of Correlation 2 for two different values of Re_w are extrapolated till $C_w = 1$ to compare with the prediction of Correlation 1. It should be mentioned that the applicable range of C_w for the correlation is 0.20 to 0.45. Although the prediction of Correlation 1 falls within the range of extrapolated values of Correlation 2 when $C_w = 1$, following points should be discussed:

a) Correlations 1 and 2 are applicable for completely different situations. Correlation 1 is to predict k_s when only water flows over a viscous wall-coating layer, while Correlation 2 is appropriate for the wall-fouling layer in a CWAF pipeline.

b) The mechanisms of sustaining wall-coating and wall-fouling are different. Flow of only water over a viscous coating layer may strip some oil to produce an equilibrium thickness for a flow rate (Re_w). Shear (i.e., velocity gradient) is the most important mechanism of developing roughness on the viscous surface. On the other hand, a wall-fouling layer in a CWAF pipeline is sustained with a dynamic equilibrium between stripping and deposition of oil droplets (see Chapter 5 for details). The continuous stripping and deposition of oil droplets, in addition to shear, play an important role in producing roughness on wall-fouling layer.

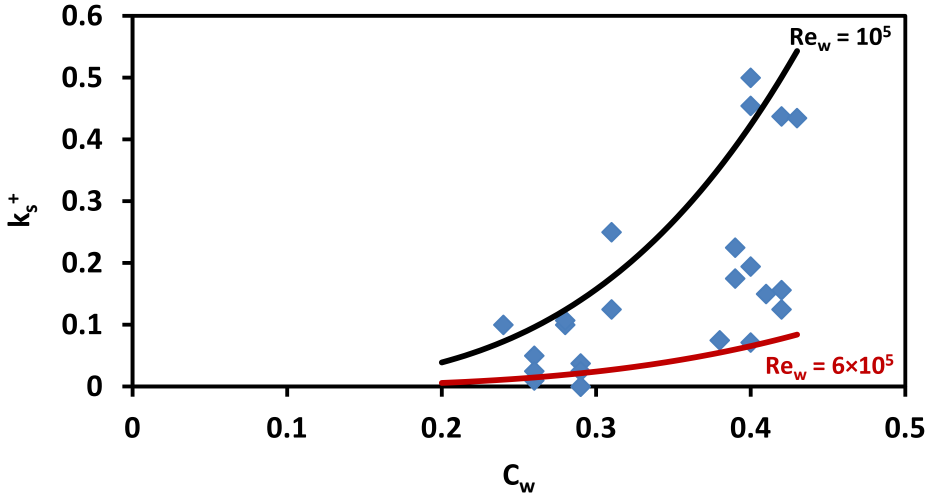

(A)

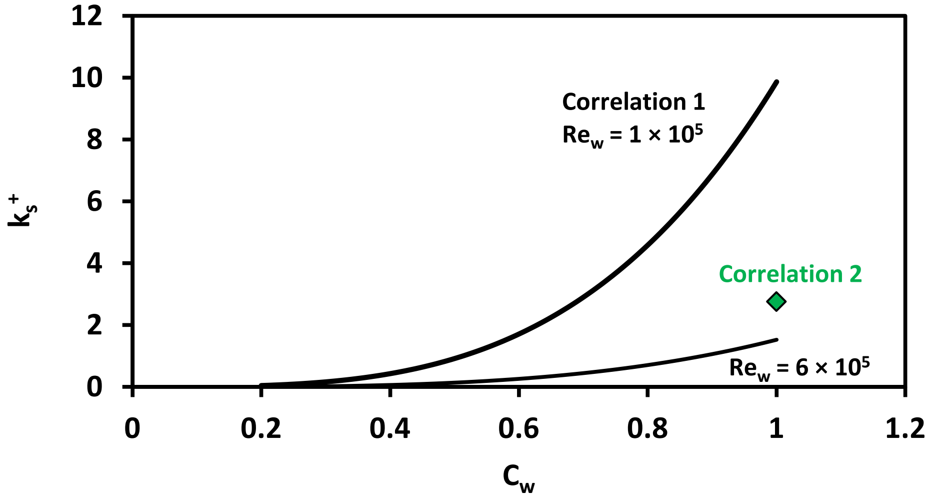

(B)

Figure A14.1. Predictions of two proposed correlations: (A) Correlation 2 in comparison to the data points; (B) Comparison of Correlations 2 and 1.